Report Title:	Final Report: Novel Adsorbent-Reactants for Treatment of Ash and Scrubber Pond Effluents
Type of Report:	Final Scientific/Technical Report
Reporting Period Start Date:	February 1, 2006
Reporting Period End Date:	January 31, 2010
Principal Author(s):	Bill Batchelor, Dong Suk Han, Eun Jung Kim
Date Report Issued:	April, 2010
DOE Award Number:	DE-FG26-06NT42731
Submitting Organization:	Texas A&M University 305 Admin Building 3121 TAMU College Station, TX 77843-3121

DISCLAIMER

ABSTRACT

The overall goal of this project was to evaluate the ability of novel adsorbent/reactants to remove specific toxic target chemicals from ash and scrubber pond effluents while producing stable residuals for ultimate disposal. The target chemicals studied were arsenic (As(III) and As(V)), mercury (Hg(II)) and selenium (Se(IV) and Se(VI)). The adsorbent/reactants that were evaluated are iron sulfide (FeS) and pyrite (FeS_2). Procedures for measuring concentrations of target compounds and characterizing the surfaces of adsorbent-reactants were developed. Effects of contact time, pH (7, 8, 9, 10) and sulfate concentration (0, 1, 10 mM) on removal of all target compounds on both adsorbent-reactants were determined. Stability tests were conducted to evaluate the extent to which target compounds were released from the adsorbent-reactants when pH changed. Surface characterization was conducted with x-ray photoelectron spectroscopy (XPS) to identify reactions occurring on the surface between the target compounds and surface iron and sulfur. Results indicated that target compounds could be removed by FeS_2 and FeS and that removal was affected by time, pH and surface reactions. Stability of residuals was generally good and appeared to be affected by the extent of surface reactions. Synthesized pyrite and mackinawite appear to have the required characteristics for removing the target compounds from wastewaters from ash ponds and scrubber ponds and producing stable residuals.

TABLE OF CONTENTS

LIST OF FIGURES

LIST OF TABLES

EXECUTIVE SUMMARY

The overall goal of this project was to evaluate the ability of novel adsorbent/reactants to remove specific toxic target chemicals from ash and scrubber pond effluents while producing stable residuals for ultimate disposal. The target chemicals studied were arsenic (As(III) and As(V)), mercury (Hg(II)) and selenium (Se(IV) and Se(VI)). The adsorbent/reactants that were evaluated are iron sulfide (FeS) and pyrite (FeS_2).

Procedures for measuring concentrations of arsenic and selenium were developed using hydride generation coupled with atomic adsorption spectroscopy (HG-AAS). Mercury analysis was conducted with a similar reduction step that produced elemental mercury which was analyzed by AAS. Acceptable precision and accuracy of all analytical procedures was demonstrated. Methods for characterizing the surfaces of adsorbent-reactants were developed and applied to both. Transmission electron microscopy was used to determine that pyrite particles sizes were 100-1000 nm and mackinawite particles sizes were less than 100 nm. Both solids were analyzed by X-ray photoelectron spectroscopy (XPS), which showed some surface oxidation and provided a baseline for use in determining changes resulting by reaction with target compounds.

Effects of contact time, pH (7, 8, 9, 10) and sulfate concentration (0, 1, 10 mM) on removal of arsenic (As(III) and As(V) were evaluated in batch experiments with pyrite and mackinawite. The rate of removal of As(III) by pyrite was slower than that of As(V). Extent of removal (amount removed/mass adsorbent-reactant) was well correlated for both forms of arsenic (As(III), As(V)) with concentration of target in solution using both Langmuir and Freundlich models. Removal of As(III) was observed by pyrite to increase over the pH range studied (7-10) and sulfate had little effect on removal. Moderate levels of stability were observed with pyrite-As(III). XPS analysis showed little evidence of surface reactions. As(V) was removed best in the range pH 8 to pH 9 and sulfate showed little effect on removals. Moderate stability of pyrite-As(V) was observed and XPS analysis showed some evidence of increased surface oxidation.

Removal of As(III) by mackinawite was rapid with half-life less than 10 minutes. There was a moderate effect of pH with greatest removals in the range pH 8-9. The Langmuir and Freundlich models did not correlate observations well, which could be the result of surface reactions. Some inhibition of As(III) removal by sulfate was observed. As(III)-FeS residuals were very stable, with littler arsenic release observed. This could be the result of surface reactions and XPS analysis indicated that As(III) was reduced on the FeS surface. Removal of As(V) by FeS was also fast, but there was a strong pH effect, with higher removals at lower pH. The classic models did not correlate observations well. Sulfate showed some inhibition of As(V) removal at high concentrations of As(V), but a smaller effect at lower concentrations. Moderate to high levels of stability were observed for As(V)-FeS and XPS showed some evidence for reduction of As(V) on the surface of FeS.

Removal of mercury by pyrite was rapid and extensive, with maximum loadings exceeding 6 mmol/g and in some cases as high as 20 mmol/g. Sulfate had little effect on mercury removal and XPS showed a little evidence of surface oxidation of iron, which could be related to reduction of mercury. XPS also indicated formation of mercury sulfides on the surface; however, reduced forms of mercury were not identified. Good stability of Hg-pyrite was observed. Removal of mercury by FeS was also observed to be rapid and extensive, with

maximum loadings as high as 50 mmol/g. The BET model was observed to best correlate loading with aqueous concentration. Sulfate had a slight effect of promoting mercury removal. Good stability of Hg-FeS was observed. XPS analysis indicated that mercury was being reduced by surface iron and sulfur.

Removal of Se(IV) by pyrite was slow with half-lives in the range of 25 to 55 hours, which indicates that surface reactions were occurring. There was little effect of pH on Se(IV) removal. Sulfate showed some inhibition at higher Se(IV) concentrations, but little effect at lower concentrations. Se(IV)-pyrite was stable with little selenium released. XPS analysis showed some oxidation of surface iron and sulfur, possibly indicating selenium reduction. Removal of Se(VI) by pyrite was rapid and pH had little effect on removal at low concentrations of Se(VI). Sulfate had little effect on removals at low Se(VI) concentration, but inhibited removal at high concentrations. Little stability of Se(VI)-pyrite was observed. XPS analysis indicated that surface iron was oxidized.

Removal of Se(IV) by mackinawite was very rapid and extensive. Removal patterns followed the BET model, indicating the possible effect of surface reactions. Sulfate had little effect on Se(IV) removal and Se(IV)-FeS mixtures showed high stability. XPS analysis indicated oxidation of surface iron, some evidence for oxidation of surface sulfur and some evidence for reduction of Se(IV). Removal of Se(VI) by mackinawite was less extensive than that of Se(IV) but was not inhibited by sulfate. The removal patterns followed the BET model, which supports the existence of surface reactions. High stability of Se(VI)-FeS was observed. XPS analysis showed some evidence of oxidation of surface iron and sulfur, but not as extensively as observed for Se(IV).

These results generally show that the two adsorbent-reactants (pyrite, mackinawite) have the chemical characteristics that make them suitable for application in treatment processes to remove arsenic, selenium and mercury from ash pond and scrubber pond wastewaters. In most cases, they were able to effectively remove the target contaminants and produce stable residuals. The effects of sulfate were generally small, so that application to waters high in sulfate is not precluded. XPS analysis as well as behavior in kinetic, removal and stability experiments indicated that surface reactions are often important. However, development of treatment processes based on these adsorbent-reactants depends on developing efficient contact methods. These contact methods could be based on using small particles, such as used in this study; however, effective separation processes would need to be developed. An alternative contact method would be to develop macro-scale adsorbent particles by aggregating smaller particles or producing small particles within a pre-formed macro-porous solid phase.

EXPERIMENTAL METHODS

Analytical Procedures

Arsenic Analysis

Analytical procedures were developed for arsenic (As(III) and As(V)), mercury, and selenium (Se(IV), Se(VI)). The technique for arsenic analysis was based on the continuous hydride generation /atomic absorption spectrometer method, Standard Method 3114C (Eaton, et al, 1995). It was modified to be conducted with a model Solar M6 atomic absorption spectrometer with model V90 continuous hydride generator manufactured by Thermo Elemental. It was also modified to speciate arsenic between As(III) and total arsenic (As(III) + As(V)) based on the relative reactivities of As(III) and As(V) at different pH (Masscheleyn et al, 1991). At low pH, both As(III) and As(V) can be reduced by sodium borohydride to arsine gas. However, at moderate pH, only As(III) is reduced. Therefore, As(III) is measured by mixing a sample flow of 7 mL/min, an equal flow of phosphate buffer (0.2 M NaH_2PO_4) and a 3.5 mL/min flow of sodium borohydride. The arsine gas is removed from the solution by purging with a 250 mL/min flow of argon and it is transferred to the flame AA where its concentration is determined by comparison with standard responses. Total arsenic is determined by a similar procedure, but the buffer flow is replaced with a flow of strong acid (5 M HCl). The concentration of As(V) is determined as the difference between the total arsenic concentration and the As(III) concentration.

Calibration curves were developed for As(III) and As(V) and they are shown in Figure 1. Regressions lines gave R^2 values of 0.999 and 0.998 for As(III) and As(V), respectively.

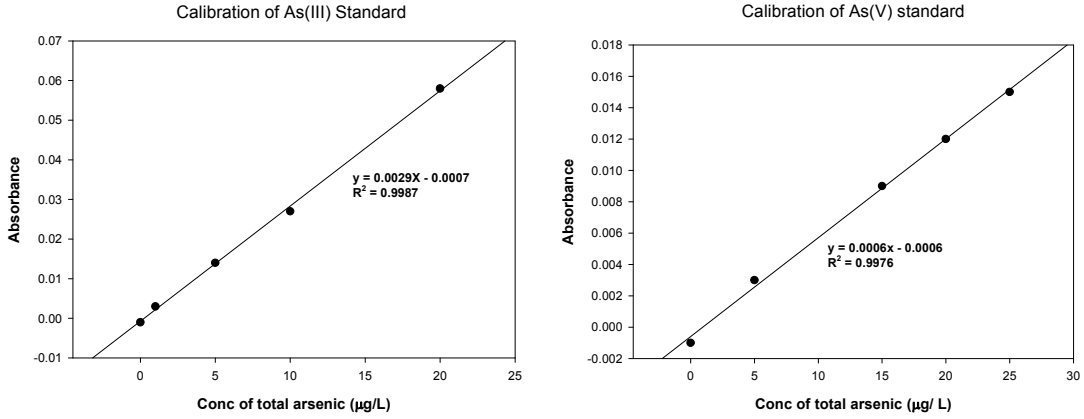

Figure 1. Calibration curves for analysis of As(III) and As(V)

Precision and accuracy of the measurement techniques for As(III) were determined by conducting replicate measurements of samples containing 10 and 15 µg/L. The results of these measurements are shown in Tables 1 and 2. The results demonstrate an average recovery (accuracy) of 100.3% and an average relative standard deviation (precision) of 0.2%. These results can also be used to calculate an average method detection limit of 0.1 µg/L. Precision and accuracy of the technique for As(V) measurement was determined by conducting replicate measurements of solutions containing 10 and 20 µg/L As(V). The results are shown in Tables 3 and 4. Average recovery (accuracy) was 100.4% and average relative standard deviation (precision) was 1.2%. The method detection limit was calculated from these results as 0.8 µg/L.

Table 1. Recovery of As(III) of 10 µg/L

Abs	Conc (µg/L)	mean	SD	Recovery (%)	Error (%)
0.0285	10.07	10.05	0.03	100.7	0.690
0.0284	10.03			100.3	0.345
0.0285	10.08			100.8	0.793
0.0283	10.00			100.0	0.034
0.0285	10.05			100.5	0.517

Table 2. Recovery of As(III) of 15 µg/L

Abs	Conc (µg/L)	mean	SD	Recovery (%)	Error (%)
0.0428	15.00	15.01	0.011	100.0	0.023
0.0428	15.01			100.0	0.046
0.0429	15.02			100.1	0.115
0.0429	15.02			100.2	0.161
0.0428	15.00			100.0	0.023

Table 3. Recovery of As(V) of 10 µg/L

Abs	Conc (µg/L)	mean	SD	Recovery (%)	Error (%)
0.0054	10.03	10	0.05	100.3	0.333
0.0054	9.98			99.8	0.167
0.0054	10.07			100.7	0.667
0.0054	9.95			99.5	0.500
0.0054	9.97			99.7	0.333

Table 4. Recovery of As(V) of 20 µg/L

Abs	Conc (µg/L)	mean	SD	Recovery (%)	Error (%)
0.0117	20.50	20.6	0.40	102.5	2.500
0.0121	21.17			105.8	5.833
0.0119	20.83			104.2	4.167
0.0115	20.17			100.8	0.833
0.0116	20.33			101.7	1.667

Mercury Analysis

A Cold Vapor Atomic Absorption Spectrometry method was adopted for use to analyze mercury. It was similar to that used for analysis of arsenic, but the VP90 "T" cell was replaced with a 15 cm quartz cell. Mercury was reduced by borohydride (1% $NaBH_4$ in 0.05% NaOH) to mercury and removed by purging. The following parameters were used during analysis: wavelength of 253.7 nm, band pass of 0.5 nm, lamp current of 75%, measurement number of 4, measurement time of 4 s, background correction is off, stabilization time of 60 s, baseline delay time of 60 s, carrier gas flow of 240 mL/min.

A calibration curve was developed for mercury analysis and the result is shown in Figure

2. The R^2 value for the regression line through the data is greater than 0.999.

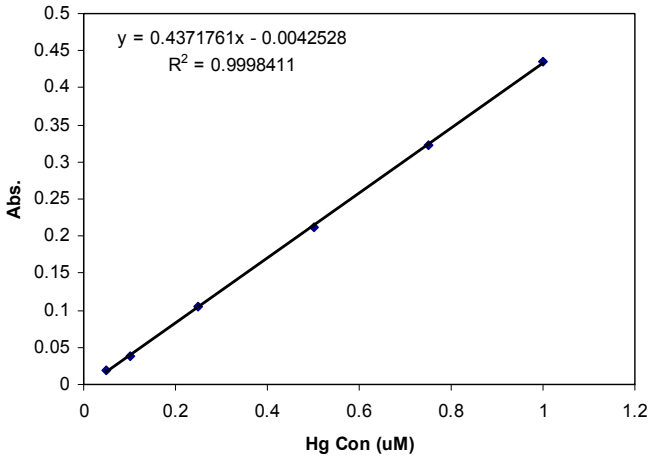

Figure 2. Calibration curve for analysis of mercury

Precision and accuracy was determined from replicate analysis of a 0.25 μM (50.1 μg/L) mercury standard. The results are shown in Table 5. The average recovery (accuracy) was 102.5% and the relative standard deviation (precision) was 0.56%. Replicate analyses were also conducted with a lower concentration of mercury to more accurately determine the method detection limit. Therese results are shown in Table 6 and result in a method detection limit of 0.002 μM (0.4 μg/L)

Table 5. Replicate Measurements of Mercury (0.25 μM)

Measurements	Conc (μM)	Recovery (%)
1	0.2533	102.9
2	0.2562	101.6
3	0.2562	101.1
4	0.2562	102.4
5	0.2573	103.4
6	0.2562	102.4
7	0.2579	101.1

Table 6. Replicate Measurements of Mercury (0.05 μM)

Measurements	Conc (μM)
1	0.0578
2	0.0560
3	0.0566
4	0.0566
5	0.0578
6	0.0566
7	0.0566

Selenium Analysis

Selenium as Se(IV) or Se(VI) was analyzed by a similar hydride generation atomic absorption spectrometry method using Thermo Elemental Solar M6 AA and VP90 continuous

hydride generator. Selenite (Se(IV)) was reduced by borohydride (0.75% $NaBH_4$ in 0.25% NaOH) and analyzed after purging by flame AA. Selenate (Se(VI)) was first reduced to selenite by acid digestion (5 mL sample, 5 mL concentrated HCl in 40 mL borosilicate glass vial placed in boiling water bath for 20 minutes). The following parameters were used for these analyses: wavelength of 196.0 nm, band pass of 0.5 nm, lamp current of 75%, measurement number of 4, measurement time of 4 s, background correction is off, stabilization time of 30 s, baseline delay time of 40 s, carrier gas flow rate of 240 mL/min.

A calibration curve was prepared for the selenite analysis procedure and it is shown as Figure 3. The R^2 value for the linear regression line through the data was 0.999.

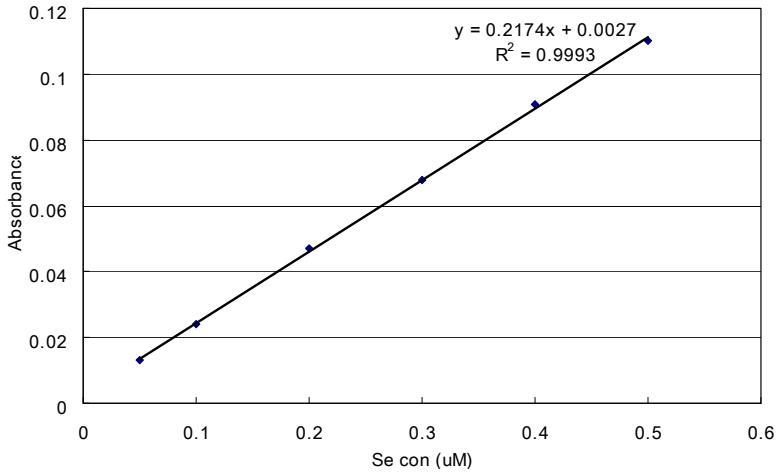

Figure 3. Calibration curve for selenite analysis.

Replicate analyses were conducted to determine the accuracy and precision of the selenite analysis procedure and the results of these tests are shown in Table 7. The average recovery (accuracy) was 101.0% and the relative standard deviation (precision) was 2.1%. Additional replicate measurements were conducted at a lower concentration (0.02 μM) to more determine the method detection limit and the results of these experiments are shown in Table 8. They provide a method detection limit of 0.006 μM (0.5 μg/L).

Table 7. Replicate Analyses of Selenite (0.30 μM)

Measurements	Conc (μM)	% recovery
1	0.310	103.5
2	0.310	103.5
3	0.306	101.9
4	0.306	101.9
5	0.292	97.4
6	0.297	98.9
7	0.301	100.4
8	0.301	100.4

Table 8. Replicate Measurements of Selenite (0.20 μM)

Measurements	Conc (μM)
1	0.015
2	0.015
3	0.020
4	0.015
5	0.015
6	0.015
7	0.015
8	0.020

A calibration curve was prepared for selenate (Se(VI)) and it is shown as Figure 4. A regression equation for this curve gave an R^2 value above 0.999. Analyses were conducted on solutions of selenite and selenium that contained the same concentration of selenium. The results are shown in Table 9 and demonstrate that near complete conversion of selenate to selenite occurs during the pre-digestion step. Replicate measurements were conducted to determine accuracy and precision of the analytical technique. Results of these experiments are presented in Table 10. they show an average recovery (accuracy) of 102% and a relative standard deviation (precision) of 0.86%. Additional replicate experiments were conducted with a lower concentration to more accurately determine the method detection limit. These results are shown in Table 11 and they result in a method detection limit of 0.0028 μM (0.22 μg/L). A mixture of selenite (0.2 μM) and selenate (0.2 μM) was analyzed for selenite (no pre-digestion) and total selenium (pre-digestion). The concentration of selenate was determined by difference. The results are shown in Table 12.

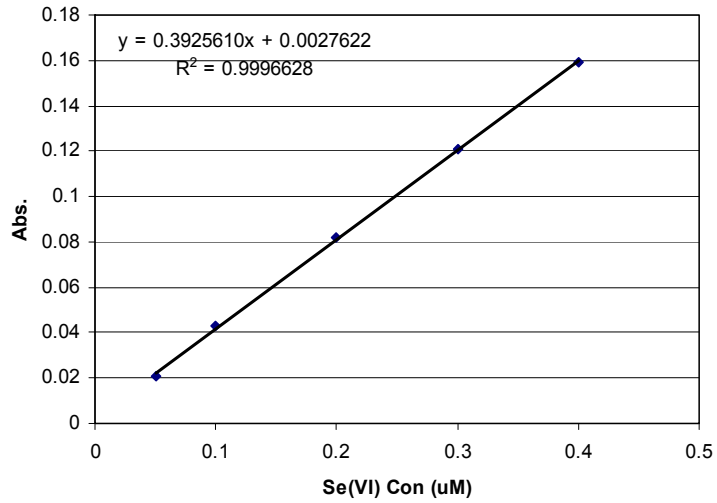

Figure 4. Calibration Curve for Selenate (Se(VI)) Analysis

Table 9. Comparison of Selenite and Selenate Measurements

Con.(μM)	Abs.		Recovery of Se(VI) compared to Se(IV) (%)
	Se(VI)	Se(IV)	
0.05	0.021	0.022	95.5
0.1	0.043	0.043	100.0
0.2	0.082	0.082	100.0
0.3	0.121	0.119	101.7
0.4	0.159	0.156	101.9

Table 10. Replicate measurements of selenate (0.25 μM)

Measurements	Conc (μM)	Recovery (%)
1	0.2573	102.9
2	0.2541	101.6
3	0.2528	101.1
4	0.2560	102.4
5	0.2585	103.4
6	0.2560	102.4
7	0.2528	101.1

Table 11. Replicate measurements of selenate (0.05 μM)

Measurements	Conc (μM)
1	0.0522
2	0.0516
3	0.0516
4	0.0503
5	0.0516
6	0.0509
7	0.0496

Table 12. Analysis of Mixture of Selenite (0.2 μM) and Selenate (0.2 μM)

Sample	Se(IV) (no digestion)	Total Se (digestion)	Se(VI) Total Se – Se(IV)
1	0.205	0.390	0.185
2	0.204	0.387	0.183

Iron Analysis

A procedure for iron analysis was developed to be used in conjunction with the methods for analyzing pyrite and iron sulfide. The ferrozine method (Gibbs, 1976) was adopted for analyzing ferrous iron (Fe(II)) and total iron (Fe(II) + Fe(III)). Fe(II) was analyzed by mixing with a ferrozine color reagent (ferrozine in 10% ammonium acetate) and determining the absorbance at 562 nm with a Hewlett-Packard 8452A diode-array spectrophotometer. Total iron was determined by including a reductant (10% hydroxylamine) with the color reagent so that all Fe(III) would be reduced to Fe(II) before color formation.

Calibration curves were developed for analysis of Fe(II) and Fe(tot) and they are shown in Figure 5. The R^2 values for the linear regression lines through the data were 0.999 for Fe(II) and 0.998 for Fe(tot). Replicate analyses for Fe(II) and Fe(tot) were conducted and the results are shown in Tables 13 and 14, respectively. The average recovery (accuracy) of the Fe(II)

analysis procedure was 95.1% and the average relative standard deviation (precision) was 1.2%. The average recovery (accuracy) for the Fe(tot) analysis procedure was 105.7% and the average relative standard deviation (precision) was 0.2%.

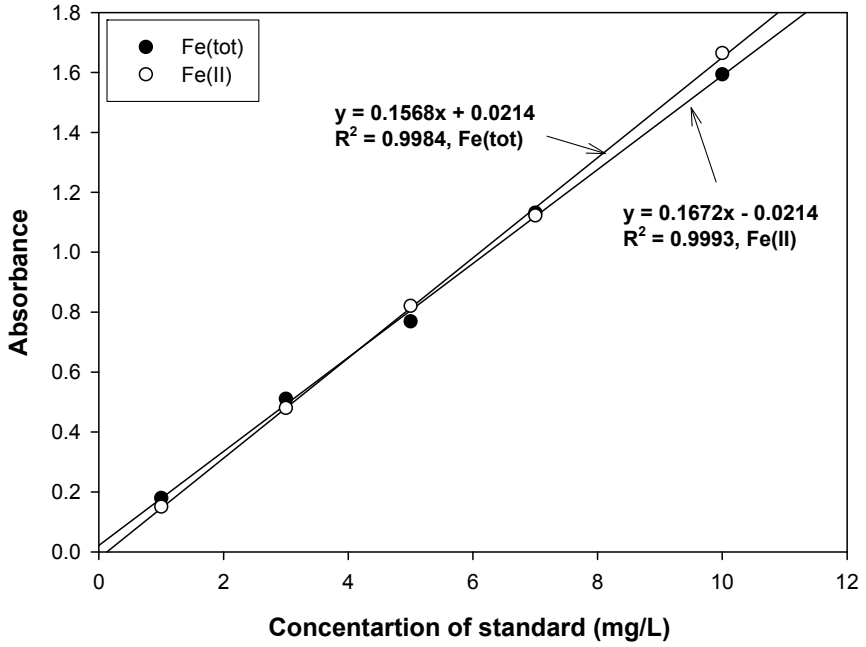

Figure 5. Calibration curves for Fe(II) and Fe(tot)

Table 13. Recovery of Fe(II) (4 mg/L and 8 mg /L)

		For 4 mg Fe(II)/L			
Abs	**Conc (mg/L)**	**mean**	**SD**	**Recovery (%)**	**Error (%)**
0.60598	3.69	3.67	0.02	92.3	7.75
0.60574	3.68			92.0	8.00
0.59888	3.65			91.2	8.75
		For 8 mg Fe(II)/L			
Abs	**Conc (mg/L)**	**mean**	**SD**	**Recovery (%)**	**Error (%)**
1.3036	7.94	7.87	0.15	99.2	0.75
1.3110	7.98			99.7	0.25
1.2644	7.70			96.3	3.75

Table 14. Recovery of Fe(tot) (4 mg/L and 8 mg/L)

		For 4 mg Fe(tot)/L			
Abs	**Conc (mg/L)**	**mean**	**SD**	**Recovery (%)**	**Error (%)**
0.7029	4.39	4.38	0.01	109	9.75
0.7012	4.38			109	9.50
0.7002	4.37			109	9.25
		For 8 mg Fe(tot)/L			
Abs	**Conc (mg/L)**	**mean**	**SD**	**Recovery (%)**	**Error (%)**
1.302	8.14	8.15	0.01	101	1.75
1.306	8.16			102	2.00
1.303	8.15			101	1.88

Iron sulfide was analyzed by dissolving the solid with HCl and measuring Fe(II) in the remaining solution. Pyrite was analyzed using its differential solubility. Pyrite will not dissolve in HCl, but it will dissolve in hot HNO_3. Therefore, the sample is contacted with HCl, the solids separated, mixed with concentrated HNO_3 and heated for 15 to 20 min. The concentration of iron in the resulting solution is measured and the concentration of FeS_2 calculated by stoichiometry.

Pyrite was synthesized using a modification of the method of Wei et al. (1997). Equal volumes of 0.1 M Fe(III) and 0.2 M NaHS stock solutions are combined. The pH is adjusted to 4.5 by addition of HCl. This solution is aged at 60 ^{o}C for 24 hr. The suspension can be analyzed for FeS and FeS_2.

Instrumental Analysis Procedures

Powder X-ray Diffraction Analysis (XRD)

X-ray diffraction analysis was carried out by a Riga automated diffractometer using Cu Kα radiation with 0.03^{o} step size and 3 s step time over range $2^{o} < 2\Theta < 65^{o}$. Before XRD analysis, all solid samples were washed with acetone (99%, Sigma-Aldrich) and then dried in anaerobic chamber to avoid oxidation of solid samples. The measured XRD data were compared to library simulation pattern.

Transmission electron microscopy (TEM)

Transmission electron microscopy (TEM) was performed using a JEOL 2010 microscope with a lanthanum hexaboride filament and an excitation voltage of 200 kV. The solid samples were diluted with ethanol (99.99%, Aldrich), and then placed on a 400-mesh copper grid, followed by dispersion of solid using sonication.

X-ray Photoelectron Spectroscopy (XPS)

The XPS spectra for pyrite and mackinawite in the presence or the absence of selenium, mercury or arsenic were obtained using a Kratos Axis Ultra Imaging X-ray photoelectron spectrometer with a monochromatized Al Kα (1253.6 eV) source. The pressure in analytical chamber was below 10^{-7} Pa. The survey and narrow scans were recorded with pass energy of 80 and 20 eV, respectively. In order to obtain oxidation status of surface sorption sites and target contaminants, narrow scan spectra of the C 1s, Fe 2p, S 2p, O 1s, Se 3d, Hg 4f, or As 3d were acquired. Since iron sulfide and disulfide are conducting solids, it would be expected that charge effects could occur, resulting in the shifts of spectra. To calibrate this region shift, the spectra

peak of C 1s at 284.5 eV was used as reference background. The narrow scan spectra of Fe $2p_{3/2}$, S 2p, O 1s, Se 3d, Hg 4f, and As 3d were fitted using a XPSPEAK fitting program with Gaussian Lorentzian function through background-subtraction corrections using a Shirley-type optimization.

Scanning Electron Microscopy (SEM)

The surface morphology and chemical composition of mackinawite (FeS) or pyrite (FeS_2) after contacts with target contaminants (As/Hg/Se) was characterized by scanning electron microscopy (SEM) using energy dispersive spectrometer (EDS) analysis. The used instrument was a JEOL JSM 6400 equipped with a PGT EDS system. Prior to inserting sample to the specimen holder, the surface of samples are coated with Pd and Au by sputtering instrument to reduce the electric charge on the surface of samples. The secondary SEM images were collected at 39 or 15 mm of working distance under 15 kV of acceleration voltage and a magnification range of 10 to 300,000x. Elements that were analyzed by EDS were Fe, S, O, As, Hg, Se, Pd, Au, and C.

Atomic Force Microscopy (AFM)

The topographic information of pyrite before and after contact with Se(IV) or Se(VI) was obtained by atomic force microscopy (Nano-R, Pacific Nanotechnology Inc., USA). An anodisc filter containing the solid sample was directly moved to the specimen holder. Two types of AFM images such as height and phase were obtained by a tapping mode (or close contact mode) that collects changes of cantilever oscillation as the tip of the cantilever assembly travels on the solid sample, and then transforms their signals to images through software (NanoRule+ Ver. 2.5, Pacific Nanotechnology Inc.). The tip assembly was composed of single-crystal silicon probe and the scan rate was set at 0.5 Hz over a selected area in the dimension of 3.22 μm × 3.22 μm for pyrite, 4 μm × 4 μm for Se(IV)-contacted pyrite, and 1.46 μm × 1.46 μm for Se(VI)-contacted pyrite.

Experimental Procedures

Kinetics tests

Arsenic

Standard stock solutions of As(III) and As(V) were prepared using $NaAsO_2$ (Sigma), $Na_2HAsO_4 \cdot 7H_2O$ (Sigma). Preliminary kinetic experiments for removal of As(III) or As(V) were performed by using 1g/L of FeS or pyrite at pH 8. The reaction vessels with 20 mL volume were used for arsenic adsorption. To start a kinetic test, FeS slurry and arsenic stock solution were added to the reaction vessels to reach 1 g/L of solid concentration and 13.3 μmol As/L. Acid (0.5 M HCl) or base (0.5 M NaOH) were added to adjust the pH. The reaction vessels were mixed on a shaker at 2000 rpm until specified sampling time. Samples of approximately 10 mL of suspension were taken and filtered using 0.02-μm anodisc membrane filters after 10, 30, 60, 120, 180, 240, 420, 660, 1000, 1440 minutes of reaction. All samples were stored in an anaerobic chamber to avoid arsenic oxidation until analysis by hydride generation atomic absorption spectrometry (HGAAS).

Mercury

A standard stock solution of mercury was prepared using $HgCl_2$ (Sigma). For FeS, experiments were conducted at pH 8 with three different initial concentrations of mercury (500,

1000, 1250 μM) in the presence of 0.05 g/L FeS. The reaction vessels with 20-mL volume were used for mercury adsorption. To avoid HgO(s), the mercury stock solution did not exceed a concentration of 1500 μM. A kinetic test was initiated by mixing a FeS slurry and the mercury stock solution to achieve concentrations of 0.05 g/L FeS and 500, 1000, 1250 μM Hg. Acid (0.5 M HNO_3) or base (0.5 M NaOH) were added to adjust the pH. The reaction vessels were mixed with a reciprocal rotator until the specified sampling time (10, 30, 60, 90, 150, 210, 330, 510, 750, 1440 min.). Approximately 10 mL of suspension were removed and filtered using 0.02-μm anodisc membrane filters. For pyrite, three tests were conducted at pH 7 with three different initial concentrations of mercury and doses of pyrite (100 μM Hg with 1 g/L FeS_2; 250 μM Hg with 0.5 g/L FeS_2; 500 μM Hg with 0.2 g/L FeS_2). Pyrite suspensions in 0.02 M MOPS were prepared in the 250 ml reaction vessels. Reactions were initiated by adding Hg(II) standard solution in pyrite suspension. The suspension was mixed by an end-over-end rotary mixer until specified sampling time. A 10-mL aliquot was sampled from the suspension at reaction times of 2, 5, 10, 15, 20, 30, 40, 60, 90, 120, 180, 240, 360, 720, 1440 min. The samples were immediately filtered using 0.02-μm anodisc membrane filters and the filtrates were stored in an anaerobic chamber until analysis.

All samples were stored prior to HGAAS analysis in an anaerobic chamber filled with 5% H_2/95% N_2 to avoid oxidation of mercury and changes in pH.

Selenium

Batch experiments were conducted to determine the kinetics of removal of Se(IV) and Se(VI) onto pyrite. For FeS, initial kinetic experiments were conducted at pH 8 to evaluate removal of Se(IV) and Se(VI) by suspensions of 1 g/L FeS with different initial concentrations of selenium (6.3, 12.7, 38, 127, 253 μM Se(IV); 12.7, 38, 127 μM Se(VI)). Reactions were initiated by adding Se(IV) or Se(VI) stock solution to a suspension of FeS and then mixing by reciprocal rotator. A 10-mL aliquot was sampled from the suspensions containing Se(IV) at reaction times of 0.5, 1, 2, 3, 6, 9, 18, 30, 43.7 hours. Similar samples were taken from the suspensions containing Se(VI) after reaction times of 1, 3, 7, 10, 19, 25, 32, 44, 49, 57, 68, 100 hours. For pyrite, Initial kinetic experiments were conducted at pH 7 and pH 10 with an initial concentration of 100 μM Se(IV) and a pyrite dose of 1 g/L. Initial kinetic experiments for Se(VI) were conducted at pH 8 with 1 g/L pyrite and different initial selenium concentrations (6.3, 12.7 and 38 μM). Experiments were initiated by spiking the suspensions with stock solution of Se(IV) or Se(VI) and adjusting pH and then mixing the reaction vessels with a reciprocal rotator. Samples were taken at times up to about 200 hours and were immediately filtered with 0.02-μm Whatman anodisk membrane filters. Filtrates were stored in an anaerobic chamber until they were analyzed for Se(IV) and Se(VI) by HGAAS. The kinetic data were expressed in terms of "% Se sorbed" as a function of reaction time.

Removal Tests

Arsenic

Removal tests at pH 7, 8, 9, and 10 were conducted to evaluate the ability of pyrite to remove As(III) and As(V). A suspension of pyrite was mixed with a sufficient amount of 2000 mg As/L arsenic stock solution to provide the desired initial arsenic concentration and a pyrite concentration of 1 g/L. Initial arsenic concentrations are shown in Table 15. The desired pH was adjusted using 0.5 M HCl or 0.5 M NaOH. The reaction vessels are mixed at 200 rpm on rotary shaker until 24 hours of reaction. All samples were filtered using 0.2-μm nitrate

membrane filter. All samples were stored until HGAAS in an anaerobic chamber to avoid arsenic oxidation and pH change Experiments to determine the effect of sulfate on arsenic removal were conducted similarly at pH 8 and at three sulfate concentrations (0, 1, 10 mM). Coefficients in the Langmuir and Freundlich equations were determined by non-linear least-squares regression using MATLAB® with its embedded function "nlinfit"

Table 15. Initial As Concentrations (μM)

pH 7	pH 8	pH 9	pH 10
8.5	8.5	7.7	8.4
16.9	16.9	15.3	16.9
33.8	50.8	30.6	67.5
67.7	102	76.6	1001
84.6	152	107	203
169	254	153	304
338	423	337	422
423	592	460	540
677	761	536	709
846	846	766	844

Removal tests at pH 7, 8, 9, and 10 were conducted to evaluate the ability of FeS to remove As(III) and As(V). A suspension of FeS was mixed with a sufficient amount of 2000 mg As/L arsenic stock solution to provide the desired initial arsenic concentration and a FeS concentration of 1 g/L. Initial arsenic concentrations are shown in Table 16. The desired pH was adjusted using 0.5 M HCl or 0.5 M NaOH. The reaction vessels are mixed at 200 rpm on rotary shaker until 24 hours of reaction. All samples were filtered using 0.2-μm membrane filters. All samples were stored in an anaerobic chamber until analysis by HGAAS in order to avoid arsenic oxidation. Experiments to determine the effect of sulfate on arsenic removal were conducted similarly at pH 8 and at three sulfate concentrations (0, 1, 10 mM). Coefficients in the Langmuir, Freundlich, and BET equations were determined by non-linear least-squares regression using MATLAB® with its embedded function "nlinfit"

Table 16. Initial As Concentration (μM)

As(III)				As(V)			
pH 7	pH 8	pH 9	pH 10	pH 7	pH 8	pH 9	pH 10
6.4	6.3	6.3	6.5	6.5	6.5	6.5	6.4
12.8	12.6	12.6	13.0	13.0	13.0	12.9	12.8
51.3	25.1	37.9	26.0	26.1	39.1	25.8	51.4
77.0	62.9	75.8	52.0	52.2	78.2	64.6	77.1
154	88.0	114	65.0	65.2	117	90.4	154
231	126	190	130	130	196	129	231
321	277	316	260	261	326	284	321
411	377	442	325	326	456	388	411
539	440	569	520	522	587	452	540
642	628	632	650	652	652	646	642

Mercury

Removal tests for mercury removal by pyrite were conducted in a similar manner to those used for kinetic testing, but were adjusted to account for the higher affinity of mercury for the pyrite surface. A pyrite dose of 0.15 g/L was used with eight initial concentrations of mercury

(50, 100, 250, 500, 1000, 2000, 3000, 4000 μM and 5000 μM at pH 8). A 24 hour reaction time was used and pH was adjusted by 0.02 M buffer solutions (pH 7 and pH 8 with MOPS; pH 9 with Borate; pH 10 with CAPS). Experiments to determine the effect of sulfate on mercury removal were conducted similarly at pH 8 and at three sulfate concentrations (0, 1, 10 mM).

Tests for removal of mercury by suspension of FeS were conducted in a similar manner as the previous experiments that evaluated removal of Hg(II) by suspensions of pyrite. However, the concentration of FeS was adjusted to account for the higher affinity of mercury for the FeS surface. A FeS dose of 0.05 g/L was used with ten initial concentrations of mercury (33 to 826 μM) and four values of pH (pH 7, 8, 9, 10). A 24 hour reaction time was used and pH was adjusted by 0.5 M HNO_3 or 0.5 M NaOH. Similar experiments were conducted to determine the effect of sulfate on mercury removal and they were conducted at pH 8 and at three sulfate concentrations (0, 1, 10 mM).

Selenium

Removal tests were conducted to evaluate the ability of pyrite to remove selenium in the selenite (Se(IV)) oxidation state. Initial kinetic experiments were conducted at pH 7 and pH 10 with an initial concentration of 100 μmol/L Se(IV) and a pyrite dose of 1 g/L. Pyrite suspensions were prepared in 250-mL reaction vessels with 0.01 M buffer solutions (MOPS for pH 7, CAPS for pH 10). Experiments were initiated by spiking the suspensions with Se(IV) and stirring the reaction vessels with a magnetic stirrer. Samples were taken at times up to about 200 hours and were immediately filtered with 0.2-μm membrane filters. Filtrates were stored in an anaerobic chamber until they were analyzed for Se(IV) by HGAAS. The effect of pH (7, 8, 10) on Se(IV) removal by pyrite was evaluated in a series of batch experiments conducted with variable initial concentrations of Se(IV) (25, 50, 75, 100, 150, 200, 300, 500, 750, 1000 μmol/L) and constant dose of pyrite (1 g/L). Suspensions were allowed to react for 24 hours before sampling and analysis of Se(IV) in the solution. The effect of sulfate concentration (0, 1, 10 mM) was evaluated in a series of batch experiments conducted at pH 7 and a range of initial concentrations of Se(IV) (25, 50, 75, 100, 150, 200, 300, 500 μmol/L) and a pyrite dose of 1 g/L. Samples were taken after 24 hours of reaction and analyzed for Se(IV).

Experiments to evaluate removal of Se(IV) and Se(VI) by suspensions of FeS were conducted with a similar way to those previously conducted to evaluate removal of Se(IV) by suspensions of pyrite. The effect of pH (7, 8, 9, 10) on removal of Se(IV) and Se(VI) by FeS was evaluated in a series of batch experiments. The initial aqueous-phase concentrations of Se(IV) ranged from 63.3 to 2508 μM and the initial concentrations of Se(VI) ranged from 6.5 to 1395 μM. A constant concentration of FeS of 1.0 g/L was used and the mineral form of FeS used was mackinawite. The pH of the suspensions was adjusted by 0.5 M HCl or 0.5 M NaOH. Samples were taken after 24 hours of reaction and analyzed for Se(IV) or Se(VI). Experiments to determine the effect of sulfate on selenium removal were conducted similarly at pH 8 and at three sulfate concentrations (0, 1, 10 mM).

Batch experiments to evaluate the effects of pH and sulfate concentration on the ability of pyrite to remove Se(VI). The effect of pH (7, 8, 9, 10) on Se(VI) removal was evaluated in a series of experiments with a constant dose of pyrite (1.0 g/L) and variable initial aqueous-phase concentrations of Se(VI) that ranged from 6.5 to 1395 μM. The pH of the suspensions was adjusted by adding 0.5 M HCl or 0.5 M NaOH. Samples were taken after 24 hours of reaction and analyzed for Se(VI). Experiments to determine the effect of sulfate on Se(VI) removal were

conducted similarly. Experiments were conducted at three initial aqueous-phase sulfate concentrations (0, 1, 10 mM), but at the same pH (pH 8).

Stability Tests

Arsenic

To investigate stability of As(III) and As(V) sorbed on pyrite, the experimental method described by Bostick and Fendorf (2003) was followed. This method measures the effect of pH on removal of As(III) and As(V) by decreasing and increasing pH with 1 or 2 M solutions of HCl or NaOH. A 1-g/L pyrite suspension was adjusted to about pH 4 for As(III) and about pH 10 for As(V). Then, the target compound (As(III) or As(V)) was added to achieve an arsenic concentration of 15.2 μM in the aqueous phase. Then, pH was adjusted to series of different values and the system was allowed to react for 30 minutes before sampling. During sampling, the suspensions were filtered using 0.02-μm anodisc membrane filters. This procedure was repeated until the pH reached the highest or lowest point desired. The filtered samples were stored before AAS analysis in an anaerobic chamber to prevent any change in the oxidation state of arsenic. The chamber contained an atmosphere of 5% H_2 and 95% N_2.

A series of experiments to measure the effect of pH on removal of As(III) and As(V) by FeS were conducted using a similar procedure as was used for pyrite suspensions. Suspensions containing 1 g/L of FeS were adjusted to initially to achieve a pH of about pH 10, before adding As(III) or As(V) to create an arsenic concentration of 15.2 μM. Then pH was reduced by addition of 1 or 2 M HCl to achieve a set of desired pH values and then 1.0 M NaOH was added to raise the pH to a number of values with the highest being near pH 10. After each pH adjustment, the system was allowed to react for 30 minutes, before removing 10-mL samples that were filtered through 0.02-μm anodisc membrane filters. Samples will be identified with the following nomenclature to simplify the discussion. The initial sample at pH 10 will be named the "pH $10_{(i)}$" sample, the sample at pH 4 after acid titration will be named the "pH $4_{(a.a.t)}$, and the final sample obtained at pH 10 after the titrations will be named the "pH $10_{(f)}$" sample. The filtered samples and the filter disk including wet solids were stored in the anaerobic chamber until analysis by both AAS and XPS.

Mercury

A series of experiments to evaluate the effect of pH on removal of Hg(II) by pyrite were conducted using similar procedures as used for arsenic and selenium. Since chloride ion can affect the sorption behavior of Hg(II) by formation of soluble complexes, HNO_3 was used as an acid to reduce pH. A 1-g/L suspension of pyrite was initially adjusted to the initial pH value and was allowed to equilibrate for 30 minutes. Then, Hg(II) stock solution was added to the suspension to create mercury concentrations of either 6.48 μM (low molar ratio of [Hg(II)]/[pyrite]) or 1 mM (high molar ratio of [Hg(II)] /[pyrite]). After pH was adjusted to the desired value, the system was allowed to react for 30 minutes before sampling. The subsequent procedures are the same as those described above or experiments with arsenic and selenium.

Experiments were conducted to evaluate removal by mackinawite using the same procedure followed for suspensions of pyrite, except that suspensions of mackinawite (FeS) were used instead of suspensions of pyrite.

Selenium

A series of experiments were conducted to evaluate the effect of pH on removal of Se(IV)

and Se(VI) by pyrite using a procedure that is similar to the one used for arsenic. Suspensions containing 1 g/L of pyrite were adjusted to the desired initial pH value and then the desired target compound (Se(VI) or Se(IV)) was added to create a selenium concentration of 16.5 μM in the aqueous phase. The subsequent procedures are the same as those described above.

Experiments to evaluate removal of selenium by mackinawite were conducted using the same procedure that was followed for examining behavior of Se(IV) and Se(VI) with suspensions of pyrite, except that the suspensions contained mackinawite (FeS).

RESULTS AND DISCUSSION

Characterization of Adsorbent/Reactants

Pyrite

Figure 6 shows that pyrite has a highly regular rectangular morphology and particle sizes within 100 ~ 1000 nm. The right hand side of the picture shows diffraction pattern where the crystalline pyrite is identified.

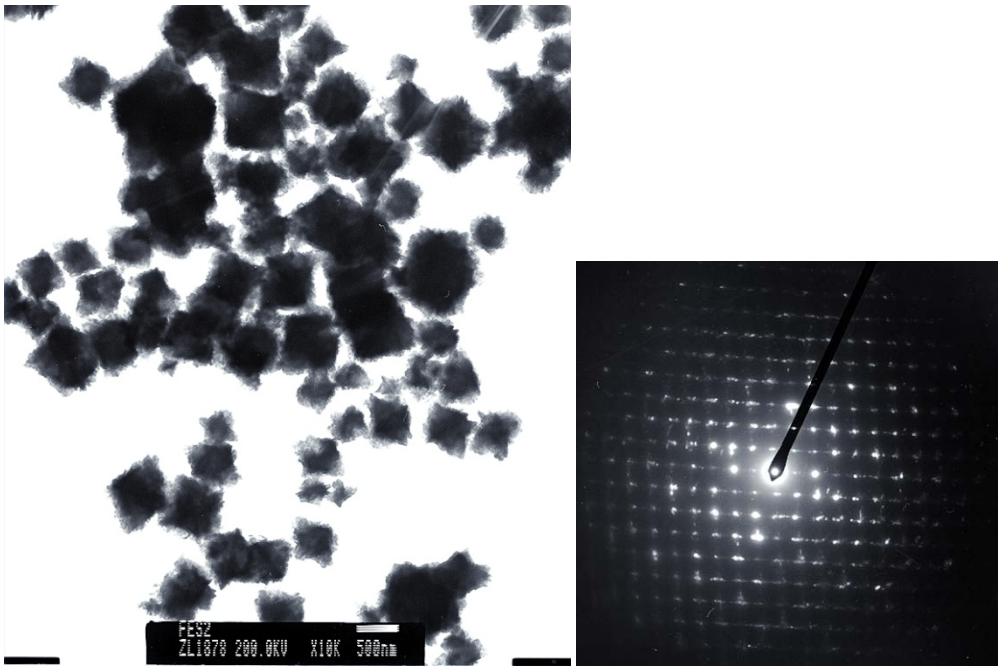

Figure 6. TEM image of synthetic pyrite

Based on library simulation search/match program, the XRD diffraction pattern in Figure 7 was concluded to be that of pyrite.

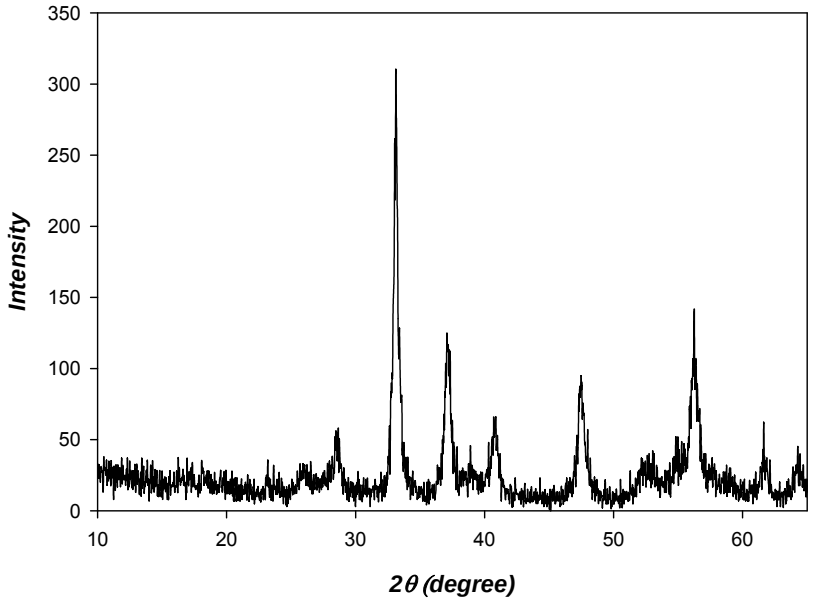

Figure 7. XRD diffractogram of synthetic pyrite

Figure 8 shows the high resolution Fe $2p_{3/2}$, S 2p and O 1s XPS spectra for synthetic pyrite at pH 8. In the Fe $2p_{3/2}$ spectra, three main peaks were observed at 706.8, 708.4, 709.8 eV, corresponding to Fe(II)-S, Fe(III)-S, and Fe(III)-O species, respectively. The Fe(III)-O peak at 708.4 eV could be assigned to ferric hydroxide species resulting from oxidation of Fe(II) by oxygen after exposure to air during the process of transferring the sample from the anaerobic chamber for XPS analysis or by surface hydroxylation (Demoisson et al. 2007). Figure 8(b) shows that the S 2p spectrum has two major peaks at 162.8 and 164 eV, corresponding to S $2p_{3/2}$ and S $2p_{1/2}$ of spin orbit doublets with 1.2 eV energy separation that are commonly assigned to S_2^{2-} chemical species. In the case of commercial pyrites, the elemental sulfur (S^o) spectrum is also observed at the binding energy range of S $2p_{3/2}$ and S $2p_{1/2}$ or more or less high ranges (Buckley et al. 1998). However, the synthetic pyrites that were synthesized in our study do not show this elemental sulfur spectrum. Figure 8(c) shows that the O 1s spectrum of pyrite contains three components with peaks at 530.1, 531.3 and 532.1 eV, corresponding to O_2^-, OH^- and molecular H_2O, respectively.

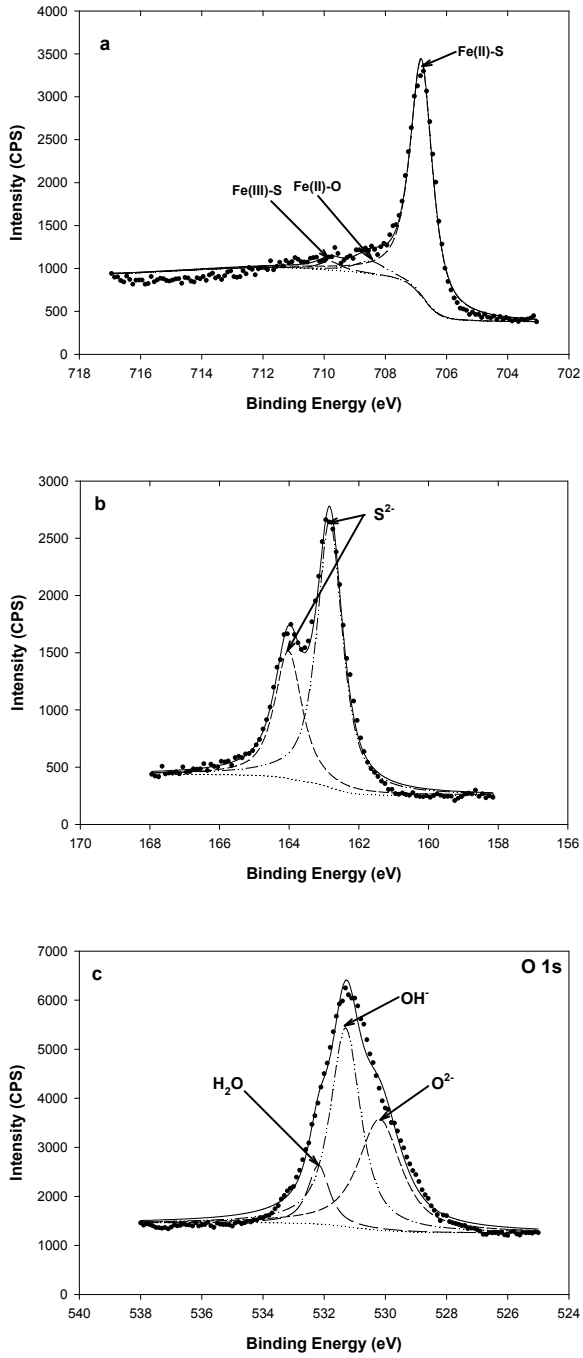

Figure 8. High resolution XPS spectra for synthetic pyrite at pH 8; (a) Fe $2p_{3/2}$, (b) S 2p, and (c) O 1s.

Figure 9 depicts the three-dimensional height images and phase image of synthesized pyrite. Figure 9(a) indicates a 3D height image in the range of 0 to 944 nm. The height profile for the cross-sectional region was in the range of about 200 to 800 nm. Figure 9(b) exhibits the phase image of pyrite that was obtained simultaneously with the height image. The phase image is often used to characterize the local changes in physical and mechanical properties of materials,

based on the phase lag between the oscillation amplitude of cantilever and driver as the probe taps the surface (Wang, et al., 2009; Dong and Yu, 2003). The phase lag is affected by the extent of the interactions between the scanning tip and the sample surface. Since the initial frequency of the cantilever was set to constant value, exterior power was added to the cantilever in order to maintain initial frequency whenever a phase lag occurs. Thus, the y-axis scale in the phase image or phase profile is expressed in terms of voltage (mV). When a solid surface consists of regions of different composition, a phase shift in the phase image will be presented by both dark-colored and bright-colored regions with different levels of voltage, which is due to bending deformation. The phase image (Figure 9(b)) shows small regions with surface heterogeneity on pyrite, but it indicates that the synthetic pyrite has a mostly homogeneous surface.

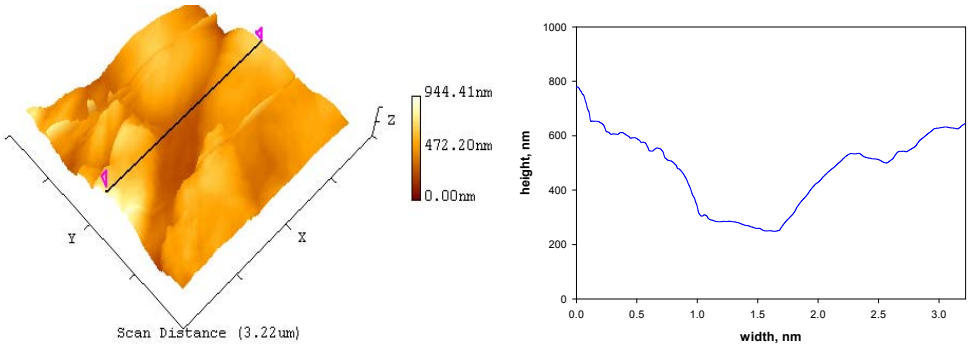

(a)

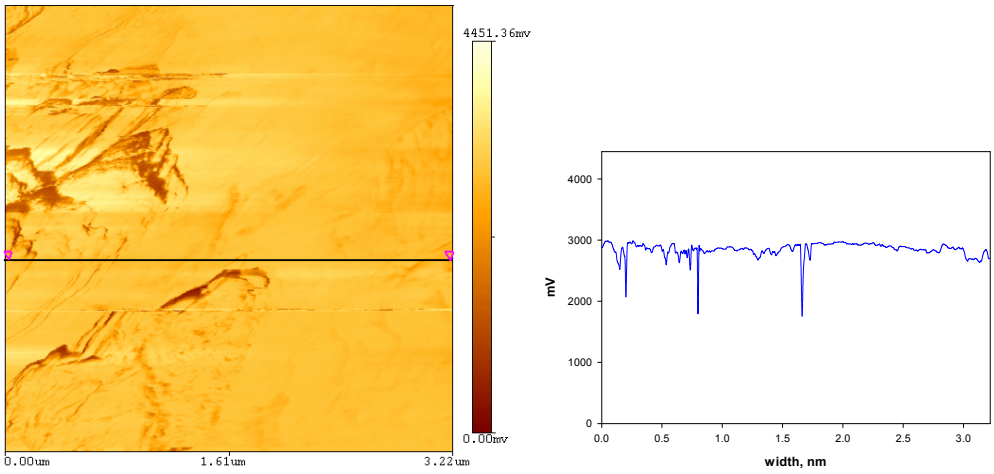

(b)

Figure 9. AFM images of synthetic pyrite before contact with selenium: (a) 3.22 µm × 3.22 µm 3D topography image (right) and height profile for cross-sectional region (left), (b) 2D phase image (right) and phase profile for cross-sectional region (left).

Mackinawite

Figure 10 shows that synthetic FeS has a particle sizes below 100 nm and diffraction pattern on left hand side supports the evidence of crystalline solid phase.

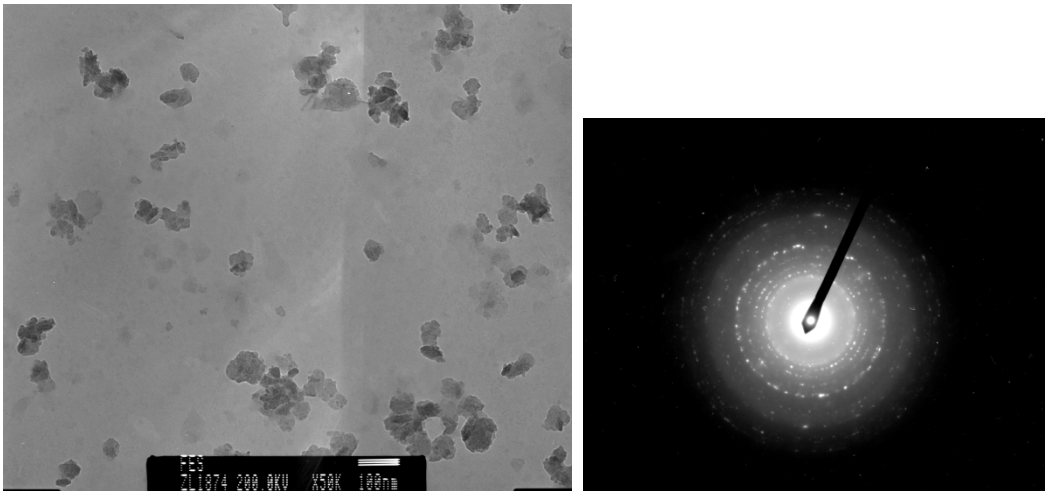

Figure 10. TEM image of synthetic FeS

Based on library simulation search/match program, the XRD diffraction pattern in Figure 11 was concluded to be that of mackinawite.

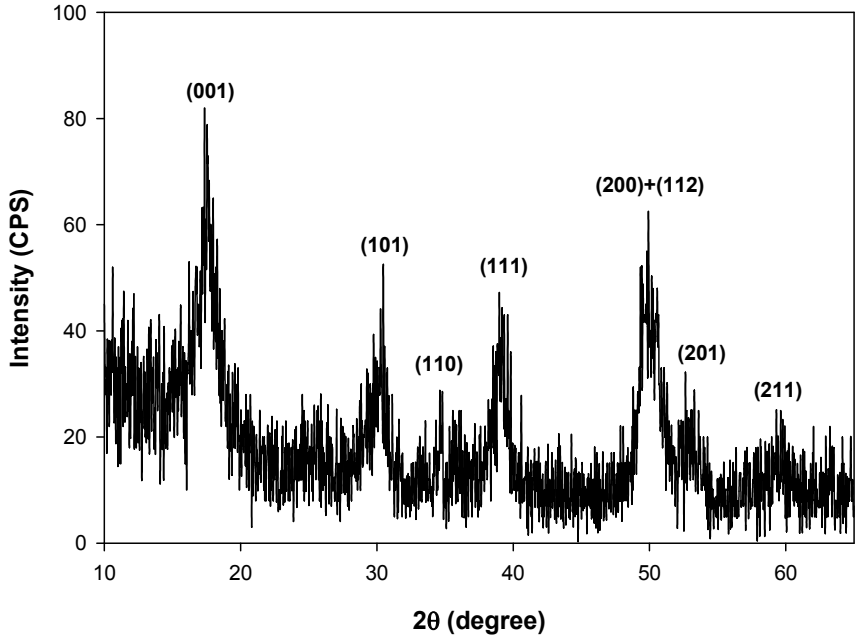

Figure 11. XRD diffractogram of synthetic mackinawite (FeS)

Figure 12 shows high resolution Fe $2p_{3/2}$ and S 2p XPS spectra for synthetic mackinawite at pH 8. When the Fe $2p_{3/2}$ spectra of mackinawite is fitted with only Fe(II) species, the left tail of the peak cannot be well fitted to the data, because the Fe $2p_{3/2}$ peak is too broad. To fit the observed spectrum more precisely, a deconvolution at high binding energy was performed with Fe(III) components that included several multiplet peaks such as Fe(II)-S, Fe(II)-O, Fe(III)-S, Fe(III)-O at 706~706.9, 707.7, 708.8, 710.1~711.8 eV. The Fe(II)-O peak at 707.7 eV could be assigned to the ferrous hydroxides species caused by surface hydroxylation

(Demoisson et al. 2007). In addition, the presence of some Fe(III)-O species could also originate from oxidation of Fe(II) by exposure to air during sample transfer prior to XPS analysis. As shown in Figure 12(b), the S 2p spectrum shows an asymmetric peak centered in the range of 161.3~162.3 eV. However, in order to fit the high energy tail of the S 2p spectra, polysulfides (S_n^{2-}) and elemental sulfur (S^o) were considered. Figure 12(c) shows the O 1s spectra of mackinawite at pH 8, in which three components (O_2^-, OH^- and H_2O) are located at 529.3, 531.1, and 532.3 eV, respectively.

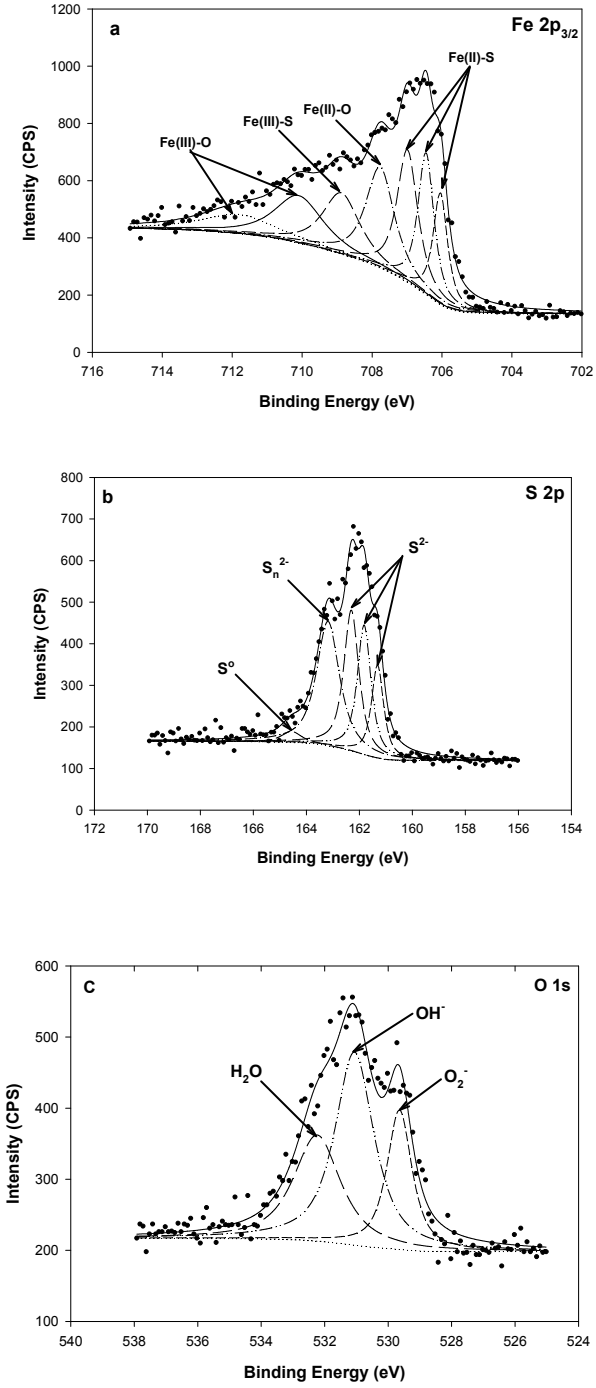

Figure 12. High resolution XPS spectra for synthetic mackinawite at pH 8; (a) Fe $2p_{3/2}$, (b) S 2p, and (c) O 1s.

Arsenic Removal and Stability

Pyrite

Arsenic(III) Removal and Stability

Figure 13 shows the results of preliminary kinetic experiments on removal of As(III) and As(V) by pyrite at pH 8. The rates of As(III) and As(V) uptake were different with As(V) being nearly completely removed within 30 minutes, while 95 % of As(V) was removed after 180 minutes. However, after 16.7 hours, As(III) was nearly completely removed.

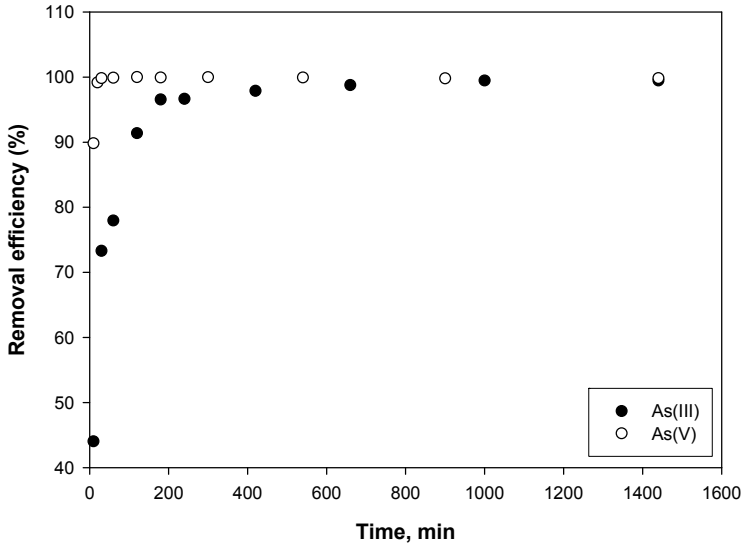

Figure 13. Removal of As(III) and As(V) by pyrite as a function of time at pH 8. Initial concentrations of As(III) and As(V) were 13.6 and 20.9 μM, respectively.

Figure 14 shows the results of removal experiments describing removal of As(III) by pyrite at four different pH values. The symbols represent the measured data and the lines represent a Langmuir equation fitted to the data. The Langmuir equation is typically used as an adsorption isotherm, but its use here is not intended to imply that adsorption equilibrium had been achieved. The Langmuir equation is shown in Equation 1.

$$q_e = \frac{q_{\max} b C_e}{1 + b C_e} \qquad (1)$$

Where, q_e is the concentration of target compound on the solid (number of moles of adsorbate adsorbed per unit mass of adsorbent, μmol/g), q_{max} is maximum concentration of target compound on the solid, i.e. the sorption capacity (μmol/g), C_e is the apparent equilibrium concentration of target compound in solution (μmol/L), and b is the Langmuir parameter (L/μmol).

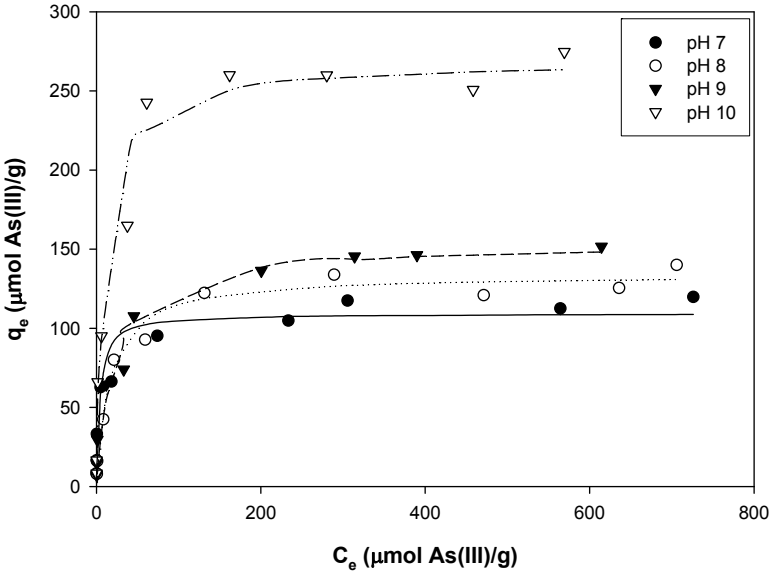

Figure 14. Measured concentrations of As(III) on pyrite (symbols) as function of concentration in water with Langmuir model fitted to data (lines) at various pH.

Figure 15 shows the same data for As(III) removal as Figure 14, however, the lines represent the Freundlich equation that was fit to the data. The Freundlich equation is typically used as an adsorption isotherm, but its use here is not intended to imply that adsorption equilibrium had been achieved. The Freundlich equation is shown by Equation 2.

$$q_e = k_f C_e^{1/n} \qquad (2)$$

Where k_f is the Freundlich constant related to the capacity of adsorbent to adsorb adsorbate ($\mu mol^{1-1/n} \cdot L^{1/n}/g$) and n is also Freundlich constant that expresses the affinity of adsorbate to the surface (the smaller n value, the higher the affinity of adsorbate to the surface).

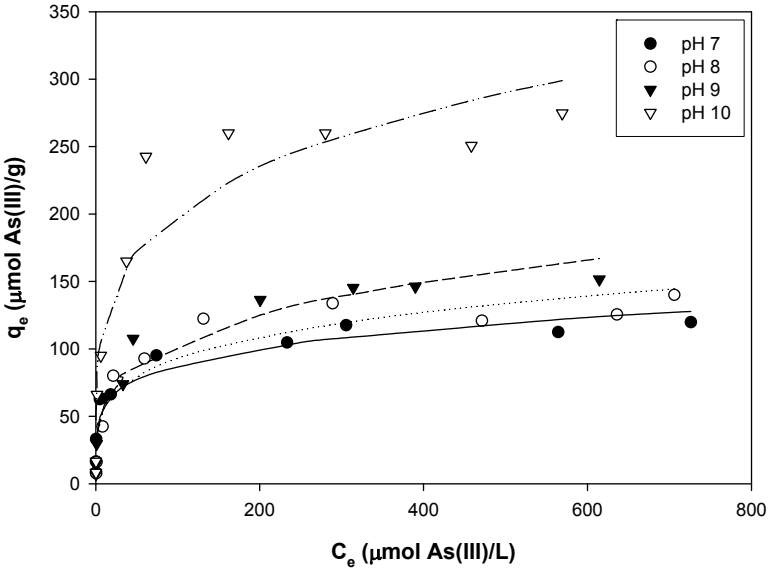

Figure 15. Measured concentrations of As(III) on pyrite (symbols) as function of concentration in water with Freundlich model fitted to data (lines) at various pH.

Table 17 shows the parameters of the Langmuir and Freundlich models obtained by non-linear regression. This procedure chooses parameters to minimize the sum of squared residual (SSR) and this parameter can be used to compare how well each model fits the data. The Langmuir model generally provided the best fit to the data. It provided the lowest SSR for three out of four data sets. Removals were observed to be higher as pH increased, as indicated by increasing maximum sorption capacities (q_{max}) and generally increasing Langmuir parameters (b).

Table 17. Model parameters for As(III) removal

pH	***Langmuir***			***Freundlich***		
	b (L/µmol)	**q_{max} (µmol/g)**	**SSR**	**K_f ($\mu mol^{1-1/n} \cdot L^{1/n}/g$)**	**n**	**SSR**
7	0.24 ± 0.22	107 ± 13.7	1286	36.3 ± 12.0	5.2 ± 1.6	1130
8	0.059 ± 0.026	133 ± 9.9	516	32.9 ± 17.1	4.4 ± 1.7	2288
9	0.046 ± 0.026	153 ± 17.3	1108	31.8 ± 12.5	3.9 ± 1.1	1464
10	0.084 ± 0.056	268 ± 27.4	3593	68.5 ± 35.4	4.3 ± 1.8	10274

Figures 16 and 17 show results of experiments to determine the effect of a competing ion (sulfate) on removal of As(III) by pyrite. Figure 16 shows a Langmuir model fitted to the data and Figure 17 shows a Freundlich model fitted to the data. Table 18 presents values of model parameters fitted to the data. The Langmuir model provided a much better fit to experimental data than the Freundlich model as shown by lower values of SSR for all data sets. Sulfate at 1 mM concentration had a negligible effect on As(III) removal by pyrite and a small effect at 10 mM.

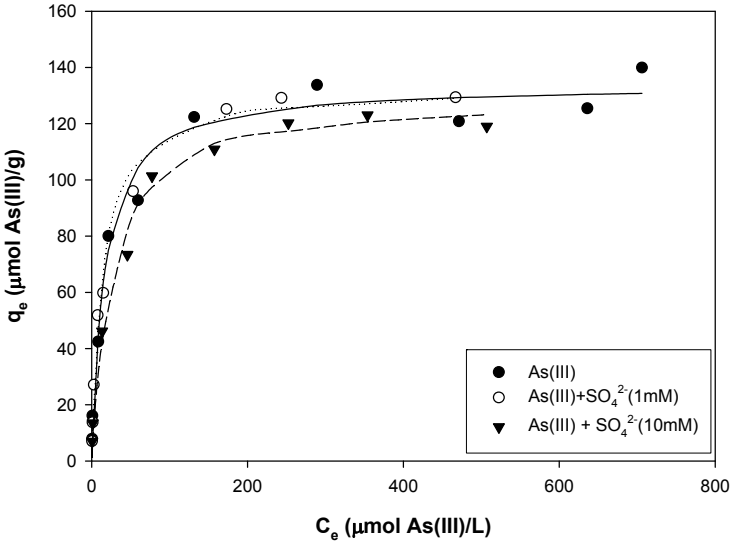

Figure 16. Measured concentrations of As(III) on pyrite (symbols) as function of concentration in water with Langmuir model fitted to data (lines) at various concentrations of sulfate.

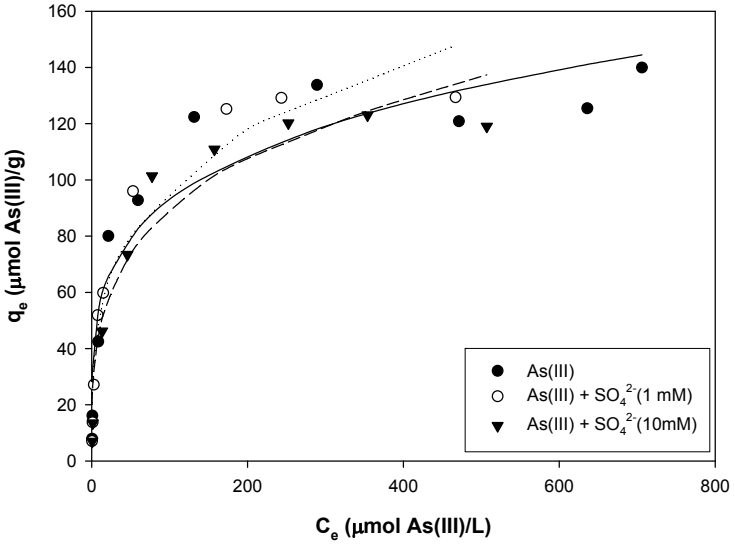

Figure 17. Freundlich model of As(III) removal by pyrite at pH 8, with 1 and 10 mM of sulfate, respectively.

Table 18. Model parameters for As(III) removal as affected by sulfate.

SO_4^{2-} (mM)	Langmuir			Freundlich		
	b (L/mol)	q_{max} (µmol/g)	SSR	K_f ($\mu mol^{1-1/n}.L^{1/n}/g$)	n	SSR
0	0.059±0.026	133±9.9	516	32.9±17.1	4.4±1.7	2288
1	0.067±0.022	133±9.3	238	26.9±12.4	3.6±1.1	1254
10	0.038±0.014	129±9.2	202	24.9±14.3	3.6±1.4	1296

Stability of mixtures of pyrite and arsenic were evaluated by experiments in which pH was changed and release of arsenic measured. Figure 18 shows that as pH is raised to the basic range, sorption of As(III) increases with a steep sorption edge in the pH range between 6 and 8. At high pH, nearly 100% removal of As(III) is achieved, while at acidic pH values (pH 4 – pH 6) only 20% removal is observed. Hysteresis was observed between in the removal curves, which indicates that strong bonds are formed between As(III) and the pyrite surface at high pH that are not easily broken when pH is reduced. Therefore, stabilization of As(III) sorbed on pyrite could be expected. These results are well in agreement with those studied by Bostick et al. (2003).

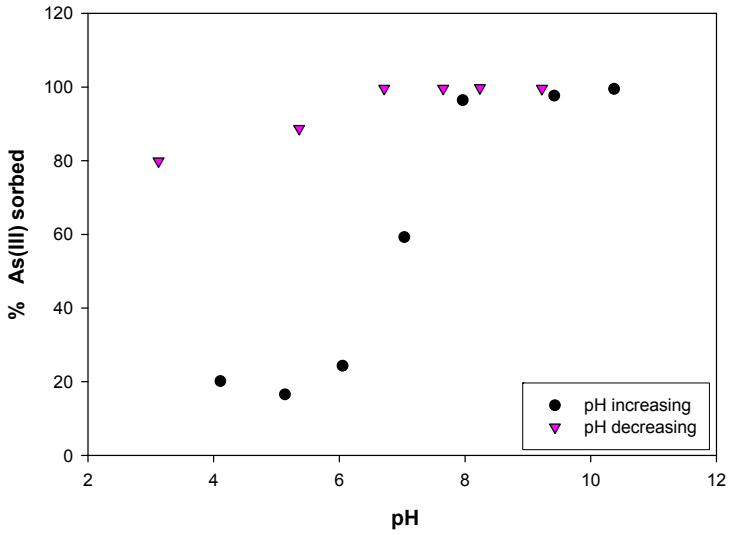

Figure 18. Effect of pH on removal of As(III) (15.2 µM) by pyrite (1 g/L) as pH was increased from pH 4 and subsequently was decreased.

Arsenic(V)Removal and Stability

Kinetics of removal of As(V) by pyrite were shown in Figure 13. Figure 19 and 20 show results of removal experiments conducted with As(V) and pyrite. Figure 19 shows a Langmuir model (line) fitted to the data (symbols) and Figure 20 shows a Freundlich model fit.

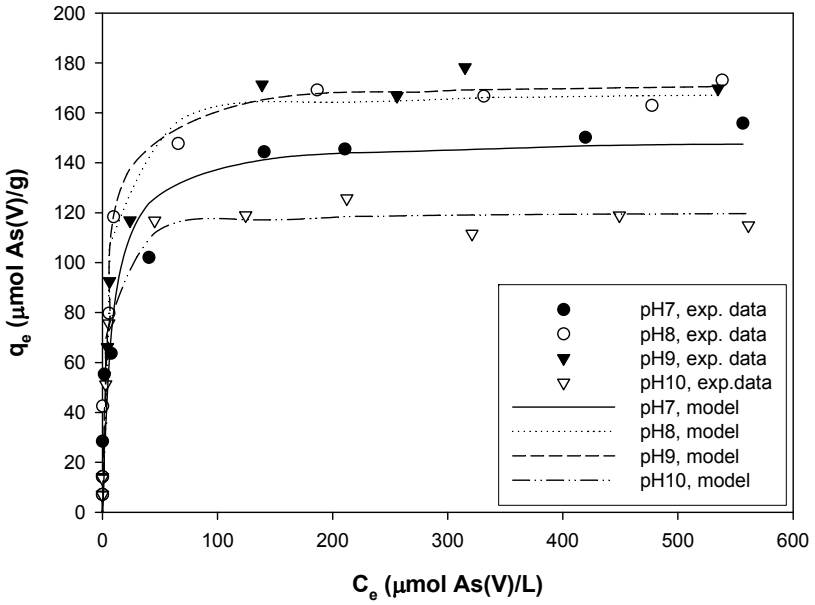

Figure 19. Measured concentrations of As(V) on pyrite (symbols) as function of concentration in water with Langmuir model fitted to data (lines) at various pH.

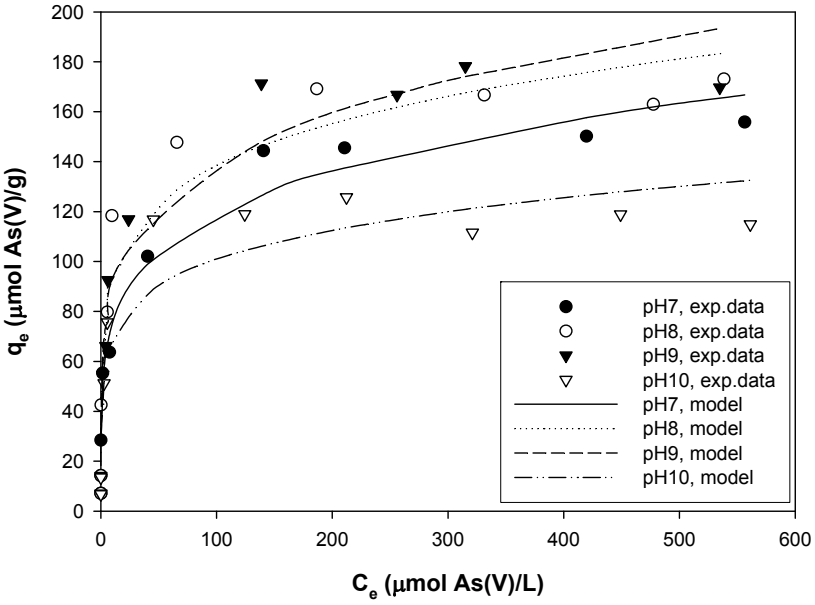

Figure 20. Measured concentrations of As(V) on pyrite (symbols) as function of concentration in water with Freundlich model fitted to data (lines) at various pH.

Table 19 shows the values of model parameters used that were calculated by non-linear regression. The Langmuir model was generally better able to fit the data having a lower SSR for three of the four data sets. The maximum adsorption capacity (q_{max}) tended toward a maximum around pH 8 to pH 9.

Table 19. Model parameters for As(V) removal by pyrite.

pH	***Langmuir***			***Freundlich***		
	b (L/µmol)	q_{max} (µmol/g)	SSR	K_f ($\mu mol^{1-1/n} \cdot L^{1/n}/g$)	n	SSR
7	0.12 ± 0.11	149 ± 22.5	2540	47.4 ± 10.6	5.0 ± 1.0	787
8	0.20 ± 0.14	168 ± 17.7	1933	63.6 ± 19.1	5.9 ± 1.9	2465
9	0.16 ± 0.07	172 ± 14.1	1084	55.6 ± 16.3	5.0 ± 1.4	2040
10	0.29 ± 0.11	120 ± 6.56	331	48.5 ± 20.2	6.3 ± 3.1	2544

Figures 21 and 22 show results of experiments to determine the effect of a competing ion (sulfate) on removal of As(V) by pyrite. Figure 21 shows a Langmuir model fitted to the data and Figure 22 shows a Freundlich model fitted to the data. Table 20 presents values of model parameters fitted to the data. The Langmuir model provided a much better fit to experimental data than the Freundlich model as shown by lower values of SSR for all data sets. Sulfate at 1 mM concentration had a negligible effect on As(V) removal by pyrite and a small effect at 10 mM.

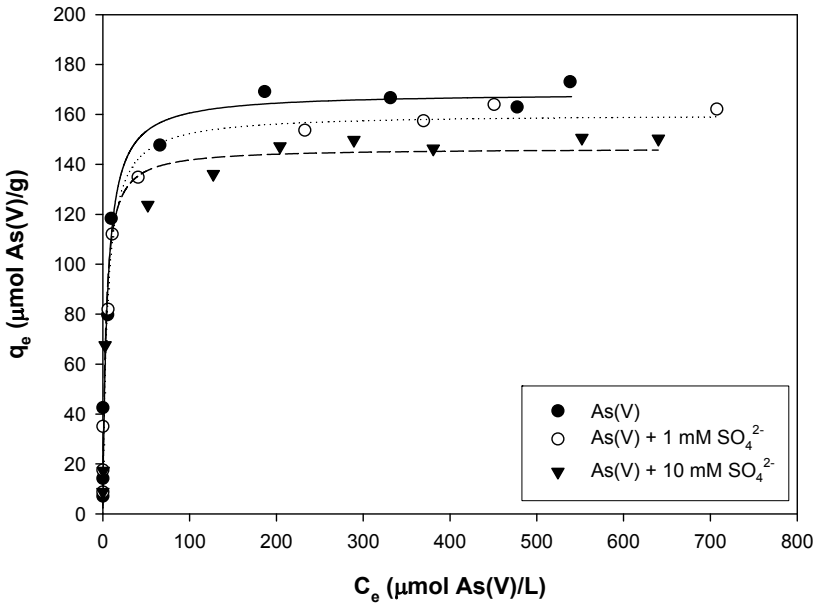

Figure 21**.** Measured concentrations of As(V) on pyrite (symbols) as function of concentration in water with Langmuir model fitted to data (lines) at various concentrations of sulfate.

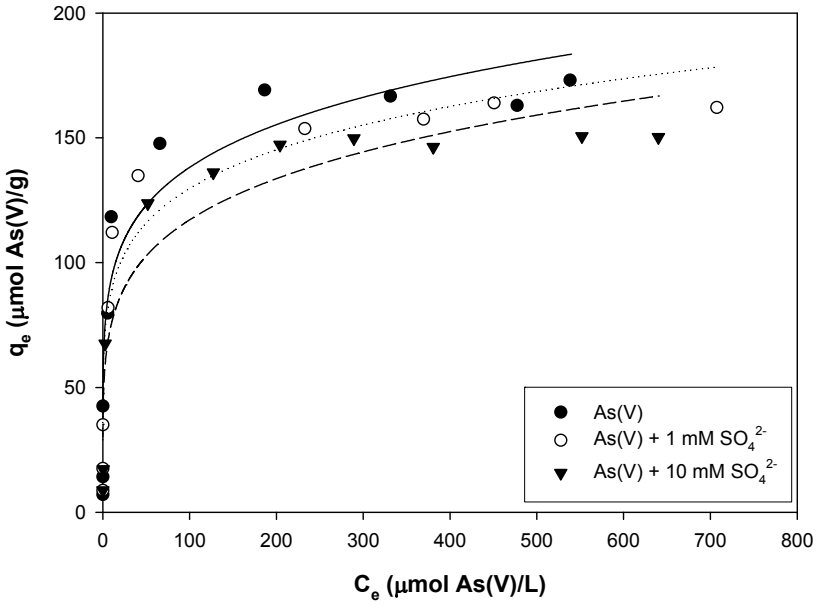

Figure 22. Measured concentrations of As(V) on pyrite (symbols) as function of concentration in water with Freundlich model fitted to data (lines) at various concentrations of sulfate.

Table 20. Model parameters for removal of As(V) by pyrite as affected by sulfate.

SO_4^{2-} (mM)	***Langmuir***			***Freundlich***		
	b (L/mol)	q_{max} (µmol/g)	SSR	K_f ($\mu mol^{1-1/n} \cdot L^{1/n}/g$)	n	SSR
0	0.20±0.14	168±17.7	1933	63.6±19.1	5.9±1.9	2465
1	0.19±0.13	160±15.7	1471	61.3±17.2	6.1±1.9	2098
10	0.30±0.12	146±6.20	356	48.8±20.4	5.3±2.0	2294

In order to investigate the stability of As(V) sorbed on pyrite, a 1-g/L suspension of pyrite containing 15.2 µM As(V) was adjusted to approximately pH 10 and then the pH was adjusted down and then back up. Results of arsenic analyses at each step of the experiment are shown in Figure 23. Near pH 10, removal of As(V) was the lowest observed (30%), but as pH decreased, removals gradually increased. However, removal of As(V) near pH 4 decreased to less than 80%. The trends of the As(V) removal curves were similar to those observed for As(V) on iron (hydr)oxides or pyrite (Dzombak and Morel, 1990; Zouboulis et al., 1993). As pH increased to near pH 10, some As(V) was released, but the amount retained on the pyrite was much greater than the amount removed initially at pH 10. In addition, the hysteresis in the As(V) sorption/desorption curves indicates that strong bonds are formed between As(V) and the pyrite surface at lower pH and that they are not easily reversed when pH is raised. Therefore, pH changes do not strongly affect the stability of As(V)-contacted pyrite.

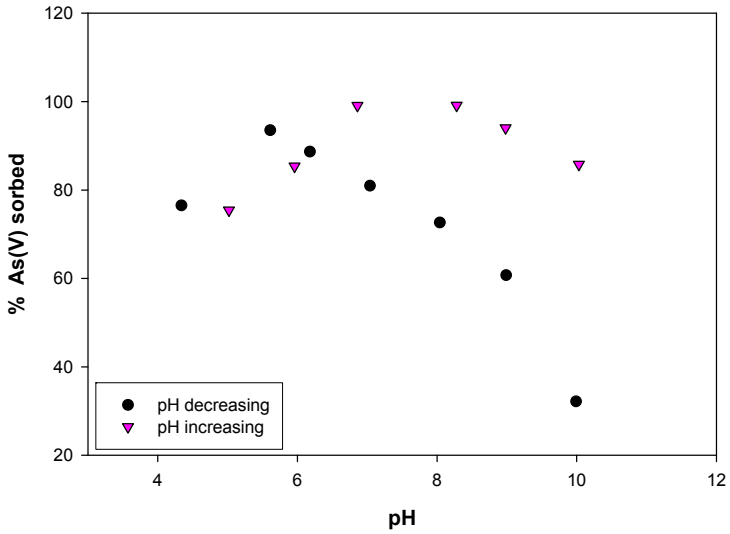

Figure 23. Effect of pH on removal of As(V) (15.2 μM) by pyrite (1 g/L) as pH was decreased from pH 10 and subsequently was increased.

Characterization of Arsenic-Pyrite

Figures 24 and 25 show the Fe $2p_{3/2}$ XPS spectra of pyrite after contact with As(III) and As(V), respectively. The spectra for synthetic pyrite before contact with As (Figure 8) shows three major peaks that are centered at 706.8, 708.4 and 709.4 eV and these peaks are assigned to Fe(II)-S, Fe(II)-O and Fe(III)-S, respectively. Since there is limited oxidation of the pyrite, the Fe(II)-S peak is much higher than the others. However, contact with As(III) and As(V) changed the spectra. Peaks associated with Fe(III)-S and Fe(III)-O increased in intensity and were found at higher bonding energy, which indicates that iron species were being oxidized. Therefore, it appears that the reduction of As(III) and As(V) is associated with the oxidation of Fe(II).

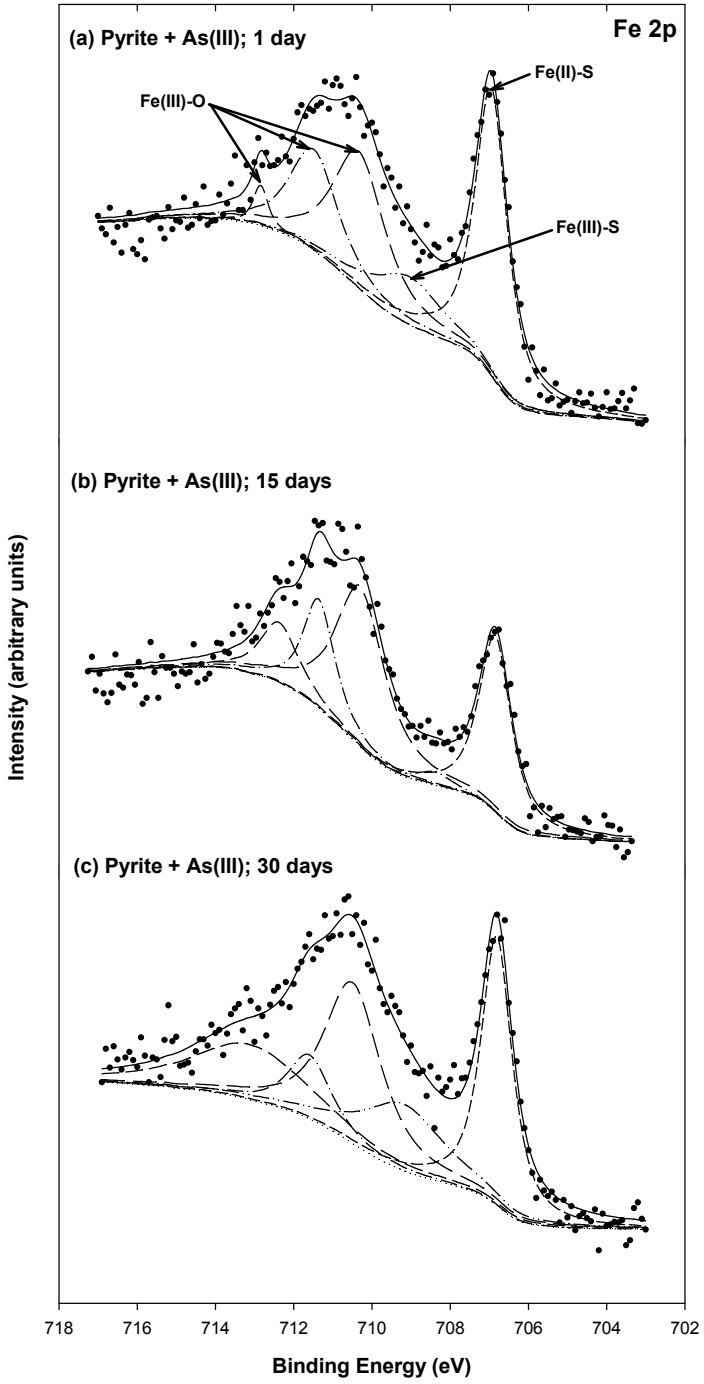

Figure 24. High resolution Fe $2p_{3/2}$ XPS spectra for synthetic pyrite (1 g/L) reacted with 3.3 mM As(III) at pH 8 for various times: (a) 1 day, (b) 15 days, (c) 30 days.

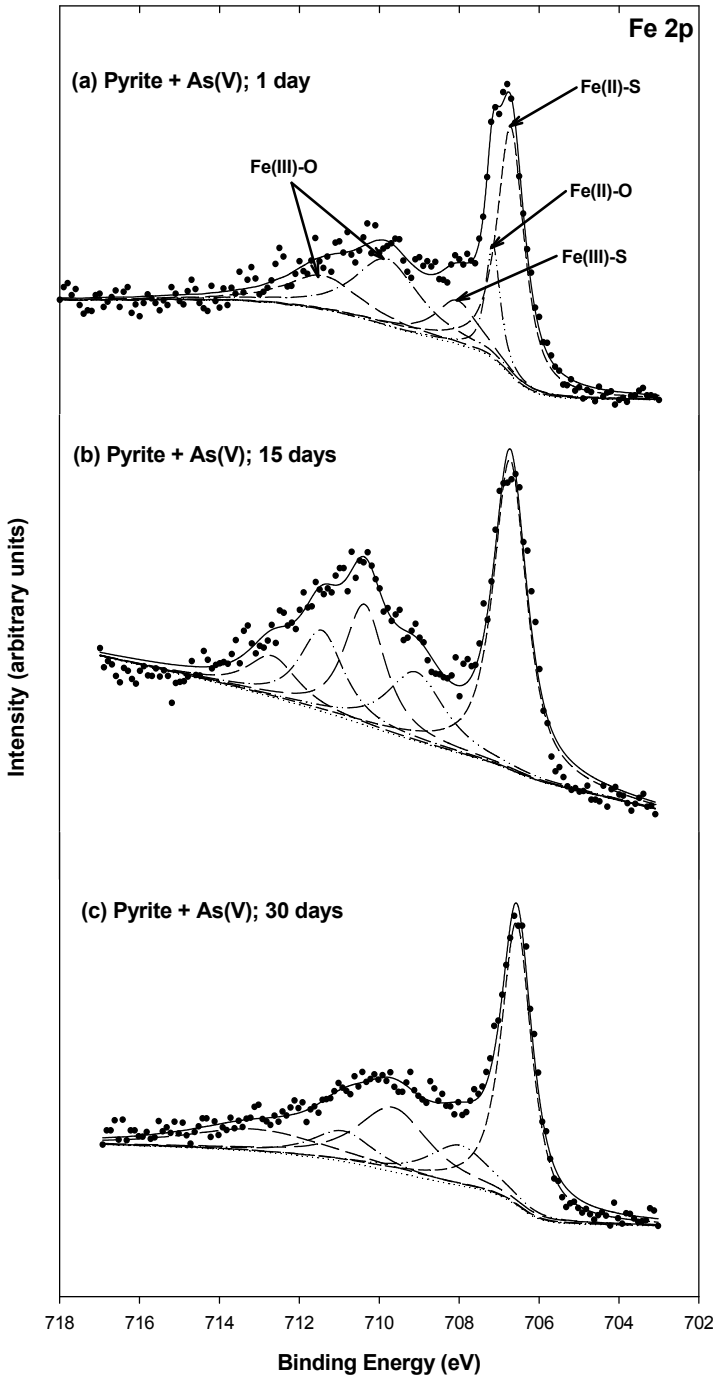

Figure 25. High resolution Fe $2p_{3/2}$ XPS spectra for synthetic pyrite (1 g/L) reacted with 3.3 mM As(V) at pH 8 for various times: (a) 1 day, (b) 15 days, (c) 30 days.

Analysis of the O 1s spectra can provide important information about the types of oxide phases that developed on pyrite surfaces after reaction with inorganic contaminants (Scott et al. 2007). In general, O 1s peaks associated with metal oxides and other components such as oxide, hydroxyl, and surface water are expected to have binding energies in the range from 529.5 to 533

eV (Knipe et al. 1995). Figure 8 showed that the peaks in the O 1s spectrum for pyrite prior to contact with target compounds were centered at 530.1, 531.3 and 532.1 eV, and were assigned to O_2^-, OH^- and H_2O molecules, respectively. Figures 26 and 27 show the O 1s spectra for pyrite contacted with As(III) and As(V), respectively. Figure 28 shows the O 1s spectra for pyrite contacted with As(III) over a wider range of binding energies. After contact with As(III) and As(V), there are no important changes in O 1s peaks present before contact. However, Figure 28 shows a new peak forming with binding energy near 540 eV. There are no peaks for oxygen in any other solids that have been reported at this binding energy, nor is it assigned to the main peak of another element (Knipe et al. 1995). Knipe et al. (1995) said that the anomalous peak near 540 eV might be caused by adsorption of electrically isolated water clusters through hydrogen bonding. Bonnissel-Gissinger et al. (1998) reported that extra peaks in O 1s spectra were observed at 535 ± 0.1 eV or 537.6 ± 0.1 eV as pyrite was oxidized by oxygen and formed islands of iron (hydr)oxides on the pyrite surface. In this study, however, we did not find evidence of iron (hydr)oxides, in spite of observing the oxidation of surface Fe(II).

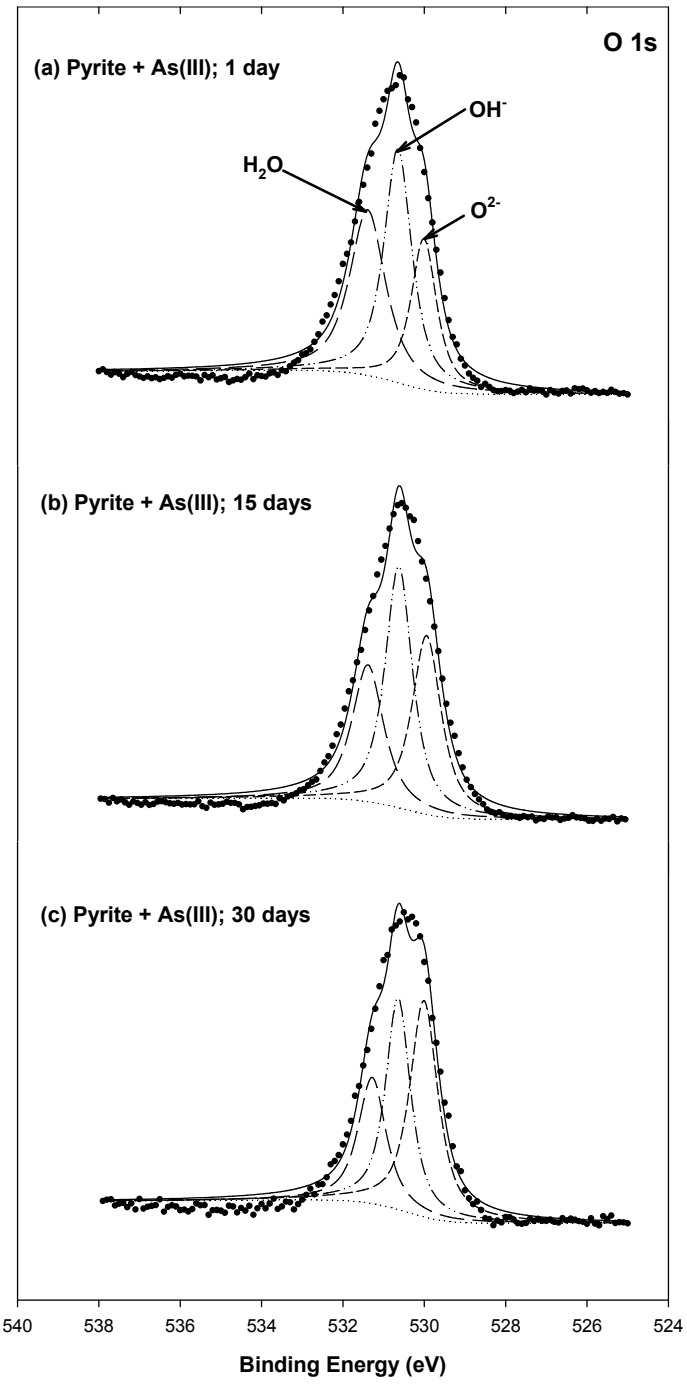

Figure 26. High resolution O 1s XPS spectra for pyrite reacted with 3.3 mM As(III) at pH 8 for various times: (a) 1 day, (b) 15 days, (c) 30 days.

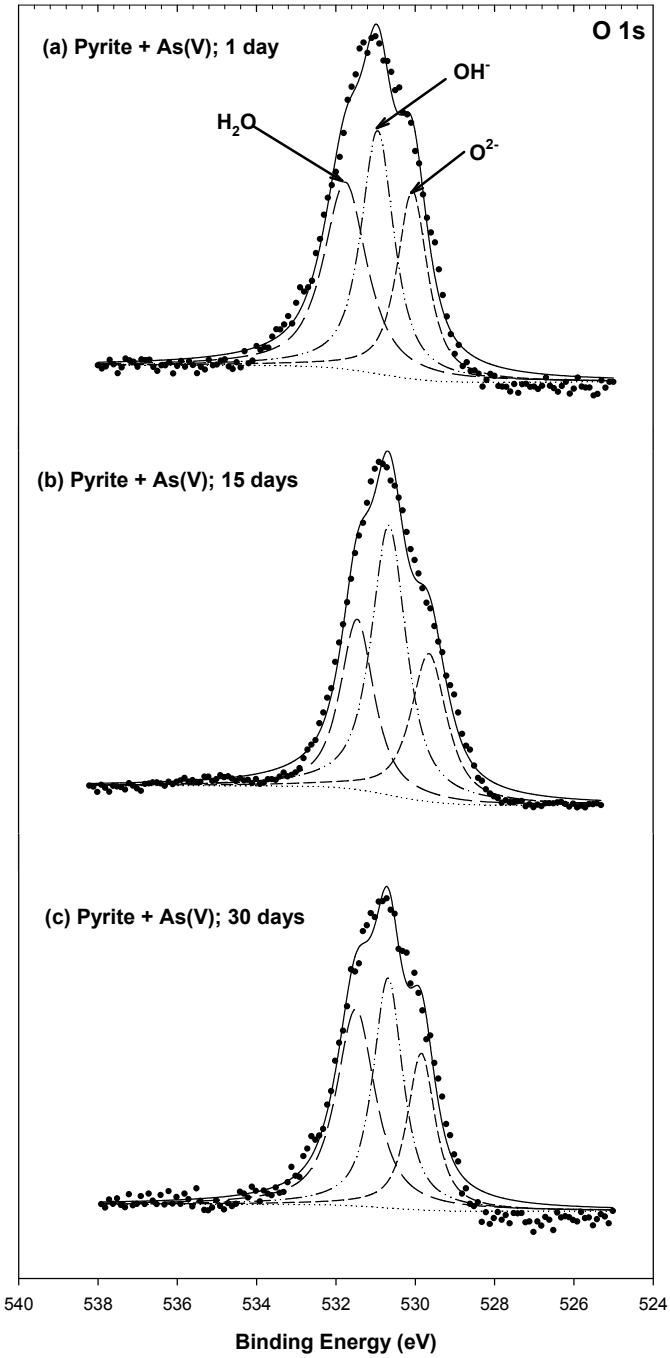

Figure 27. High resolution O 1s XPS spectra for pyrite reacted with 3.3 mM As(V) at pH 8 for various times: (a) 1 day, (b) 15 days, (c) 30 days.

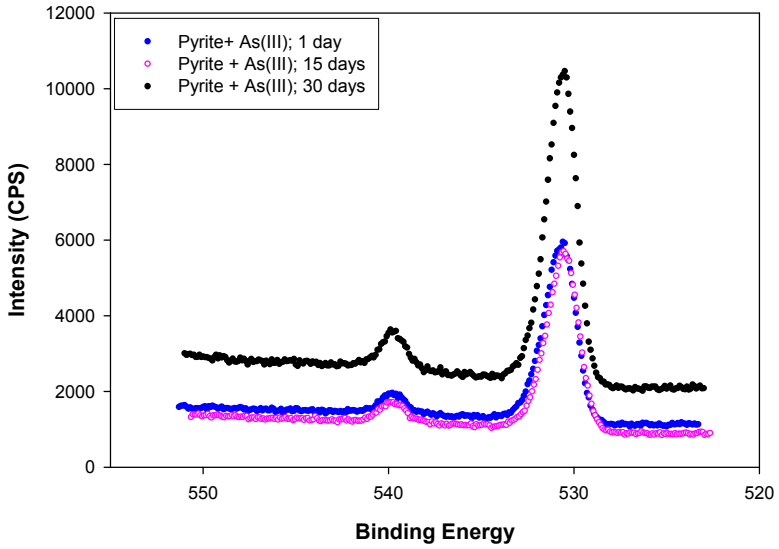

Figure 28. The O 1s XPS spectra for pyrite reacted with As(III) (3.3 mM) at pH 8 and various reaction times (1, 15, 30 days).

Figures 29 and 30 show the S 2p XPS spectra of pyrite after contact with As(III) and As(V), respectively. Prior to contact with arsenic, the S $2p_{3/2}$ and S $2p_{1/2}$ spectra contained two main peaks, which were centered at 162.8 and 164 eV with 1.2 eV energy separation (Figure 8). These peaks were assigned to S_2^{2-} species. After contact with As(III), there were no important changes in the S 2p spectra. However, after contact with As(V), the spectra developed a long tail at binding energy near 169 eV. This indicated that a small amount of SO_4^{2-} was present, which is evidence that sulfur on the surface may be oxidized in connection with reduction of As(V).

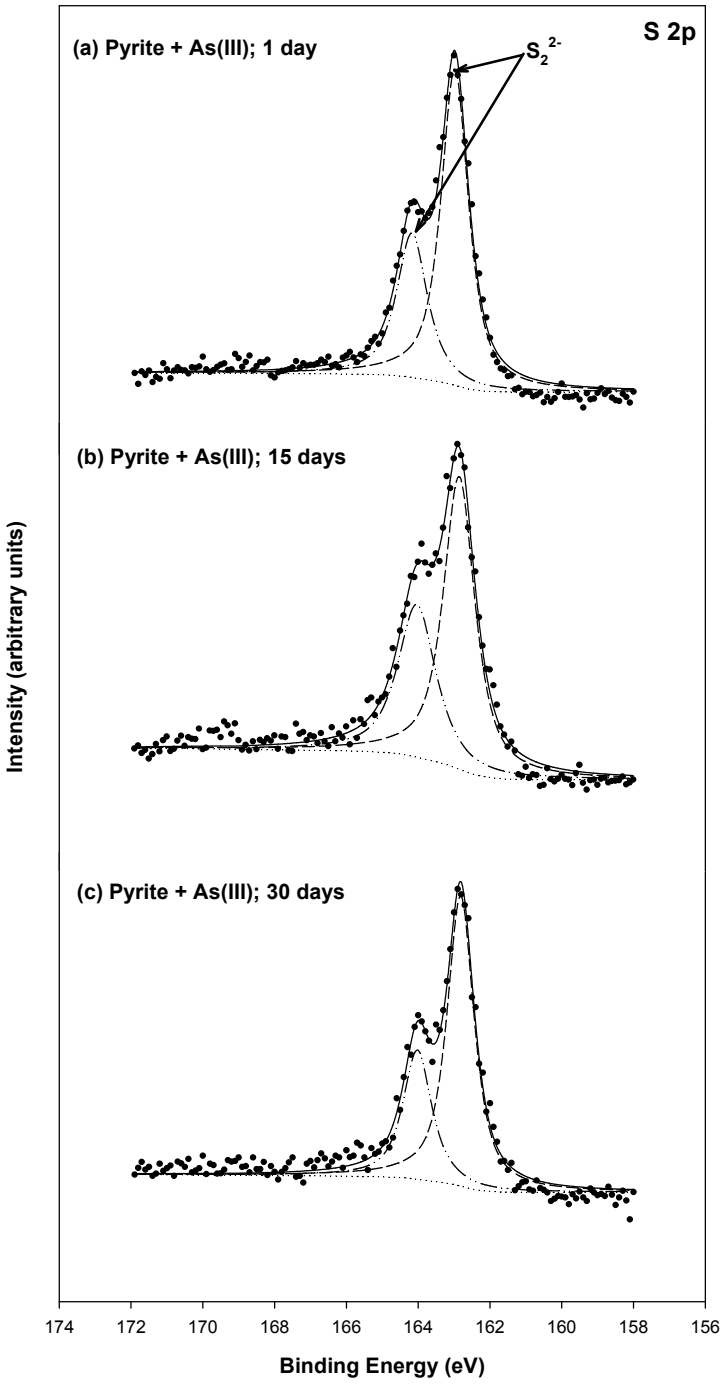

Figure 29. High resolution S 2p XPS spectra for synthetic pyrite (1 g/L) reacted with 3.3 mM As(III) at pH 8 for various times: (a) 1 day, (b) 15 days, (c) 30 days.

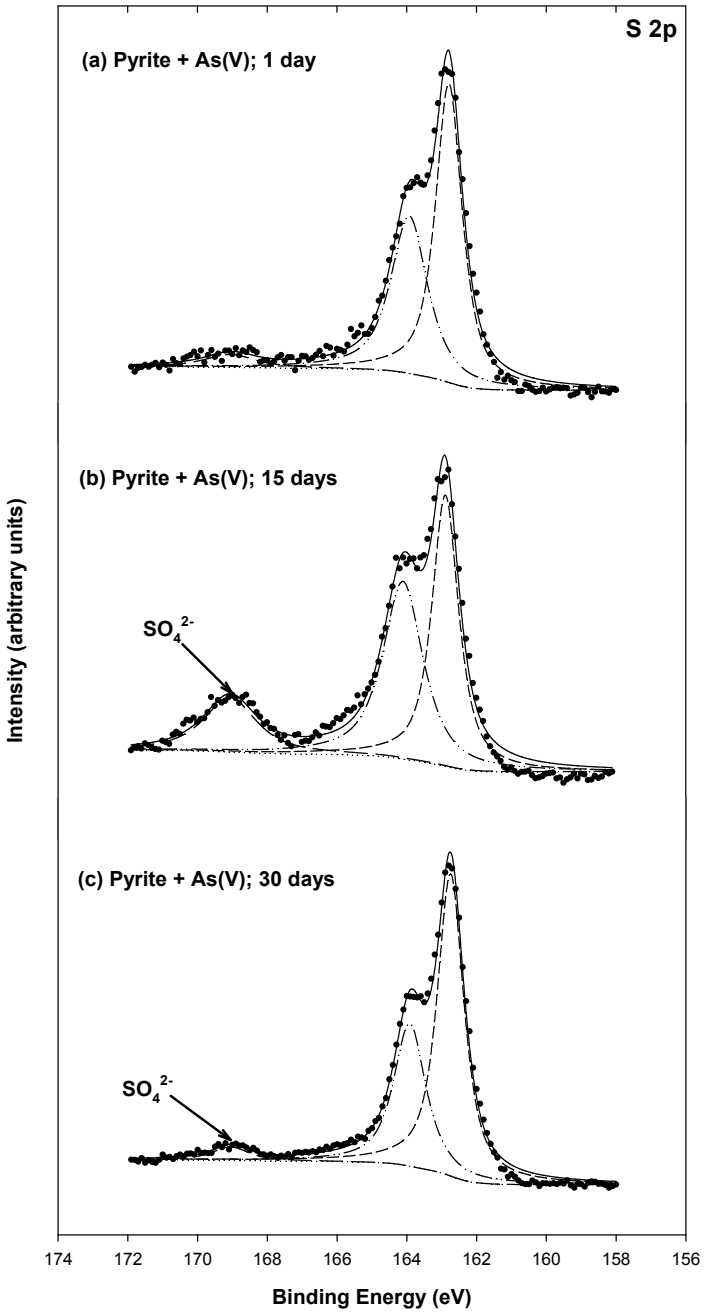

Figure 30. High resolution S 2p XPS spectra for synthetic pyrite (1 g/L) reacted with 3.3 mM As(V) at pH 8 for various times: (a) 1 day, (b) 15 days, (c) 30 days.

Figures 31 and 32 show the As 3d XPS spectra of pyrite after contact with As(III) and As(V), respectively. The As 3d peaks after 1 day are centered at 44.6 eV for As(III) and at 45.9 eV for As(V). At longer contact times, a minor shift of the position of the central peak was observed for only As(V). These results suggest that there was little As(III) reduction occurring during the 30-day period of reaction, even though oxidation of iron on the surface was observed. Reduction of As(V) to As(III) is likely to occur slowly.

Some evidence exists that may help identify some of surface species and surface reactions. The previous results from experiments that measured removal of arsenic (As(III) and As(V)) from solution by pyrite at pH 8 showed a relationship between surface concentrations of arsine and solution concentrations of arsenic that had the shape of a Langmuir model. There was no evidence of a relationship like a BET model that would indicate the existence of surface reactions such as surface precipitation. Farquhar et al. (2002) demonstrated with As K-edge EXAFS spectroscopy that the interaction of As(III) or As(V) with pyrite at pH 5.5-6.5 results in formation of outer-sphere complexes in which arsenic is coordinated to four oxygen atoms (As-O: 1.69-1.76 Å) with further sulfur (~3.1 Å) and iron (3.4-3.5 Å) shells. In contrast, Bostick et al. (2003) indentified other products of surface reaction between As(III) and pyrite at pH 4. They used EXAFS to conclude that arsenopyrite (FeAsS) or a similar compound was present. This was based on measurements of As-Fe and As-S bond lengths of about 0.24 nm, which is similar to those found in arsenopyrite. They also reported that As-O bonds were not detected, which was taken to indicate that the arsenic compounds had oxidized the surface and had formed reduced arsenic compounds that did not contain oxygen. Since that had insufficient high-quality data to characterize the As-S and As-Fe features, the presence and identity of surface precipitates could not be determined (Bostick et al. 2003).

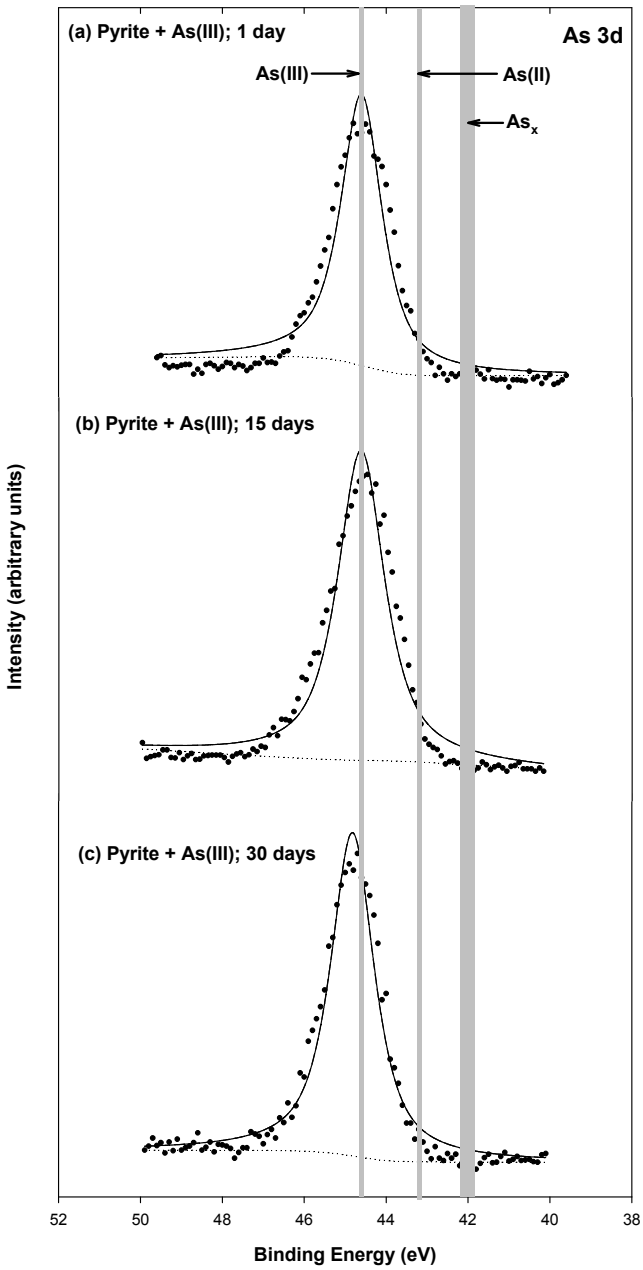

Figure 31. High resolution As 3d XPS spectra for pyrite after contact with 3.3 mM As(III) for various times: (a) 1 day, (b) 15 days, (c) 30 days. Gray bars indicate reported ranges of binding energies associated with As(III), As(II) and As_x.

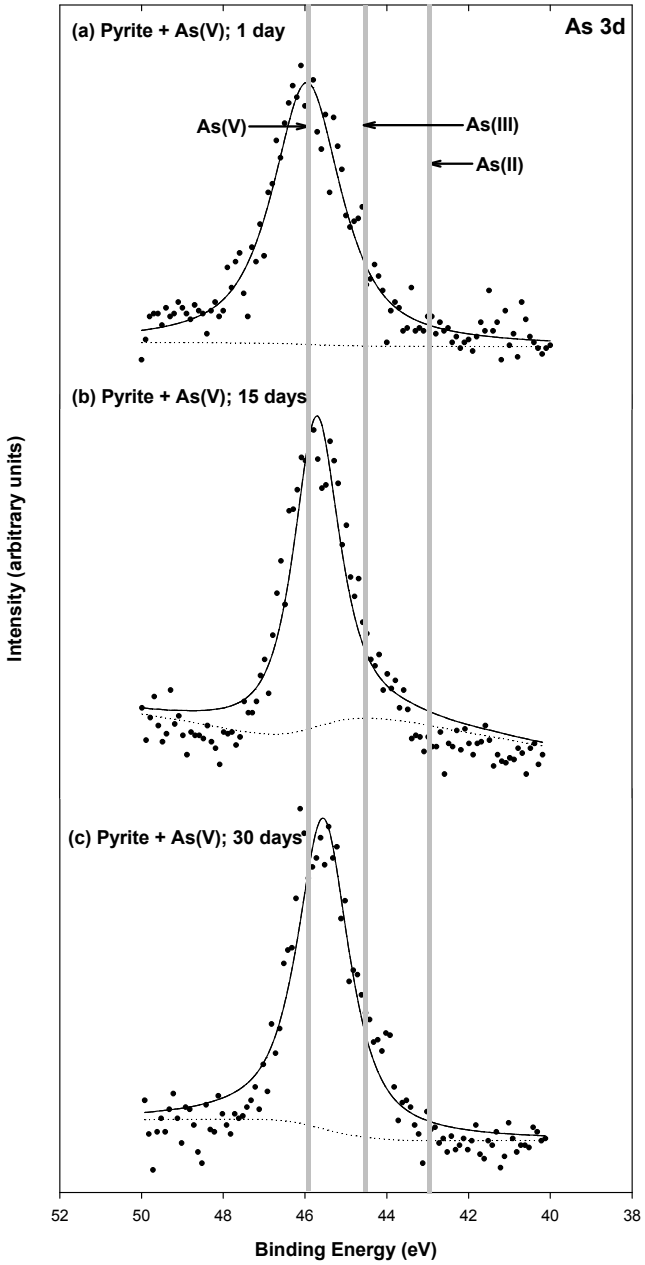

Figure 32. High resolution As 3d XPS spectra for pyrite after contact with 3.3 mM As(V) at pH 8 for various times: (a) 1 day, (b) 15 days, (c) 30 days. Gray bars indicate reported ranges of binding energies associated with As(III), As(II) and As_x.

Mackinawite

Arsenic(III) Removal and Stability

Figure 33 shows the results of preliminary kinetic experiments on removal of As(III) and As(V) by mackinawite (FeS) at pH 8. The rates of As(III) and As(V) uptake were different with As(V) being nearly removed completely within 10 minutes, while 96% of As(V) was removed

after 180 minutes. However, after 9.0 hours, As(III) was nearly completely removed.

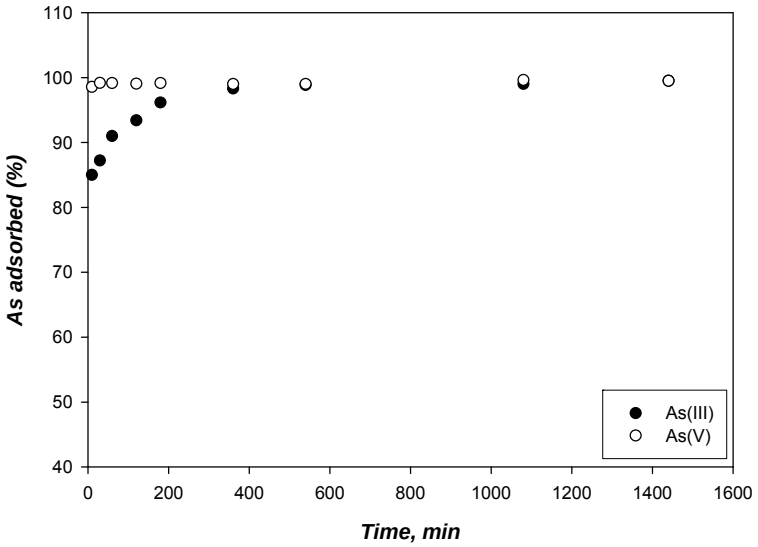

Figure 33. Removal of As(III) and As(V) by FeS as a function of time at pH 8. Initial concentrations of As(III) and As(V) were fixed at 13.3 μM.

Figure 34 shows the results of removal experiments conducted with As(III) and FeS at four different pH values. The symbols represent the measured data and the lines represent a Langmuir equation that was fitted to the data. Figure 35 shows the same data for As(III) removal as Figure 34, however, the lines represent the Freundlich equation which was fit to the data.

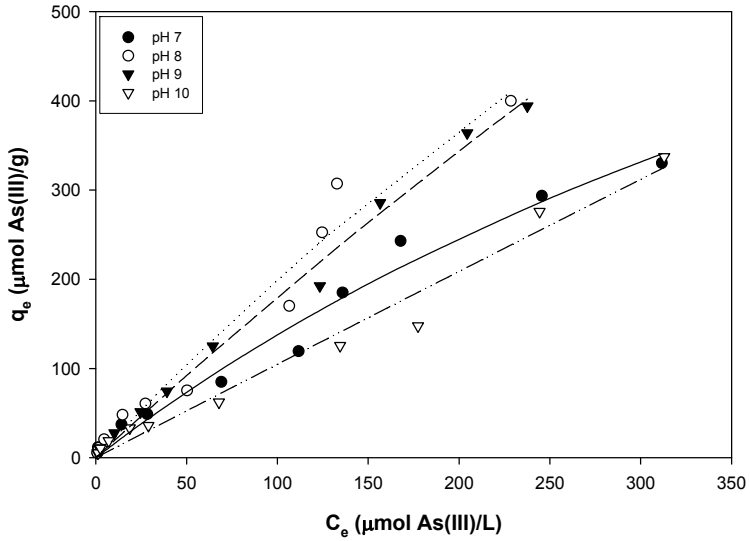

Figure 34. Measured concentrations of As(III) on FeS as function of concentration in water with Langmuir equation (lines) fitted to data (symbols) at various pH.

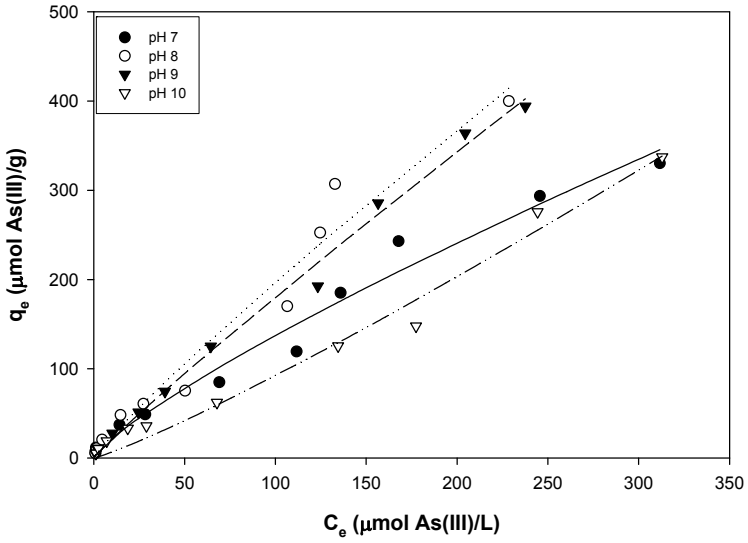

Figure 35. Measured concentrations of As(III) on FeS as function of concentration in water with Freundlich equation (lines) fitted to data (symbols) at various pH.

Figure 36 shows the same data for As(III) removal as Figure 34, however, the lines represent BET equations that were fitted to the data. The BET equation is often used to describe adsorption equilibrium when adsorption occurs in multiple layers. However, its use here does not imply that adsorption equilibrium occurred. The BET equation is shown in Equation 3.

$$q_e = \frac{q_{\max} A C_e}{(C_s - C_e)\left(1 + (A-1)\frac{C_e}{C_s}\right)} \qquad (3)$$

where q_e is the concentration of target compound on the solid (moles of target per unit mass of solid, (µmol/g); q_{max} is maximum concentration of target compound on the solid at a monolayer coverage, (µmol/g); C_e is the concentration of target compound in solution (µmol/L); A is adsorption energy parameter (e.g., A/C_s corresponds to b in the Langmuir model); and C_s is saturation concentration in solution (µmol/L).

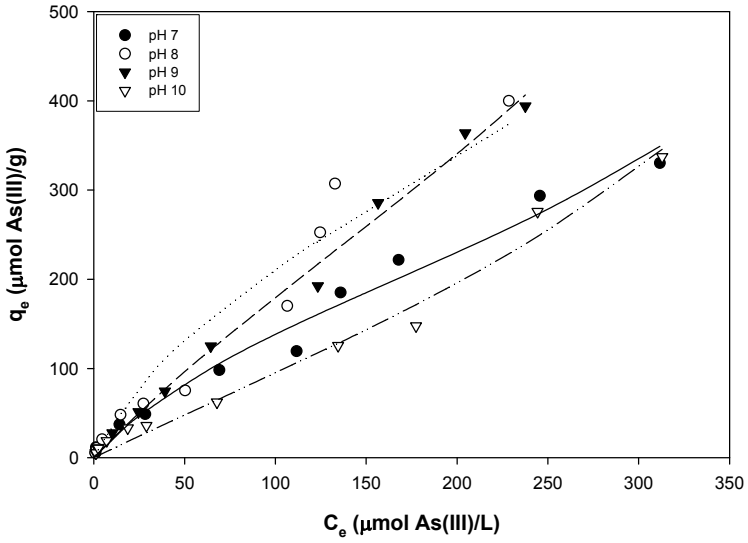

Figure 36. Measured concentrations of As(III) on FeS as function of concentration in water with BET equation (lines) fitted to data (symbols) at various pH.

Table 21 shows the parameters of the Langmuir, Freundlich, and BET models obtained by nonlinear regression. This procedure chooses parameters to minimize the sum of squared residuals (SSR) and this parameter can be used to compare how well each model fits the data.

Table 21. Parameters of models describing removal of As(III) by FeS as affected by pH.

	pH			
Models	**pH 7**	**pH 8**	**pH 9**	**pH 10**
Langmuir				
b (L/µmol)	1.4 × 10-3	9.26 × 10-4	4.71× 10-4	3.79 × 10-5
qmax (µmol/g)	1.12 × 103 ± 0.78 × 103	2.34 × 103 ± 5.07 × 103	3.92 × 103 ± 7.79 × 103	2.78 × 104
SSR	2680	5666	1322	2741
Δq (%)	41	41	34	44
Freundlich				
kf	3.35 ± 2.30	3.10 ± 3.69	2.48 ± 1.46	0.48 ± 0.64
n	1.24 ± 0.20	1.10 ± 0.29	1.07 ± 0.13	0.88 ± 0.18
SSR	2922	5862	1246	2194
Δq (%)	30	34	29	54
BET				
A	7.04 ± 3.79	4.05 ± 3.46	3.61 ± 1.51	2.43 ± 1.58
qmax	213 ± 30	402 ± 157	392 ± 71	268 ± 73
SSR	2474	6331	1392	1946
Δq (%)	35	39	31	45

$$\Delta q\ (\%) = 100\sqrt{\frac{\sum\left[\left(q_{e,\exp} - q_{e,cal}\right)/q_{e,\exp}\right]^2}{(N-1)}}$$

Figure 37 shows the experimental data at lower concentrations.

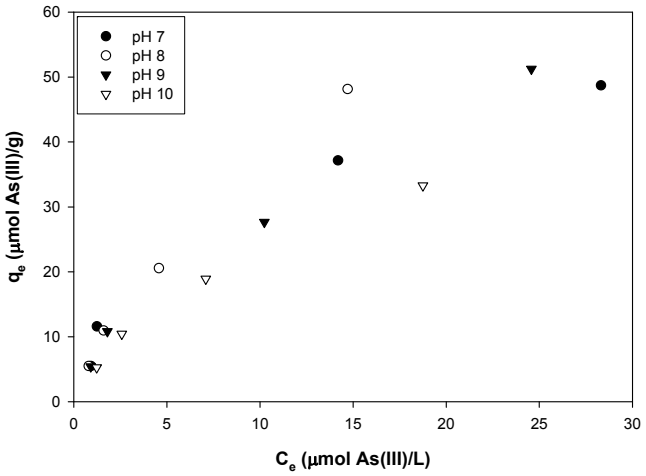

Figure 37. Measured concentrations of As(III) on FeS as a function of concentration in water for various pH using data at lower concentrations

Figures 38-40 show results of experiments to determine the effect of a competing ion (sulfate) on removal of As(III) by FeS. Figures 38-40 show Langmuir, Freundlich, and BET equations fitted to the data, respectively. Table 22 presents values of model parameters fitted to the data. When 1 or 10 mM of sulfate concentration was added, the amount of As(III) removal by FeS decreased.

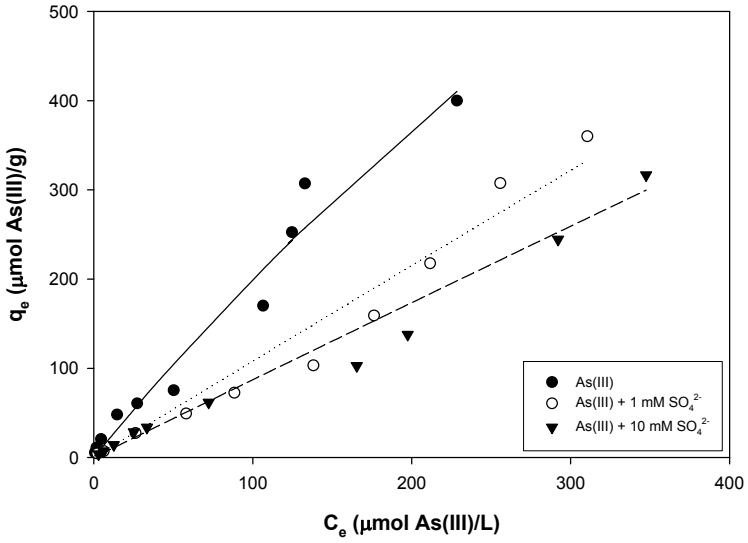

Figure 38. Measured concentrations of As(III) on FeS as function of concentration in water with Langmuir equation (lines) fitted to data (symbols) at various concentrations of sulfate

Table 22. Parameters of models describing removal of As(III) by FeS as affected by sulfate concentration.

SO_4^{2-} (mM)	*Langmuir* b (L/µmol)	q_{max} (µmol/g)	SSR	Δq (%)
0	≈ 0	2.3E+3±5.1E+3	5666	41
1	≈ 0	4.7E+5±3.3E+8	5655	27
10	≈ 0	5.9E+5±5.4E+8	3221	23
	Freundlich			
	K_f ($\mu^{mol1-1/n}.L^{1/n}/g$)	n	SSR	Δq (%)
0	3.10 ± 3.69	1.10 ± 0.29	5862	34
1	0.15 ± 0.17	0.73 ± 0.11	1594	44
10	0.19 ± 0.28	0.79 ± 0.16	1677	51
	BET			
	q_{max} (µmol/g)	a	SSR	Δq (%)
0	402 ± 157	4.05 ± 3.46	6331	39
1	367 ± 125	1.41 ± 0.88	1802	25
10	218 ± 39	2.08 ± 0.95	747	31

$$\Delta q\ (\%) = 100\sqrt{\frac{\sum\left[\left(q_{e,\exp} - q_{e,cal}\right)/q_{e,\exp}\right]^2}{(N-1)}}$$

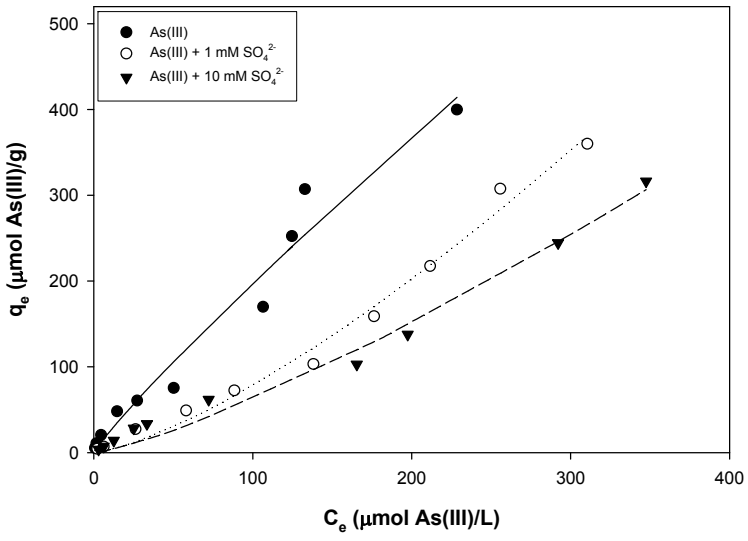

Figure 39. Measured concentrations of As(III) on FeS as function of concentration in water with Freundlich equation (lines) fitted to data (symbols) at various concentrations of sulfate

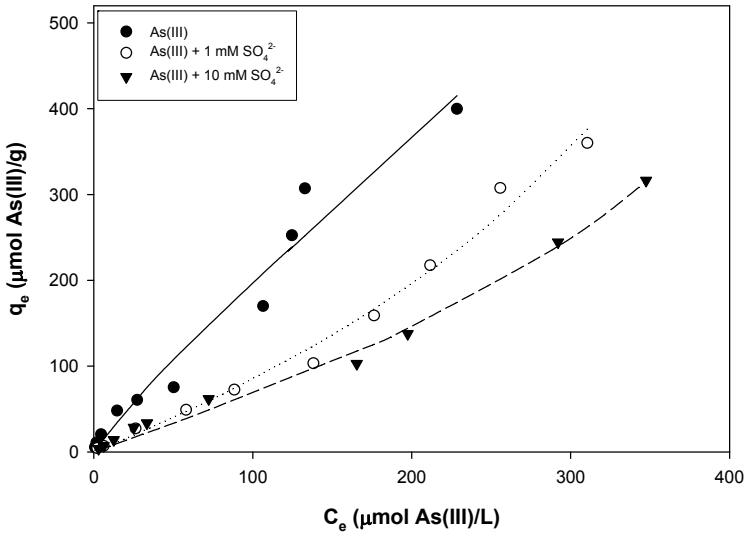

Figure 40. Measured concentrations of As(III) on FeS as function of concentration in water with BET equation (lines) fitted to data (symbols) at various concentrations of sulfate

Stability experiments were conducted by first contacting FeS with solutions of As(III) and providing time for reactions to occur between arsenic and the solid surface. Then the solution pH was changed in a series of steps and the concentration of As(III) was measured in the aqueous phase after 30 minutes reaction. The extent of release of As(III) as pH changed was used as a measure of the stability of the combination of arsenic and FeS. The initial pH was chosen as the value where the best removal of As(III) had been observed, so that high loadings would be obtained initially. Figure 41 shows that as pH decreased from an initial value near pH 10, As(III) removal by mackinawite (FeS) increased as pH was decreased from pH 10 with nearly complete removal observed for pH less than about pH 6.5. This result is in contrast to what has been reported for As(III) removal by troilite (FeS), where higher removals occurred above pH 5 and very little As(III) was removed below pH 5 (Wang, et al., 2009). However, experiments on As(III) sorption by synthetic mackinawite (FeS) that were performed by Gallegos (2007), showed a comparable sorption trend with our results. The difference in As(III) sorption edges may be caused by higher solubility of synthetic mackinawite than troilite (Gallegos, 2007). At low pH, the dissolved sulfide from mackinawite can react with soluble As(III) to form As-S precipitates, resulting in higher As(III) removal. Hysteresis was observed in the sorption/desorption curves when pH was raised from pH 4. Little arsenic was released as pH was raised, indicating that strong bonds were formed between As(III) and the surface at low pH that were not be broken when pH was raised.

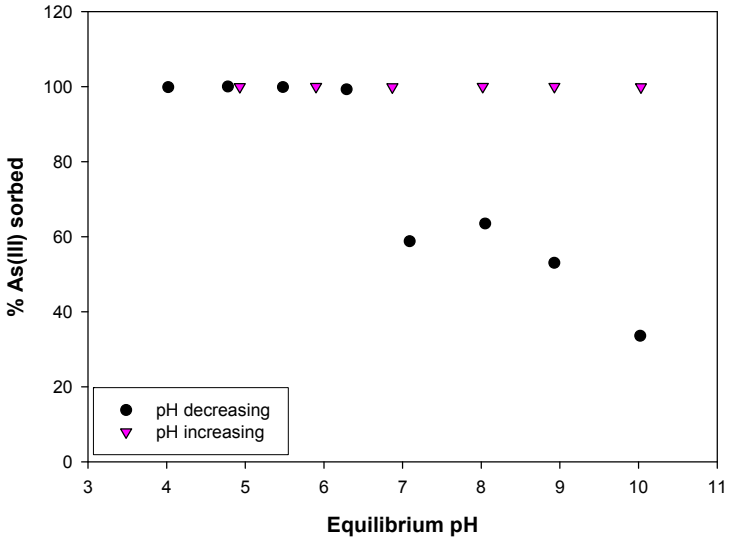

Figure 41. Effect of pH on removal of As(III) (15.2 μM) by FeS (1 g/L) as pH was decreased from pH 10 and subsequently was increased.

Arsenic(V)Removal and Stability

Kinetics of As(V) removal by FeS were shown previously in Figure 33. Figure 42-44 show results of removal experiments conducted with As(V) and FeS. Figure 42 shows a Langmuir equation (line) fitted to the data (symbols) with normal axes and an inset with a logarithmic y-axis used to better display low values. Figure 43 shows the fit of the Freundlich equation and Figure 44 shows the fit of the BET equation. Table 23 shows the values of model parameters that were calculated by non-linear regression and used to generate the lines in Figures 42-44. The Freundlich model was generally better able to fit the data as shown by its lower SSR (or Δq(%)). The maximum solid-phase concentration for As(V) on FeS tended to increase with lower pH.

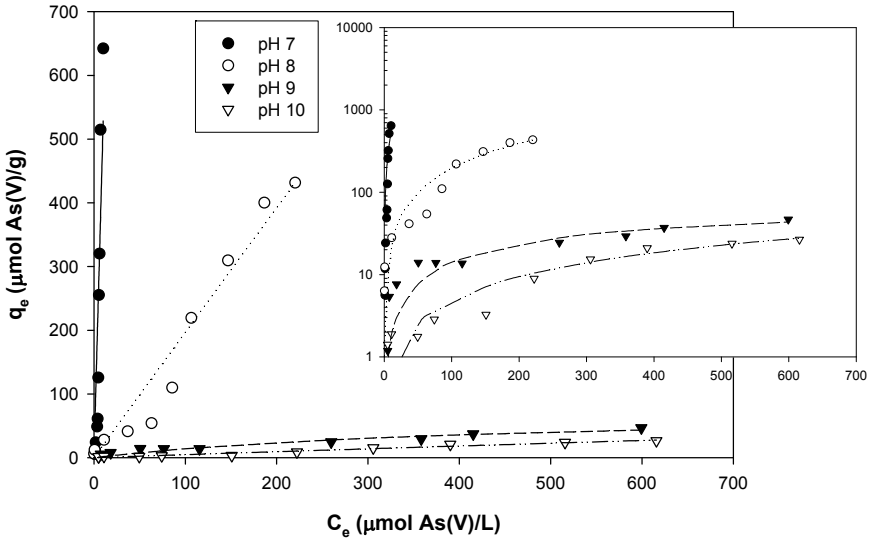

Figure 42. Measured concentrations of As(V) on FeS as function of concentration in water with Langmuir equation (lines) fitted to data (symbols) at various pH.

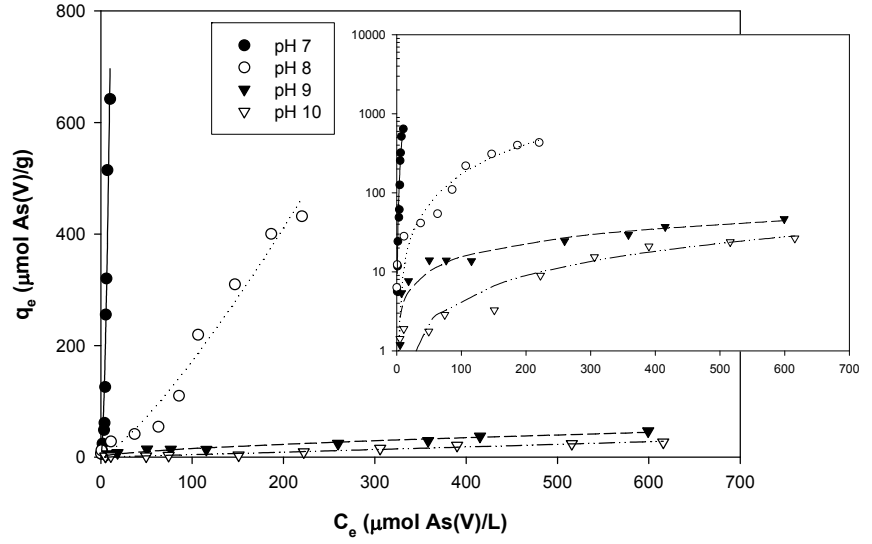

Figure 43. Measured concentrations of As(V) on FeS as function of concentration in water with Freundlich equation (lines) fitted to data (symbols) at various pH.

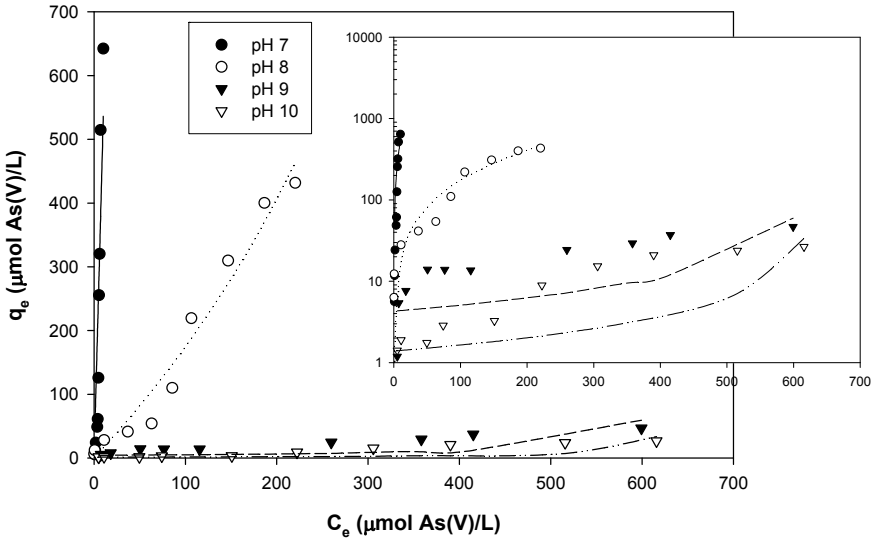

Figure 44. Measured concentrations of As(V) on FeS as function of concentration in water with BET equation (lines) fitted to data (symbols) at various pH.

Table 23. Parameters of models describing removal of As(V) by FeS as affected by pH.

	pH			
Models	**pH 7**	**pH 8**	**pH 9**	**pH 10**
Langmuir				
b (L/µmol)	1.7×10^{-4}	3.6×10^{-6}	2.2×10^{-3}	1.0×10^{-4}
q_{max} (µmol/g)	3.1×10^{5}	5.5×10^{4}	75.5	438
SSR	1.0×10^{5}	1.1×10^{4}	133	2741
Δq (%)	338	68	38	186
Freundlich				
k_f	11.6	0.52	0.98	0.04
n	0.56	0.79	1.68	0.97
SSR	3.5×10^{4}	6975	60	33
Δq (%)	71	58	45	56
BET				
A	0.05	1.3	1.5×10^{5}	2.6×10^{5}
q_{max}	6.1×10^{5}	800	4.3	1.4
SSR	9.7×10^{4}	8765	1734	847
Δq (%)	332	59	104	57

Figure 45-47 show results of experiments to determine the effect of a competing ion (sulfate) on removal of As(V) by FeS. Figure 45-47 show Langmuir, Freundlich, and BET equations fitted to the data, respectively. Table 24 presents values of model parameters fitted to the data. When sulfate was added, better fits to the data were obtained with the Langmuir equation, as shown by lower values of SSR. Lower amounts of As(V) were removed when sulfate was present at 1 or 10 mM.

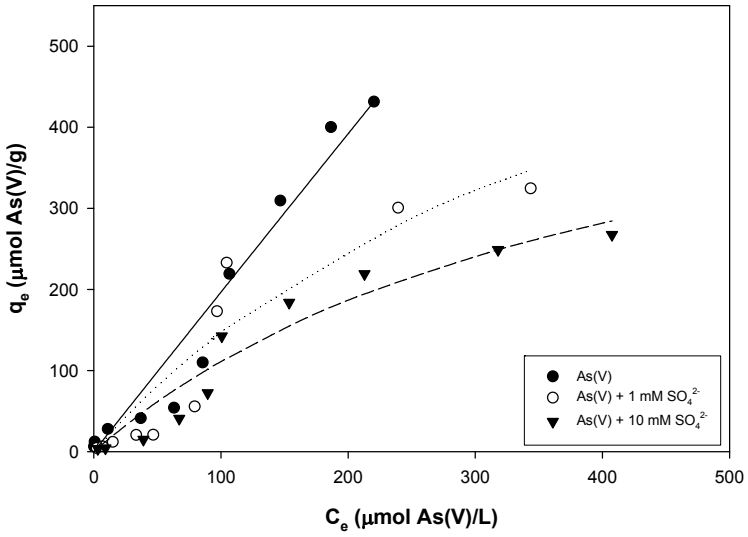

Figure 45. Measured concentrations of As(V) on FeS as function of concentration in water with Langmuir equation (lines) fitted to data (symbols) at various concentrations of sulfate

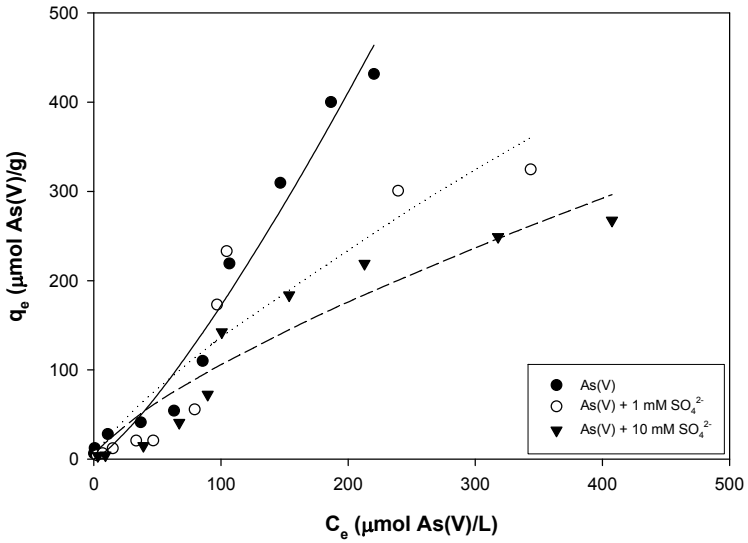

Figure 46. Measured concentrations of As(V) on FeS as function of concentration in water with Freundlich equation (lines) fitted to data (symbols) at various concentrations of sulfate

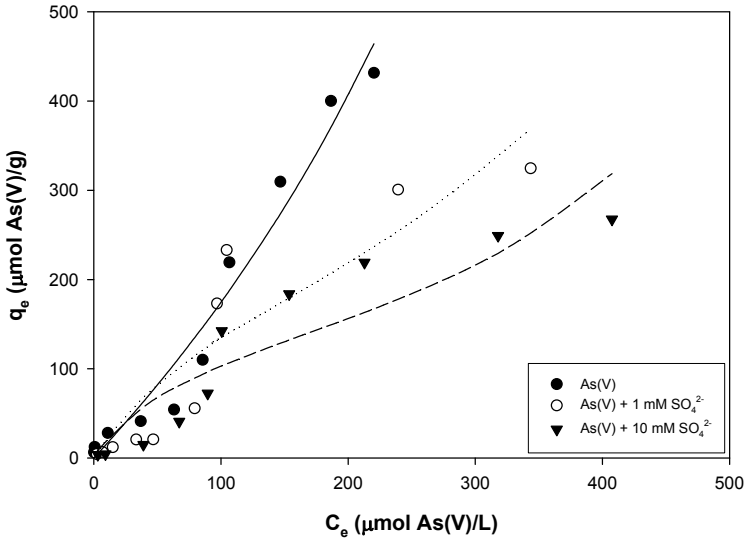

Figure 47. Measured concentrations of As(V) on FeS as function of concentration in water with BET equation (lines) fitted to data (symbols) at various concentrations of sulfate

Table 24. Parameters for models describing removal of As(V) by FeS as affected by sulfate concentration

SO_4^{2-} (mM)	*Langmuir*			
	b (L/µmol)	**q_{max} (µmol/g)**	**SSR**	**Δq (%)**
0	≈ 0	8.1E+5 ± 8.3E+8	1.1E+4	68
1	≈ 0.002	760 ± 962	1.7E+4	123
10	≈ 0.002	580± 426	6311	104
	Freundlich			
	K_f ($\mu^{mol1-1/n}.L^{1/n}/g$)	**n**	**SSR**	**Δq (%)**
0	0.52 ± 0.81	0.79 ± 0.19	6975	58
1	3.60 ± 7.23	1.26 ± 0.59	2.0E+4	134
10	3.59 ± 5.53	1.36 ± 0.51	8688	148
	BET			
	q_{max} (µmol/g)	**a**	**SSR**	**Δq (%)**
0	818 ± 783	1.26± 1.74	8765	39
1	203 ± 84	7.34 ± 11.1	2.3E+4	25
10	132 ± 40	11.0 ± 18.6	1.5E+4524	31

Stability experiments for As(V) were conducted similarly to those for As(III). A 1-g/L of suspension of FeS containing 15.2 µM As(V) was initially adjusted to near pH 10 and then

titrated with acid to near pH 4 and then with base to above pH 10 . Figure 48 shows that initially at near pH 10, removal of As(V) was low (20%), but as pH decreased, the removals gradually increased to about 80% near pH 4. This could be caused by formation of strongly bound surface species. The trend of As(V) removal shown in Figure 18 for decreasing pH was similar to that observed for As(V) on iron (hydr)oxides or pyrite (Dzombak and Morel, 1990; Zouboulis et al., 1993). As pH increased, arsenic was initially released to the solution between pH 5 and pH 7 and then additional removal occurred above pH 7. It is difficult to explain this behavior simply, but it is possible that surface reactions occurred that produced new compounds that determined arsenic binding as pH was increased. For example, at low pH, As(V) might be reduced to As(III) by FeS along with oxidation of Fe or S, resulting in the formation of SO_4^{2-} and Fe(III) which could be responsible for formation of sulfate green rust (GR-SO_4) or other oxidized products. If this occurred, interaction of arsenic with the GR-SO_4 surface could be important in determining soluble arsenic concentrations.

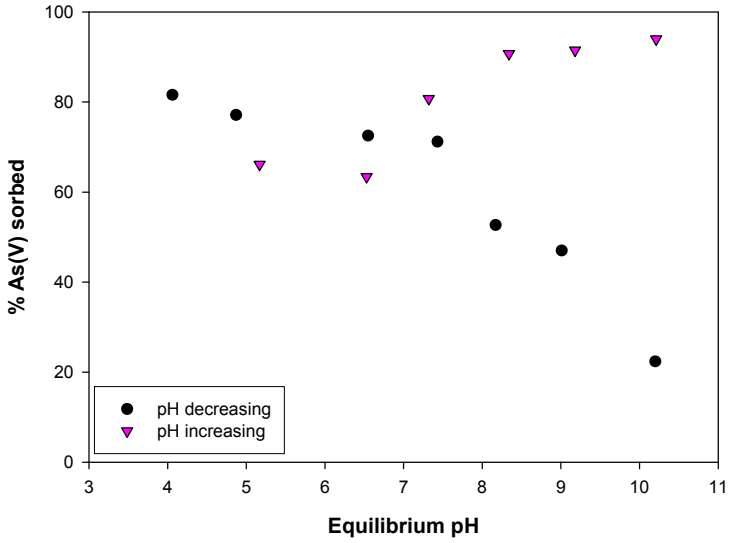

Figure 48. Effect of pH on removal of As(V) (15.2 μM) by FeS (1 g/L) as pH was decreased from pH 10 and subsequently was increased.

Characterization of Mackinawite-Arsenic

Figure 49 shows the Fe $2p_{3/2}$ XPS spectra of mackinawite after contact with As(III) for various times. There are four major peaks for Fe(II)-S, Fe(II)-O, Fe(III)-S, Fe(III)-O at 706.2~706.6, 707.3~707.5, 708.0~709.2, 709.8~712.6 eV, respectively. After contact times increased, the percent of peak area for Fe(III)-S and Fe(III)-O species increased while the relative peak area related to Fe(II)-S and Fe(II)-O species decreased due to surface oxidation of iron sorption sites. Also, Figure 50 shows the Fe $2p_{3/2}$ XPS spectra for As(V) contacted with mackinawite for various times. The spectra for As(V)-contacted mackinawite presented four major peaks, which are similar to those observed for As(III)-contacted mackinawite. Longer contact times resulted in larger peaks for Fe(III)-S and Fe(III)-O. In particular, the Fe(III)-O peaks at 710.3~712.3 eV are attributed to Fe(III) hydr(oxides) and the peak at 713.3 eV may be due to an Fe(III) multiplet structure (Bonnissel-Gissinger et al., 1998).

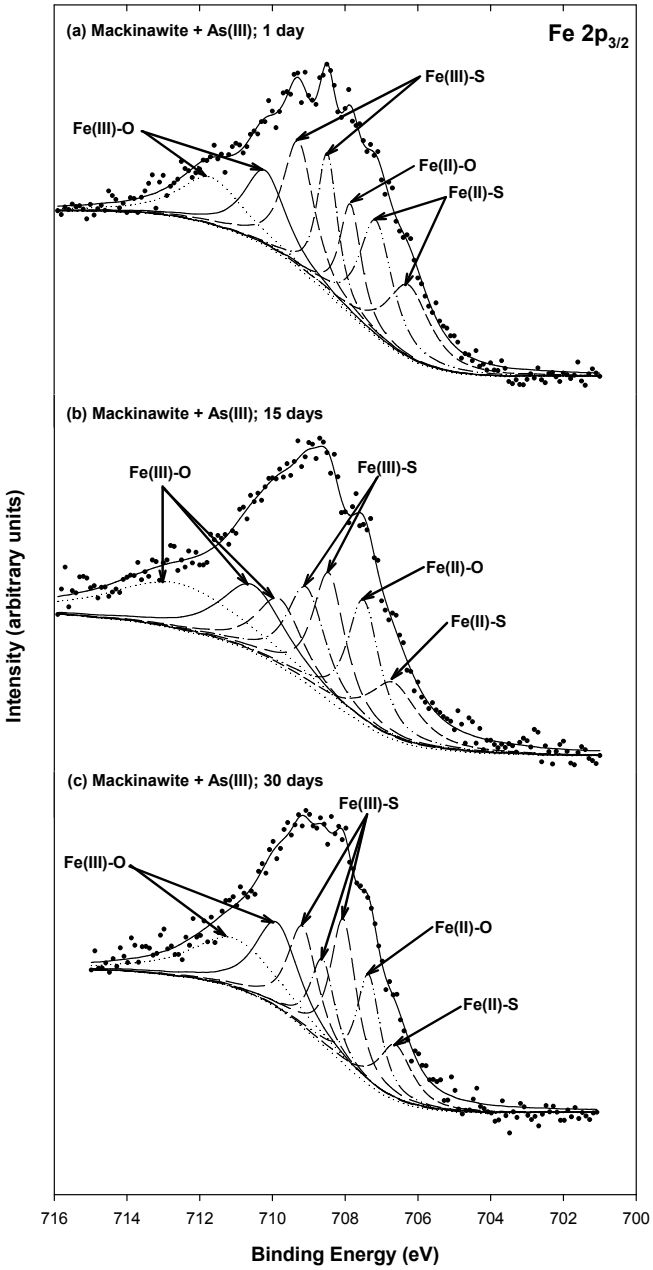

Figure 49. High resolution Fe $2p_{3/2}$ XPS spectra of FeS (1 g/L) reacted with 3.3 mM As(III) at pH 8 for various times: (a) 1 day, (b) 15 days, (c) 30 days.

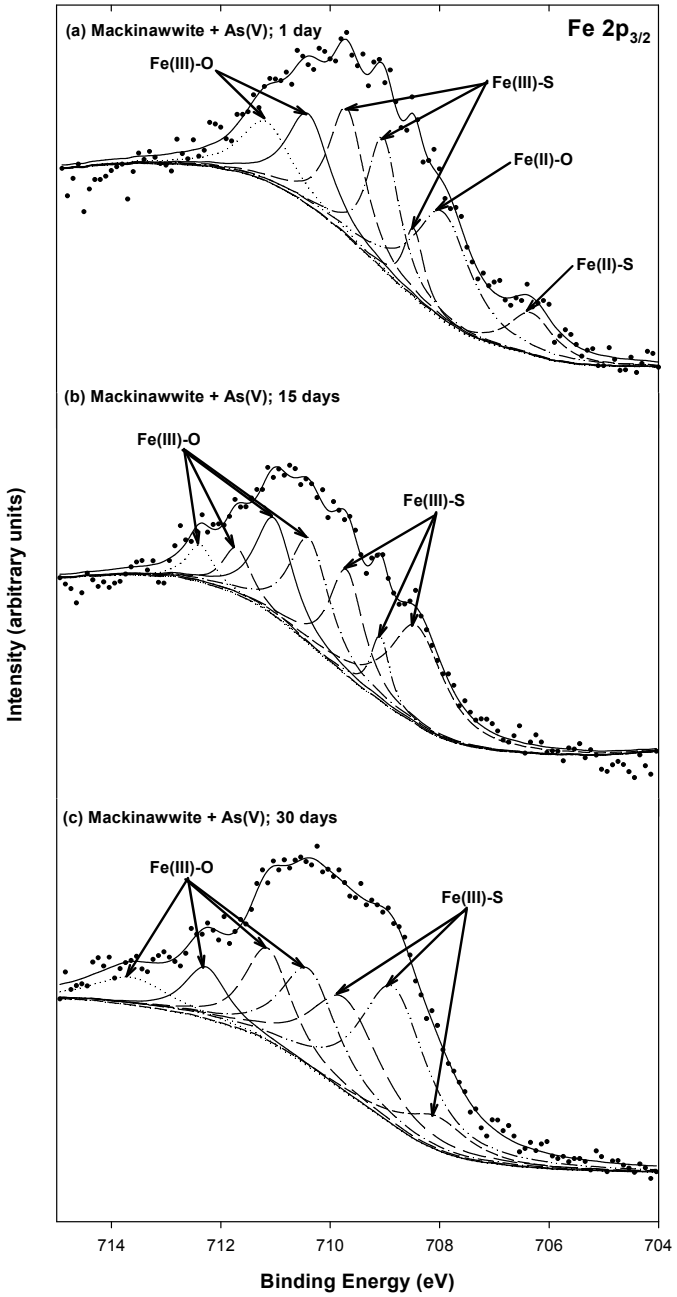

Figure 50. High resolution Fe $2p_{3/2}$ XPS spectra of FeS (1 g/L) reacted with 3.3 mM As(V) at pH 8 for various times: (a) 1 day, (b) 15 days, (c) 30 days.

Figure 51 shows the S 2p XPS spectra for mackinawite reacted with As(III) for various times. The major component of the S 2p spectra is located at ~161.9 eV and this peak is assigned to sulfide (S^{2-}) in mackinawite. However, more components are required to fit the high energy tail more precisely, so polysulfides (S_n^{2-}) and elemental sulfur (S^o) are included as sulfur species. A peak for SO_4^{2-} in the S 2p spectra is observed at 168.4 eV in systems that had reacted for 30 days. Figure 52 shows the S 2p XPS spectra for mackinawite reacted with As(V) for various

times. For mackinawite reacted with As(V) for 1 and 15 days, the S 2p spectra are decomposed by four multiplets associated with S^{2-} and singlet associated with S_n^{2-}, whereas the spectra for mackinawite reacted for 30 days includes peaks associated with elemental sulfur (S^o), which is needed to the fit the high energy tail. Tables 25 and 26 summarize binding energies (BE), peak full width at half maximum (FWHM), peak area percentage for Fe $2p_{3/2}$ and S 2p photoelectron spectra of mackinawite contacted with As(III) and As(V) for various times.

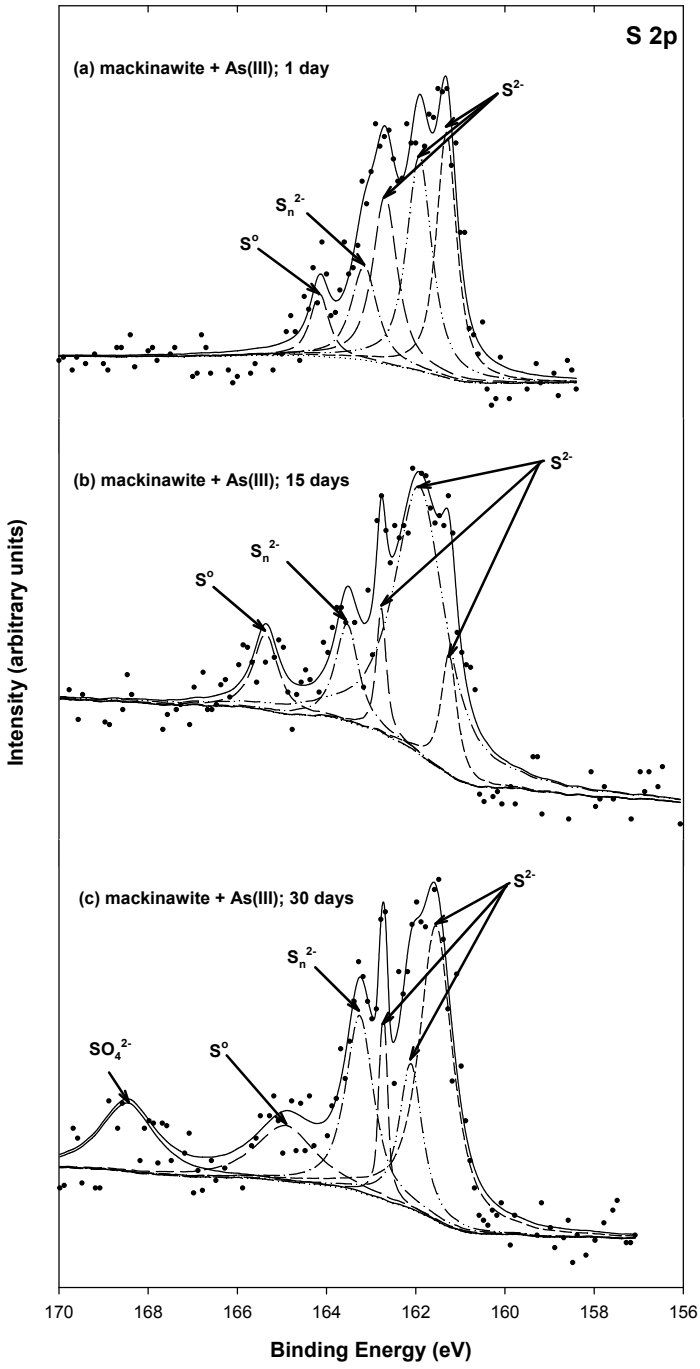

Figure 51. High resolution S 2p XPS spectra of FeS (1 g/L) reacted with 3.3 mM As(III) at pH 8 for various times: (a) 1 day, (b) 15 days, (c) 30 days.

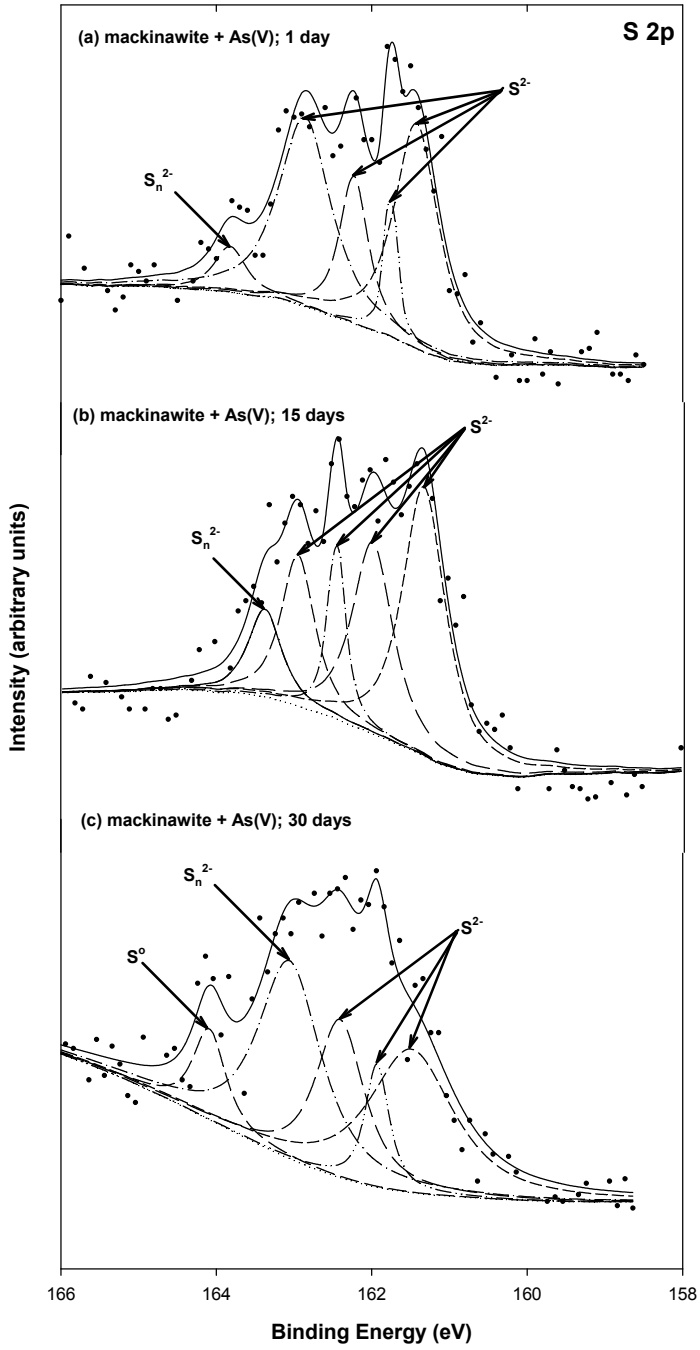

Figure 52. High resolution S 2p XPS spectra of FeS (1 g/L) reacted with 3.3 mM As(V) at pH 8 for various times: (a) 1 day, (b) 15 days, (c) 30 days.

Table 25. Binding energies (BE), peak full width at half maximum (FWHM), peak area percentage for Fe $2p_{3/2}$ photoelectron spectra of mackinawite contacted with As(III) and As(V) for various times.

Sample	Time (days)	χ^2	BE (eV)	FHWM (eV)	Area (%)	Chemical states
Mackinawite	0	0.49	706.0	0.49	10.4	Fe(II)-S
			706.4	0.55	14.6	Fe(II)-S
			706.9	0.71	17.8	Fe(II)-S
			707.7	0.98	18.7	Fe(II)-O
			708.8	1.26	14.6	Fe(III)-S
			710.1	1.67	14.9	Fe(III)-O
			711.8	2.51	9.0	Fe(III)-O
Mackinawite+As(IIII)	1	0.63	706.2	1.43	14.3	Fe(II)-S
			707.1	1.07	16.9	Fe(II)-O
			707.8	0.72	10.8	Fe(II)-O
			708.4	0.67	12.8	Fe(III)-S
			709.2	1.03	17.7	Fe(III)-S
			710.2	1.36	13.9	Fe(III)-O
			711.7	2.08	13.3	Fe(III)-O
	15	0.56	706.6	1.63	9.9	Fe(II)-S
			707.5	1.05	14.1	Fe(II)-O
			708.4	1.06	14.6	Fe(III)-S
			709.1	1.28	13.2	Fe(III)-S
			709.8	1.53	11.1	Fe(III)-O
			710.5	2.12	15.3	Fe(III)-O
			712.6	4.35	21.6	Fe(III)-O
	30	0.75	706.6	1.11	8.8	Fe(II)-S
			707.3	0.78	12.3	Fe(II)-O
			708.0	0.84	17.4	Fe(III)-S
			708.6	0.81	9.8	Fe(III)-S
			709.1	0.98	14.0	Fe(III)-S
			709.8	1.45	17.7	Fe(III)-O
			711.0	2.82	19.9	Fe(III)-O
Mackinawite+As(V)	1	0.72	706.3	0.98	7.6	Fe(II)-S
			707.9	1.22	24.3	Fe(III)-S
			708.4	0.44	5.6	Fe(III)-S
			709.0	0.69	16.8	Fe(III)-S
			709.6	0.78	18.4	Fe(III)-S
			710.4	0.93	15.6	Fe(III)-O
			711.1	1.07	11.8	Fe(III)-O
	15	1.03	708.4	1.19	26.4	Fe(III)-S
			709.0	0.41	6.03	Fe(III)-S
			709.6	0.74	17.5	Fe(III)-S
			710.3	0.87	20.6	Fe(III)-O
			711.0	0.84	18.2	Fe(III)-O
			711.7	0.62	6.5	Fe(III)-O
			712.3	0.58	4.8	Fe(III)-O
	30	0.47	708.0	1.41	6.83	Fe(III)-S
			708.8	1.45	28.6	Fe(III)-S
			709.7	1.52	20.3	Fe(III)-S
			710.3	1.22	17.2	Fe(III)-O
			711.1	1.03	13.7	Fe(III)-O
			712.2	0.93	6.9	Fe(III)-O
			713.3	1.61	6.4	Fe(III)-O

Table 26. Binding energies (BE), peak full width at half maximum (FWHM), peak area percentage for S 2p photoelectron spectra of mackinawite contacted with As(III) and As(V) for various times.

Sample	Contact time (days)	χ^2	BE (eV)	FHWM (eV)	Area (%)	Chemical states
Mackinawite	0	0.46	161.3	0.55	14.0	S^{2-}
			161.8	0.62	22.0	S^{2-}
			162.3	0.68	26.3	S^{2-}
			163.1	1.03	35.0	S_n^{2-}
			164.5	0.88	2.60	S^o
Mackinawite+As(III)	1	0.78	161.3	0.54	27.7	S^{2-}
			161.9	0.67	30.0	S^{2-}
			162.6	0.65	22.7	S^{2-}
			163.1	0.69	13.2	S_n^{2-}
			164.1	0.44	6.40	S^o
	15	0.64	161.2	0.43	9.20	S^{2-}
			161.9	1.34	65.0	S^{2-}
			162.7	0.26	5.80	S^{2-}
			163.5	0.62	10.7	S_n^{2-}
			165.3	0.66	9.20	S^o
	30	0.47	161.5	0.89	36.9	S^{2-}
			162.1	0.61	12.6	S^{2-}
			162.7	0.20	5.70	S^{2-}
			163.2	0.74	18.3	S_n^{2-}
			164.9	1.56	12.4	S^o
			168.4	1.46	14.0	SO_4^{2-}
Mackinawite+As(V)	1	0.60	161.4	0.68	36.3	S^{2-}
			161.7	0.21	7.30	S^{2-}
			162.2	0.45	15.5	S^{2-}
			162.8	0.80	35.8	S^{2-}
			163.8	0.50	5.20	S_n^{2-}
	15	0.74	161.3	0.67	37.9	S^{2-}
			162.0	0.63	25.6	S^{2-}
			162.4	0.28	10.6	S^{2-}
			162.9	0.52	16.5	S^{2-}
			163.4	0.51	9.40	S_n^{2-}
	30	0.87	161.5	1.30	31.9	S^{2-}
			161.9	0.37	7.90	S^{2-}
			162.4	0.74	19.9	S^{2-}
			163.0	0.96	32.7	S_n^{2-}
			164.1	0.50	7.60	S^o

Figures 53 and 54 show the As 3d XPS spectra of mackinawite reacted with As(III) or As(V) for various times. The main peaks for As(III) and As(V) are centered at 44.6 eV and 45.3 eV, respectively. For As(III)-contacted mackinawite, the As 3d spectra include peaks associated with As(II) in the low energy tail, but they are not major contributors, because the shape of As 3d spectra is highly symmetric. Also, there is no effect of contact time on reduction of As(III) species as shown by the fact that the widths of the peaks measured as FWHM (full width at half maximum) are relatively constant. Peak width is typically affected by the extent of change of chemical status. For As(V)-contacted mackinawite, peaks associated with As(V) and As(III) are the major components of the As 3d spectra. However, there is little evidence that As(V) is reduced by mackinawite. Even though the positions of peaks associated with As(V) deviate from the general binding energy for As(V), the shapes of As 3d peaks are highly symmetric.

Furthermore, there is no significant change in the FWHM of As 3d peaks, which suggests that there are no surface reactions of As(V) sorbed on mackinawite that lead to stable precipitates.

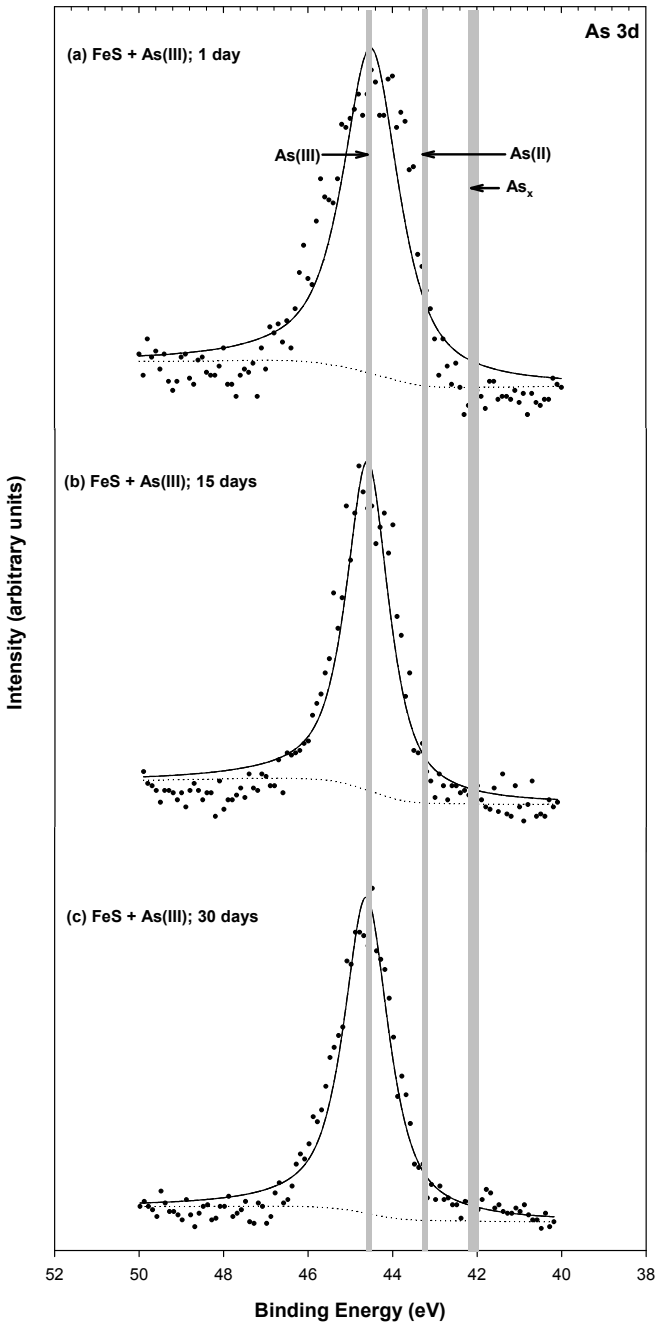

Figure 53. High resolution As 3d XPS spectra of synthetic mackinawite (1 g/L) reacted with 3.3 mM As(III) at pH 8 for various times: (a) 1 day, (b) 15 days, (c) 30 days. Gray bars indicate reported ranges of binding energies associated with As(III), As(V) and As_x.

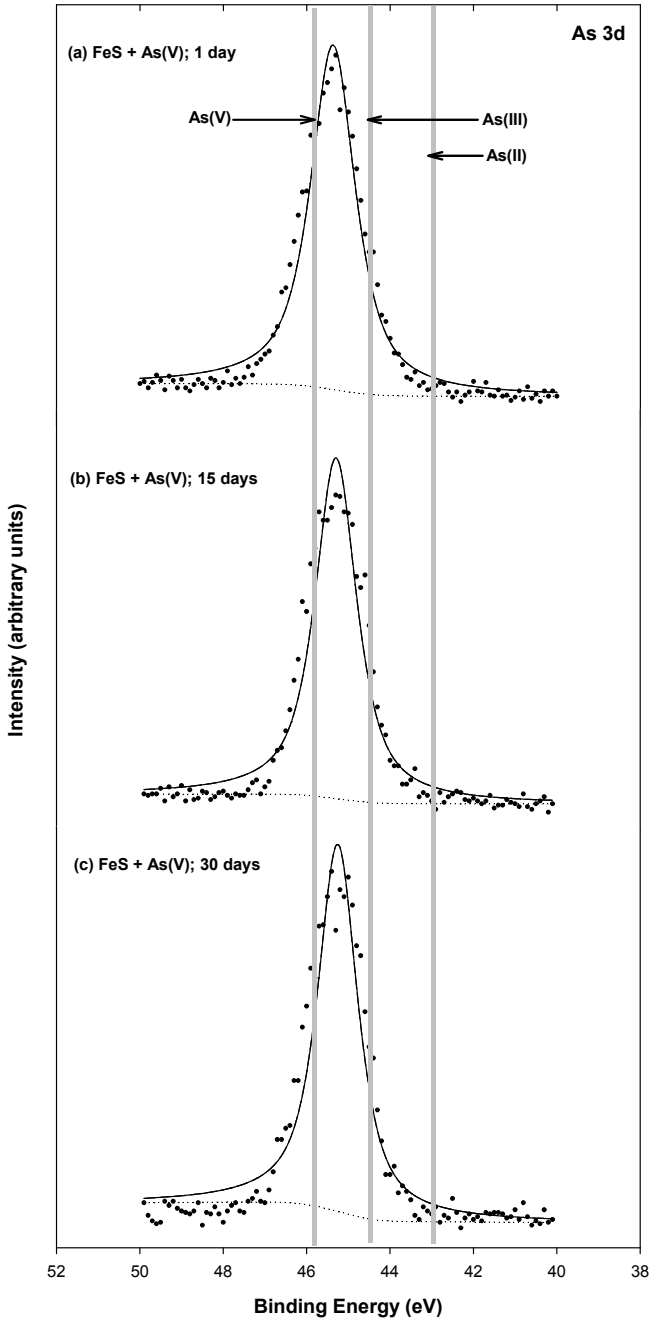

Figure 54. High resolution As 3d XPS spectra of synthetic mackinawite (1 g/L) reacted with 3.3 mM As(V) at pH 8 for various times: (a) 1 day, (b) 15 days, (c) 30 days. Gray bars indicate reported ranges of binding energies associated with As(V), As(III) and As(II).

To investigate reaction mechanisms affecting the stability of As(III)-contacted FeS as pH is changed, the oxidation states of the surface-bound Fe and S were analyzed for samples taken during stability tests and analyzed by XPS. Figure 55 shows the As 3d XPS spectra of FeS after contact with As(III) at pH $10_{(i)}$) and pH $4_{(a.a.t)}$. The As 3d spectra was not useful in determining oxidation state of As, because the solid-phase As concentration was too low. Nonetheless, a

minimal arsenic peak was centered at the binding energy near 44.3 eV, which is representative of As(III). In addition, a large peak associated with Fe 3p was observed near 55 eV.

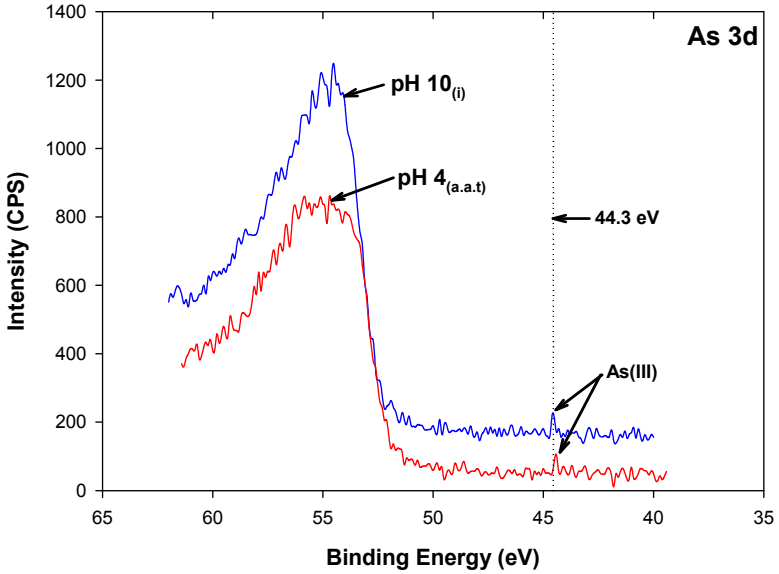

Figure 55. High resolution As 3d XPS spectra for FeS after contact with As(III)(15.2 µM) at (a) pH $10_{(i)}$) and (b) pH $4_{(a.a.t)}$.

The Fe $2p_{3/2}$ XPS spectra (Figure 56) shows that more oxidation of the surface-bound Fe was observed in the pH $4_{(a.a.t)}$ sample than in the pH $10_{(i)}$ sample as shown by the peak area for Fe(III)-O being larger by a factor of 2.4. Analogous to the XPS results for the Fe $2p_{3/2}$ spectra, the S 2p spectra of the pH $4_{(a.a.t)}$ sample exhibited evidence for more oxidation of the surface S species, as indicated by the presence of a peak associated with elemental sulfur (S^o) that was not observed in the spectra for the pH $10_{(i)}$ sample (Figure 57). Based on the results of XPS analysis and the stability test (Figure 41), high removal of As(III) at pH 4 may be the result of redox reaction in which surface species are oxidized and As(III) is reduced, leading to formation of strongly bound surface species that are not easily released to solution as pH is changed. Table 27 presents information on the peaks shown in Figures 56 and 57.

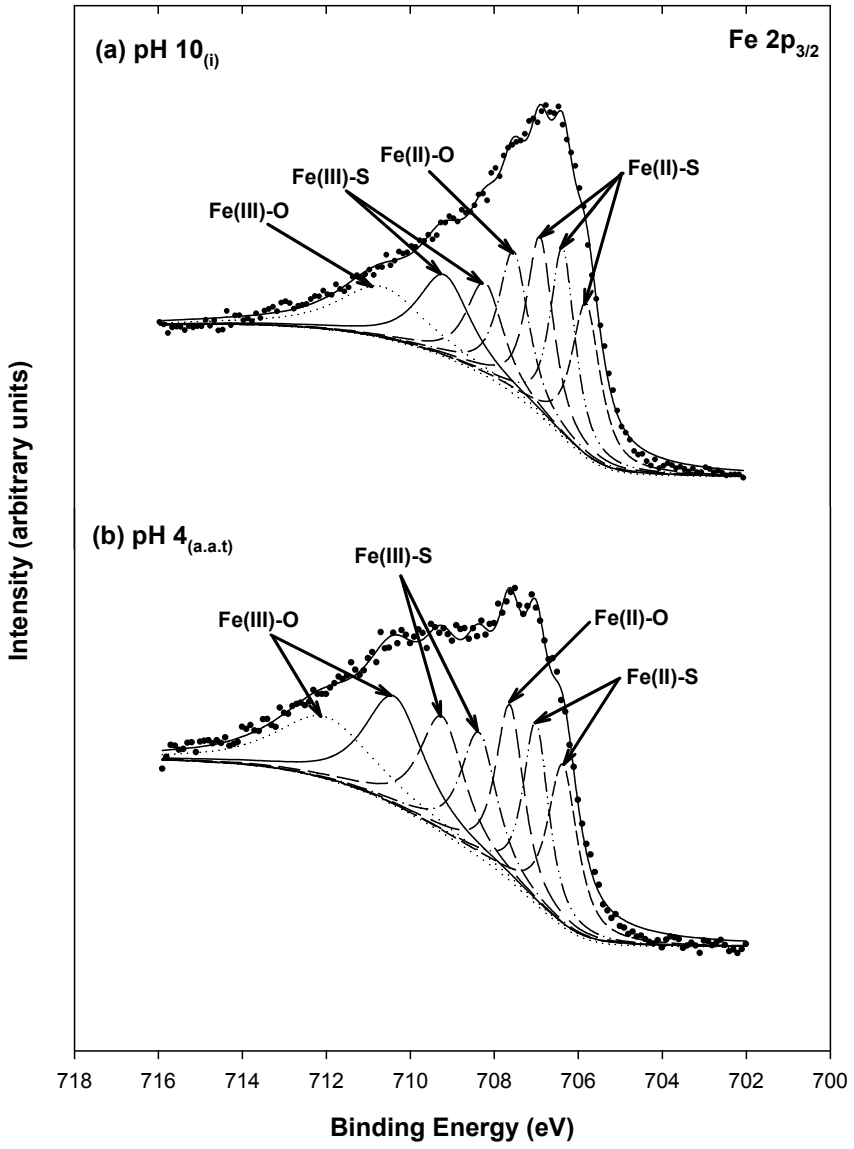

Figure 56. High resolution Fe $2p_{3/2}$ XPS spectra for FeS reacted with As(III) (15.2 μM) at (a) pH $10_{(i)}$ and (b) pH $4_{(a.a.t)}$.

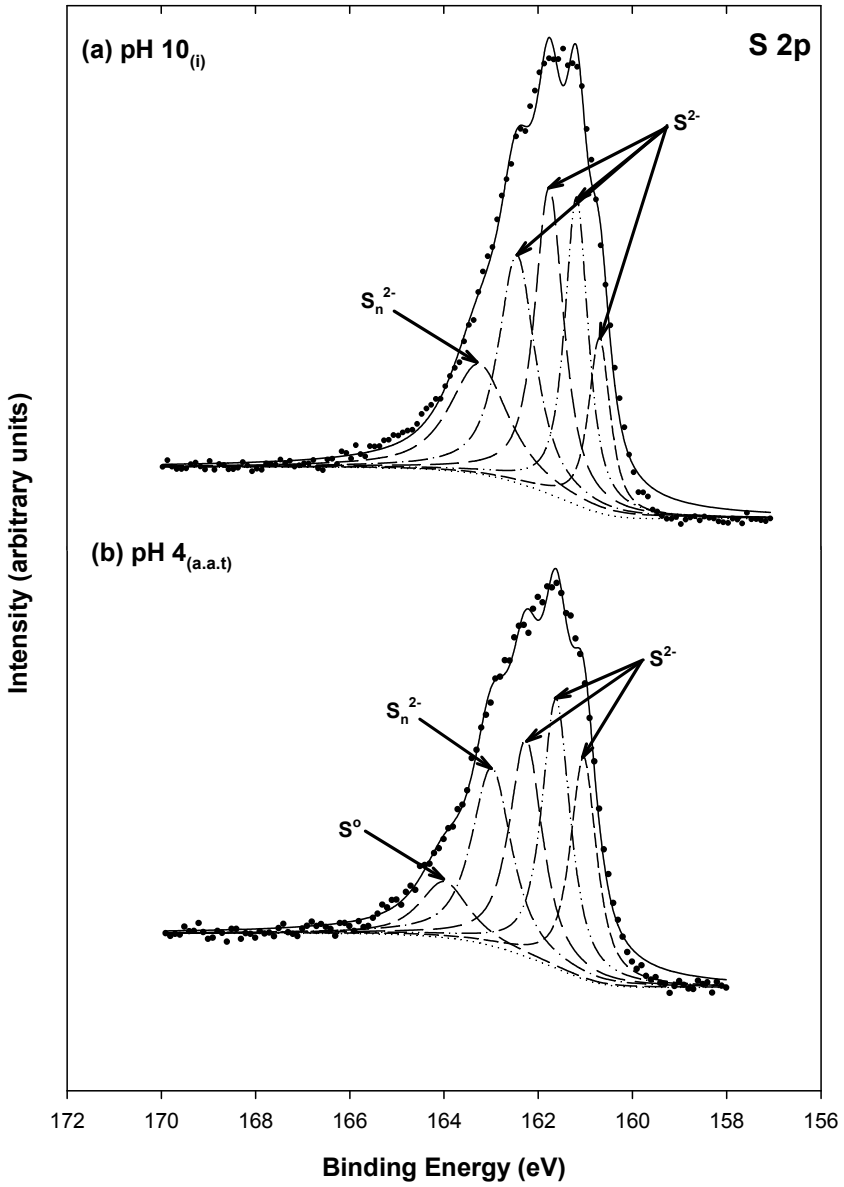

Figure 57. High resolution S 2p XPS spectra for FeS reacted with As(III) (15.2 μM) at (a) pH $10_{(i)}$and (b) pH $4_{(a.a.t)}$.

Table 27. Binding energies (BE), full width at half maximum (FWHM), and area percentage for peaks in the Fe 2p3/2 and S 2p XPS spectra of FeS after contact with As(III) at pH $10_{(i)}$ and pH $4_{(a.a.t)}$.

Samples	BE (eV)	FHWM (eV)	Area (%)	Chemical states
Fe 2p$_{3/2}$				
pH 10$_{(i)}$	705.8	0.81	14.5	Fe(II)-S
	706.4	0.71	15.5	Fe(II)-S
	706.9	0.76	15.8	Fe(II)-S
	707.5	0.85	14.1	Fe(II)-O
	708.2	1.06	11.4	Fe(III)-S
	709.2	1.50	14.3	Fe(III)-S
	710.7	2.41	14.4	Fe(III)-O
pH 4$_{(a.a.t)}$	706.3	0.84	13.1	Fe(II)-S
	707.0	0.72	12.6	Fe(II)-S
	707.6	0.80	13.5	Fe(II)-O
	708.3	1.01	12.1	Fe(III)-S
	709.2	1.27	14.1	Fe(III)-S
	710.4	1.71	17.9	Fe(III)-O
	712.0	2.75	16.5	Fe(III)-O
S 2p				
pH 10$_{(i)}$	160.7	0.55	10.9	S^{2-}
	161.2	0.59	20.7	S^{2-}
	161.7	0.73	25.6	S^{2-}
	162.4	0.93	24.1	S^{2-}
	163.2	1.48	18.6	S_n^{2-}
pH 4$_{(a.a.t)}$	161.0	0.66	19.1	S^{2-}
	161.6	0.72	25.0	S^{2-}
	162.2	0.84	23.6	S^{2-}
	162.9	1.00	23.3	S^{2-}
	163.9	1.23	8.9	S_n^{2-}

The solids in samples from the As(V) stability tests at pH $10_{(i)}$ and pH $4_{(a.a.t)}$ were analyzed using XPS. Figure 58 shows the As 3d XPS spectra of FeS reacted with As(V) at pH $4_{(a.a.t)}$, pH $10_{(i)}$, and pH $10_{(f)}$. As shown previously in the As 3d spectra of As(III)-contacted FeS, the spectra for As(V)-contacted FeS also exhibited a relatively large Fe 3p peaks near 55 eV. All of the peaks in the As 3d XPS spectra are of low intensity relative to Fe 3p peaks, because the As loading on solids was low, so determination of arsenic species on the surface is difficult. However, we can recognize that the main peaks of the As 3d spectra for the pH $10_{(i)}$ and pH $4_{(a.a.t)}$ are located near 46 eV, which is representative of As(V), although there is a minor shift of As(V) peak to lower binding energy in the pH $4_{(a.a.t)}$ sample. In the case of pH $10_{(f)}$ sample, the occurrence of species that are more reduced than As(V) could not be totally ruled out, because a weak peak was observed at 43.77 eV, which is assigned to As(III). The additional removal of As(V) as pH increased could be explained by sorption of As(V) onto newly formed surface species or onto patches of oxidized products of FeS, such as GR-SO_4 or iron (hydro)oxides. To confirm this hypothesis, the Fe $2p_{3/2}$ and S 2p XPS spectra were obtained and evaluated.

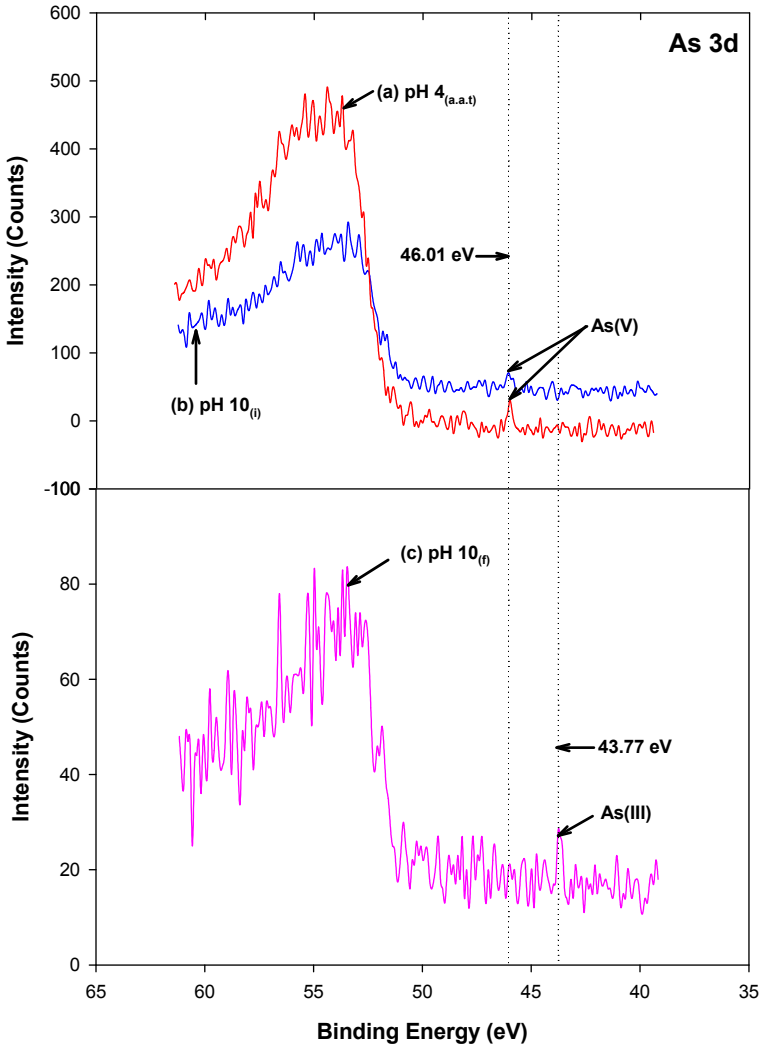

Figure 58. High resolution As 3d XPS spectra for (a) pH $4_{(a.a.t)}$ sample, (b) pH $10_{(i)}$ sample, and (c) pH $10_{(f)}$ sample after contact with As(V) (15.2 µM).

Figure 59 indicated that surface Fe species on the three samples had not undergone appreciable surface oxidation, compared to pure FeS at pH 4 and 10. In contrast to the Fe $2p_{3/2}$ spectra, the S 2p spectra shows that the surface S species had experienced surface oxidation whenever pH was changed (Figure 60). Although removal of As(V) was initially low at pH 10, a peak associated with elemental sulfur (S^o) was present and is evidence of surface oxidation. This suggests that surface S species are acting as sorbent/reactant for As(V), rather than the surface Fe species. Moreover, the extent of the surface S oxidation increased at lower pH, where removal of As(V) increased strongly. In addition to showing increased removal of As(V), the pH $10_{(f)}$ sample exhibited more oxidation of surface-bound S, as indicated by peaks associated with polysulfides (S_n^{2-}) and elemental sulfur (S^o) showing higher intensity. These results may be attributed not only to the simple chemical reaction between As(V) and the surface, but to the complicated interactions between As(V) itself or forms of reduced As and the FeS surface. As(V) can strongly sorb onto newly formed surface species as a result of mixture of iron-sulfur-arsenic,

resulting in nearly complete removal of arsenic. Table 28 presents information on the peaks shown in Figures 59 and 60.

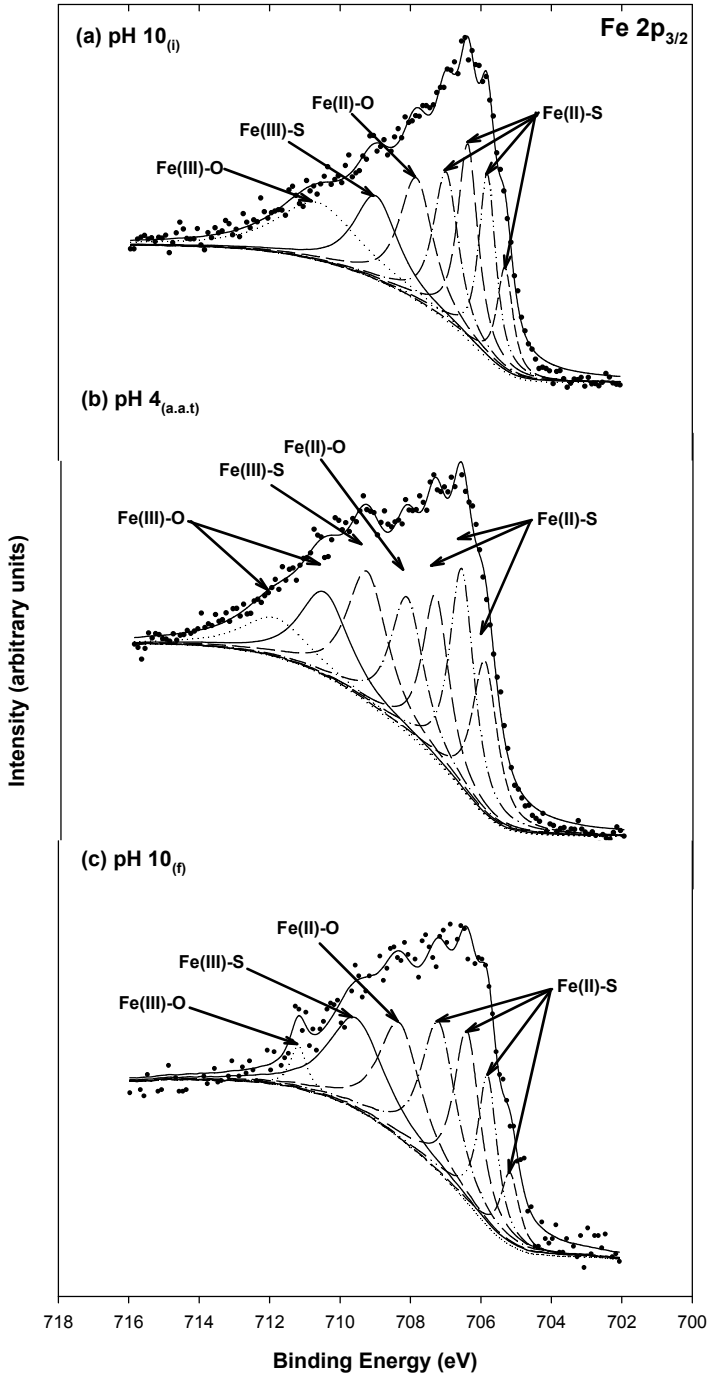

Figure 59. High resolution Fe $2p_{3/2}$ XPS spectra for (a) pH $10_{(i)}$ sample, (b) pH $4_{(a.a.t)}$, and (c) pH $10_{(f)}$ sample after contact with As(V) (15.2 μM) .

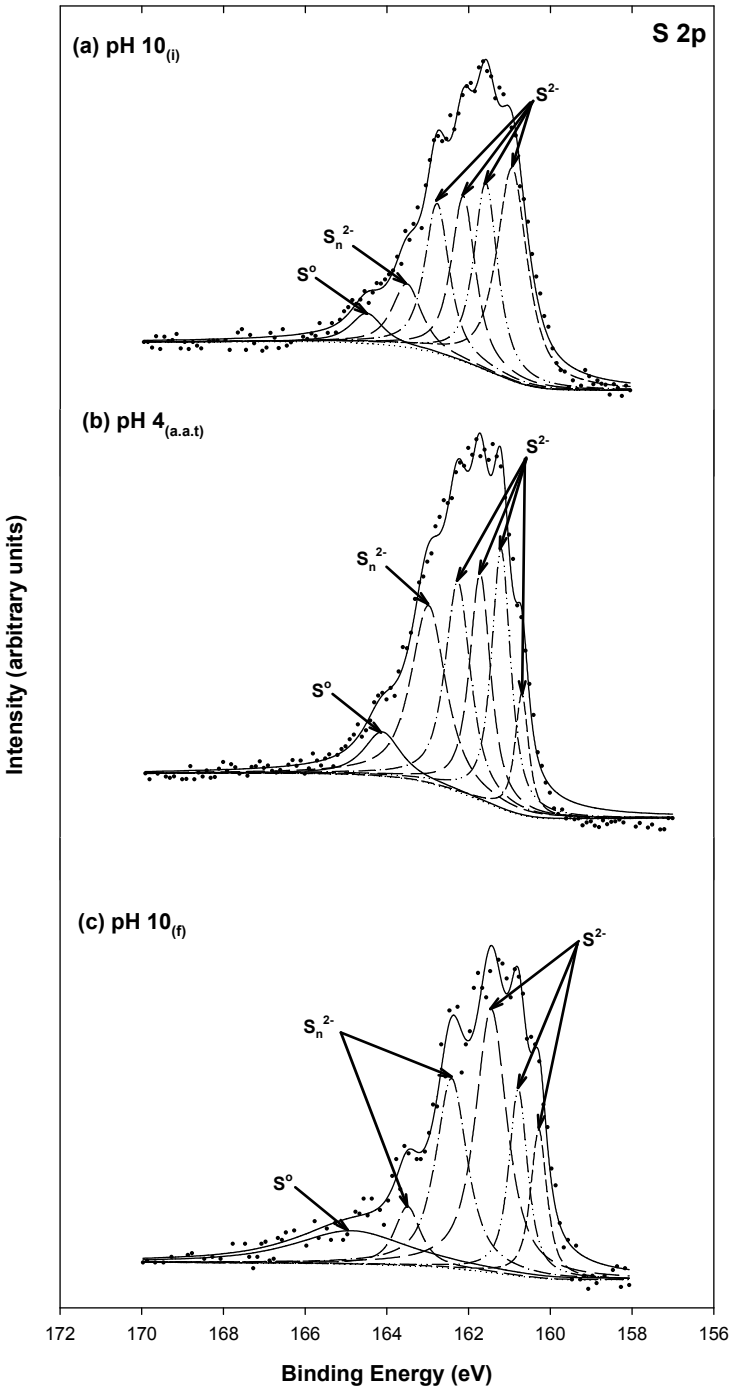

Figure 60. High resolution S 2p XPS spectra for (a) pH $10_{(i)}$ sample, (b) pH $4_{(a.a.t)}$, and (c) pH $10_{(f)}$ sample after contact with As(V) (15.2 μM).

Table 28. Binding energies (BE), full width at half maximum (FWHM), and area percentage for peaks in the Fe $2p_{3/2}$ and S 2p XPS spectra of pH $10_{(i)}$ sample, pH $4_{(a.a.t)}$, and pH $10_{(f)}$ sample after contact with As(V) (15.2 μM).

Samples	BE (eV)	FHWM (eV)	Area (%)	Chemical states
Fe $2p_{3/2}$				
pH $10_{(i)}$	705.3	0.54	6.7	Fe(II)-S
	705.8	0.58	12.7	Fe(II)-S
	706.3	0.69	15.9	Fe(II)-S
	706.9	0.85	14.9	Fe(II)-S
	707.8	1.14	16.5	Fe(II)-O
	708.9	1.48	14.7	Fe(III)-S
	710.6	2.71	18.6	Fe(III)-O
pH $4_{(a.a.t)}$	705.9	0.84	12.6	Fe(II)-S
	706.6	0.82	17.7	Fe(II)-S
	707.3	0.89	14.5	Fe(II)-O
	708.1	1.13	15.0	Fe(III)-S
	709.3	1.35	17.1	Fe(III)-S
	710.5	1.68	13.9	Fe(III)-O
	711.8	2.29	9.11	Fe(III)-O
pH $10_{(f)}$	705.2	0.62	5.4	Fe(II)-S
	705.8	0.66	11.9	Fe(II)-S
	706.4	0.88	18.2	Fe(II)-S
	707.2	1.18	21.3	Fe(II)-O
	708.3	1.41	19.6	Fe(III)-S
	709.5	1.90	20.8	Fe(III)-S
	711.2	0.56	2.9	Fe(III)-O
S 2p				
pH $10_{(i)}$	160.9	0.89	30.3	S^{2-}
	161.5	0.69	20.8	S^{2-}
	162.1	0.71	18.7	S^{2-}
	162.7	0.71	17.1	S^{2-}
	163.5	0.86	8.7	S_n^{2-}
	164.5	0.93	4.5	S^o
pH $4_{(a.a.t)}$	160.6	0.40	6.8	S^{2-}
	161.2	0.55	20.1	S^{2-}
	161.7	0.61	19.5	S^{2-}
	162.2	0.74	21.9	S^{2-}
	162.9	1.01	25.1	S^{2-}
	164.1	1.07	6.6	S^o
pH $10_{(f)}$	160.2	0.47	9.5	S^{2-}
	160.7	0.55	13.8	S^{2-}
	161.4	0.92	32.6	S^{2-}
	162.4	0.91	23.3	S^{2-}
	163.5	0.75	5.8	S_n^{2-}
	164.8	3.30	14.9	S^o

Mercury Removal and Stability

Pyrite

Mercury Removal and Stability

Table 29 shows the results of the kinetic experiments conducted to evaluate mercury removal by pyrite and Figure 61 shows the results of the experiment using an initial concentration of 500 μM and pyrite dose of 0.2 g/L. Additional kinetic tests were run at the higher mercury/pyrite ratios because initial tests showed very fast removal to below detection limits.

Table 29. Results of Kinetic Experiment on Hg Removal

Reaction Time (min)	Hg Con. (μM)		
	100 μM Hg 1 g/L FeS2	250 μM Hg 0.5 g/L FeS2	500 μM Hg 0.2 g/L FeS2
2	-	-	230.3
5	0.533	3.714	197.4
10	ND	0.511	160.2
15	ND	0.444	131.2
20	ND	0.688	111.4
30	ND	0.243	88.98
40	ND	0.072	71.99
60	ND	ND	51.08
90	ND	ND	32.61
120	ND	ND	22.32
180	ND	ND	13.40
240	ND	ND	10.84
360	ND	ND	9.34
720	ND	ND	6.20
1440	ND	ND	0.168

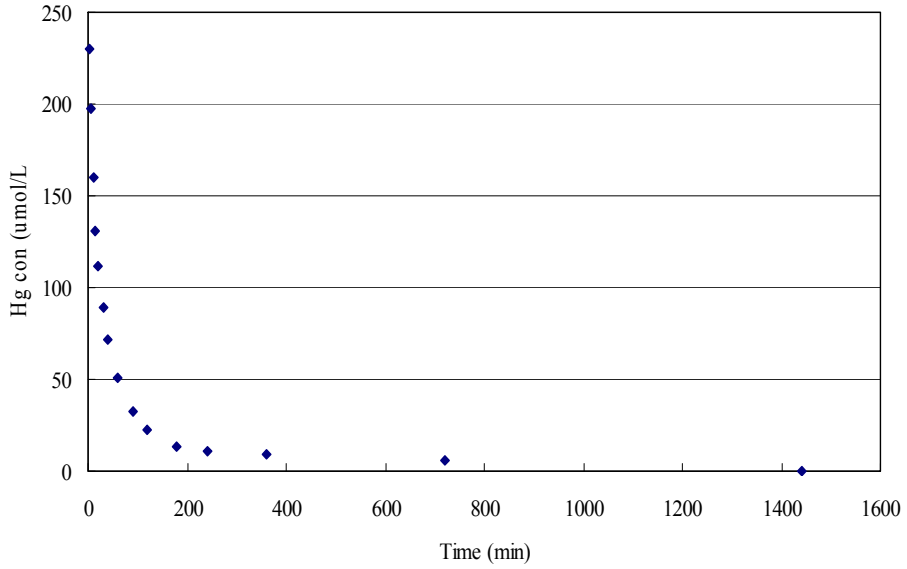

Figure 61. Removal of Hg as a function of time at pH 7 (initial concentration = 500 μM, pyrite dose = 0.2 g/L).

Table 30 shows results of experiments to characterize removal of mercury by pyrite over a range of pH values and Figures 62 and 63 display them graphically. Figure 62 shows all of the data and Figure 63 modifies the scales of the axes to more accurately display data at lower concentrations. These data indicate that mercury is strongly attracted to the surface of pyrite. They also show evidence of surface reactions at higher concentrations and at higher pH. The amount of mercury on the surface tends to increase at higher concentrations giving the relationship the appearance of a BET isotherm. The erratic behavior at intermediate mercury doses at pH 7 and 9 also supports surface reactions that could be slow to be initiated under some circumstances.

Table 30. Results of Experiments on Removal of Hg by Pyrite

Ci (μmol/L)	pH 7		pH 8		pH 9		pH 10	
	C (μmol/L)	q (μmol/g)	C (μmol/L)	q (μmol/g)	C (μmol/L)	q (μmol/g)	C (μmol/L)	q (μmol/g)
50	2.7	303	0.14	606	0.1	324	12.5	230
100	14.1	549	14.3	1042	0.2	647	31.6	420
250	49.2	1284	114	1648	45.5	1326	101	915
500	108	2509	314	2261	343	1018	269	1415
1000	337	4242	757	2953	787	1380	673	2009
2000	1531	3001	1722	3377	880	7263	1774	1388
3000	2541	2939	2571	5215	516	16102	2622	2322
4000*	3483	3309	4394	7365	675	21556	2463	9434

* 5000 at pH 8

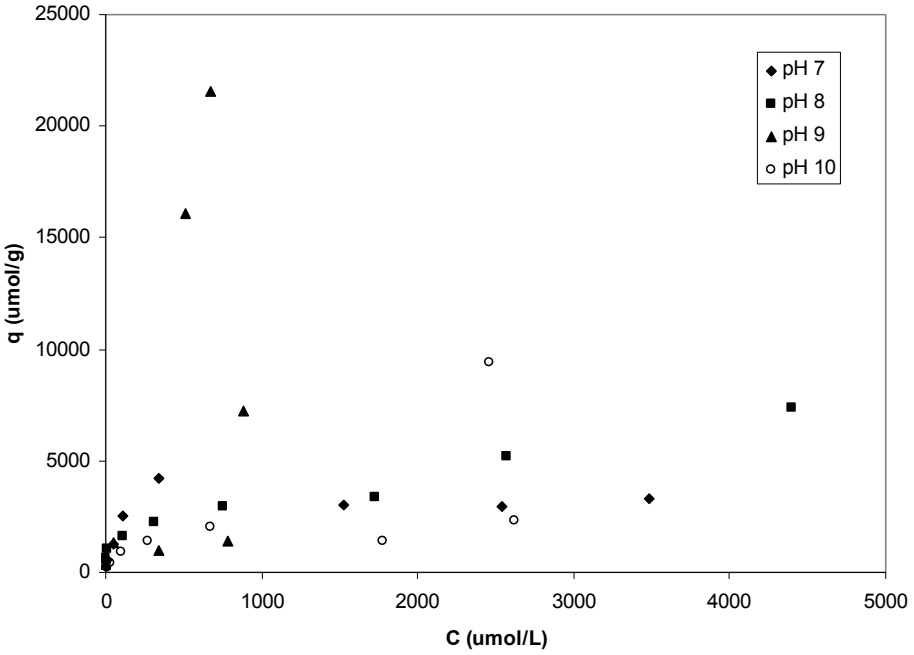

Figure 62. Measured concentrations of Hg on pyrite as functions of concentration in water for various pH.

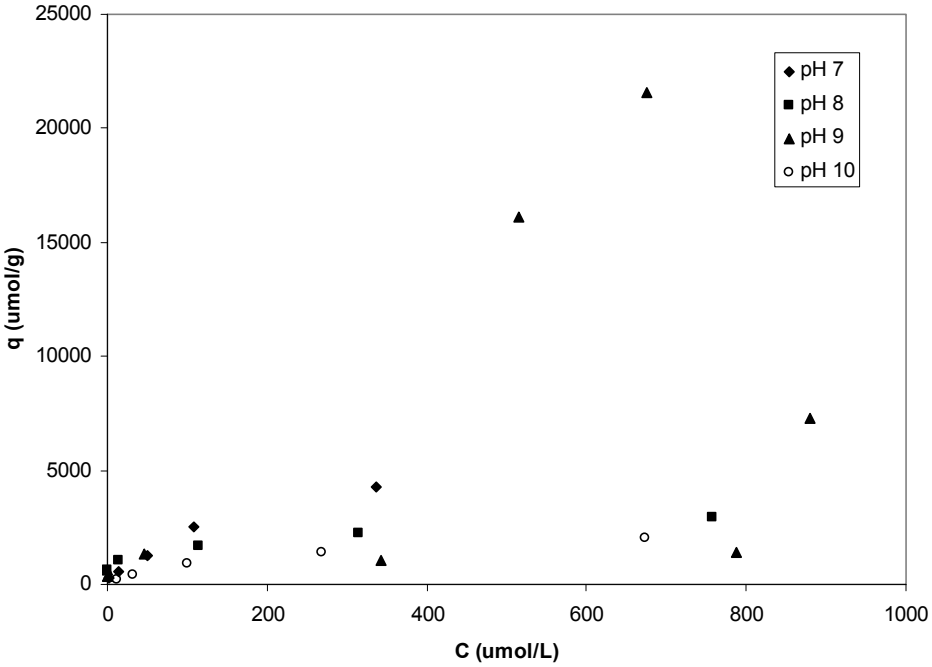

Figure 63. Measured concentrations of Hg on pyrite as function of concentration in water for various pH using data at lower concentrations.

Table 31 and Figure 64 show results of experiments to determine the effect of sulfate on

removal of mercury by pyrite. Sulfate appears to have little effect on mercury removal. The fact that the amount of mercury removed per unit mass of pyrite continues to increase supports the hypothesis that mercury is reacting on the surface of pyrite. If removal were due to simple adsorption onto the pyrite surface, then a maximum amount removed would be observed when the entire surface was covered. However, the results shown here do not display a tendency to reach a maximum.

Table 31. Results of Experiments to Determine Effect of Sulfate on Removal of Hg

Ci (umol/L)	0 mM of SO_4^{2-}		1 mM of SO_4^{2-}		10 mM of SO_4^{2-}	
	C (umol/L)	q (umol/g)	C (umol/L)	q (umol/g)	C (umol/L)	q (umol/g)
50	0.14	606	0.03	313	0.0	313
100	14.3	1042	20.3	499	7.1	581
250	114	1648	95	973	108.0	889
500	314	2261	204	1855	212	1801
1000	757	2953	561	2747	456	3406
2000	1722	3377	1390	3819	1383	3866
3000	2571	5215	2216	4906	2031	6066
4000*	4394	7365	3015	6169	3044	5986

* 5000 for 0 mM SO_4^{2-}

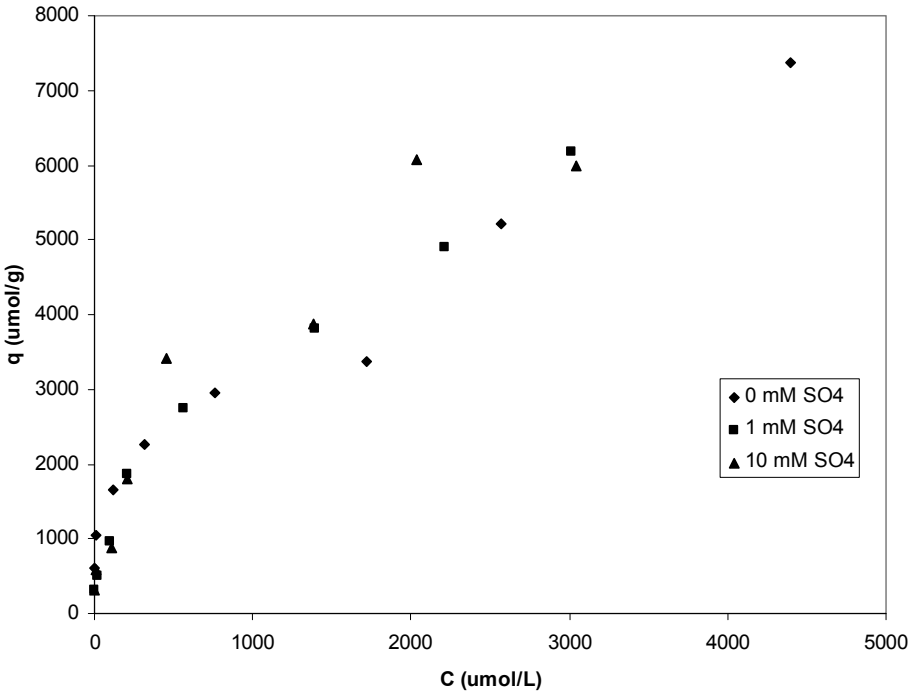

Figure 64. Measured concentrations of Hg on pyrite (symbols) as function of concentration in water at various concentrations of sulfate.

Figure 65 shows results of stability experiments for Hg(II) on pyrite as affected by pH. Since sorption of Hg(II) by pyrite is expected to be lowest below pH 4 (Bower et al. 2008), the suspension was initially adjusted to near pH 3.4. Hg(II) was nearly completely removed at all pH

values tested.

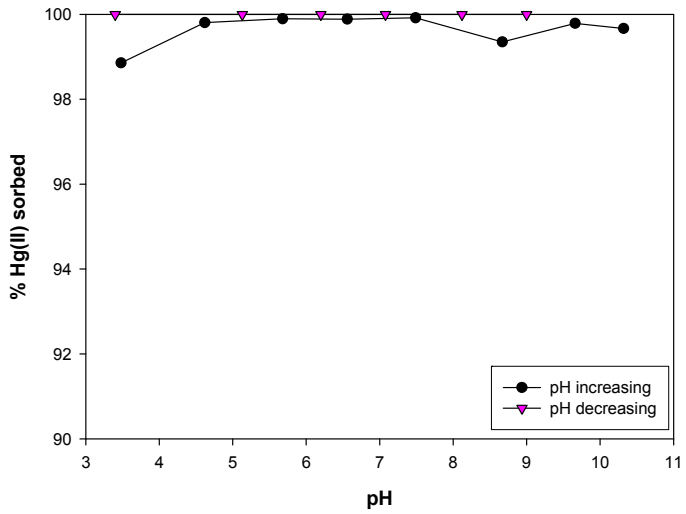

Figure 65. Effect of pH on removal of Hg(II) (6.48 μM) by pyrite (1 g/L) as pH was increased from pH 3.4 and subsequently was decreased

Figure 66 shows the results stability experiments conducted with Hg(II) on pyrite as affected by pH. These experiments were conducted at higher concentration of Hg(II) (1 mM) than the experiments discussed previously (6.48 μM). The results are similar in the two experiments, but experiments with the higher Hg(II) concentrations show a more pronounced increase in removal when pH was increased above the lowest value and although removals were high as pH was decreased, they were not near 100%. However, there was no release of mercury as pH was decreased. This suggests that relatively insoluble species were formed by reaction of mercury and pyrite at pH 10. Formation of precipitates such as $HgS_{(s)}$ or $Hg_2S_{(s)}$ could explain the observed behavior. Behra et al. (2001) suggested that the following mechanism shown in Equations 4-6 can lead to formation of precipitates in systems with Hg(II) and pyrite.

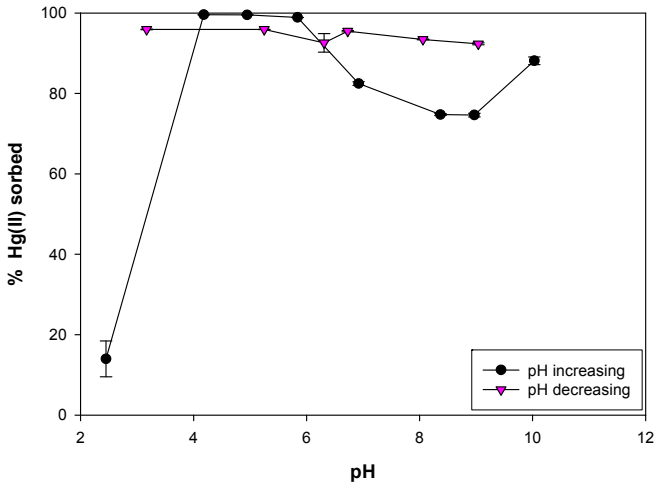

Figure 66. Effect of pH on removal of Hg(II) (1 mM) by pyrite (1 g/L) as pH was increased from pH 2.4 and subsequently was decreased

$$FeS_{2(s)} + 7Hg^{2+} + 8H_2O \rightarrow 7Hg^{o} + Fe^{2+} + 2SO_4^{2-} + 16H^{+} \quad (4)$$

$$FeS_{2(s)} + 4Hg^{2+} + 4H_2O \rightarrow 3Hg^{o} + HgS_{(s)} + Fe^{2+} + SO_4^{2-} + 8H^{+} \quad (5)$$

$$FeS_{2(s)} + 4Hg^{2+} + 4H_2O \rightarrow 2Hg^{o} + Hg_2S_{(s)} + Fe^{2+} + SO_4^{2-} + 8H^{+} \quad (6)$$

In summary, the pyrite reacted with higher concentrations of Hg(II) at pH 10 produces a stable system that shows no release of Hg(II) as pH was changed. This stability could be the result of formation of precipitates ($HgS_{(s)}$ or $Hg_2S_{(s)}$).

Characterization of Mercury-Pyrite

Figure 67 shows the Fe $2p_{3/2}$ XPS spectra for pyrite after contact with Hg(II) for various times. After contact with Hg(II), the Fe $2p_{3/2}$ spectra comes to have more peaks at higher binding energies and these peaks represent Fe(III)-S and Fe(III)-O species. In addition, the intensities of those peaks increase with reaction time. If formation of these Fe(III) species is caused by surface reactions between Fe(II) sorption sites and Hg(II) ions, the reduced species, Hg(I) or Hg(0) should be found on the surface of pyrite. The evidence for Hg(II) reduction will be discussed in detail when the Hg 4f spectra are discussed. However, the Fe(III)-O species produced on the surface could exist as Fe(III) oxyhydroxides and differential charge effects could occur due to the formation of heterogeneous surfaces. The confirmation of these charge effects is important, because these Fe(III) species plays an important role in catalyzing oxidation processes (references given in Behra et al. 2001). Behra et al. (2001) provided the evidence for existence of charge effects on a pyrite surface after contact with Hg(II) through the investigation of O 1s XPS spectrum.

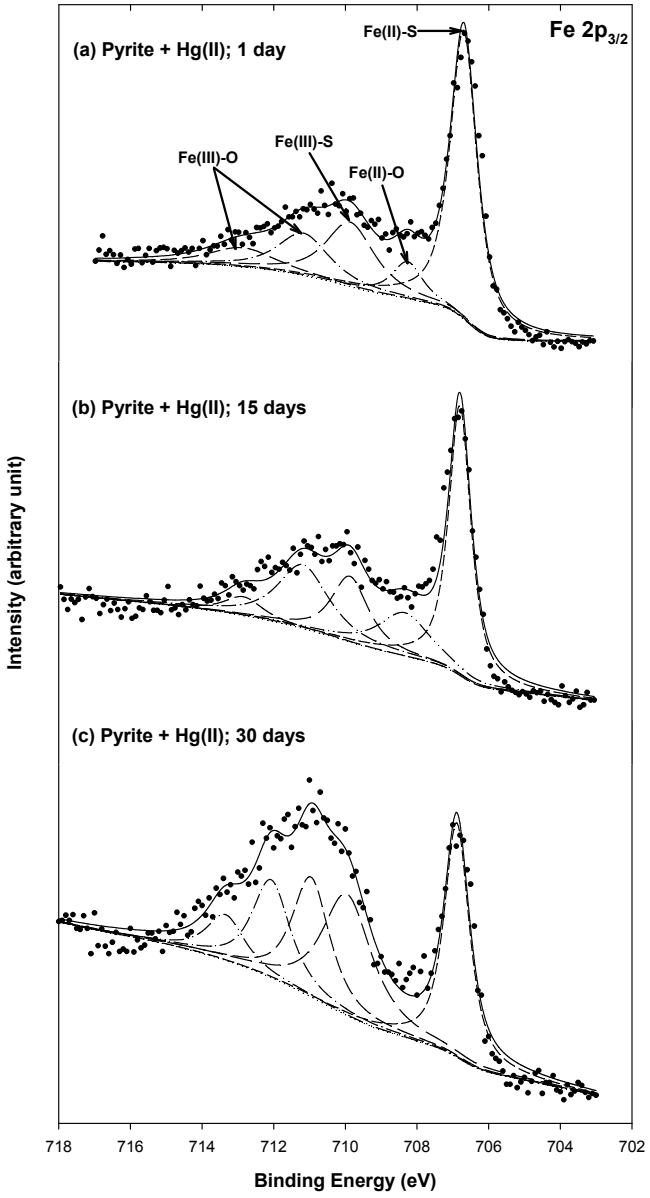

Figure 67. High resolution Fe $2p_{3/2}$ XPS spectra for synthetic pyrite (1 g/L) reacted with 200 μM Hg(II) at pH 8 for various times: (a) 1 day, (b) 15 days, (c) 30 days.

Figure 68 shows the O 1s XPS spectra for pyrite after contact with solutions of Hg(II) for various times. The O 1s spectra display three peaks located at approximately 531.0, 531.5, 532.6 eV, corresponding to O^{2-}, OH^- and molecular H_2O environments, respectively. Ehrhardt et al. (2000) showed that in addition to the H_2O peak at 532.6 eV, there is an extra peak located near 535.0 eV that is caused by the sorption of water molecules onto isolated islands of Fe(III) oxyhydroxide, which results in a differential charge effect. However, Figure 68 does not show those peaks at any contact time. These results indicate that even though Fe(III) species are observed, the formation of isolated islands of Fe(III) oxyhydroxide overlayer on the pyrite surface could be neglected.

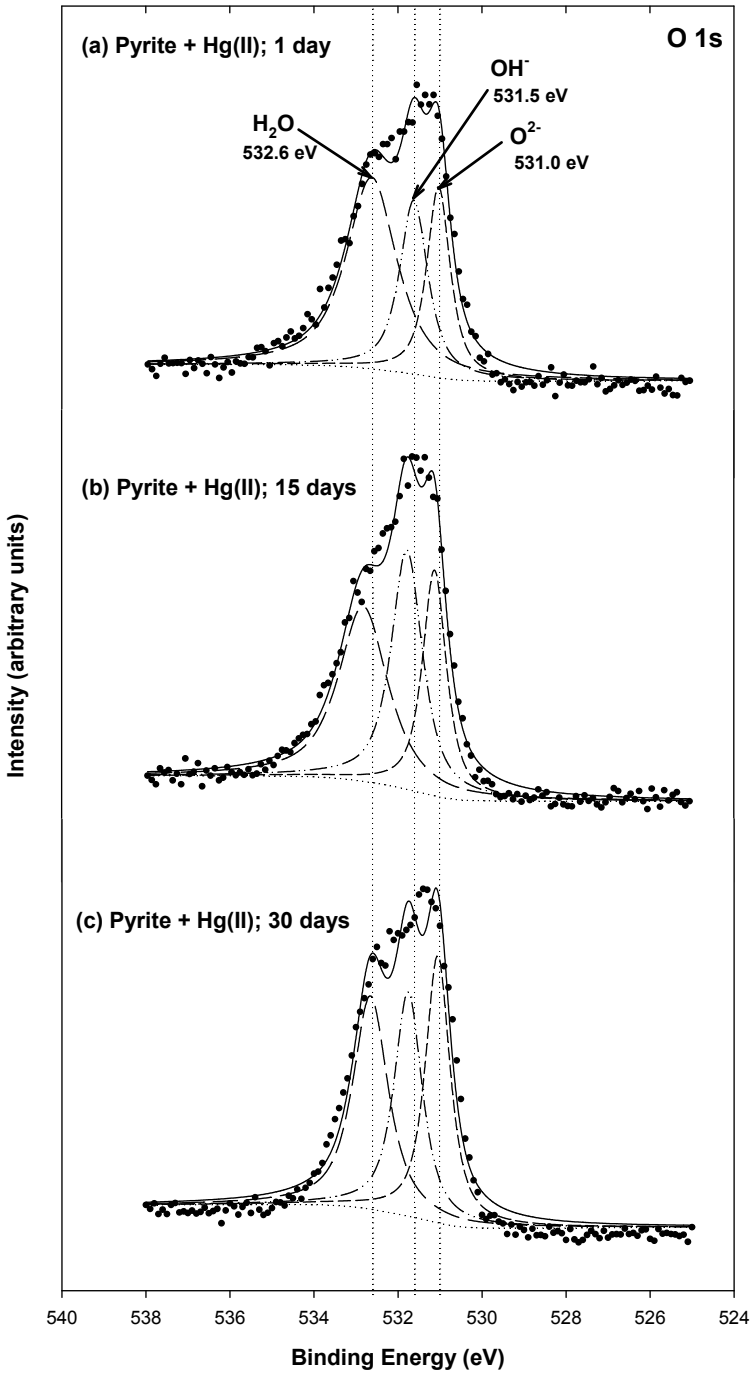

Figure 68. High resolution O 1s XPS spectra (Al Kα) for synthetic pyrite (1 g/L) reacted with 200 μM Hg(II) at pH 8 for various times: (a) 1 day, (b) 15 days, (c) 30 days.

Table 32 shows the binding energies (BE), full width at half maximum (FWHM), and relative area for peaks in the Fe $2p_{3/2}$ XPS spectra of pyrite contacted with Hg(II) for various times.

Table 32. Binding energies (BE), full width at half maximum (FWHM), and area percentage for peaks in the Fe $2p_{3/2}$ XPS spectra of pyrite contacted with Hg(II) for various times.

Sample	Contact time (days)	BE (eV)	FHWM (eV)	Area (%)	Chemical states
Pyrite	0	706.8	0.87	90	Fe(II)-S
		708.4	1.19	6.7	Fe(III)-S
		709.8	0.88	3.3	Fe(III)-O
Pyrite + Hg(II)	1	706.7	0.89	50.1	Fe(II)-S
		708.2	1.04	7.4	Fe(II)-O
		709.8	1.62	20.2	Fe(III)-S
		711.1	1.72	14.1	Fe(III)-O
		712.8	2.19	8.1	Fe(III)-O
	15	706.8	0.74	41.2	Fe(II)-S
		708.3	1.71	15.2	Fe(II)-O
		709.8	1.22	16.4	Fe(III)-S
		711.1	1.70	22.3	Fe(III)-O
		712.8	1.26	4.9	Fe(III)-O
	30	706.8	0.84	26.9	Fe(II)-S
		709.9	1.66	27.5	Fe(III)-S
		710.9	1.25	20.5	Fe(III)-O
		712.0	1.26	16.9	Fe(III)-O
		713.3	1.26	7.92	Fe(III)-O

Figure 69 shows S 2p spectra of pyrite after contact with Hg(II) for various times. These spectra were fitted with a single doublet (S $2p_{1/2}$ and S $2p_{3/2}$) separated by 1.2 eV that represents an S_2^{2-} species. Contact with Hg(II) does not appear to cause any important changes in oxidation state of sulfur sites on pyrite, which is in agreement with the results obtained by others (Hyland et al., 1990). These results indicate that sulfur on the surface does not participate in redox reactions of Hg(II) sorbed onto pyrite during the 30-day contact time.

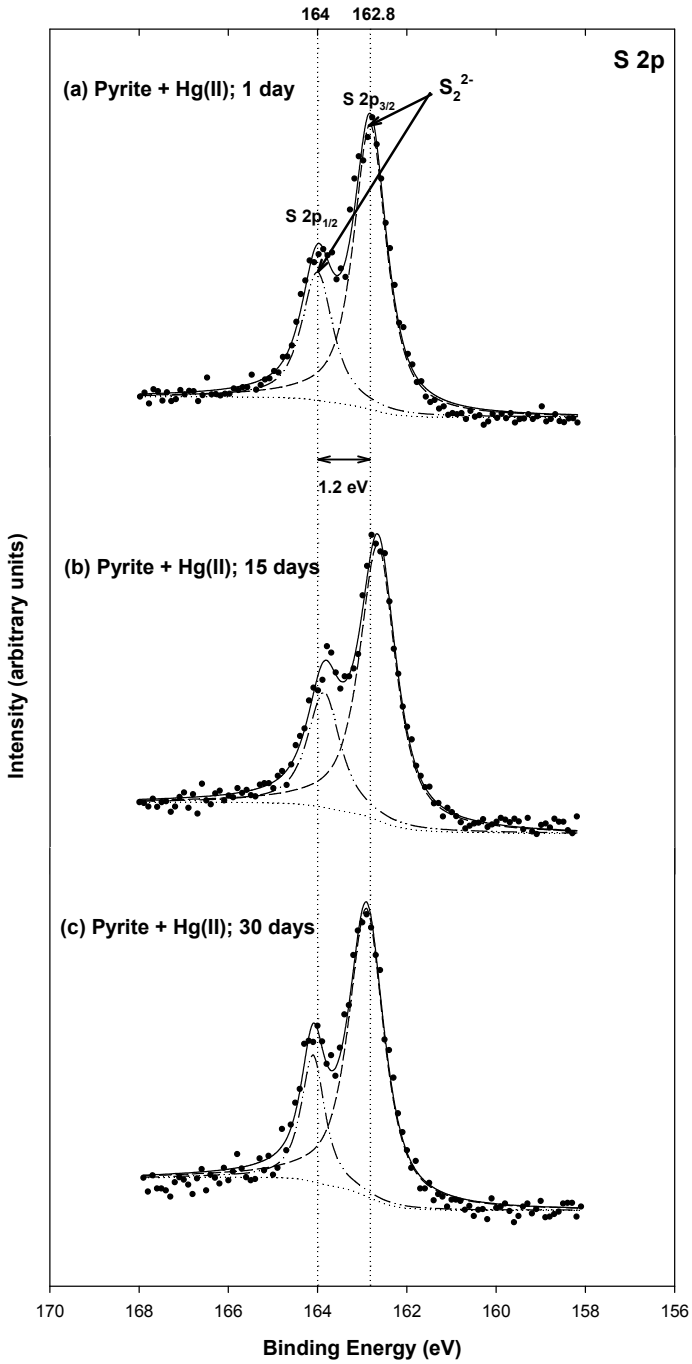

Figure 69. High resolution S 2p XPS spectra for synthetic pyrite (1 g/L) reacted with 200 μM Hg(II) at pH 8 for various times: (a) 1 day, (b) 15 days, (c) 30 days.

Figure 70 shows the Hg 4f XPS spectra for pyrite after contacted with Hg(II) for various times. The Hg 4f spectra were fitted with two peaks (Hg $4f_{7/2}$ and $4f_{5/2}$) separated by a spin orbit splitting of 4.0 eV. The binding energy of Hg $4f_{7/2}$ peak was observed in the range from 100.5 to 100.7 eV, compared to the binding energy for element mercury, which is between 99.2 and 99.8 eV. Therefore, it is not likely that Hg(II) is being reduced to Hg(0) on the pyrite surface. In

addition, Ehrhardt et al. (2000) reported that the broadening of Hg $4f_{7/2}$ peaks is associated with the existence of a multiplicity of sorption sites. Since Figure 70 shows that the $4f_{7/2}$ peak becomes broader, this may indicate that different sites are being formed over time. Ehrhardt et al. (2000) also reported that Hg 4f peaks caused by Fe(III) oxyhydroxides are centered at 103.8 eV. However, such peaks are not shown in Figure 70, even though the Fe $2p_{3/2}$ showed the presence of Fe(III)-O peaks after contact with Hg(II).

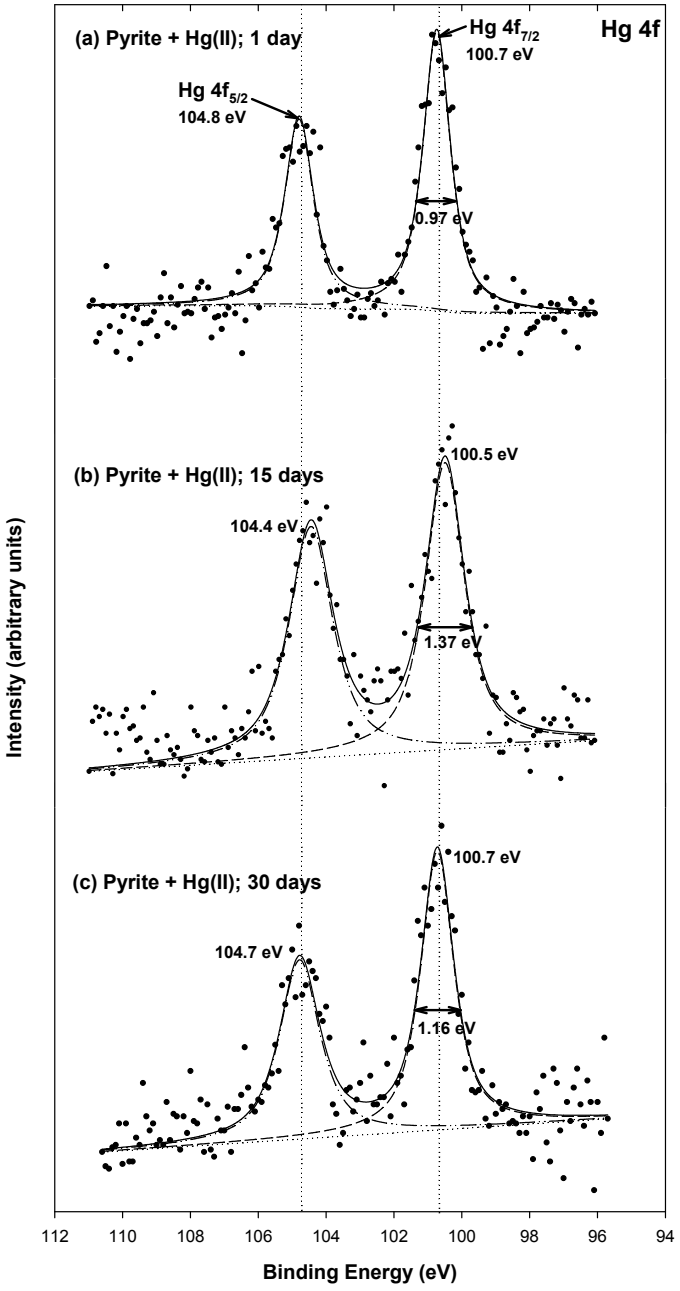

Figure 70. High resolution Hg 4f XPS spectra for synthetic pyrite (1 g/L) reacted with 200 μM Hg(II) at pH 8 for various times: (a) 1 day, (b) 15 days, (c) 30 days.

Samples from stability tests were also characterized. The surface of Hg(II)-contacted pyrites formed at pH 3.4 and pH 10 were analyzed by SEM-EDS and XPS to investigate the feasibility of surface precipitation leading to $HgS_{(s)}$ or $Hg_2S_{(s)}$. Figure 71 shows SEM images of Hg(II)-contacted pyrites at pH 3.4 and 10, respectively. For samples contacted only at pH 3.4, there are no important changes on the surface of Hg(II)-contacted pyrite. However, the pyrite that had contacted at a series of solutions with different pH and ending with pH 10 shows the presence of thin small particles on the pyrite surface. XPS analysis was conducted on these

samples in order to identify the chemical states of mercury in the system.

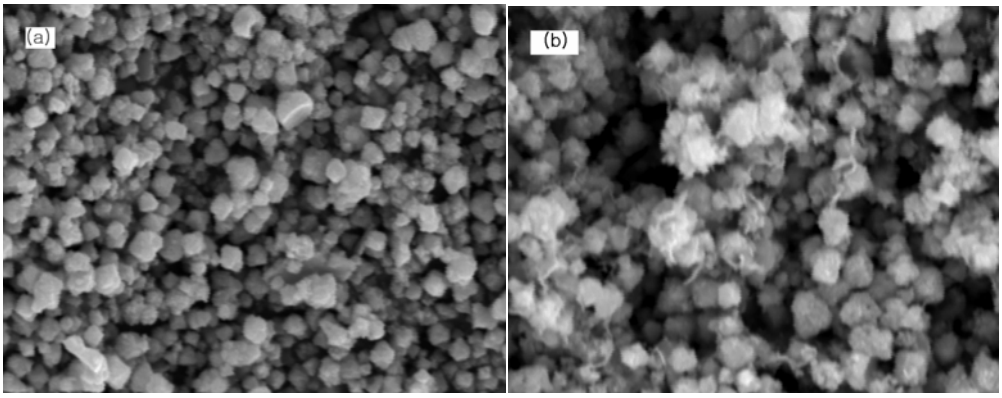

Figure 71. Secondary images of SEM analysis for synthetic pyrite reacted with Hg(II) (6.48 μM) at (a) pH 3.4 and (b) pH 10 after contact with solution at lower pH values.

Figure 72 shows the Hg 4f spectra of Hg(II)-contacted pyrites at pH 3.4 and pH 10. For Hg(II)-contacted pyrite at pH 3.4, the peaks of Hg $4f_{5/2}$ and Hg $4f_{7/2}$ are located at 104.8 eV and 100.6 eV of binding energy, respectively, and the values of FWHM (full width at half maximum) for Hg $4f_{7/2}$ peak is 1.28 eV. These results do not show evidence of reduced forms of Hg(II), which would be expected to display peaks located between 99.2 and 99.8 eV. This similar to results obtained previously for Hg(II)-contacted pyrite at pH 8, which also did not show evidence of reduced forms. However, the spectra for Hg(II)-contacted pyrite at pH 10, show minor differences in the Hg $4f_{7/2}$ peak, which becomes broader (larger FWHM). This broadening could be the result of peaks in the Hg $4f_{7/2}$ spectra between 99.2 and 100 eV that are caused by the presence of Hg(I) or Hg(0).

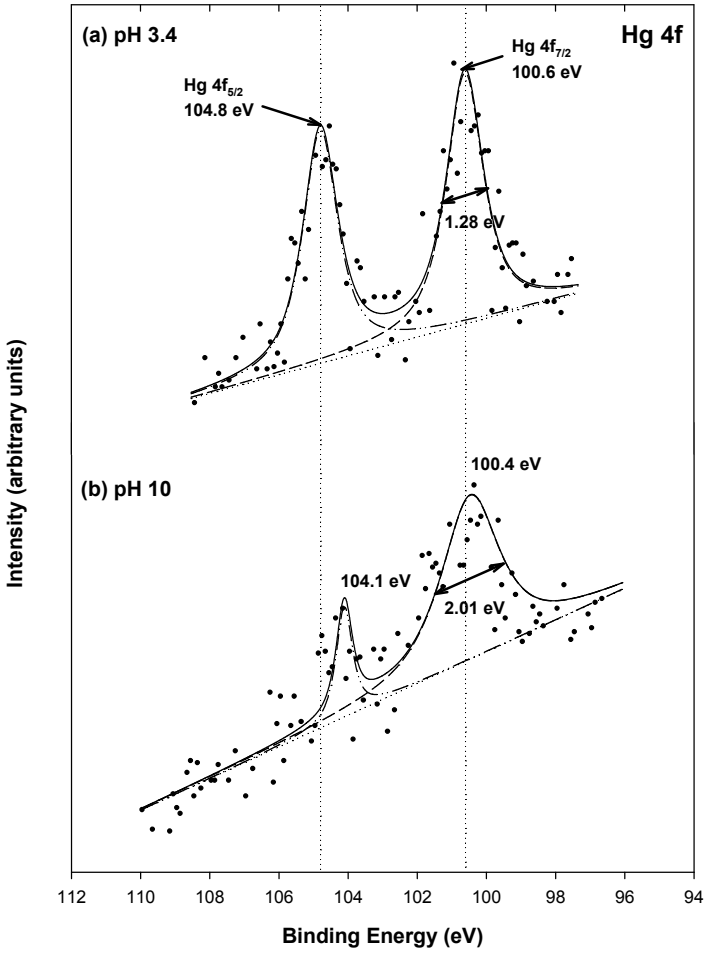

Figure 72. High resolution Hg 4f XPS spectra for synthetic pyrite (1 g/L) reacted with Hg(II) (6.48 μM) at (a) pH 3.4 and (b) pH 10 after previous contact with lower pH.

Figure 73 shows the Fe $2p_{3/2}$ spectra of Hg(II)-contacted pyrite at pH 3.4 and pH 10. High oxidation of Fe sorption sites was observed only for pyrite reacted with Hg(II) at pH 10, in which the intensity of the high energy tail was increased due to the higher contribution of the peak associated with Fe(III)-O to Fe $2p_{3/2}$ spectra. This could be caused by the oxidation of Fe sites that occurs concurrently with the reduction of Hg(II) although Fe could also be oxidized by other compounds.

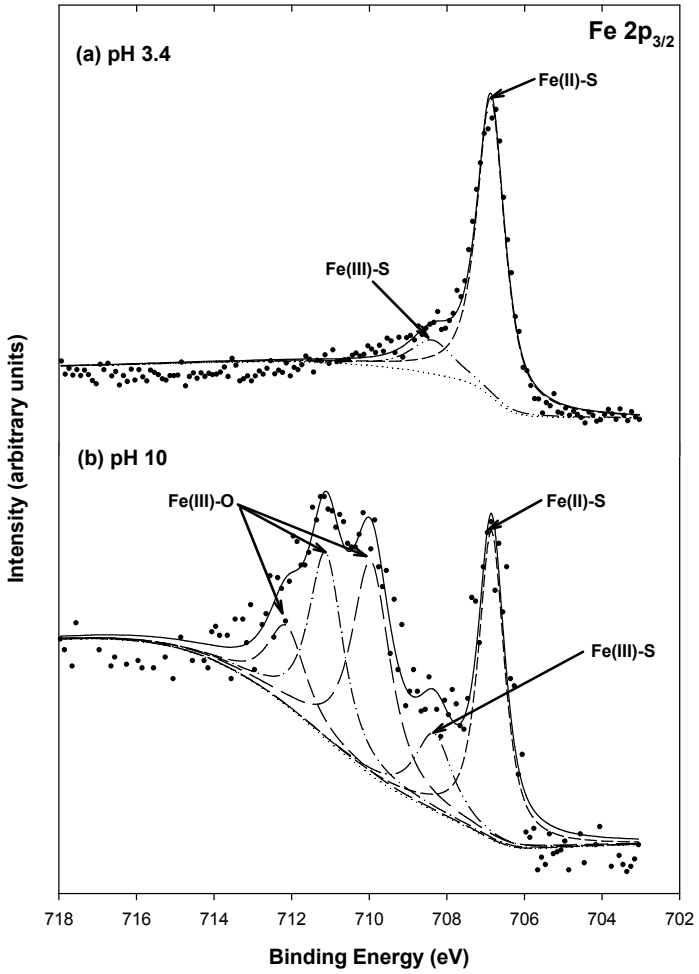

Figure 73. High resolution Fe $2p_{3/2}$ XPS spectra for synthetic pyrite (1 g/L) reacted with Hg(II) (6.48 μM) at (a) pH 3.4 and (b) pH 10 after previous contact with lower pH.

Figure 74 shows the S 2p spectra of Hg(II)-contacted pyrites at pH 3.4 and pH 10. There are no major changes in the S $2p_{3/2}$ and S $2p_{1/2}$ peaks, compared to S 2p spectra for pure pyrite. This suggests that it is unlikely that surface precipitates such as HgS or $Hg_2S_{(s)}$ form on the pyrite surface, because there is no evidence for disproportionation reactions of surface sulfur.

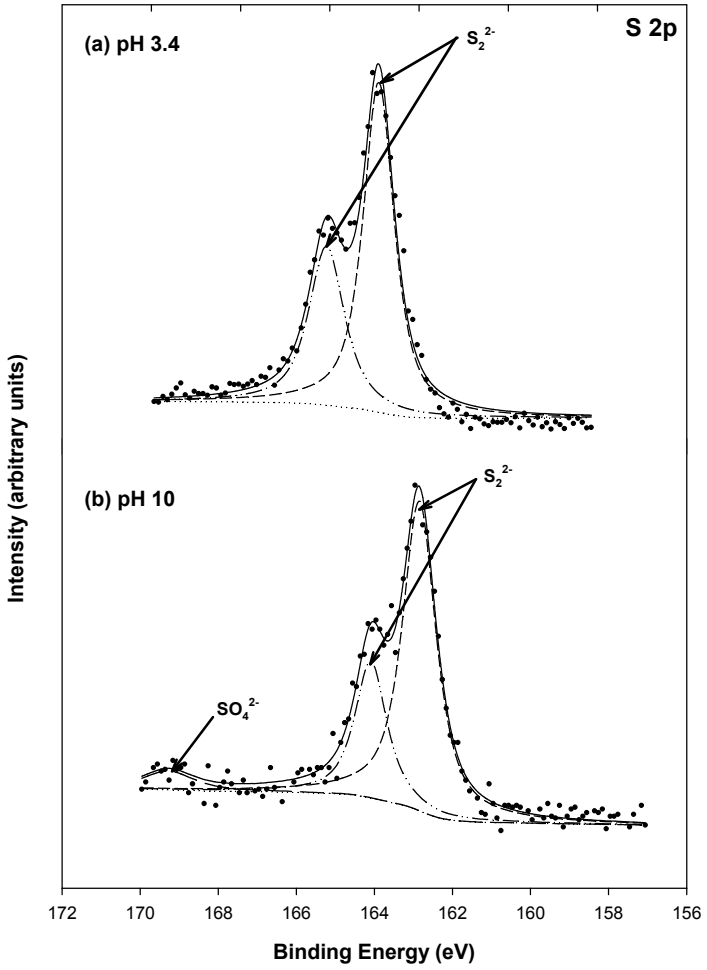

Figure 74. High resolution S 2p XPS spectra for synthetic pyrite (1 g/L) reacted with Hg(II) (6.48 μM) at (a) pH 3.4 and (b) pH 10 after previous contact with lower pH.

To verify the mechanisms described by Equations 4-6, SEM and XPS analyses were performed on samples from stability tests. Figure 75 shows the results of secondary image SEM analysis for pyrite reacted with Hg(II) at pH 2.4 and pH 10. There are no specific changes in the morphology of pyrite observable in Figure 75.

Figure 75. Secondary images of SEM analysis for synthetic pyrite reacted with Hg(II) (1.0 mM) at (a) pH 2.4 and (b) pH 10 after previous contact with lower pH.

Figure 76 shows the Hg 4f XPS spectra for pyrite reacted with Hg(II) (200 μM) at pH 2.4 and pH 10. The peaks of Hg $4f_{5/2}$ and Hg $4f_{7/2}$ are centered between 100.5 and 100.7 eV and between 104.5 and 1004.8 eV. These values are in good agreement with those reported in the literature (Behra et al., 2001 and Ehrhardt et al., 2000). Furthermore, the FHWM values of Hg $4f_{7/2}$ are within between 1.02 and 1.08 eV, which are in accordance with the previous results or other studies, suggesting that Hg(II) or Hg(I) are the main contributors to the intensity of Hg $4f_{7/2}$ peaks. The Hg(I) component is located between 100.0 eV and 99.8 eV. Since the FHWM values at both pH values are not considerably different and both are below 1.08 eV, it can be concluded that there were no major changes in the chemical state of Hg(II) or Hg(I) in these samples. Therefore, it is unlikely that Hg(0) is formed, as is required by Behra's mechanism (Equations 4-6).

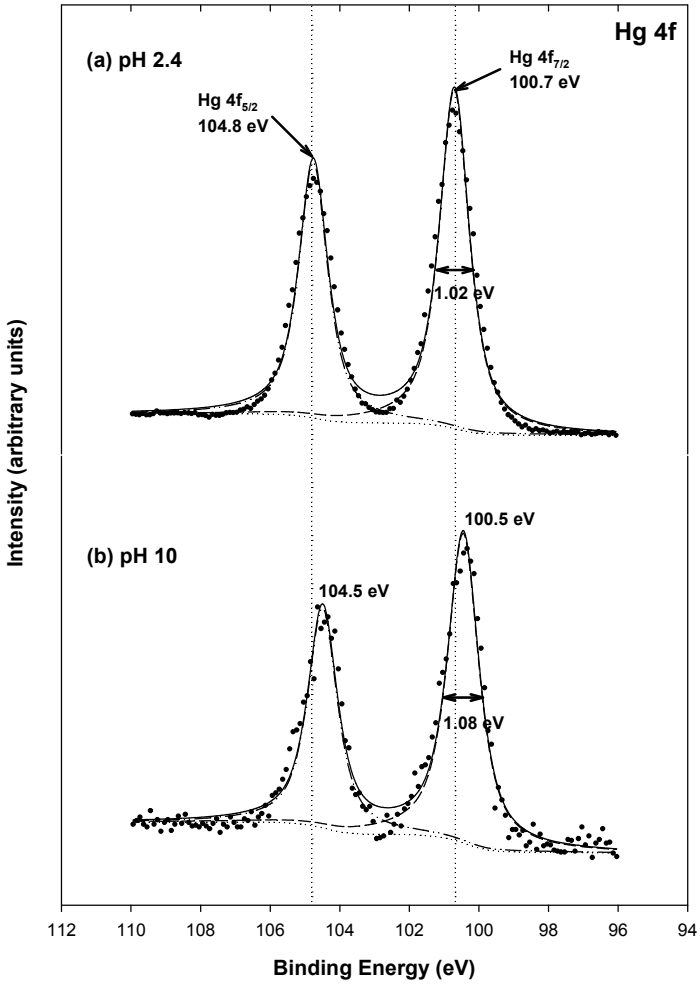

Figure 76. High resolution Hg 4f XPS spectra for synthetic pyrite (1 g/L) reacted with Hg(II) (1 mM) at (a) pH 2.4 and (b) pH 10 after previous contact with lower pH.

Figure 77 shows the results of Fe $2p_{3/2}$ XPS spectra for pyrite reacted with Hg(II) (1 mM) at pH 2.4 and pH 10. As shown in Figure 77(a), Hg(II)-contacted pyrite at pH 2.4 has peaks associated with three different Fe species (Fe(II)-S, Fe(III)-S, Fe(III)-O) that are located at 706.7, 709.3, and 710.6 eV, respectively. Hg(II)-contacted pyrite at pH 3 shows a higher intensity for peaks associated with Fe(III)-O species than does pure pyrite at pH 8. For Hg(II)-contacted pyrite at pH 10, however, only oxidized forms of Fe such as Fe(III)-S and Fe(III)-O are observed. The difference of the extent of Fe oxidation for both Hg(II)-contacted pyrites are caused by different amounts of Hg(II) on the surface and subsequent surface reaction, or by other reactions that oxidize surface Fe.

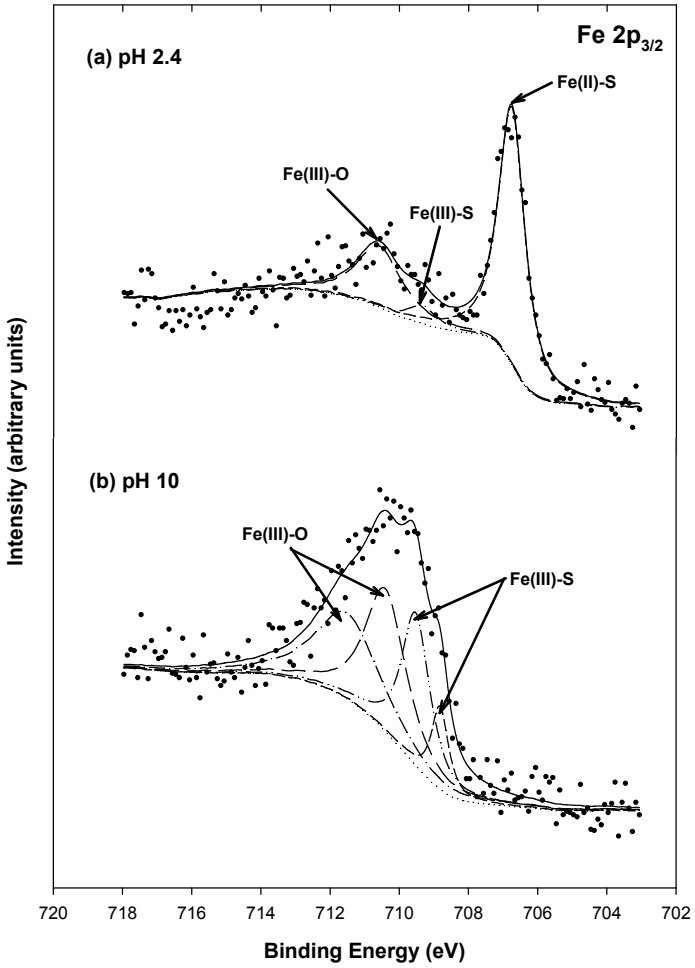

Figure 77. High resolution Fe $2p_{3/2}$ XPS spectra for synthetic pyrite (1 g/L) reacted with Hg(II) (1 mM) at (a) pH 2.4 and (b) pH 10 after previous contact with lower pH.

Figure 78 shows the S 2p XPS spectra for pyrite reacted with Hg(II) at pH 2.4 and pH 10. The pH 10 sample had previously contacted solutions at lower pH. Figure 78(a) shows that spectra for Hg(II)-contacted pyrite at pH 2.4 indicates that there were no important changes in chemical states for surface S, compared to pure pyrite at pH 8. However, S 2p spectra for Hg(II)-contacted pyrite at pH 10 shows the presence of different sulfur species (S(-I), S(-II), S(+VI)) that could be produced by surface disproportionation reactions between sulfur sorption sites and Hg(II)/Hg(I) or other chemicals. At high pH, the presence of thiosulfates, sulfates and sulfites could be caused by the oxidative dissolution of pyrite (Behra et al. 2001). However, the occurrence of S(-II) can be explained by Equations (5) and (6), and thus support the formation of $HgS_{(s)}$ or $Hg_2S_{(s)}$, even though Hg 4f (in Figure 76) did not show the occurrence of Hg(0).

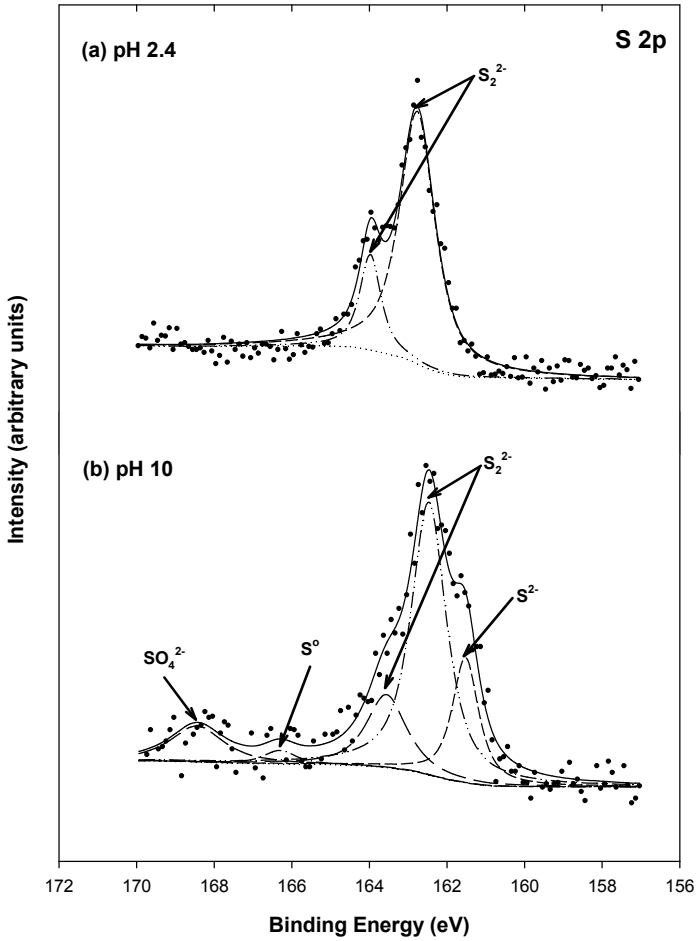

Figure 78. High resolution S 2p XPS spectra for synthetic pyrite (1 g/L) reacted with Hg(II) (1 mM) at (a) pH 2.4 and (b) pH 10 after previous contact with lower pH.

Mackinawite

Mercury Removal and Stability

Figure 79 shows the percentage of Hg(II) removed by mackinawite (FeS) as a function of time. The experiments were conducted with solid concentration of 0.05 g/L and different initial concentrations of Hg(II) (500, 1000, 1250 μM). The experiment conducted with an initial concentration of 500 μM Hg(II)was observed to reach complete removal most rapidly and did so within 10 minutes. Experiments conducted with other initial concentrations required longer reaction times to reach more than 99 % removal. To investigate the possibility that FeS dissolved and HgS precipitated, the concentration of total Fe in solution was measured. Figure 79 shows values of total Fe released, which were calculated by subtracting the measured total Fe concentration measured in the blank sample from the value of total Fe concentration measured in samples contacted with Hg(II). The blanks were filtered solutions of 0.05 g/L FeS stock solution that was adjusted to pH 8 but did not receive additions of Hg(II). Figure 79 shows that the values of total Fe released are less than about 0.5 % of the total amount of Fe added as FeS (569 μM). The amount of Fe released to solution is too small to explain the amounts of mercury

removed (500, 1000, 1250 μM), if the removal is due to precipitation of Hg(II) and solubilization of Fe(II). However, Hg(II) could precipitate as HgS and release Fe(II) that reacts to form another solid phase such as $Fe(OH)_2$.

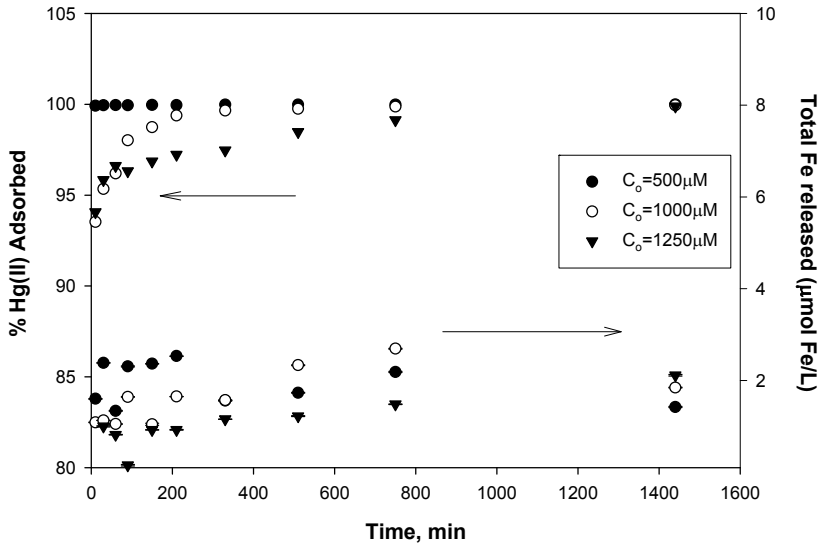

Figure 79. Percentage removal of Hg(II) and concentration of total Fe released as a function of time at pH 8 as affected by initial Hg(II) concentration.

Figure 80 shows the amounts of Hg(II) removed per mass of FeS at pH 7, 8, 9, 10. These experiments were conducted with a solid concentration of FeS of 0.005 g/L and a contact time of 24 hours. The method of presentation is similar to that used to describe equilibrium sorption isotherms, but in this case there is no intention to imply that equilibrium has been reached. The hard/soft acid/base theory indicates that Hg(II) would be strongly attracted to sulfide and likely to form soluble complexes, surface complexes and separate solid phases, such as cinnabar or metacinnabar by substitution. These forms of HgS would be produced by substitution of Fe(II) in FeS by Hg(II), which is consistent with the tendency of a soft Lewis acid to strongly react with soft Lewis base. The tendency of Hg(II) to form surface complexes and solid phases with sulfide could lead to observed relationships between concentration of Hg(II) on solid phase and concentration of Hg(II) in aqueous phase that have the appearance of a BET isotherm. However, the relationships between solid phase concentration and aqueous phase concentration that are presented here are not equilibrium relationships, so they are not isotherms. The results obtained at pH 10, show behavior that is similar to a BET isotherm (Figure 80). However, not all results that have been obtained follow the shape of a BET isotherm. At pH 7, 8, and 9, Hg(II) sorption behavior seems to follow a relationships that is similar to a Langmuir isotherm, although there is a decrease in solid phase concentration at higher aqueous phase concentrations that is not consistent with a Langmuir isotherm. The Langmuir-like behavior is also evident in data obtained at lower concentrations which is shown in Figure 81.

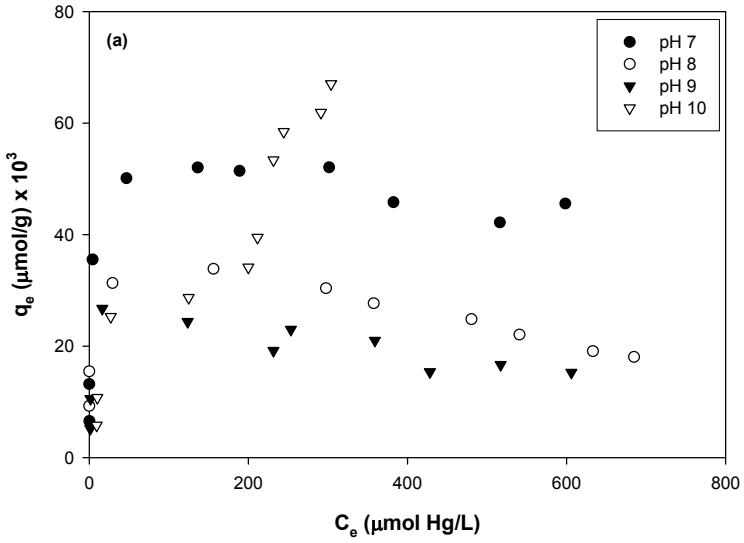

Figure 80. Amounts of Hg(II) removed per mass of solid (FeS) as functions of concentration of Hg(II) in water for various pH

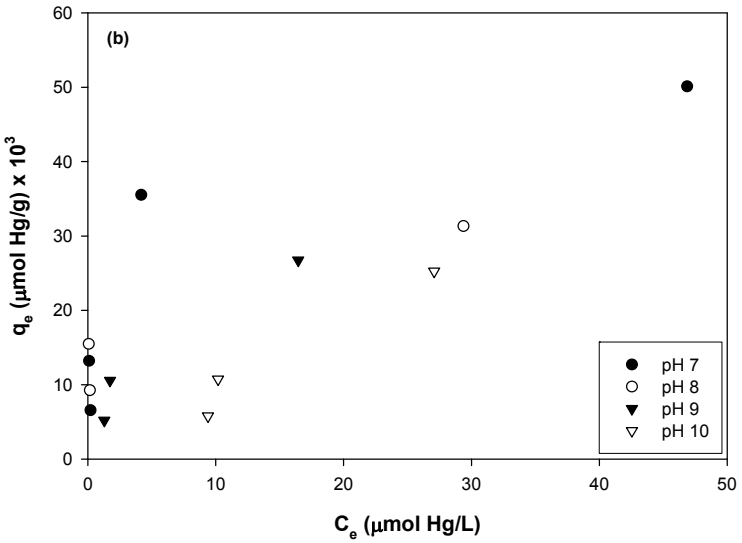

Figure 81. Amounts of Hg(II) removed per mass of solid (FeS) as functions of concentration of Hg(II) in water for various pH, using only data at lower concentrations.

Other hypotheses are required to explain this behavior. Above pH 7, the Fe(II) released from FeS by exchange with Hg(II) may precipitate as a solid ferrous hydroxide ($Fe(OH)_2$) and this solid could accumulate on the surface FeS. This would reduce the area available for removal of Hg(II) from solution. How this mechanism would result in the observed behavior is not clear. Experiments that result in higher aqueous concentrations were the experiments that had higher initial concentrations. The higher initial concentrations would result in more rapid removal kinetics initially and this could result in different amounts of Hg(II) removed at later times due

to different levels of $Fe(OH)_2$ being formed or other processes. The experiment conducted at pH 10 gave results that are similar to those that would be predicted by a BET isotherm (Figure 80), which can be interpreted as being the result of adsorption followed by surface precipitation. Behra et al. (2001) and Bonnissel-Gissinger et al. (1998) observed that the surface of pyrite was oxidized under basic conditions (pH $\geq$ 10) and was covered by Fe(III) oxyhydroxides that can also serve sorption sites for Hg(II). Similar behavior could occur on the surface of FeS at pH 10. FeS could undergo oxidative dissolution and form Fe(III) oxyhydroxides that provide additional opportunities for Hg(II) removal. Alternatively, other surface reactions could lead to formation of HgS and $Fe(OH)_2$ or mixed solid phases containing Hg(II), Fe(II), S(-II) and other anions such as hydroxide or chloride.

Figure 82 shows the effect of sulfate on solid-phase concentration of Hg(II) at pH 8. These results were obtained from a batch experiment with solid concentration of 0.005 g/L and 24 hour contact time. The same behavior is shown in the presence of sulfate as in its absence. The solid-phase concentrations of Hg(II) increase and then decrease with liquid-phase concentration of Hg(II). The solid-phase concentrations are slightly higher when sulfate is present. One explanation for the positive effect of sulfate, is that mixed solid phases are being formed after removal of Hg(II) from solution. If Hg(II) were the only compound being removed from solution, then the surface would develop a positive charge, which would limit the amount of Hg(II) removed. This could be balanced by release of positive charge by release of Fe(II). However, this was not found to occur (Figure 79). Another way to balance charge would be for a negatively charged ion to be removed from solution. Sulfate could act as such an anion and could sorb onto the surface and become incorporated into a mixed mercury-iron-sulfide-sulfate solid phase. Figure 83 shows that sulfate was being removed from solution and that more was removed at higher concentrations.

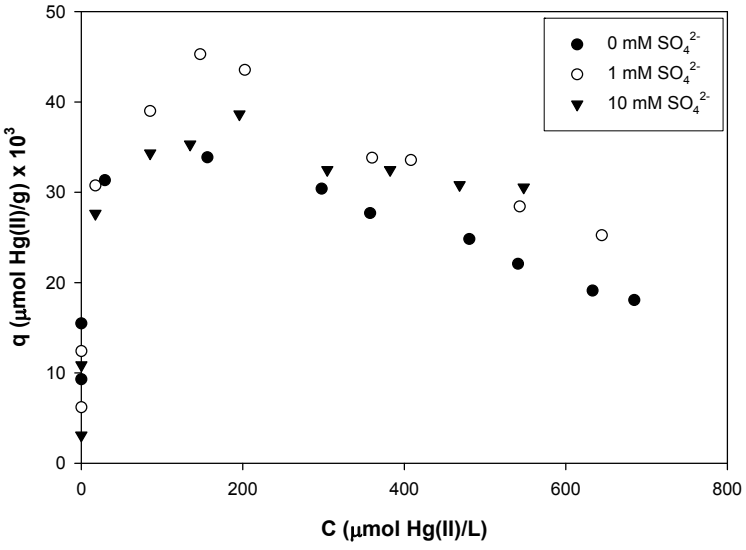

Figure 82. Amounts of Hg(II) removed per mass of solid (FeS) as functions of concentration of Hg(II) in water as affected by sulfate concentration (1 and 10 mM) at pH 8

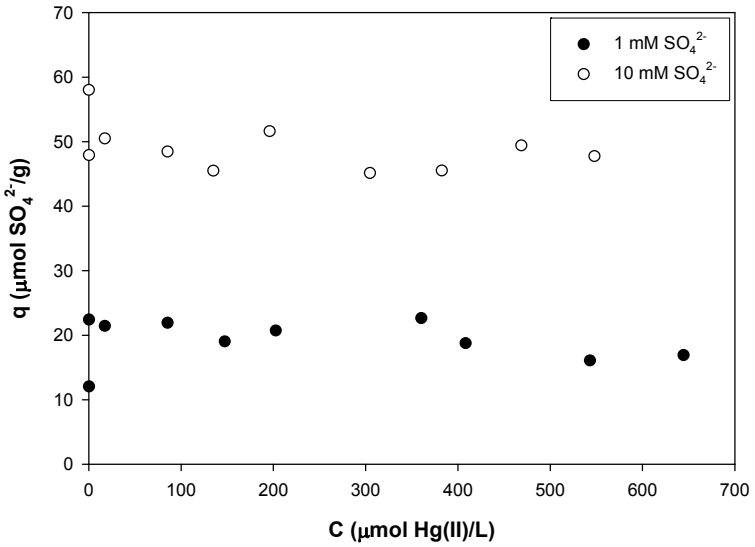

Figure 83. Amounts of sulfate removed per mass of solid (FeS) as function of aqueous concentration of Hg(II) at different initial sulfate concentrations.

An alternative mechanism for the positive effect of sulfate is formation of a mixed Fe(II)-Fe(III)-OH-SO_4 solid phases called green rust. This mechanism could be initiated by formation of a Hg-rich sulfide and release of Fe(II) as suggested by Jeong (2005) and shown in Equation 7.

$$FeS_{(s)} + (1-y)Hg(II) = [Hg_{1-y}, Fe_y]S(s) + (1-y)Fe(II) \qquad (7)$$

The next step would be oxidation of Fe(II) to Fe(III) and reduction of Hg(II) to Hg(I) or Hg(0). The final step would be formation of green rust ($Fe_4^{II}Fe_2^{III}(OH)_{12}(SO_4)$) , However, this mechanism is less likely that formation of other mixed solid phases, because there is no evidence available to document the redox reaction that produces Fe(III) by reduction of Hg(II).

Characterization of Mercury-Mackinawite

Figure 84 shows the Fe $2p_{3/2}$ XPS spectra of mackinawite reacted with Hg(II) for 1, 15, and 30 days. After 1 day of reaction time, three different Fe species (Fe(II)-S, F(III)-S, Fe(III)-O) are observed. However, the intensity of peaks associated with Fe(III) species increases with reaction time, while those of Fe(II)-S species decrease. Oxidation of iron sorption sites could be related to reduction of Hg(II) to Hg(I)/Hg(0)or to reactions with other chemicals.

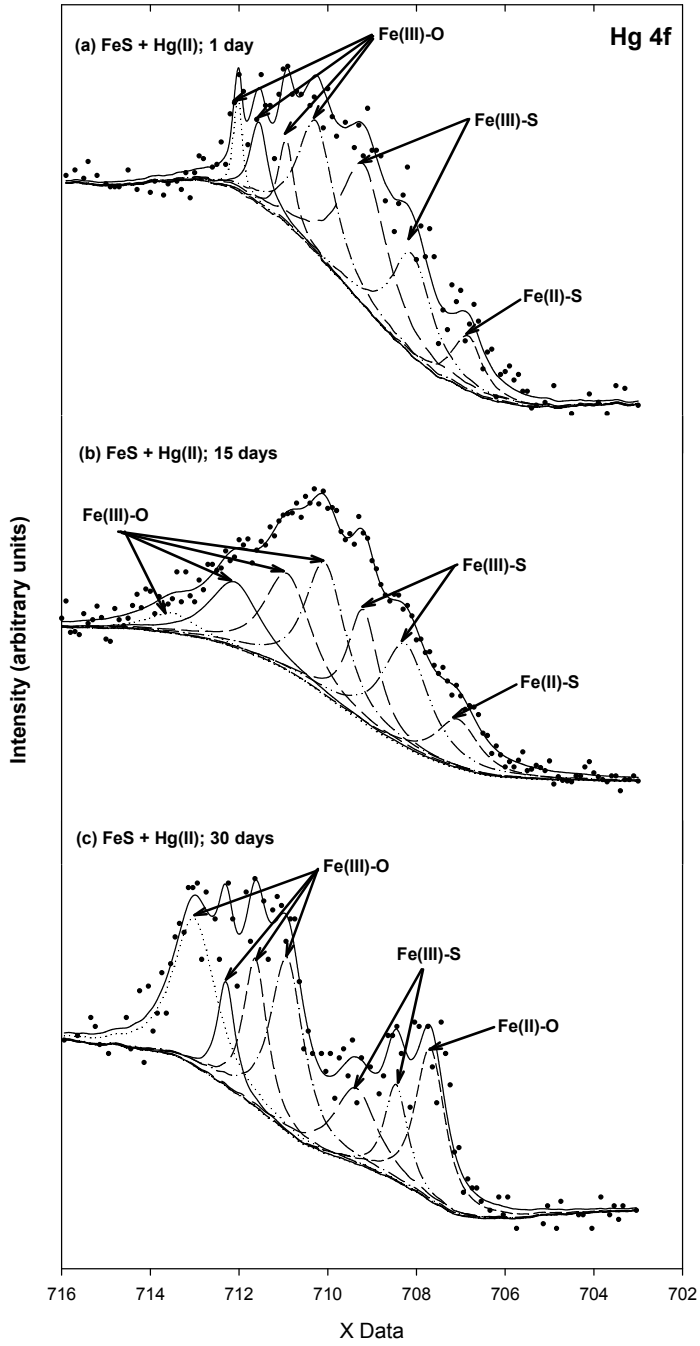

Figure 84. High resolution Fe $2p_{3/2}$ XPS spectra for FeS (1 g/L) reacted with 200 μM Hg(II) at pH 8 for various times: (a) 1 day, (b) 15 days, (c) 30 days

Figure 85 shows the S 2p XPS spectra of mackinawite reacted with Hg(II) for different times. Oxidation of S(-II) species is not observed in the S 2p spectra until 15 days of reaction. After more time passes, peaks associated with products of reaction of S(-II), such as polysulfides (S_n^{2-}) appear.

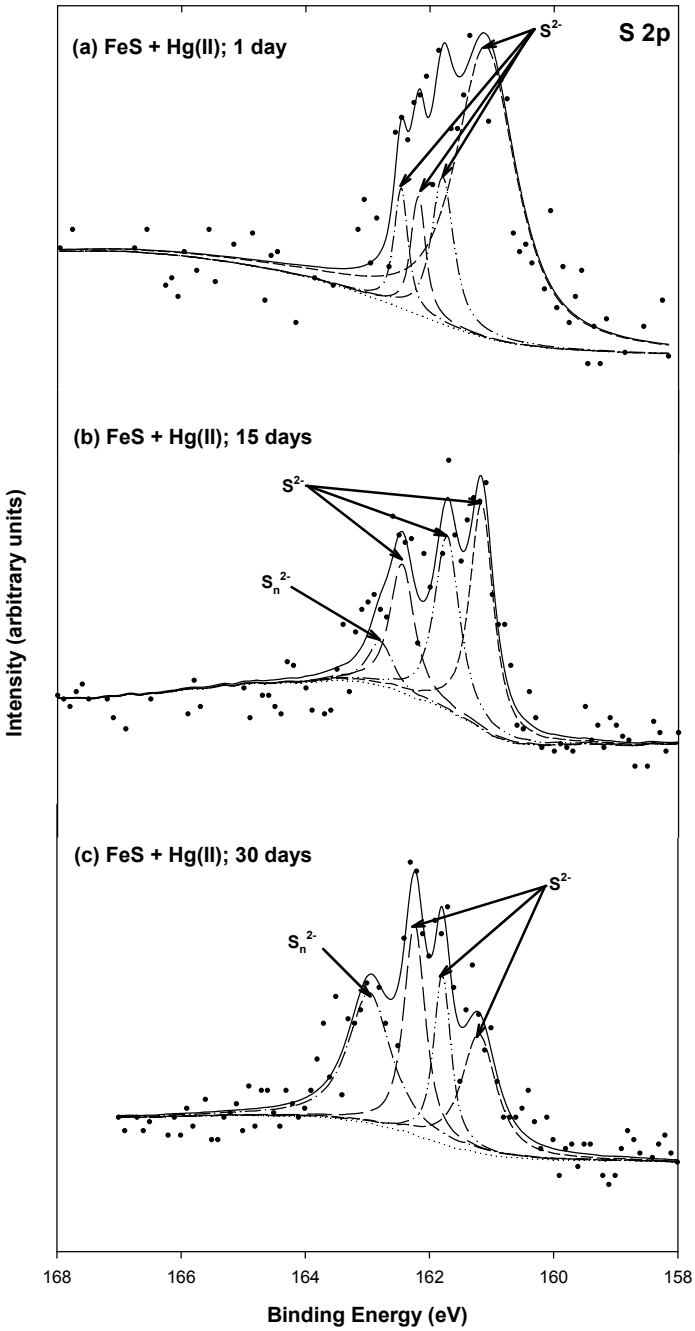

Figure 85. High resolution S 2p XPS spectra for FeS (1 g/L) reacted with 200 μM Hg(II) at pH 8 for various times: (a) 1 day, (b) 15 days, (c) 30 days

Figure 86 shows the Hg 4f XPS spectra of mackinawite reacted with Hg(II) for different times. As previously shown in Figure 70, the Hg 4f spectra can be expressed with two peaks (Hg $4f_{7/2}$ and Hg $4f_{5/2}$) separated by a spin orbit splitting of about 4.0 eV. Hg $4f_{7/2}$ peaks are centered in the range of 100.4 to 100. 7 eV and include the binding energy of Hg(II) and Hg(I) species that are observed at around 100.0 eV. However, Hg(0) species, which are usually observed at

binding energies between 99.2 and 99.8 eV, are located in the low binding energy tail of the Hg $4f_{7/2}$ spectra. Therefore, Hg(II) and Hg(I) species rather than Hg(0) are present as the component of Hg that interacts with the surface of mackinawite until 30 days of contact time.

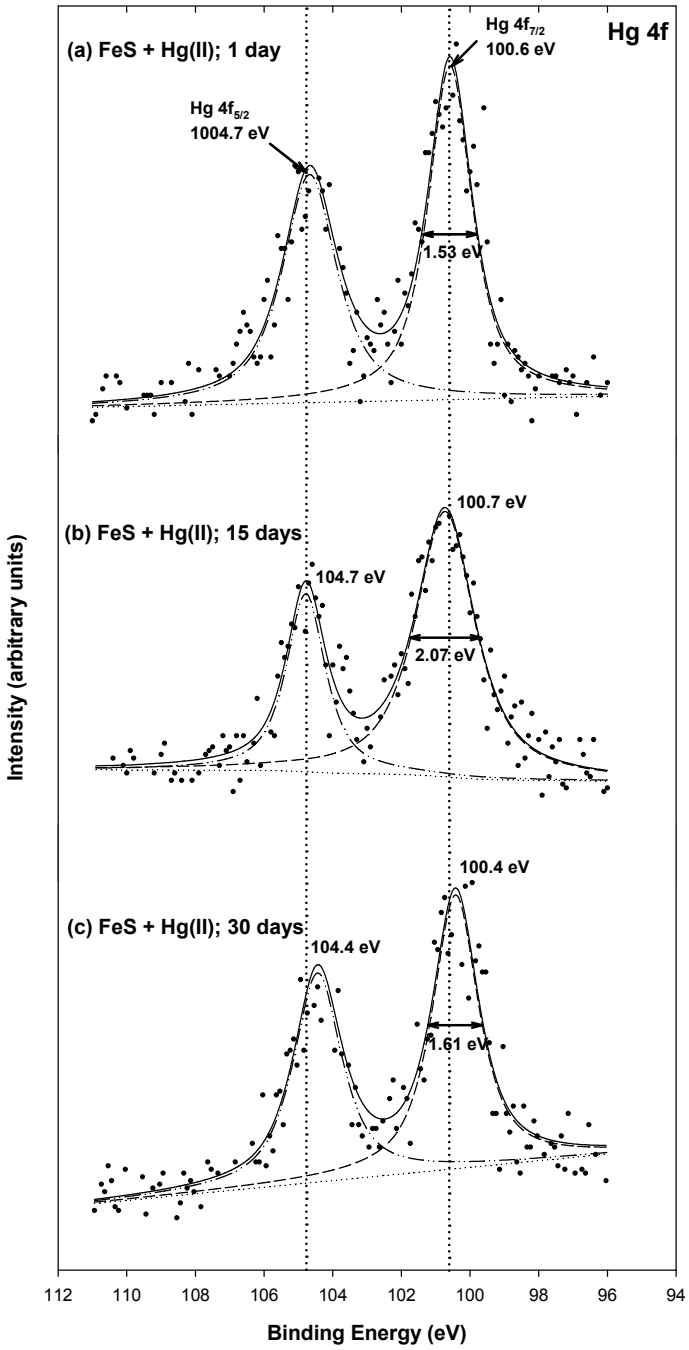

Figure 86. High resolution Hg 4f XPS spectra for FeS (1 g/L) reacted with 200 μM Hg(II) at pH 8 for various times: (a) 1 day, (b) 15 days, (c) 30 days.

Tables 33 and 34 summarize data for binding energies (BE), peak full width at half

maximum (FWHM), peak area percentage for Fe $2p_{3/2}$ and S 2p photoelectron spectra of FeS contacted with Hg(II) for different times.

Table 33. Binding energies (BE), peak full width at half maximum (FWHM), peak area percentage for Fe $2p_{3/2}$ photoelectron spectra of FeS contacted with Hg(II) for various times

Sample	Contact time (days)	χ^2	BE (eV)	FHWM (eV)	Area (%)	Chemical states
Mackinawite	0	0.49	706.0	0.49	10.4	Fe(II)-S
			706.4	0.55	14.6	Fe(II)-S
			706.9	0.71	17.8	Fe(II)-S
			707.7	0.98	18.7	Fe(II)-O
			708.8	1.26	14.6	Fe(III)-S
			710.1	1.67	14.9	Fe(III)-O
			711.8	2.51	9.00	Fe(III)-O
Mackinawite+Hg(II)	1	0.70	706.8	0.81	7.90	Fe(II)-S
			708.1	1.07	19.6	Fe(III)-S
			709.2	1.24	31.6	Fe(III)-S
			710.3	0.99	23.4	Fe(III)-O
			710.9	0.41	6.14	Fe(III)-O
			711.6	0.48	7.10	Fe(III)-O
			712.0	0.23	3.85	Fe(III)-O
	15	0.54	707.1	1.14	8.51	Fe(II)-S
			708.3	1.26	19.7	Fe(III)-S
			709.2	0.83	14.1	Fe(III)-S
			710.1	1.08	21.8	Fe(III)-O
			710.9	1.25	18.3	Fe(III)-O
			712.1	1.37	13.5	Fe(III)-O
			713.5	1.29	3.98	Fe(III)-O
	30	1.02	707.7	0.78	16.3	Fe(II)-O
			708.5	0.62	7.95	Fe(III)-S
			709.4	1.13	11.7	Fe(III)-S
			710.9	0.89	21.3	Fe(III)-O
			711.6	0.64	12.9	Fe(III)-O
			712.3	0.47	6.69	Fe(III)-O
			713.0	1.13	23.0	Fe(III)-O

Table 34. Binding energies (BE), peak full width at half maximum (FWHM), peak area percentage for S 2p photoelectron spectra of FeS contacted with Hg(II) for various times

Sample	Contact time (days)	χ^2	BE (eV)	FHWM (eV)	Area (%)	Chemical states
Mackinawite	0	0.46	161.3	0.55	14.0	S^{2-}
			161.8	0.62	22.0	S^{2-}
			162.3	0.68	26.3	S^{2-}
			163.1	1.03	35.0	S_n^{2-}
			164.5	0.88	2.60	S^o
Mackinawite+As(III)	1	0.76	161.1	1.16	72.2	S^{2-}
			161.8	0.43	13.6	S^{2-}
			161.2	0.27	7.22	S^{2-}
			162.4	0.26	6.95	S^{2-}
	15	0.99	161.2	0.46	38.5	S^{2-}
			161.7	0.48	31.2	S^{2-}
			162.5	0.47	22.4	S^{2-}
			162.8	0.47	7.85	S_n^{2-}
	30	0.96	161.2	0.66	24.0	S^{2-}
			161.8	0.33	17.2	S^{2-}
			162.2	0.41	26.3	S^{2-}
			162.9	0.82	32.6	S_n^{2-}

Figure 87 shows the results of stability experiments for Hg(II)-contacted mackinawite as affected by changes in pH. Removal of Hg(II) was high (>98%) but increased as pH was decreased from the initial value and resulted in nearly complete removal below pH 7. When pH was increased, no release of Hg(II) to the solution was observed.

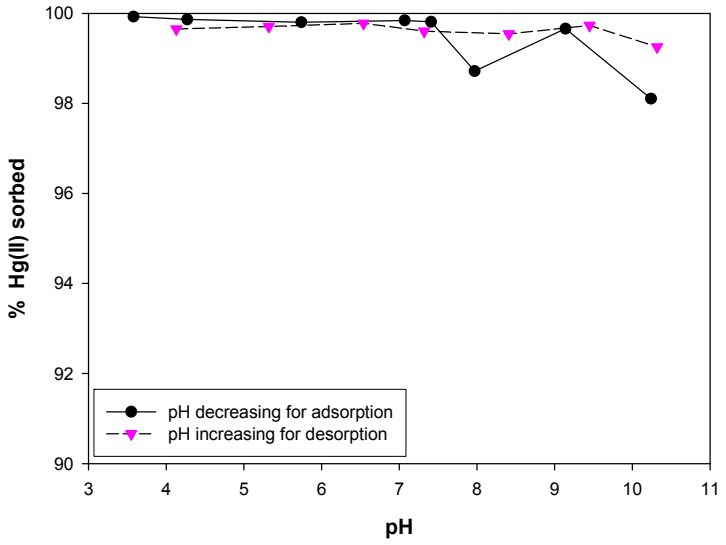

Figure 87. Effect of pH on removal of Hg(II) (6.48 μM) by FeS (1 g/L) as pH was decreased from pH 10.5 and subsequently was increased

Figure 88 shows results of SEM analysis for mackinawites reacted with Hg(II) at pH 10.5 and pH 3.5 after contact at higher pH. Both SEM images show the presence of small particles surrounding particles of mackinawite, which could be precipitates of other solid phases.

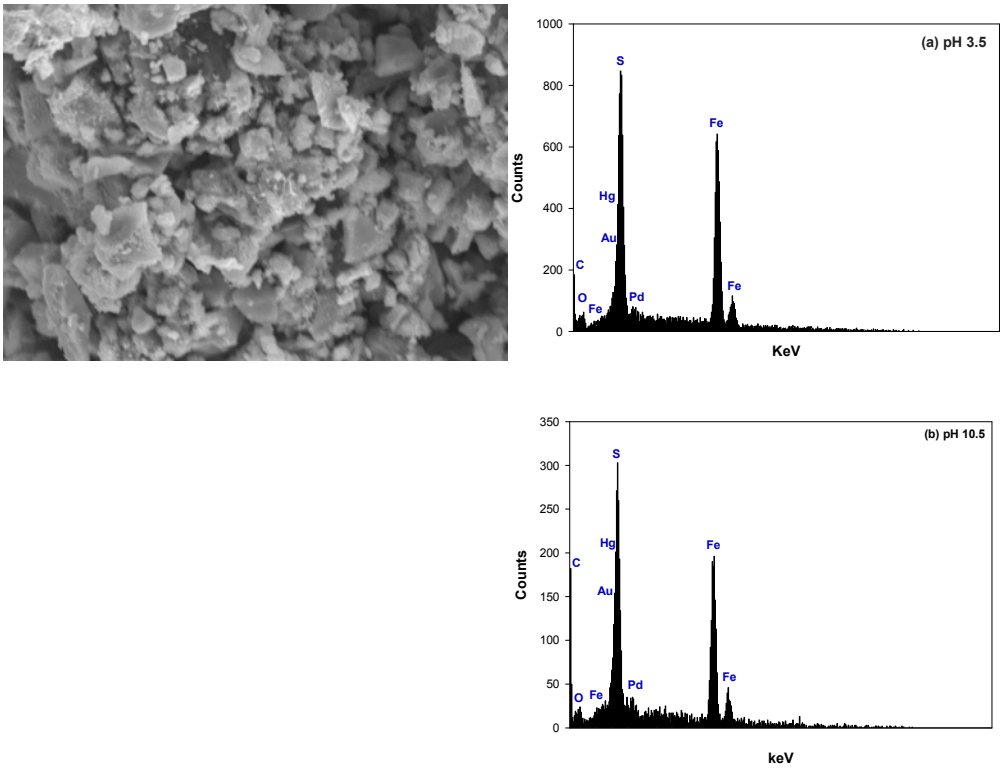

Figure 88. Secondary images of SEM analysis for mackinawite reacted with Hg(II) (6.48 μM) at (a) pH 3.5 and (b) pH 10.5 after contact at lower pH.

Figure 89 shows the Hg 4f XPS spectra for FeS reacted with Hg(II) at pH 3.5 and 10.5. In both spectra, the peaks representative of Hg(II) or Hg(I) are centered between 100.2 and 100.5 eV. Also, peaks associated with Hg(0) are included in the tail of the Hg $4f_{7/2}$ peak between 99.2 and 99.8 eV. However, these peaks are not major contributors to the Hg $4f_{7/2}$ spectra, because the shapes of peaks in the spectra were very symmetric.

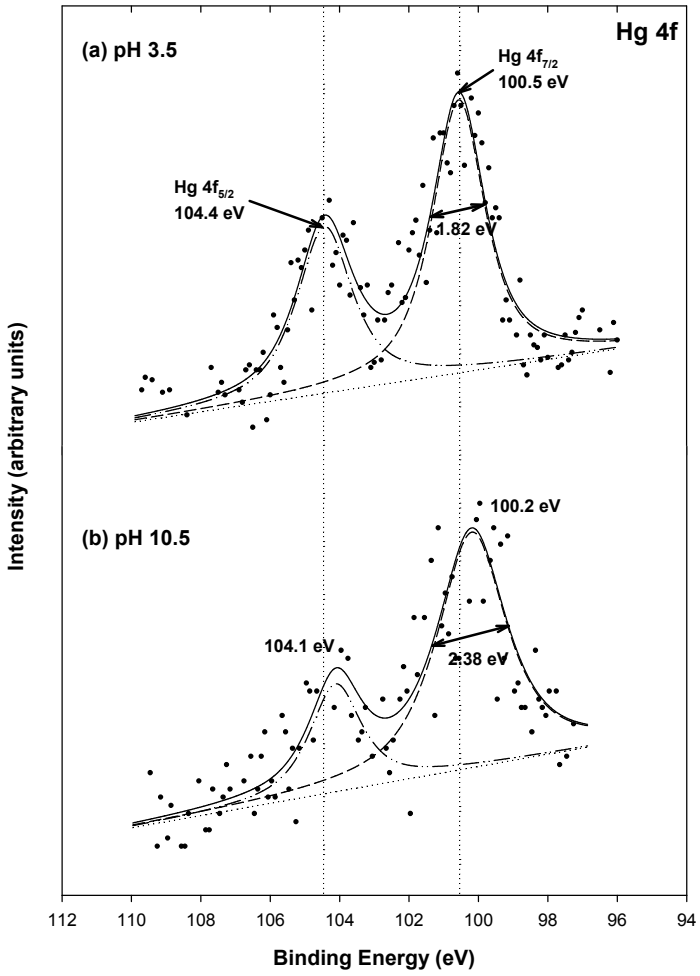

Figure 89. High resolution Hg 4f XPS spectra for mackinawite (1 g/L) reacted with Hg(II) (6.48 μM) at (a) pH 3.5 and (b) pH 10.5 after contact at lower pH.

Figure 90 shows the Fe $2p_{3/2}$ XPS spectra for Hg(II)-contacted mackinawites at both pH 3.5 and pH 10.5 after contact at lower pH. All peaks associated with Fe(II)-O components are lost, which increases the relative intensity of peaks associated with oxidized forms of iron (Fe(III)-S and Fe(III)-O). This oxidation of Fe might be caused by redox reactions with Hg(II) or with other chemicals.

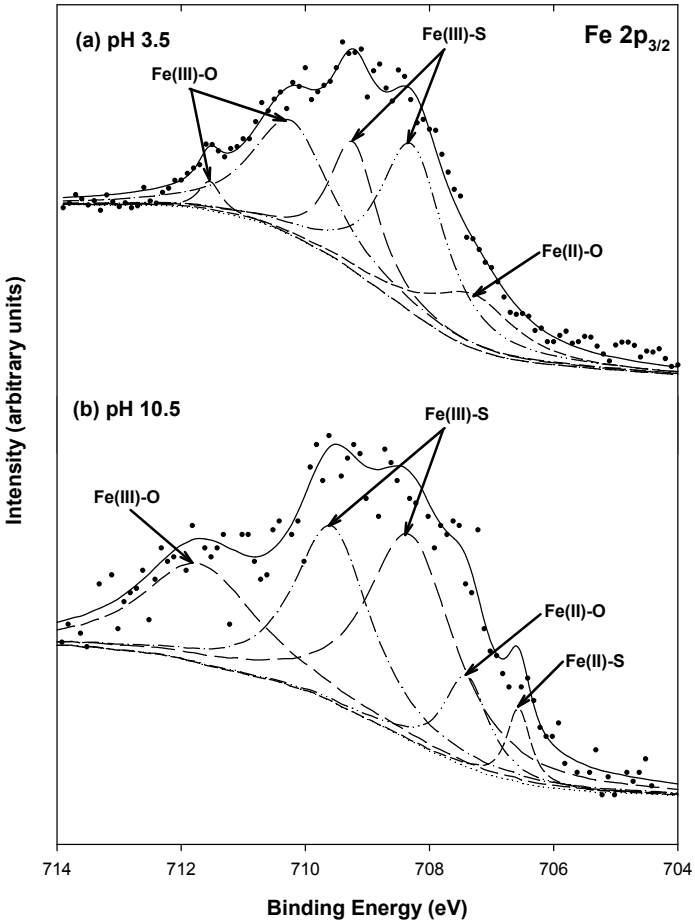

Figure 90. High resolution Fe $2p_{3/2}$ XPS spectra for mackinawite (1 g/L) reacted with Hg(II) (6.48 μM) at (a) pH 3.5 and (b) pH 10.5 after contact at lower pH.

Figure 91 shows the S 2p XPS spectra for Hg(II)-contacted FeS at pH 3.5 and 10.5 after contact at lower pH. Both spectra show the presence of oxidized components of sulfur (S_n^{2-}, S^o, SO_4^{2-}) as well as S(-II). The oxidation of S(-II) could be caused by oxidative dissolution at both extreme pH values. However, the continued presence of S(-II) indicates the potential to form precipitates such as (Fe,Hg)S or HgS.

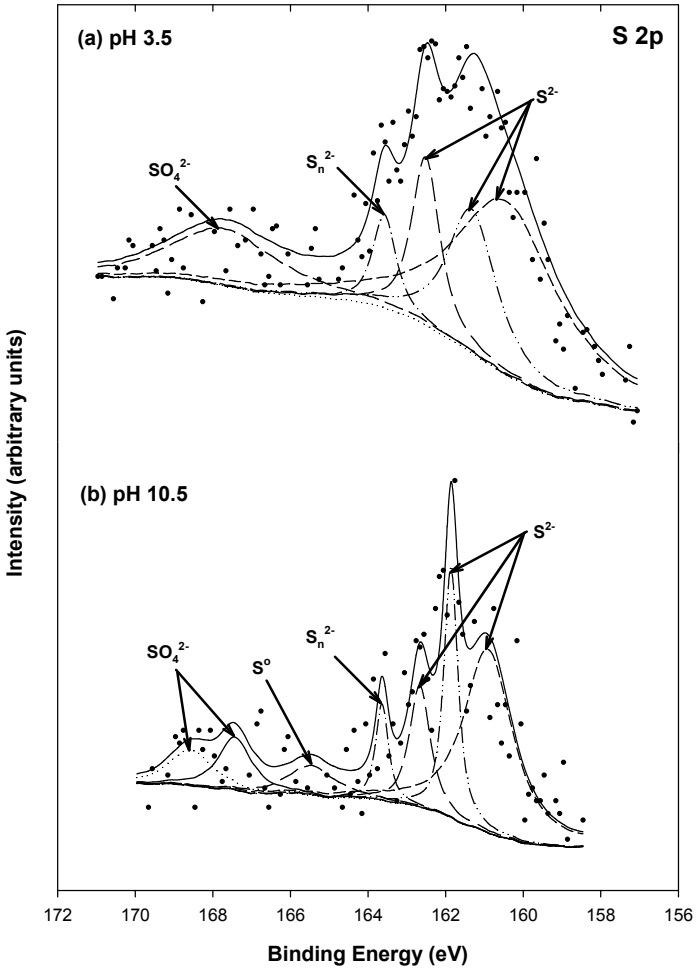

Figure 91. High resolution S 2p XPS spectra for mackinawite (1 g/L) reacted with Hg(II) (6.48 μM) at (a) pH 3.5 and (b) pH 10.5 after contact at lower pH.

Figure 92 shows how pH affects removal of Hg(II) by FeS and how reaction at different pH affects release of Hg(II). Removal of Hg(II) increased as pH was decreased from the initial value, but good removal of Hg(II) (>99%) was observed for all conditions. Furthermore, as pH was increased, there is no release of Hg(II) to solution, indicating that mercury was strongly bound. Jeong et al. (2007) suggested several reaction mechanisms leading to formation of precipitates (Equations 8, 9) or surface complexes (Equation 10).

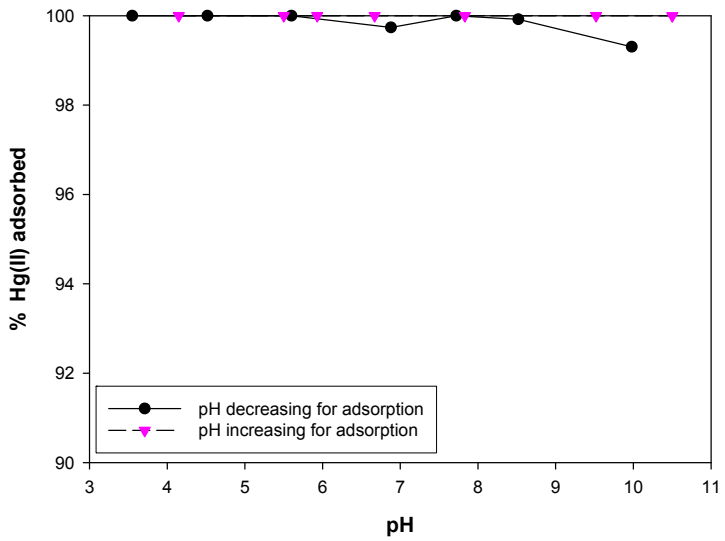

Figure 92. Effect of pH on removal of Hg(II) (1.0 mM) by FeS (1 g/L) as pH was decreased from pH 10 and subsequently was increased

$$FeS_{(s)} + xHg(II) \rightarrow [Fe_{1-x}, Hg_x]S_{(s)} + xFe(II) \quad (8)$$

$$FeS_{(s)} + Hg(II) \rightarrow HgS_{(s)} + Fe(II) \quad (9)$$

$$\equiv FeS + Hg(II) \rightarrow \equiv FeS\text{-}Hg(II) \quad (10)$$

Figure 93 shows SEM images and EDS spectra for Hg(II)-contacted FeS at pH 3.5 and pH 10 after contact at lower pH. The SEM images for both solids show that spherical and other small particles are formed on the surface of FeS. To investigate the chemical composition of the spherical particles, EDS analyses were conducted and their results indicate that those solids are composed of Fe, S and Hg. This supports formation of mixed iron-mercury sulfide precipitates ($[Fe_{1-x}, Hg_x]S_{(s)}$), rather than $HgS_{(s)}$. Formation of such precipitates could be responsible for the stability of Hg(II) in contact with FeS.

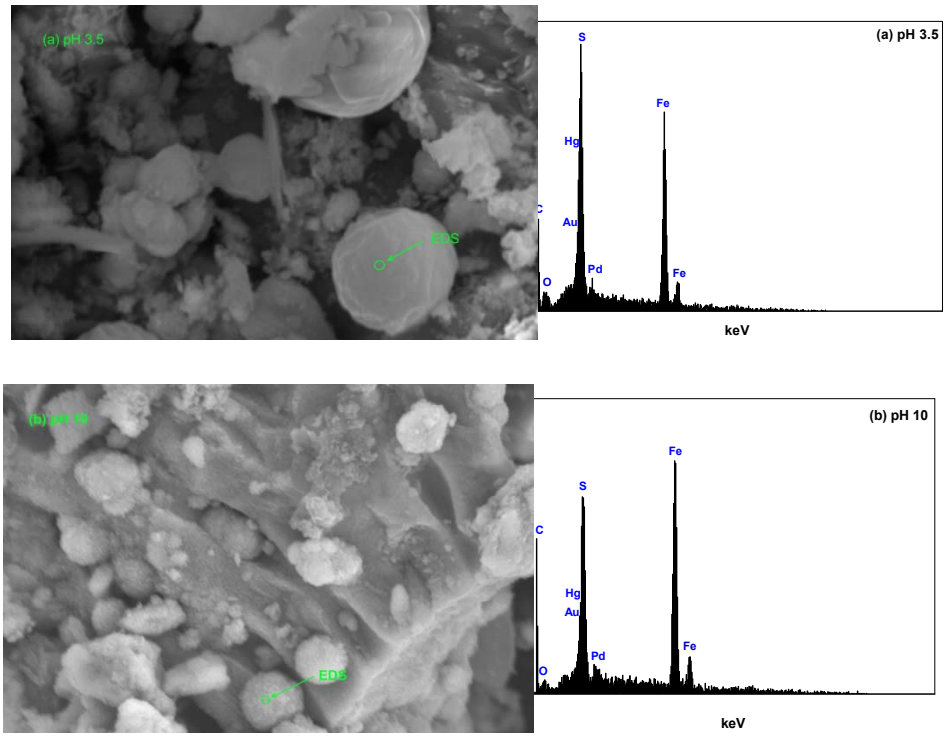

Figure 93. Secondary images of SEM and EDS analysis for FeS reacted with Hg(II) (1.0 mM) at (a) pH 3.5 and (b) pH 10 after previous contact with lower pH.

Figure 94 shows XPS results for Hg 4f spectra of Hg(II)-contacted FeS at pH 3.5 and pH 10 after reaction at lower pH. Hg $4f_{7/2}$ peaks for both solids are centered at 100.2 eV and FHWM values for their peaks are about 0.98 eV. This indicates presence of Hg(II) or Hg(I) species. Also, the highly symmetric shape of the Hg $4f_{7/2}$ peaks indicates that other Hg species (e.g., Hg(0)) are not present, even though low energy tails of the Hg $4f_{7/2}$ peaks covers the binding energies (99.2 to 99.8 eV) associated with Hg(0).

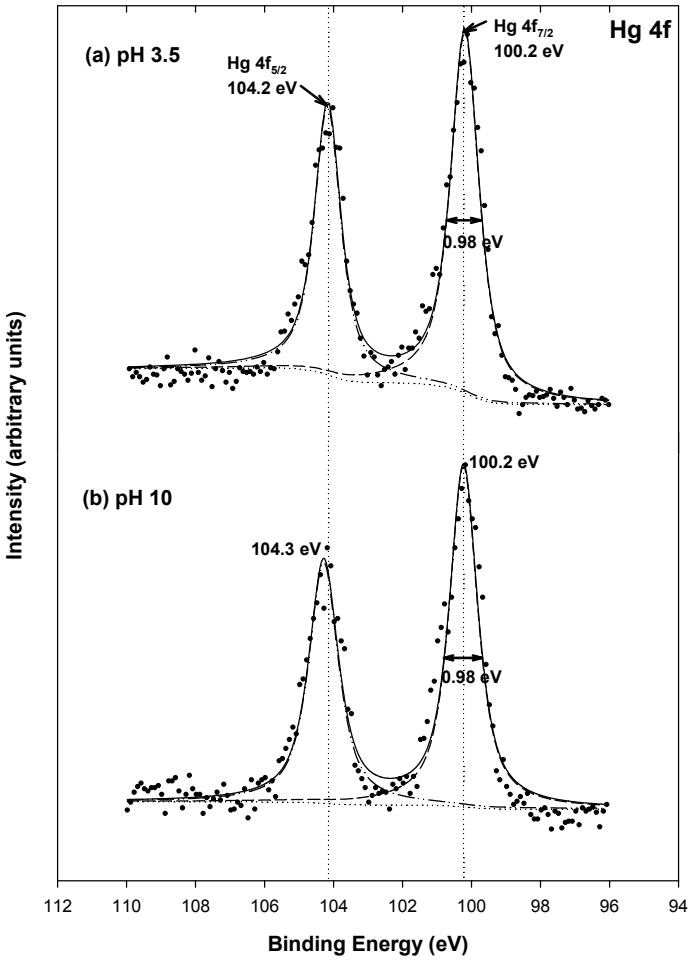

Figure 94. High resolution Hg 4f XPS spectra for mackinawite (1 g/L) reacted with Hg(II) (1 mM) at (a) pH 3.5 and (b) pH 10 after previous contact with lower pH.

Figure 95 shows XPS results for Fe $2p_{3/2}$ spectra of Hg(II)-contacted FeS at pH 3.5 and pH 10. Both spectra show that peaks associated with oxidized forms of Fe such as Fe(III)-S and Fe(III)-O are important. Oxidation of surface Fe could occur by redox reactions with Hg(II) or with other chemicals.

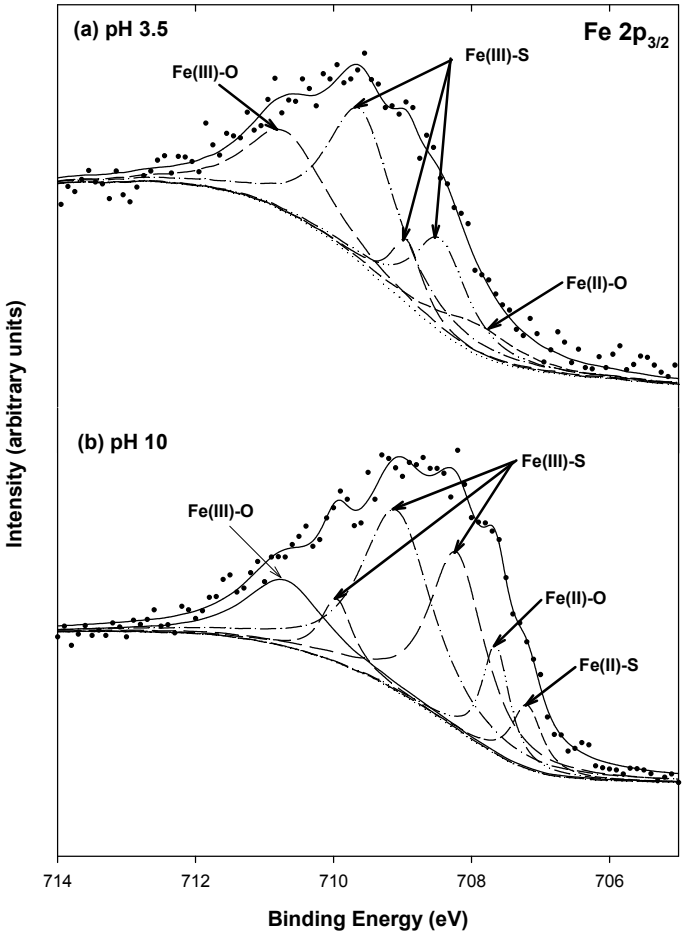

Figure 95. High resolution Fe $2p_{3/2}$ XPS spectra for mackinawite (1 g/L) reacted with Hg(II) (1 mM) at (a) pH 3.5 and (b) pH 10 after previous contact with lower pH.

Figure 96 shows S 2p spectra for Hg(II)-contacted FeS at pH 3.5 and pH 10. Both spectra show presences of oxidized species such as polysulfides (S_n^{2-}) or elemental sulfur (S^o) in addition to S(-II). However, S(-II) species contribute more to the overall intensity of the S 2p spectra, so it is more likely that they react with Hg(II) to form precipitates or surface complexes. Jeong et al. (2007) suggested an alternative theoretical mechanism for the formation of discrete precipitates (HgS(s)) through a disproportionation reaction with elemental sulfur (Equation 11).

$$4S(0) + 3Hg(II) + 4H_2O \rightarrow 3HgS(s) + SO_4^{2-} + 8H^+ \qquad (7) \qquad (11)$$

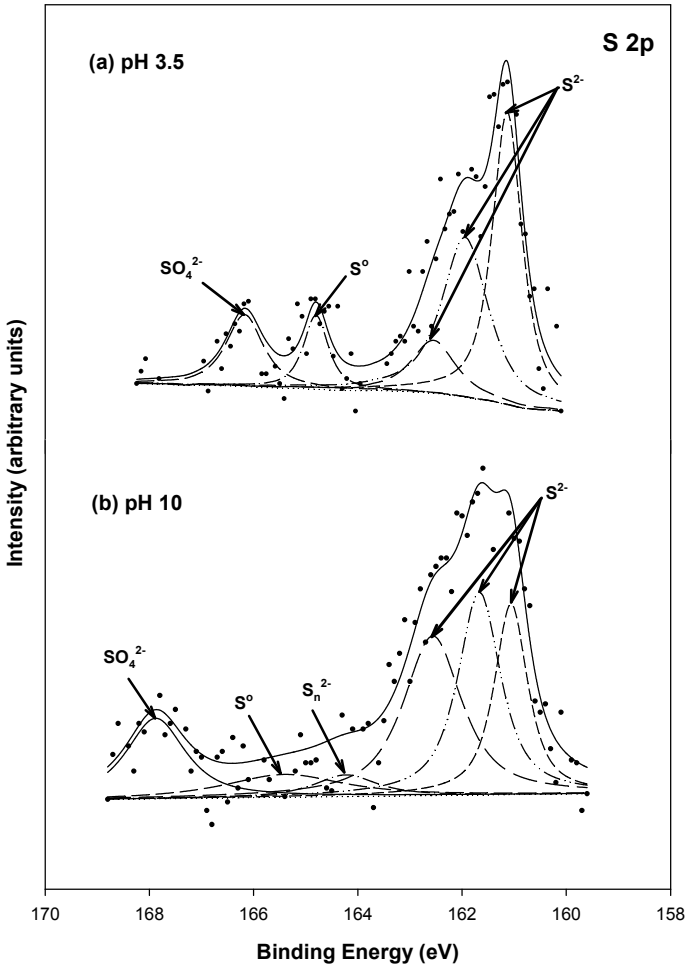

Figure 96. High resolution S 2p XPS spectra for mackinawite (1 g/L) reacted with Hg(II) (1 mM) at (a) pH 3.5 and (b) pH 10 after previous contact with lower pH.

Selenium Removal and Stabilization

Pyrite

Selenium(IV) Removal and Stability

Results of the initial kinetic experiment are shown in Figure 97. Removal of Se(IV) is relatively slow, with half-lives of approximately 25 hr and 55 hr at pH 7 and pH 10, respectively. The slow removal kinetics is consistent with removal being controlled by slower surface reactions, rather than transport to the surface. The effect of pH on removal kinetics could be related to the effect of pH on the surface reaction.

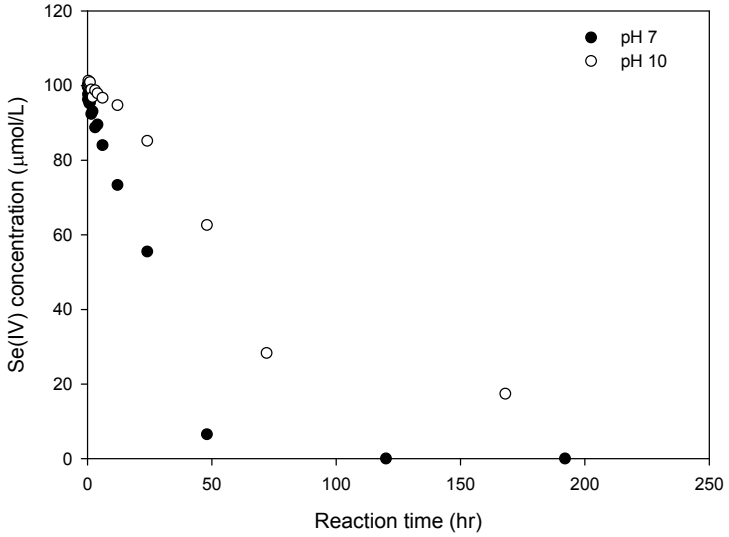

Figure 97. Effect of time on concentrations of Se(IV) in presence of 1 g/L pyrite at pH 7 and pH 10.

The effect of pH on removal of Se(IV) by pyrite after 24 hours of reaction is shown in Figure 98. The data obtained from this experiment is plotted as the solid-phase concentration of Se(IV) as a function of the aqueous phase concentration, which is the way that results of sorption experiments are typically reported. However, conditions in this experiment are not at equilibrium and adsorption is not the only process occurring. The results show that the solid-phase concentration of Se(IV), which is proportional to the amount removed, increases as pH decreases. This could be the result of faster removal kinetics at lower pH (Figure 97). Faster removal kinetics would give higher solid phase concentrations in experiments with constant reaction times. If longer times were allowed for reaction of Se(IV) with the pyrite surface, greater removal and higher solid-phase concentrations would be expected. However, the effect of pH is not large. At pH 7 and pH 8, the solid phase concentration does not approach zero as liquid-phase concentration approaches zero. This indicates that Se(IV) is being very effectively removed when sufficient time is provided to allow surface reactions to proceed.

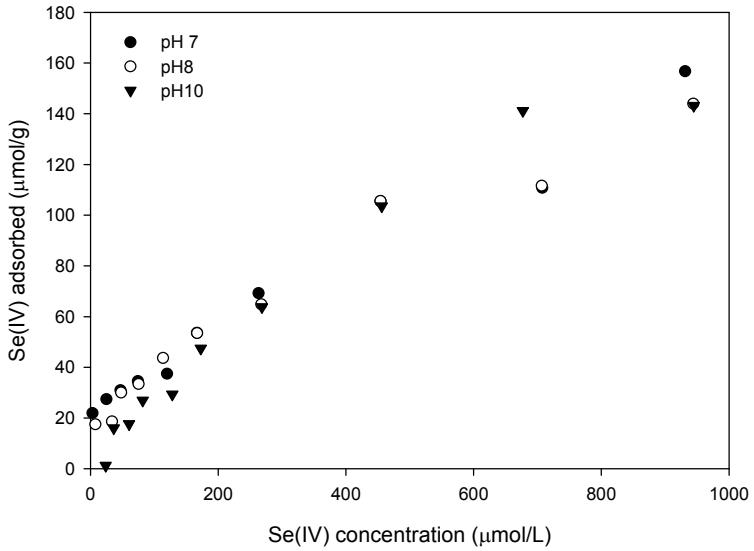

Figure 98. Effect of pH on Solid-phase Concentration of Se(IV) on Pyrite.

Figure 99 shows the effect of sulfate on the solid phase concentration of Se(IV). Higher concentrations of sulfate are seen to lower solid-phase concentrations of Se(IV) when the solid phase and liquid phase concentrations are high. However, there is little effect of sulfate at lower concentrations. This behavior can be explained by sulfate competition with Se(IV) for surface sites on pyrite. The presence of sulfate will initially reduce the concentration of Se(IV) adsorbed to the surface of pyrite. However, if sufficient time is provided for the surface reactions of Se(IV) to occur, the effect of sulfate is reduced. More time may be required for higher surface concentrations to react, so that the effect of sulfate is more pronounced at higher concentrations.

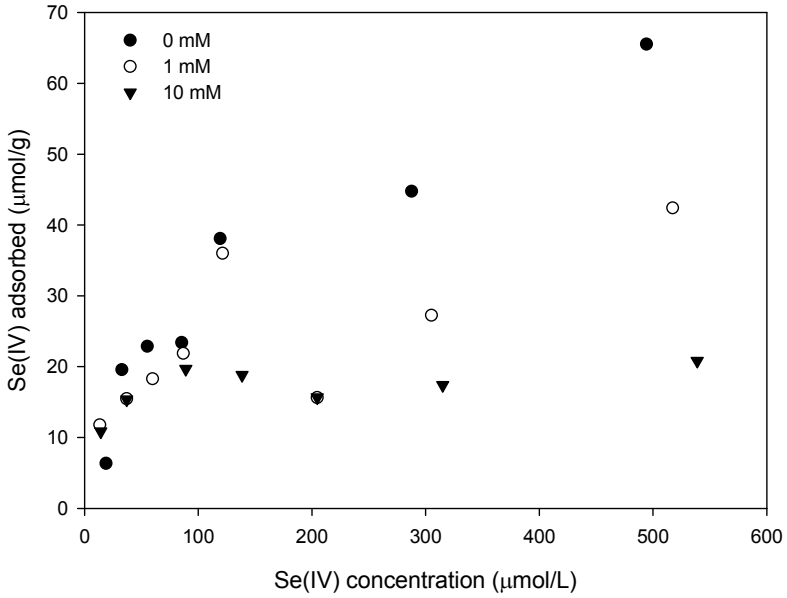

Figure 99. Effect of Sulfate on Solid-phase Concentration of Se(IV) on Pyrite.

Figure 100 shows experimental results for the effect of pH change on the stability of Se(IV)-contacted pyrite. The experiments were conducted by adjusting pH initially to near pH 10 and then decreasing pH and finally increasing pH. When pH was decreased, removal of Se(IV) was observed to increase over the range between pH 9 and pH 10 and nearly complete removal was observed below pH 9. When pH was subsequently increased, no selenium was released from the pyrite. This indicates that strong bonds were formed between Se(IV) and the pyrite surface at lower pH. Previous XPS results indicated that Se(IV) on the surface of pyrite at pH 8 was reduced to species with a range of oxidation states (Se(0), Se(-I), Se(-II)). Thus, it appears that the formation of FeSe or $FeSe_2$ leads to stable solid-phase products with low tendencies to be released to solution when pH is changed.

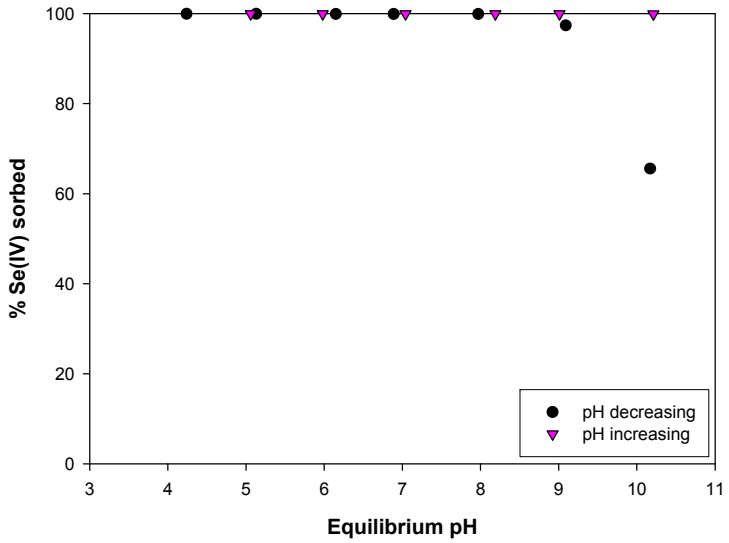

Figure 100. Effect of pH on removal of Se(IV) (16.6 μM) by pyrite (1 g/L) as pH was decreased from near pH 10 and subsequently was increased.

Selenium(VI) Removal and Stability

Figure 101 shows the results of the effect of time on solid-phase concentration of Se(VI) in suspensions of pyrite at pH 8. Data is shown for experiments at three different initial aqueous-phase concentrations of Se(VI) (6.3, 12.7, 38 μM). For the two lower initial concentrations, the solid-phase concentration of Se(VI) was constant over the course of the experiment, which indicates that removal was rapid enough to be complete before the first sample was taken at 1 hour of contact time. In the experiments with the highest initial aqueous-phase concentration, the solid-phase concentration increases over the first 12 hours, plateaus until about 40 hours, and then increases for the rest of the experiment. This unusual kinetic behavior indicates that surface reactions may be occurring at the higher concentrations.

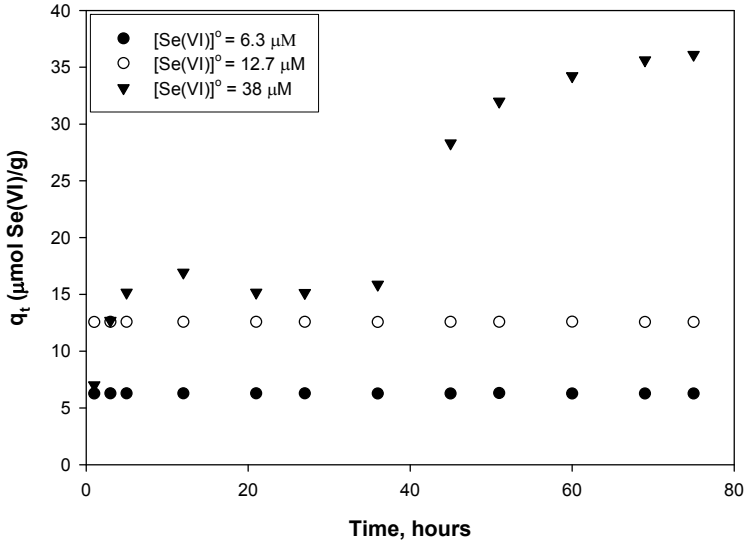

Figure 101. Effect of time on solid-phase concentrations of Se(VI) (1 g/L pyrite, pH 8)

The effect of pH on removal of Se(VI) by pyrite after 24 hours of reaction was investigated and the results are shown in Figure 102. These results show that at lower concentrations, there is little effect of pH on removal. However, at higher concentrations, there is some effect of pH on Se(VI) removal. The best removals (higher amounts of Se(VI) removed and higher solid-phase concentrations) were observed at pH 7, intermediate removals at pH 8 and pH 9, with lower removals at pH 10. Se(VI) removal is relatively low compared to removal of Se(IV) over the same range of pH.

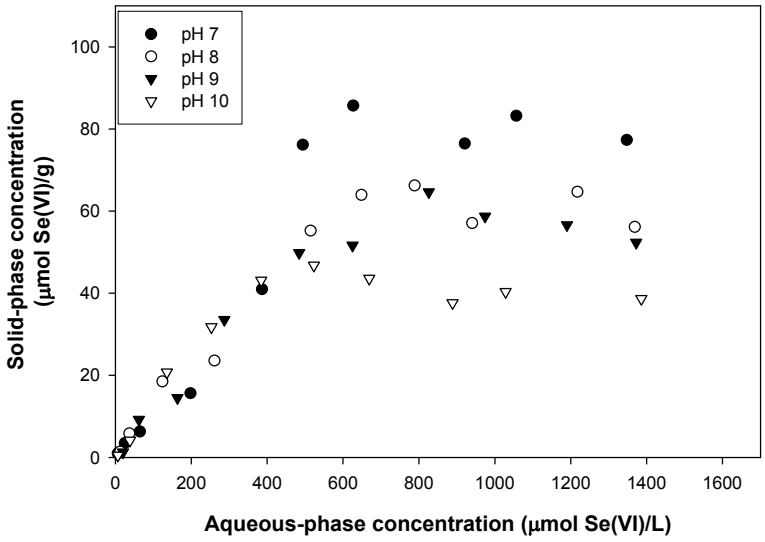

Figure 102. Effect of pH on solid-phase concentration of Se(VI) (1 g/L pyrite, pH 8).

Experiments were conducted to investigate the effect of sulfate concentration (1 and 10 mM) on Se(VI) removal by pyrite. These experiments used a solid concentration of 1 g/L pyrite, 24 hours of contact time and were conducted at pH 8. The results are shown in Figure 103 and they indicate that there is little effect of sulfate on removal of Se(VI) when the concentrations are lower. At higher concentrations, sulfate does appear to inhibit removal of Se(VI), but the behavior is unusual in that peaks in removal are observed at intermediate concentrations when sulfate is present.

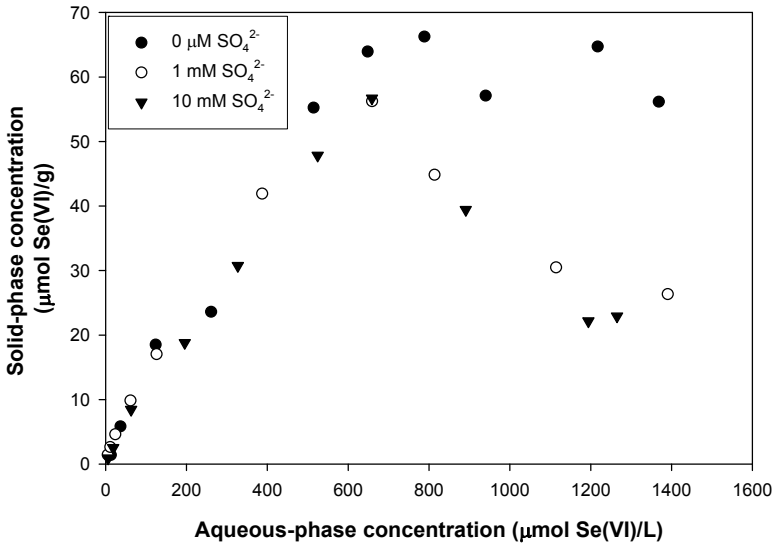

Figure 103. Effect of sulfate concentration on solid-phase concentrations of Se(VI) (1 g/L pyrite, pH 8).

Figure 104 shows experimental results for the effect of pH change on the stability of Se(VI)-contacted pyrite. The suspension was initially adjusted to near pH 4 and then the pH was raised in increments to near pH 10, then decreased in increments back to near pH 4. The highest removals of Se(VI) were observed at the extremes of pH (pH 4, pH 10) and formation of low-solubility species by surface reaction is a possible explanation. To investigate such possible reactions, surface morphology and the oxidation status for Se(VI)-contacted pyrite at pH 10 were investigated by SEM-EDS and XPS.

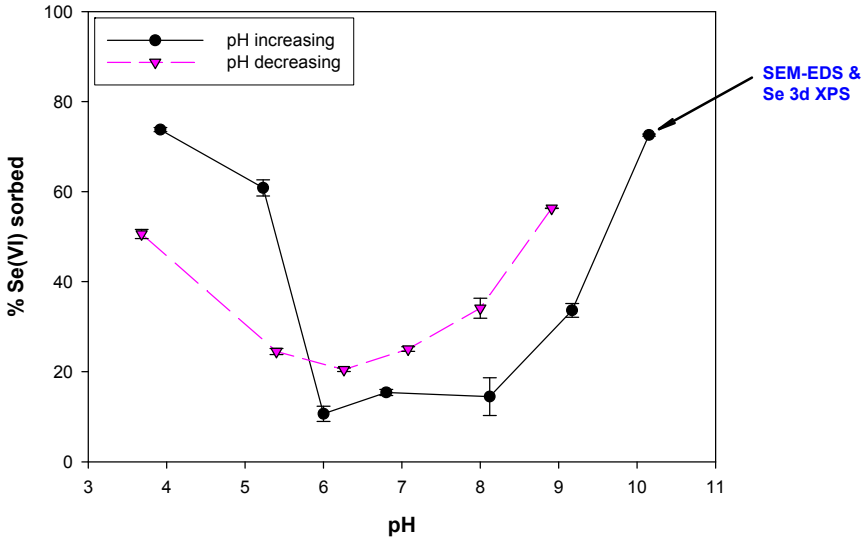

Figure 104. Effect of pH on removal of Se(VI) (16.6 μM) by pyrite (1 g/L) as pH was increased from near pH 4 and subsequently was decreased.

Figures 105 and 106 shows high resolution Fe $2p_{3/2}$ XPS spectra for pyrite reacted with Se(IV) and Se(VI), respectively. Three major Fe $2p_{3/2}$ peaks are seen at 706.7~706.8 eV, 708.4~709.1 eV, and 710.2~711.5 eV, which correspond to Fe(II)-S, Fe(III)-S, and Fe(III)-O, respectively. These peaks are observed in all spectra, regardless of the type of selenium and contact time. However, the 30 day sample for Se(IV) and the 1 day sample for Se(VI) exhibited another peak at 707.4 eV and 707.3 eV, indicative of a Fe(II)-O specie. However, the peak associated with this specie is added by the fitting program when the major Fe(II)-S peak is observed to be wide. The width of this peak could be the result of things other than the formation of Fe(II)-O species. In the case of pyrite reacted with Se(IV), the relative areas for the Fe(III)-S and Fe(III)-O peaks tend to increase with increasing contact time (Table 35), but not excessively. In the case of pyrite contacted with Se(VI), the relative areas for the Fe(III)-S and Fe(III)-O peaks decrease slightly with increasing contact time (Table 35), but the changes are not substantial. Therefore, it could be concluded that the iron in pyrite is somewhat associated with the reduction of Se(IV) rather than Se(VI). A somewhat different observation was reported for Se(IV)/Se(-II) sorption to synthetic or natural chalcopyrite where surface-bound metals (Fe or Cu) apparently were not involved in the reduction of Se(IV) or Se(-II) (Naveau et al., 2007)

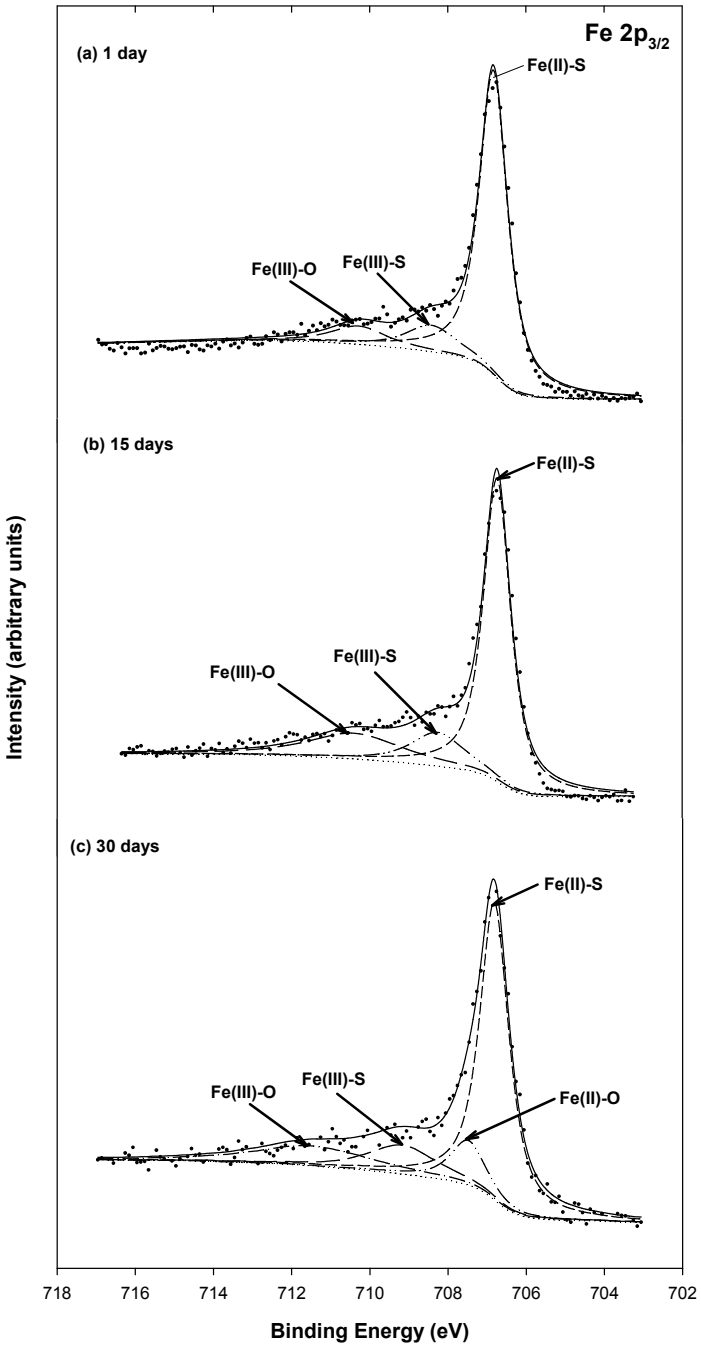

Figure 105. High resolution Fe $2p_{3/2}$ XPS spectra of synthetic pyrite (1 g/L) reacted with 3.1mM Se(IV) at pH 8 for various times: (a) 1 day, (b) 15 days, (c) 30 days.

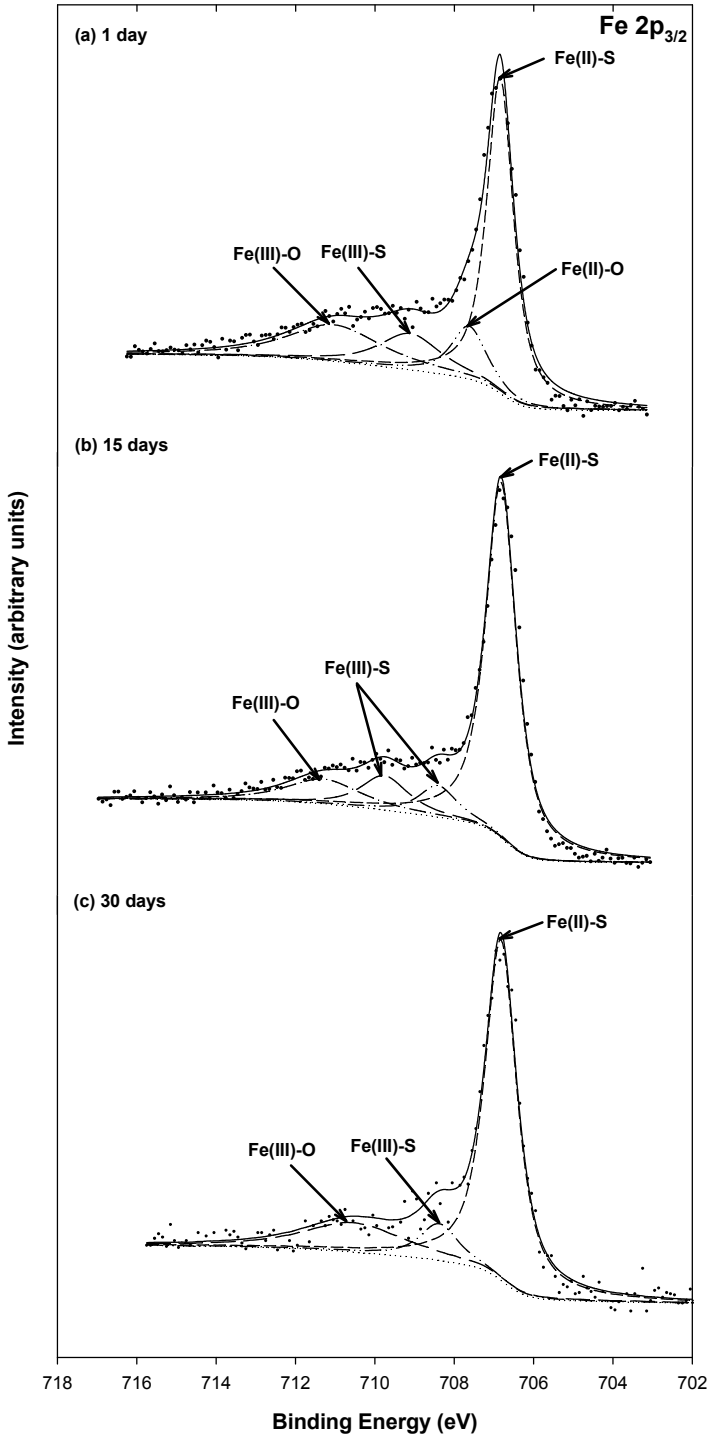

Figure 106. High resolution Fe $2p_{3/2}$ XPS spectra of synthetic pyrite (1 g/L) reacted with 3.1mM Se(VI) at pH 8 for various times: (a) 1 day, (b) 15 days, (c) 30 days.

Figures 107 and 108 show the S 2p spectra for pyrites reacted with Se(IV) and Se(VI), respectively. These spectra are fitted with doublets to characterize the spin-orbit splitting of the S

$2p_{1/2}$ and S $2p_{3/2}$ peaks assigned to S_2^{2-} species. Unlike the S 2p peak distribution for pyrite that had not contacted selenium, pyrites reacted with Se(IV) appear to have spectra indicating that sulfur is present in other forms, presumably formed by surface disproportionation (Figure 107). There is evidence for S^{2-} species at about 161.5 eV and evidence for SO_4^{2-} species at higher binding energies in the range of 167.2-167.5 eV. This observation indicates that the sulfur in pyrite undergoes both oxidation and reduction reactions when Se(IV) sorbs to the surface. Based on these observations, reduction of Se(IV) by pyrite coupled with production of sulfate (SO_4^{2-}) could occur through several reaction pathways. One possible way is that pyrite reacted with Se(IV) could produce thiosulfate ($S_2O_3^{2-}$) and tetrathionate ($S_4O_6^{2-}$) via sequential redox reactions. Similar reactions have been observed in Cr(VI) reduction by pyrite (Demoisson et al., 2007). When thiosulfate ions are produced, they tend to disproportionate into elemental sulfur and tetrathionate. Finally, tetrathionate can be oxidized to sulfate as Se(IV) is reduced. However, the presence of intermediate species of sulfur was not observed for all samples and peaks associated with sulfate species did not appear until 15 days of contact time. An alternative explanation for the occurrence of sulfate, especially in the 15 days sample, is that it could be produced when the surface-bound sulfur is oxidized by Fe(III)-oxyhydroxide surface species. The presence of these species is indicated by development of a broad Fe(III) peaks in the Fe 2p spectra. This was particularly evident in the 15 day sample, which showed the sum of relative peak areas for Fe(III)-S and Fe(III)-O to be 34%, compared to 21 % for the 1 day sample. However, the evidence for sulfate on the pyrite surface may also be the result of aqueous sulfate sorbing to the surface, because the pyrite solids were not washed before analysis (Demoisson et al., 2007). In addition, reduction of Se(IV) by pyrite coupled with oxidation of surface-bound Fe can be associated with production of monosulfide (S^{2-}) and sulfate (SO_4^{2-}) to fulfill charge balance. Nesbitt et al. showed that the presence of the three S species such as monosulfide (S^{2-}), disulfide (S_2^{2-}) and polysulfide (S_n^{2-}) on the vacuum-fractured pyrite could be explained by charge compensation for ferric iron, resulting in disproportionation of disulfide to monosulfide and polysulfide, as follows (Nesbitt and Muir, 1994).

$$3FeS_2(\text{pyrite}) \rightarrow \equiv Fe(III)_2S_3 + \equiv Fe(II)S_3 \qquad (12)$$

where "≡" indicates a surface species. Nesbitt et al. emphasized the uncertainty of the origin of the high energy tail of Fe 2p spectrum and suggested that more detailed studies of the oxidation states of Fe and S are required to clarify relationships among Fe(III), S^{2-}, and S_n^{2-} (Nesbitt and Muir, 1994). Based on our results, Se(IV) reduction by pyrite may be responsible for oxidation of Fe(II) that leads to formation of monosulfide bonded to Fe(III) ($\equiv Fe(III)_2S_3$) and polysulfide (S_3^{2-}) bonded to Fe(II) ($\equiv Fe(II)S_3$). Subsequently, polysulfide bonded to Fe(II) can be continuously oxidized to sulfate by reduction of Se(IV). Relative peak areas for S^{2-} and SO_4^{2-} were observed to increase with reaction time (Table 36), although S_3^{2-} species were not detected. However, in the case of Se(VI)-contacted pyrite, important changes in S 2p spectra were not observed. This could be caused by the fact that lower amounts of Se(VI) compared to Se(IV) were sorbed onto pyrite, or that Se(VI) was less prone to undergo redox reactions on the surface.

Another possibility for occurrence of S^{2-} and sulfate species on pyrite after contact with Se(IV) may be related to interference of Se 3p spectra with spin-orbit splitting of Se $3p_{3/2}$ and Se $3p_{1/2}$ peaks (Ihanus et al., 2004). This overlap may make the S 2p spectra an unexpected pattern, if the range of binding energies in the Se 3p spectra is slightly different from that in the S 2p spectra. Alternatively, the intensity of entire S 2p spectra may increase, if the range of binding energies for both the S 2p and the Se 3p spectra are exactly in accordance. If we believe that the

Se 3p spectra overlap with the S 2p spectra, but that the overlap is not exact, then the occurrence of peaks associated with S^{2-} or SO_4^{2-} and their increasing intensities over time could be caused by the increased amount of Se(IV) sorbed to the surface or by the reduction of sorbed Se(IV). Naveau et al (2007) showed that after pyrite was contacted with Se(IV) there was small doublet at 168.2 eV and a broadening doublet at 162.5 eV in the S 2p spectra that was attributed to oxidized species formed from S_2^{2-}. However, they described the S 2p spectra without considering possible overlap with the Se 3p spectra, concluding that the oxidation of sulfur species is attributed to reduction of Se(IV) sorbed on pyrite. However, the only observation that is different between this study and Naveau's result is that S^{2-} species were observed only by this study, suggesting that the presence of S^{2-} may be the result not of overlapping peaks, but from the surface disproportionation of surface-bound sulfur, as described above. Also, the occurrence of sulfate may be caused by overlap of S 2p with Se 3p spectra or sequential oxidation of surface-bound sulfur in conjunction with the reduction of Se(IV).

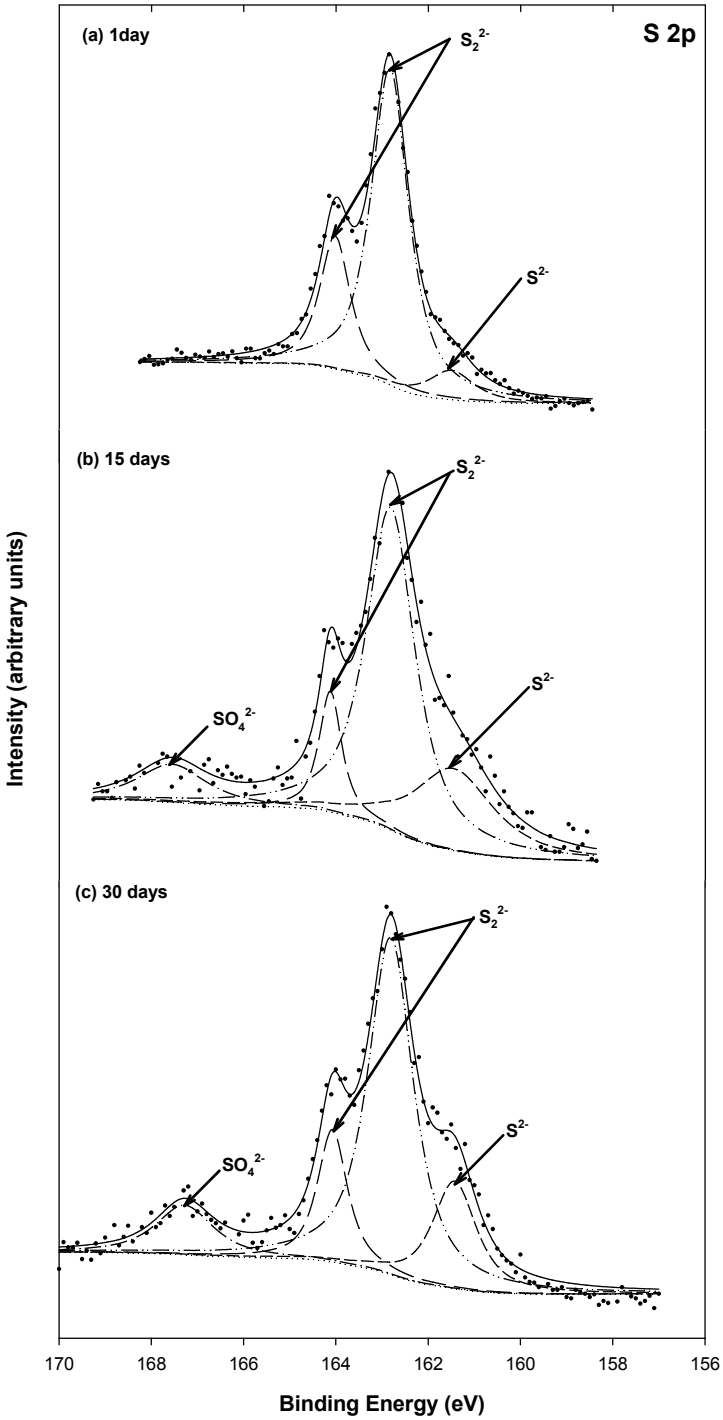

Figure 107. High resolution S 2p XPS spectra of synthetic pyrite (1 g/L) reacted with 3.1 mM Se(IV) at pH 8 for various times: (a) 1 day, (b) 15 days, (c) 30 days; fitting of S 2p XPS spectra was conducted without considering overlap of Se 3p XPS spectra.

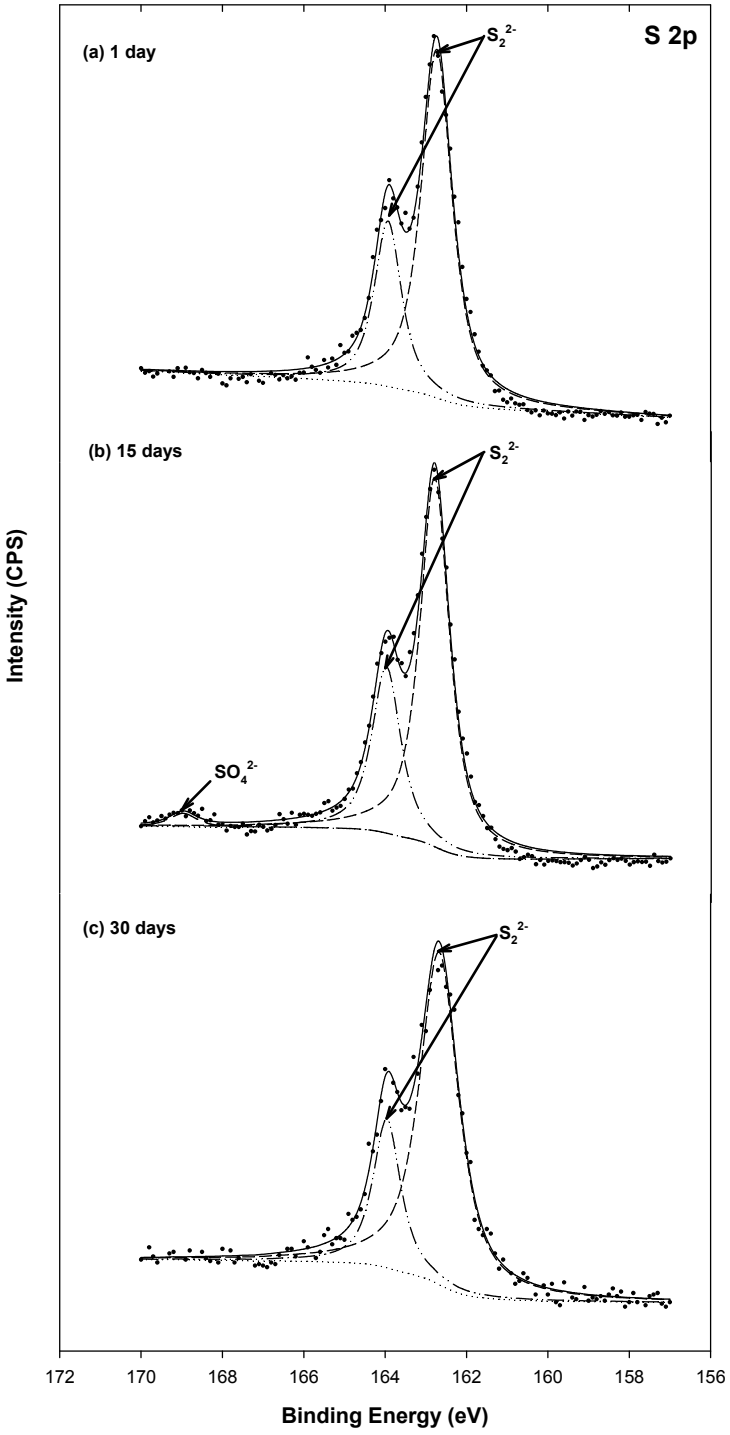

Figure 108. High resolution S 2p XPS spectra of synthetic pyrite (1 g/L) reacted with 3.1 mM Se(VI) at pH 8 for various times: (a) 1 day, (b) 15 days, (c) 30 days; fitting of S 2p XPS spectra was conducted without considering overlap of Se 3p XPS spectra.

Table 35. Binding energies (BE), full width at half maximum (FWHM), and area percentage for peaks in the Fe $2p_{3/2}$ XPS spectra of pyrite contacted with Se(IV) and Se(VI) for various times.

Sample	Contact time (days)	BE (eV)	FHWM (eV)	Area (%)	Chemical states
Pyrite	0	706.8	0.86	72.4	Fe(II)-S
		708.3	1.66	14.2	Fe(III)-S
		710.4	2.09	13.4	Fe(III)-O
Pyrite+Se(IV)	1	706.8	0.86	78.5	Fe(II)-S
		708.4	1.54	12.2	Fe(III)-S
		710.2	1.69	9.3	Fe(III)-O
	15	706.7	0.83	65.9	Fe(II)-S
		708.2	1.64	14.5	Fe(III)-S
		710.3	2.89	19.5	Fe(III)-O
	30	706.8	0.89	59.7	Fe(II)-S
		707.4	1.07	10.6	Fe(II)-O
		709.1	2.1	13.7	Fe(III)-S
		711.5	3.57	15.9	Fe(III)-O
Pyrite+Se(VI)	1				
		706.8	0.75	45.3	Fe(II)-S
		707.3	0.73	13.6	Fe(II)-O
	15	708.6	1.86	16.0	Fe(III)-S
		710.8	2.96	25.1	Fe(III)-O
		706.7	0.86	65.3	Fe(II)-S
	30	708.0	1.52	11.6	Fe(III)-S
		709.7	1.68	13.2	Fe(III)-S
		711.4	2.12	9.8	Fe(III)-O

Table 36. Binding energies (BE), full width at half maximum (FWHM), and area percentage for peaks in the S 2p XPS spectra of pyrite contacted with Se(IV) and Se(VI) for various times.

Sample	Contact time (days)	BE (eV)	FHWM (eV)	Area (%)	Chemical states
Pyrite	0	162.8	0.87	64.7	S_2^{2-}
		164.0	0.95	33.5	S_2^{2-}
Pyrite+Se(IV)	1	161.5	1.17	7.7	S^{2-}
		162.8	0.97	68.7	S_2^{2-}
		164.0	0.79	23.6	S_2^{2-}
	15	161.4	2.08	23.8	S^{2-}
		162.8	1.27	57.1	S_2^{2-}
		164.1	0.58	9.7	S_2^{2-}
		167.5	1.77	9.4	SO_4^{2-}
	30	161.4	1.13	17.6	S^{2-}
		162.8	1.17	57.1	S_2^{2-}
		164.0	0.77	14.7	S_2^{2-}
		167.2	1.49		SO_4^{2-}
Pyrite+Se(VI)	1	162.7	0.91	70.6	S_2^{2-}
		163.9	0.80	29.4	S_2^{2-}
	15	162.7	0.87	69.7	S_2^{2-}
		163.9	0.84	30.3	S_2^{2-}
	30	162.7	1.15	76.1	S_2^{2-}
		163.9	0.81	23.9	S_2^{2-}

Figure 109 presents the Se 3d XPS spectra of pyrite before and after contact with Se(IV) or Se(VI) for various times. Pyrite displays a peak in the Se 3d spectra at binding energy in the range of 50-65 eV that is due to iron (Naveau et al., 2007). Figure 109(a) shows that important shifts in binding energies for this peak occur at different times after contact with Se(IV). The most important change is the shift in binding energy from 54.2 eV to 55.2 eV. This shift could be caused by Se(IV) being sorbed to the surface of pyrite and subsequently being reduced by surface reactions to form a variety of reduced species (Se(0), Se(-I), Se(-II)). Reduced species of selenium produce spectra with peaks in the range of 53.7~56.3 eV, which is the range where peaks are observed in Figure 109(a). In addition, it was also observed that the binding energy of the main peak in Se 3d spectra in Figure 109(b) did not shift substantially at contact times larger than one day. This is unlike the case of Se(VI), where the Se 3d spectra (Figure 109(b)) does not show shifts in location of any important peaks. This difference could be due to low amounts of Se(VI) being sorbed onto pyrite or to the greater resistance of sorbed Se(VI) to being reduced by surface reactions. However, after 30 days of contact, the peak begins to widen, probably due to Se(VI) reduction.

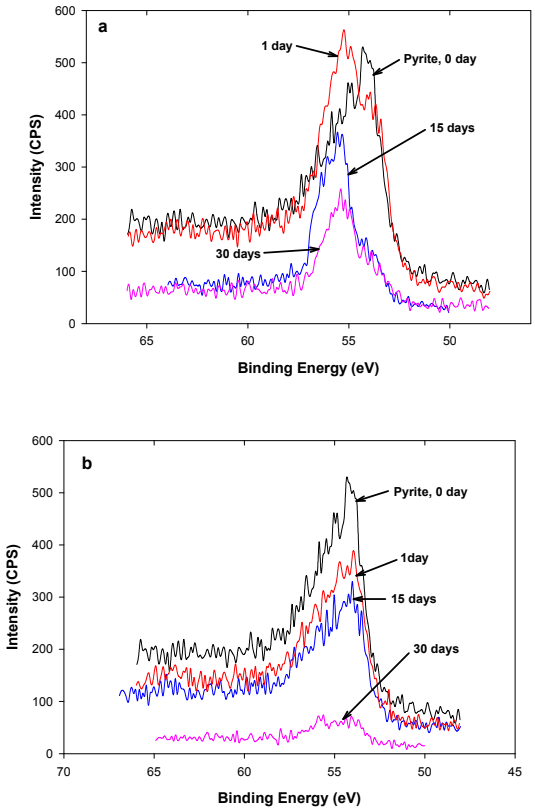

Figure 109. High resolution Se 3d XPS spectra of synthetic pyrite (1 g/L) reacted with (a) 3.1×10^3 µM Se(IV) and (b) 3.1×10^3 µM Se(VI) at pH 8 and various contact times.

Figure 110 shows the SEM image of Se(VI)-contacted pyrite and it demonstrates the presence of thin bundles of thread-like particles. Some parts of these particles could be precipitates that are formed by surface reactions between reduced forms of Se(VI) and pyrite, but their formation is reversible as indicated by release of selenium when pH was reduced (Figure 104).

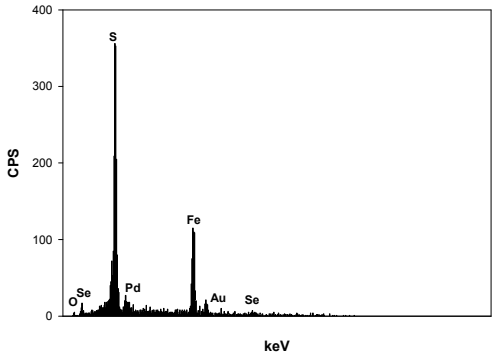

Figure 110. Secondary image and EDS of SEM for Se(VI)-contacted pyrite reacted at pH 10 for 30 minutes.

Figure 111 shows the Se 3d spectra for Se(VI)-contacted pyrite formed at pH 10. These results are similar to previous spectra, in that the center of Se 3d spectrum for is shifted to higher binding energies, which indicates that oxidation status of Se(VI) has changed. Therefore, it supports the hypothesis that Se(VI) is being reduced by reaction with the pyrite surface.

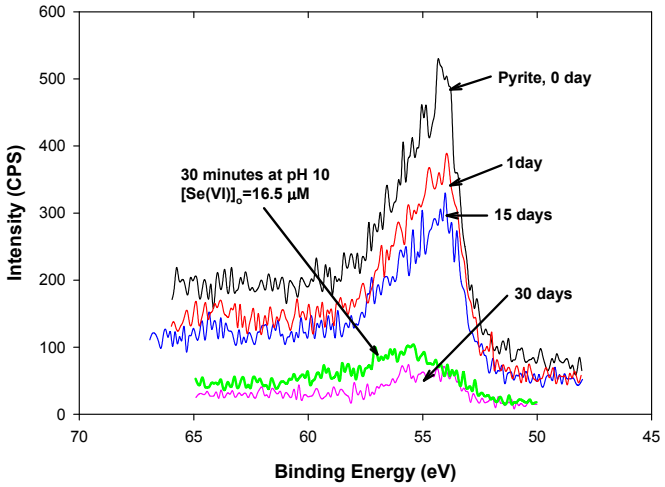

Figure 111. Comparison of Se 3d spectra of Se(VI)-contacted pyrite (1 g/L, 16.5 µM) reacted at pH 10 for 30 minutes with previous XPS data for Se(VI)-contacted pyrite (1 g/L, 3.1 mM) reacted at pH 8 for 1, 15 and 30 days.

Mackinawite

Selenium(IV) Removal and Stability

Results of kinetic experiment for removal of Se(IV) by FeS are shown in Figures 112 and 113. Figure 112 shows that removal of Se(IV) by 1 g/L of FeS is so fast that Se(V) can be completely removed within 30 minutes at all initial concentrations studied (6.3, 12.7, 38 µM). No release of Se(IV) was observed after complete removal. Since 1 g/L of FeS is enough high to remove Se(IV) completely, kinetic experiments were also conducted at higher Se(IV)/FeS molar ratio. These experiments were conducted with a FeS dose of 0.5 g/L and initial concentrations of Se(IV) of 127 and 253 µM and the results are shown in Figure 113. Se(IV) was completely removed by 0.5 g/L of FeS within 120 minutes when the initial concentration was 127 µM, while complete removal of Se(IV) dosed at 253 µM occurs after 480 minutes. Also, no release of Se(IV) was observed at times longer than needed for complete removal.

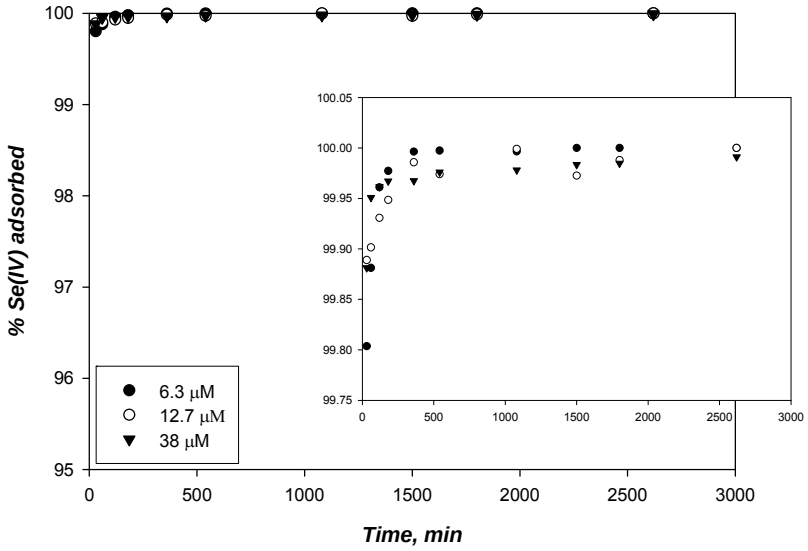

Figure 112. Effect of time on percentage Se(IV) removal by FeS at pH 8 and lower initial Se(IV)/FeS molar ratio. Initial dose of FeS = 1 g/L and initial [Se(IV)] = 6.3, 12.7, 38 μM.

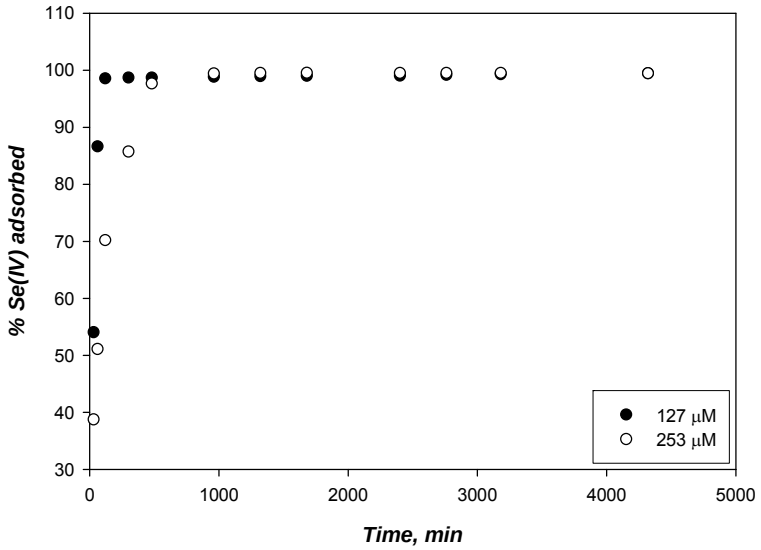

Figure 113. Effect of time on percentage Se(IV) removal by FeS at pH 8 and higher initial Se(IV)/FeS molar ratio. Initial dose of FeS = 0.5 g/L and initial [Se(IV)] = 127, 253 μM.

Figure 114 shows the results of experiments describing removal of Se(IV) by FeS at four different pH values. These experiments were conducted with a solid concentration of FeS of 0.5 g/L and a contact time of 24 hours. The symbols represent the measured data and the lines represent predictions of different models. The models used to correlate the data were equations (Langmuir, Freundlich, BET) that are typically used to describe data from equilibrium adsorption experiments. However, they are being used here without implication that the experimental systems had reached equilibrium nor that adsorption was the only mechanism affecting results.

Table 37 shows the parameters of the different models that were obtained by nonlinear regression. This procedure chooses parameters to minimize the sum of squared residuals (SSR). A goodness of fit parameter (GFP) was calculated using the SSR in order to numerically compare the fits to different data sets (Equation 13). It is the ratio of the standard deviation of the points about the regression line divided by the average value of the data. As such, it represents the ratio of an average error to the average value. Smaller values represent better fits of the model to the data.

$$GFP = \frac{\sqrt{\frac{SSR}{(n-2)}}}{\bar{y}} \tag{13}$$

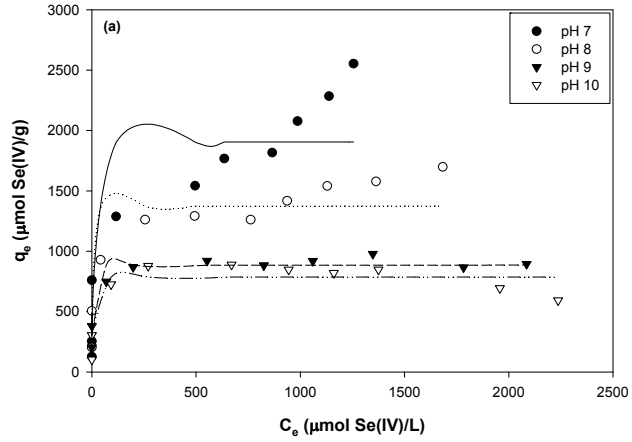

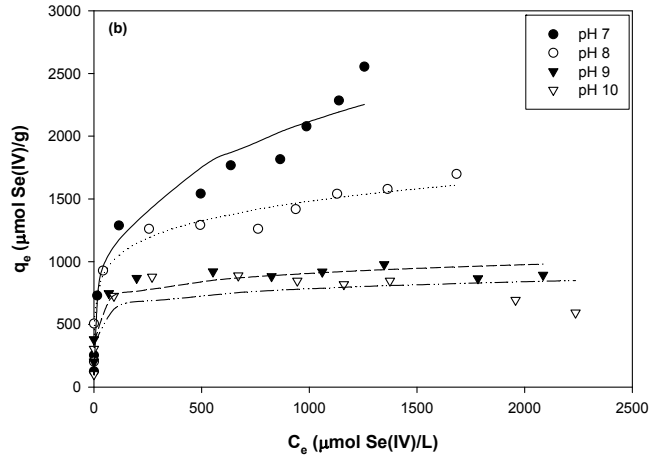

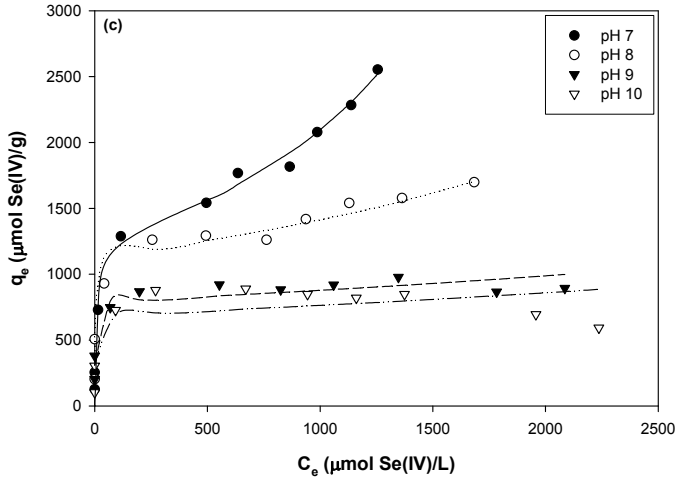

Figure 114. Amounts of Se(IV) removed per mass of FeS (symbols) as functions of concentration of Se(IV) in water at various pH with (a) Langmuir, (b) Freundlich, and (c) BET models (lines) fitted to the data.

Figure 114 shows that different patterns of removal were observed at different pH values. Results from experiments conducted at pH 7 and pH 8 are described best by the BET model and results at other pH values are described best by the Langmuir model. These comparisons are made using the goodness of fit parameter. Since Se(IV) removal at pH 7 and 8 is well described by the BET model, it can be inferred that some surface reactions were occurring. For example, Se(IV) could be reduced to Se(-II) and precipitate as FeSe. The results shown in Figure 114 also indicate that greater amounts of Se(IV) were removed at lower pH where BET-like behavior was observed.

Table 37. Summary of fitting model parameters for Se(IV) removed by FeS

	Solution pH			
Models	**pH 7**	**pH 8**	**pH 9**	**pH 10**
Langmuir				
q_{max} (µmol/g)	2206 ± 438	1377 ± 184	886 ± 56.6	787 ± 80
b (L/µmol)	0.00 ± 0.00	2.4 ± 3.3	3.67 ± 2.15	3.46 ± 3.94
SSR	1.6×10^4	4.7×10^5	3.9×10^4	7.7×10^4
Goodness of fit	0.281	0.209	0.092	0.147
Freundlich				
k_f	319 ± 191	492 ± 136	436 ± 120	395 ± 215
n	3.65 ± 1.19	6.26 ± 1.62	9.43 ± 3.65	10.1 ± 8.2
SSR	2.2×10^5	7.8×10^4	6.0×10^4	1.9×10^5
Goodness of fit	0.116	0.085	0.114	0.231
BET				
A	234 ± 193	$1.6\times10^4 \pm 1.0\times10^4$	$4.4\times10^4 \pm 3.1\times10^4$	$4.4\times10^4 \pm 8.2\times10^4$
q_{max}	1276 ± 67	1130 ± 62	790 ± 57	687 ± 107
SSR	9.9×10^4	4.9×10^9	4.9×10^4	1.7×10^5
Goodness of fit	0.077	0.080	0.102	0.223

Experiments were conducted to investigate the effect of sulfate concentration on Se(IV) removal by FeS. Initial concentrations of 1 and 10 mM of sulfate were added to batch reactors containing 1 g/L of FeS at pH 8. Figure 115 shows the amount of Se(IV) removed per mass of FeS as a function of Se(IV) concentration in the liquid as affected by total sulfate concentration and a Langmuir model is fitted to the data. Figure 116 presents the same data but fitted with the Freundlich model. These figures show that sulfate concentrations of 1 and 10 mM had a negligible effect on removal of Se(IV) on FeS. Table 38 shows the fitting model parameters that were obtained by nonlinear least square regression. The goodness of fit parameters (GFP) shows that the Langmuir model provides the better fit to data on removal of Se(IV) than does the Freundlich model. The BET model was not fitted to this data, because there was no indication in the data that BET-like behavior was occurring.

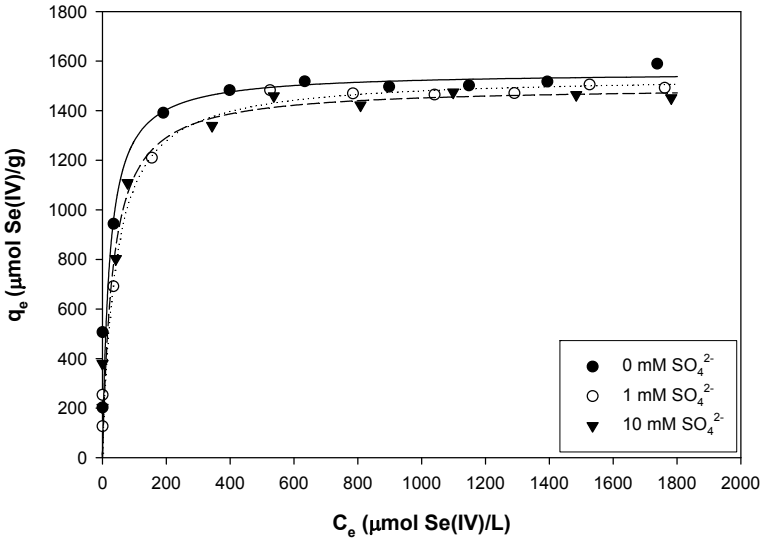

Figure 115. Amounts of Se(IV) removed per mass of solid (FeS) as functions of concentration of Se(IV) in water as affected by sulfate concentration (1 and 10 mM) at pH 8. Symbols represent data and lines represent Langmuir model.

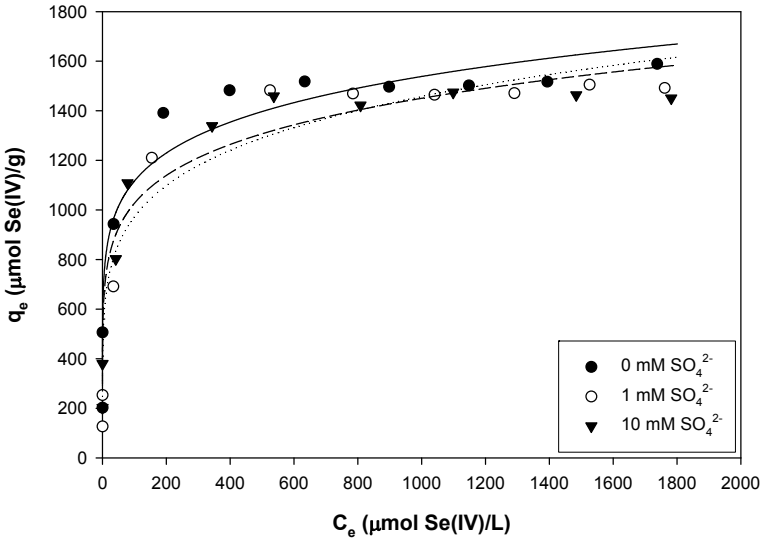

Figure 116. Amounts of Se(IV) removed per mass of solid (FeS) as functions of concentration of Se(IV) in water as affected by sulfate concentration (1 and 10 mM) at pH 8. Symbols represent data and lines represent Freundlich model.

Table 38. Model parameters for Se(IV) removal by FeS as affected by sulfate

SO_4^{2-} (mM)	Langmuir				Freundlich			
	b (L/mol)	q_{max} (µmol/g)	SSR	GFP	K_f ($\mu mol^{1-1/n} \cdot L^{1/n}/g$)	n	SSR	GFP
0	0.046±0.058	1560±198	$2.8x10^5$	0.16	588±162	7.19±2.16	$5.1x10^5$	0.17
1	0.024±0.014	1540±114	$8.1x10^4$	0.09	432±157	5.68±1.73	$1.0x10^5$	0.11
10	0.031±0.026	1500±173	$1.8x10^5$	0.13	495±147	6.43±1.87	$9.0x10^5$	0.19

Figure 117 shows results of experiments on the stability of Se(IV)-contacted FeS over a range of pH. The pH was initially adjusted to near pH 10 and then lowered in a series of steps. Nearly complete removal was observed for all pH values below about pH 9. As pH was raised in a series of steps, there was no release of Se(IV), even near pH 10. Retention of Se(IV) near pH 10 indicates that stronger bonds between Se(IV) and mackinawite were formed at the lower pH. It is also possible that the time of the experiments resulted in formation of stronger bonds, rather than the effects of lower pH.

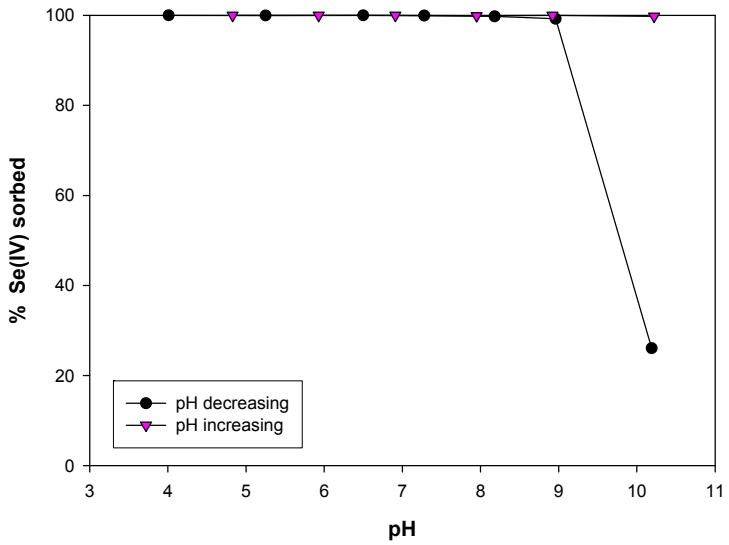

Figure 117. Effect of pH on removal of Se(IV) (16.6 µM) by FeS (1 g/L) as pH was decreased from pH 10 and subsequently was increased.

Selenium(VI) Removal and Stability

Results of the initial kinetic experiment to evaluate removal of Se(VI) by FeS are shown in Figure 118. These experiments were conducted with 1 g/L FeS at pH 8 and various initial concentrations of Se(VI) (12.7, 38, 127 µM). Figure 118 shows that an initial stage of removal of Se(VI) occurs in the first hour of contact where about 10 % of Se(VI) is removed. After one hour, the removal continues at a slow rate at lower initial concentrations of Se(VI), but at more rapid rate at the highest initial concentration. The slower rate of uptake of Se(VI) compared to uptake of Se(IV) may be due a lower affinity of Se(VI) for the FeS surface. This would occur if the surface were negatively charged at pH 8. Se(VI) would be present as an anion with two

negative charges at pH 8, compared to Se(IV) which would be present mostly as an anion with one negative charge. Figure 118 also shows that increasing initial Se(VI) concentration results in higher amounts removed.

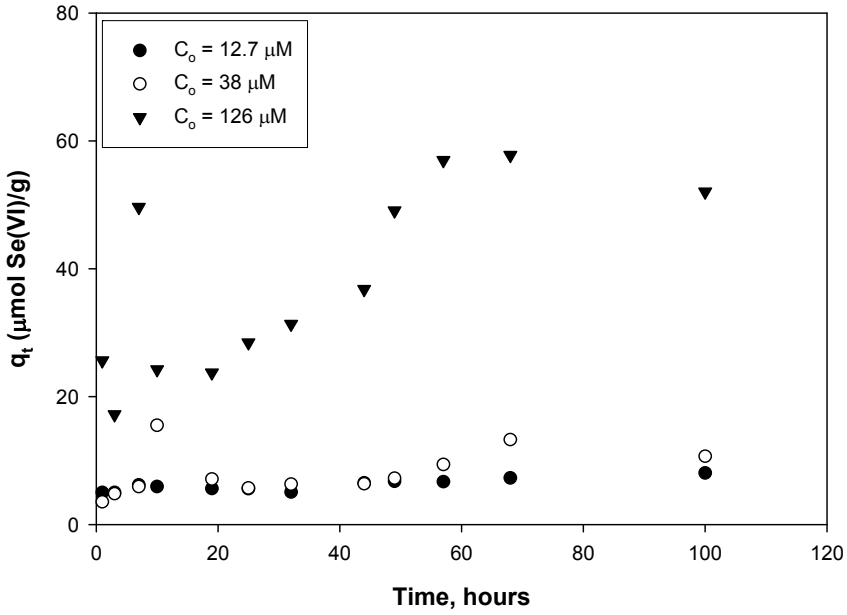

Figure 118. Amounts of Se(VI) removed per mass of solid (FeS) as functions of time with 1 g/L FeS at pH 8.

Figure 119 shows the results of experiments for removal of Se(VI) by FeS at four different pH values (i.e., 7, 8, 9, 10), but the same concentration of FeS (1.0 g/L) and contact time (24 hours). The symbols represent the measured data and the lines represent predictions made by the fitting models (Langmuir, Freundlich, BET). Table 39 shows the parameters of the Langmuir, Freundlich, and BET models that were obtained by nonlinear regression. Figure 119 shows that the solid-phase concentrations of Se(VI) are below 140 μmol Se/g in all experiments, indicating that the sorption capacity of FeS for Se(VI) is much lower than for Se(IV). Maximum solid phase concentrations (q_{max}) of Se(IV) on FeS were observed to be in the range 800 - 1200 μmol/g. This range is similar to what was observed for removal of Se(IV) by pyrite. At pH 7 and pH 8, solid-phase concentration increases rapidly with increasing aqueous concentration, indicating that Se(IV) can undergo surface reactions. The BET model fits this data best, as indicated by the goodness of fit parameter in Table 39. Results of experiments conducted at pH 9 and pH 10 shows a pattern of removal that is better described by the Langmuir model (Table 39). A pattern of removal that is more like that observed for experiments at lower pH might be observed at higher pH, if higher concentrations were investigated.

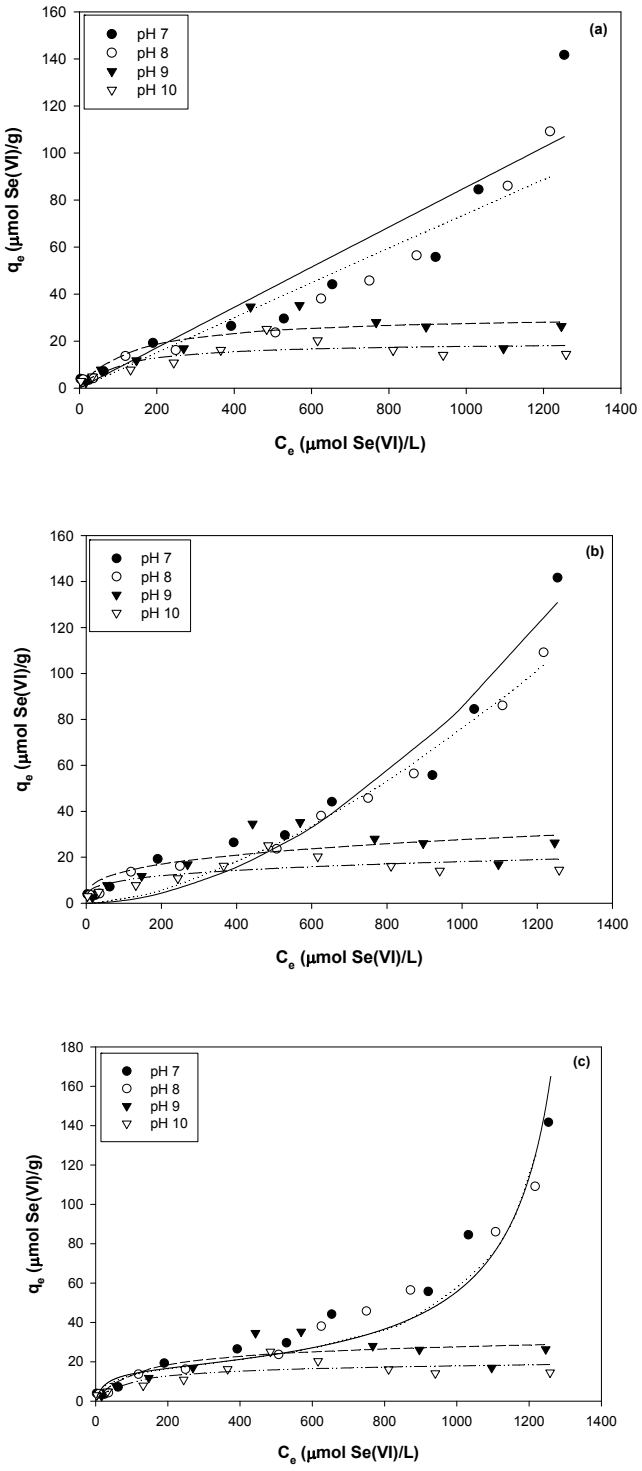

Figure 119. Amounts of Se(VI) removed per mass of FeS (symbols) as functions of concentration of Se(VI) in water at various pH with (a) Langmuir, (b) Freundlich, and (c) BET models (lines) fitted to the data.

Table 39. Summary of equilibrium model parameters for Se(VI) sorption onto FeS

Models	Solution pH			
	pH 7	pH 8	pH 9	pH 10
Langmuir				
q_{max} (µmol/g)	$3.94\times10^{4} \pm 1.29\times10^{7}$	$1.67\times10^{5} \pm 2.17\times10^{8}$	31.2 ± 12.9	19.7 ± 7.95
b (L/µmol)	$2.16\times10^{-6} \pm 8.12\times10^{-4}$	$4.45\times10^{-7} \pm 5.89\times10^{-4}$	$7.4\times10^{-3} \pm 1.34\times10^{-2}$	$9.25\times10^{-3} \pm 1.8\times10^{-2}$
SSR	2.2×10^{3}	8.8×10^{2}	3.7×10^{2}	1.4×10^{2}
Goodness of fit	0.40	0.264	0.333	0.32
Freundlich				
k_f	$2.3\times10^{-4} \pm 1.0\times10^{-3}$	$1.32\times10^{-3} \pm 4.4\times10^{-2}$	3.39 ± 7.24	3.01 ± 2.8
n	0.54 ± 0.19	0.63 ± 0.14	3.28 ± 3.55	3.85 ± 4.02
SSR	9.6×10^{2}	2.8×10^{2}	5.2×10^{2}	1.8×10^{2}
Goodness of fit	0.263	0.15	0.392	0.359
BET				
A	15.8 ± 2.5	15.8 ± 2.4	28.3 ± 11.2	17.9 ± 6.86
q_{max}	55.2 ± 279	44.1 ± 175	1.21×10^{2} ± 237	$1.56\times10^{2} \pm 3.24\times10^{2}$
SSR	1.3×10^{2}	8.1×10^{2}	4.0×10^{2}	1.5×10^{2}
Goodness of fit	0.30	0.254	0.345	0.331

Experiments were conducted to investigate the effect of sulfate concentration (1, 10 mM) on Se(VI) removal by FeS. These experiments used a concentration of 1 g/L FeS, 24 hour contact time and pH 8. Figure 120 shows that there is little effect of sulfate on the amount of Se(VI) removed, although there is some indicated that increased sulfate resulted in increased Se(VI) removal at intermediate concentrations of Se(VI).

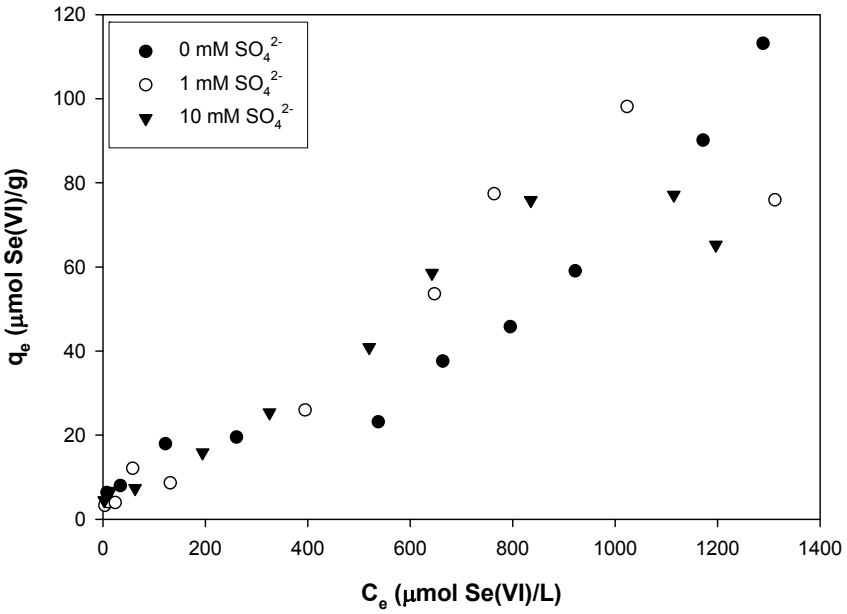

Figure 120. Amounts of Se(VI) removed per mass of solid (FeS) as functions of concentration of Se(VI) in water as affected by sulfate concentration (1 and 10 mM) at pH 8.

Figure 121 shows results of experiments on the stability of Se(VI)-contacted FeS. For these experiments, pH was initially adjusted to near pH 4 and then raised in a series of steps. Removal of Se(VI) decreased as pH increased with a minimum near pH 6. Removals increased above pH 6 with near complete removal observed near pH 8 and above. No Se(VI) was released when pH was decreased. This indicates that strong bonds were formed by reaction between selenium and the FeS, possibly including redox reactions, such as in the Se(VI)-pyrite sorption system. Both Se(IV) and Se(VI) are stable after contact with FeS when pH is optimal and sufficient time is allowed for surface reactions.

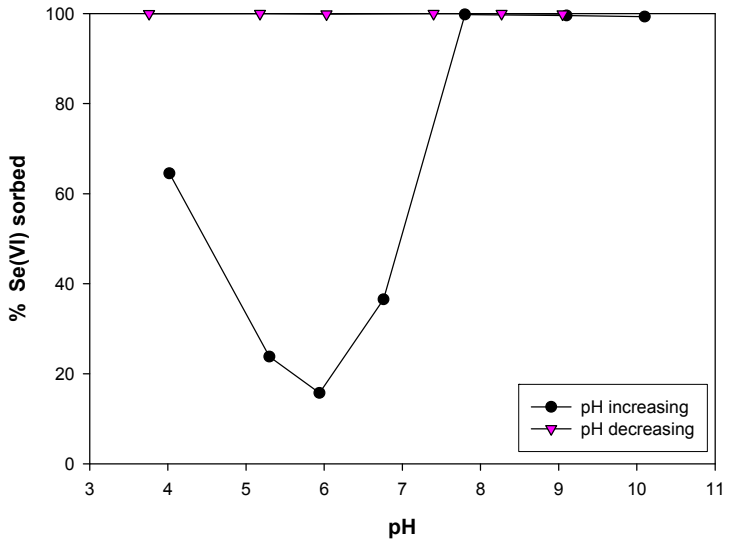

Figure 121. Effect of pH on removal of Se(VI) (16.6 μM) by FeS (1 g/L) as pH was increased from near pH 4 and subsequently was decreased.

Characterization of Selenium-Mackinawite

Figure 122 shows Fe $2p_{3/2}$ XPS spectra for mackinawite reacted with a solution of Se(IV) for various times. Four major peaks are observed at 705.9~707.2, 707.4~707.8, 708.7~709.6, 709.8~712.2 eV, corresponding to Fe(II)-S, Fe(II)-O, Fe(III)-S, Fe(III)-O, respectively. As contact time increases, the relative areas of the peaks associated with Fe(III)-S and Fe(III)-O increase and the relative peak areas associated with Fe(II)-S, Fe(II)-O decrease, indicating an oxidation of the iron on the pyrite surface.

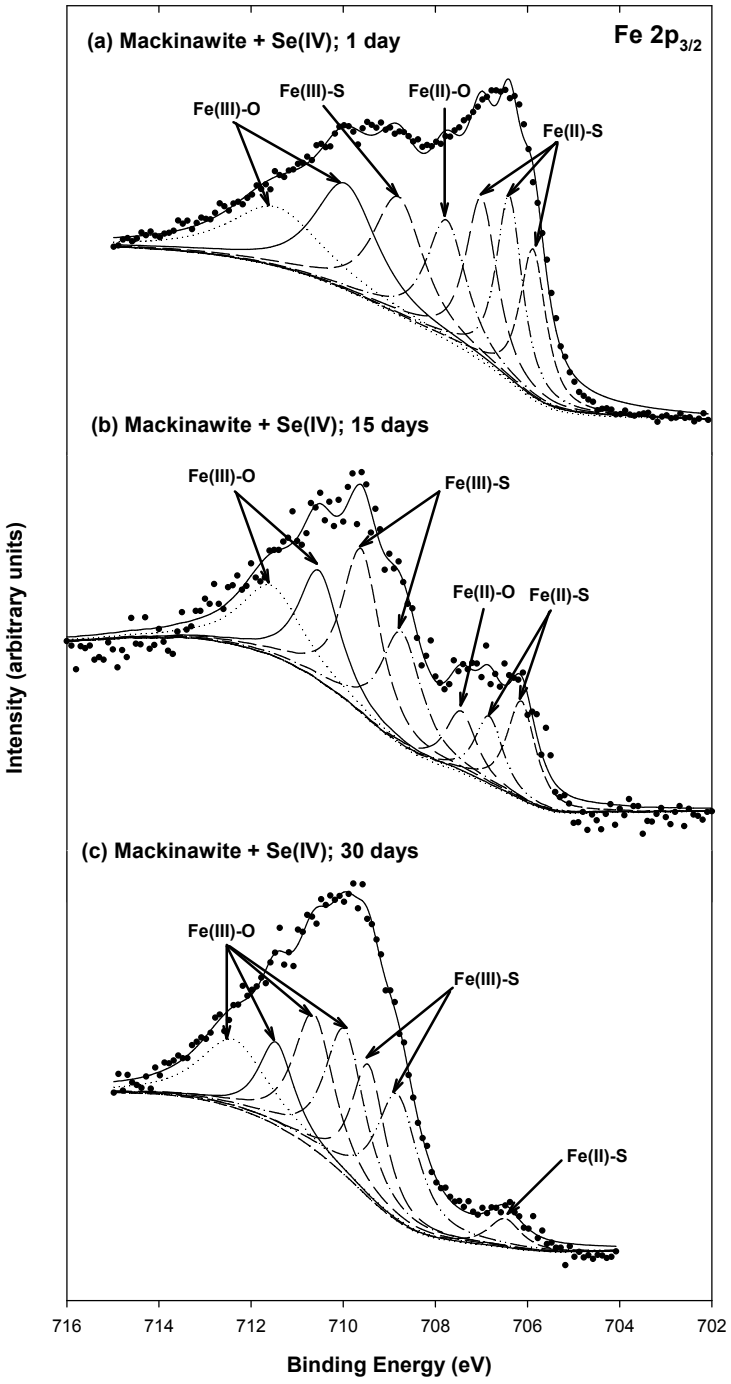

Figure 122. High resolution Fe $2p_{3/2}$ XPS spectra of synthetic mackinawite (1 g/L) reacted with 3.1×10^3 μM Se(IV) at pH 8 for various times: (a) 1 day, (b) 15 days, (c) 30 days.

Figure 123 shows the Fe $2p_{3/2}$ XPS spectra for mackinawite contacted with a solution of Se(VI) for various times. As contact time increases, the relative area of the peak associated with Fe(III)-O increases, but magnitude of the change is not as great as was observed for Se(IV). These results indicate that Fe(II) on the pyrite surface undergoes a redox reaction with Se(IV)

and Se(VI) resulting in formation of Fe(III) and reduced chemical species (Se(IV), Se(0), Se(-I), Se(-II)). However, the extent of oxidation of Fe(II) by Se(IV) is greater than by Se(VI).

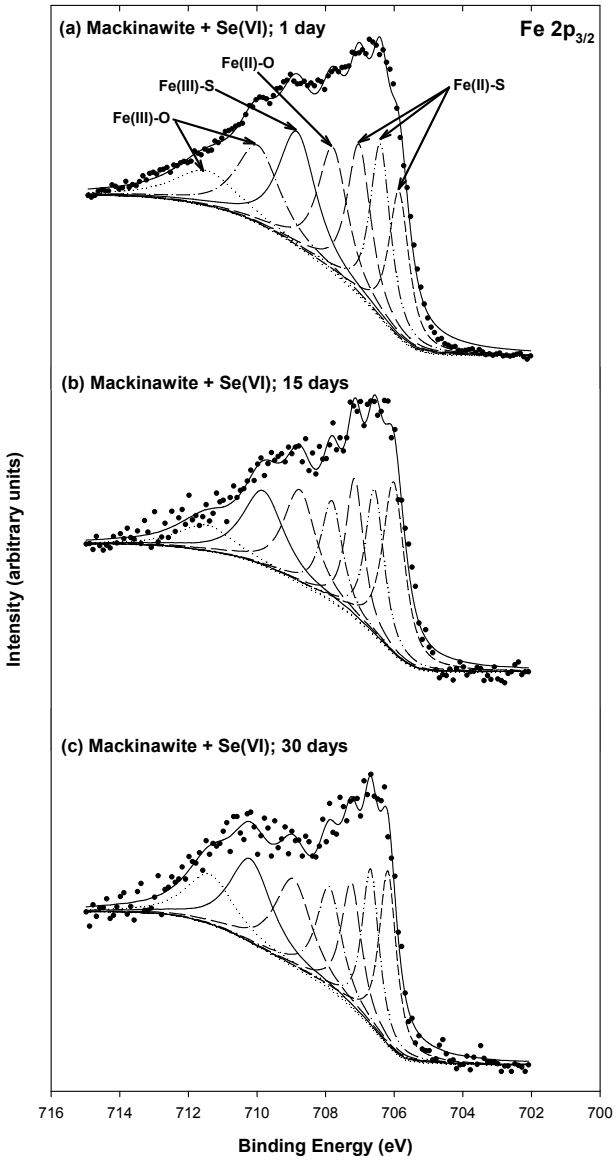

Figure 123. High resolution Fe $2p_{3/2}$ XPS spectra of synthetic mackinawite (1 g/L) reacted with 3.1×10^3 μM Se(VI) at pH 8 for various times: (a) 1 day, (b) 15 days, (c) 30 days.

Figures 124 and 125 show the S 2p XPS spectra for mackinawite reacted with Se(IV) and Se(VI), respectively. In order to fit the asymmetric peak centered near 161.8 eV and the high energy tail, polysulfides (S_n^{2-}) and elemental sulfur (S^o) were considered as surface species. Some oxidation of mackinawite surface could occur during the transfer of samples for XPS analysis. In case of Se(IV), peaks associated with the sulfate ion (SO_4^{2-}) were observed after 15 days of contact, whereas there were no sulfate peaks in the S 2p spectra after contact with Se(VI). These results support the hypothesis that sulfur on the surface of mackinawite act as reductants to reduce Se(IV) or Se(VI), but with a greater affinity for Se(IV).

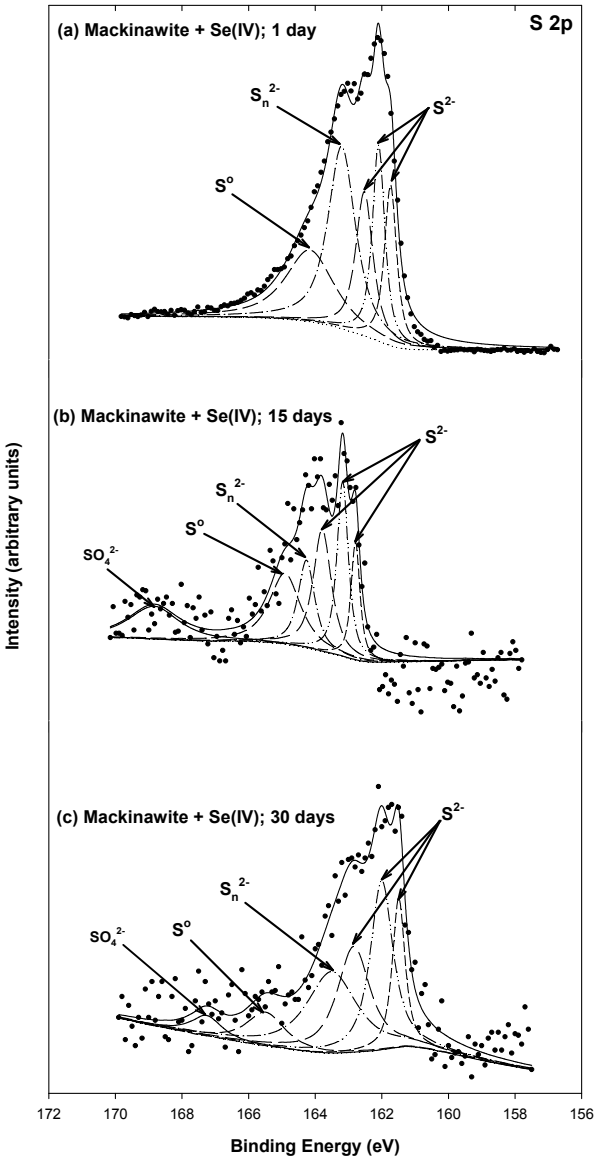

Figure 124. High resolution S 2p spectra of synthetic mackinawite (1 g/L) reacted with 3.1×10^3 μM Se(IV) at pH 8 for various times: (a) 1 day, (b) 15 days, (c) 30 days.

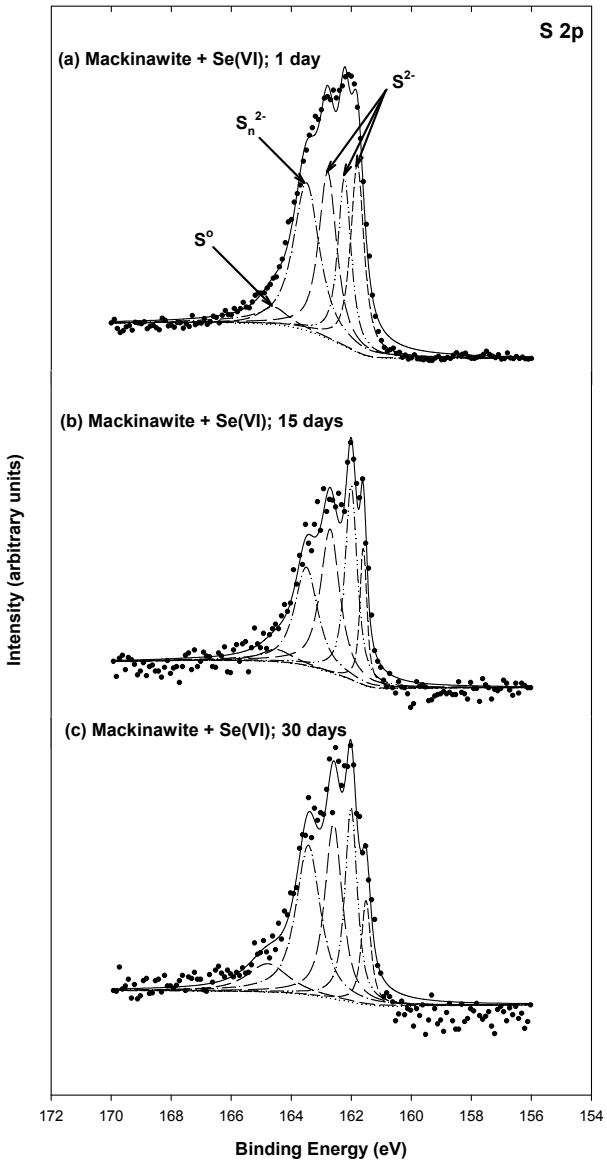

Figure 125. High resolution S 2p spectra of synthetic mackinawite (1 g/L) reacted with 3.1×10^3 μM Se(VI) at pH 8 for various times: (a) 1 day, (b) 15 days, (c) 30 days.

Tables 40 and 41 present binding energies (BE), full width at half maximum (FWHM), and relative areas for peaks in the Fe $2p_{3/2}$ and S 2p XPS spectra of mackinawite contacted with Se(IV) and Se(VI) for various times.

Table 40. Binding energies (BE), full width at half maximum (FWHM), and area percentage for peaks in the Fe $2p_{3/2}$ XPS spectra of mackinawite contacted with Se(IV) and Se(VI) for various times.

Sample	Contact time (days)	BE (eV)	FHWM (eV)	Area (%)	Chemical states
Mackinawite	0	706.0	0.49	10.4	Fe(II)-S
		706.4	0.55	14.6	Fe(II)-S
		706.9	0.71	17.8	Fe(II)-S
		707.7	0.98	18.7	Fe(II)-O
		708.8	1.26	14.6	Fe(III)-S
		710.1	1.67	14.9	Fe(III)-O
		711.8	2.51	9.0	Fe(III)-O
Mackinawite+Se(IV)	1	705.9	0.68	10.7	Fe(II)-S
		706.4	0.68	13.2	Fe(II)-S
		707.0	0.81	13.9	Fe(II)-S
		707.7	1.03	13.0	Fe(II)-O
		708.8	1.30	16.2	Fe(III)-S
		709.9	1.61	18.0	Fe(III)-O
		711.5	2.39	15.0	Fe(III)-O
	15	706.1	0.75	10.9	Fe(II)-S
		706.8	0.72	7.3	Fe(II)-S
		707.4	0.82	7.2	Fe(III)-O
		708.7	1.05	17.5	Fe(III)-S
		709.6	0.98	23.8	Fe(III)-S
		710.5	1.06	17.1	Fe(III)-O
		711.6	1.56	16.3	Fe(III)-O
	30	706.5	0.82	3.1	Fe(II)-S
		708.9	1.17	22.6	Fe(III)-S
		709.5	0.79	13.9	Fe(III)-S
		710.1	1.02	21.4	Fe(III)-O
		710.7	0.89	13.7	Fe(III)-O
		711.4	0.65	6.4	Fe(III)-O
		712.2	1.82	19.0	Fe(III)-O
Mackinawite+Se(VI)	1	705.8	0.70	12.5	Fe(II)-S
		706.4	0.71	14.9	Fe(II)-S
		707.0	0.82	15.1	Fe(II)-S
		707.7	1.03	15.7	Fe(II)-O
		708.8	1.30	18.1	Fe(III)-S
		709.9	1.50	14.2	Fe(III)-O
		711.4	2.21	9.5	Fe(III)-O
	15	706.0	0.76	20.1	Fe(II)-S
		706.5	0.65	14.6	Fe(II)-S
		707.1	0.62	13.4	Fe(II)-S
		707.8	0.75	11.6	Fe(II)-O
		708.7	1.11	16.1	Fe(III)-S
		709.8	1.43	16.5	Fe(III)-O
		711.4	1.91	7.6	Fe(III)-O
	30	706.1	0.59	15.2	Fe(II)-S
		706.6	0.59	13.4	Fe(II)-S
		707.2	0.70	12.7	Fe(II)-S
		707.8	0.87	12.9	Fe(II)-O
		708.9	1.27	16.1	Fe(III)-S
		710.1	1.47	17.7	Fe(III)-O
		711.3	1.66	12.0	Fe(III)-O

Table 41. Binding energies (BE), full width at half maximum (FWHM), area percentage for peaks in the S 2p XPS spectra of mackinawite contacted with Se(IV) and Se(VI) for various times.

Sample	Contact time (days)	BE (eV)	FHWM (eV)	Area (%)	Chemical states
Mackinawite	0	161.3	0.55	14.0	S^{2-}
		161.8	0.62	22.0	S^{2-}
		162.3	0.68	26.3	S^{2-}
		163.1	1.03	35.0	S_n^{2-}
		164.5	0.88	2.6	S^o
Mackinawite+Se(IV)	1	161.7	0.44	12.8	S^{2-}
		162.0	0.44	15.8	S^{2-}
		162.5	0.62	16.2	S^{2-}
		163.2	0.99	32.6	S_n^{2-}
		164.1	1.73	22.5	S^o
	15	161.6	0.50	10.1	S^{2-}
		162.0	0.46	18.9	S^{2-}
		162.7	0.73	21.0	S^{2-}
		163.2	0.67	13.8	S_n^{2-}
		164.0	1.25	20.8	S^o
		168.4	1.99	15.4	SO_4^{2-}
	30	161.4	0.45	12.4	S^{2-}
		162.0	0.81	25.3	S^{2-}
		162.8	1.18	23.0	S^{2-}
		163.5	1.79	27.0	S_n^{2-}
		165.4	1.37	8.4	S^o
		167.2	1.08	3.9	SO_4^{2-}
Mackinawite+Se(VI)	1	161.8	0.53	21.0	S^{2-}
		162.2	0.51	18.4	S^{2-}
		162.7	0.71	24.8	S^{2-}
		163.4	1.03	31.7	S_n^{2-}
		164.6	1.13	4.2	S^o
	15	161.5	0.50	11.0	S^{2-}
		162.0	0.48	27.2	S^{2-}
		162.7	0.76	31.6	S^{2-}
		163.5	0.91	26.0	S_n^{2-}
		164.5	1.24	4.3	S^o
	30	161.5	0.50	8.9	S^{2-}
		162.0	0.48	21.3	S^{2-}
		162.5	0.69	27.1	S^{2-}
		163.4	0.96	32.3	S_n^{2-}
		164.7	1.63	10.4	S^o

Figure 126 shows the Se 3d XPS spectra of mackinawite before and after contact with Se(IV) or Se(VI) for various reaction times. Before contact with Se, the Se 3d spectra for mackinawite show a peak, because the Fe 3p spectra with binding energy in the range of 50-65 eV interfere. Figure 126 shows major changes in the Se 3d spectra after mackinawite contacts a solution of Se(IV). The binding energy of the main peaks shift from 53.5 eV to around 55.6 eV and the area of the peaks increase. These results can be attributed to sorption of Se(IV) to the surface of mackinawite and subsequent reduction via surface reaction to form species such as Se(0), Se(-I), or Se(-II)). The main peaks of these reduced selenium species occur with binding

energies in the range of 53.7~56.3 eV, which is range where peaks are observed in Figure 126(a). Figure 126(b) indicates that there are no important changes in Se 3d spectra for mackinawite after contact with Se(VI). The lack of major changes could be caused by low amounts of Se(VI) being and small fractions of sorbed Se(VI) being reduced.

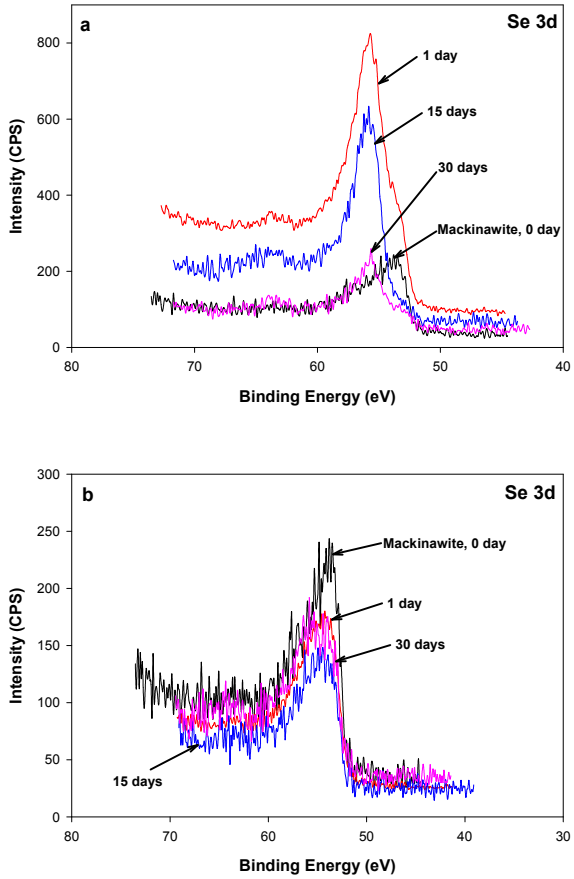

Figure 126. High resolution Se 3d spectra of synthetic mackinawite (1 g/L) reacted with (a) 3.1 $\times 10^3$ μM Se(IV) and (b) 3.1 $\times 10^3$ μM Se(VI) at pH 8 and various contact times.

To further investigate possible surface reactions, the surface of Se(VI)-contacted FeS formed at pH 10 was analyzed by SEM-EDS and XPS. Figure 127 shows the results of SEM-EDS analysis for Se(VI)-contacted FeS. Analogous to the Se(VI)-contacted pyrite formed at pH 10, the Se(VI)-contacted FeS shows the formation of precipitates presenting as small thin rod-like solids. Figure 128 indicated the results of Se 3d XPS spectra for Se(VI)-contacted FeS along with the previous XPS data. In contrast to previous results, the center of the main peak was shifted, which means that Se(VI) was reduced to forms such as Se(III), Se(0), Se(-I), or Se(-II). These more reduced species may be more tightly bound to the surface or may form insoluble solid phases distinct from FeS. Such transformations would explain the behavior observed in the stability experiments.

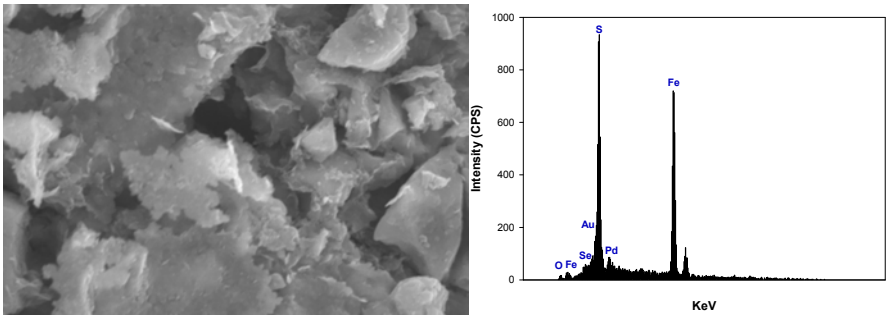

Figure 127. Secondary image and EDS spectra of SEM analysis for mackinawite reacted with Se(VI) (16.5 µM) at pH 10.

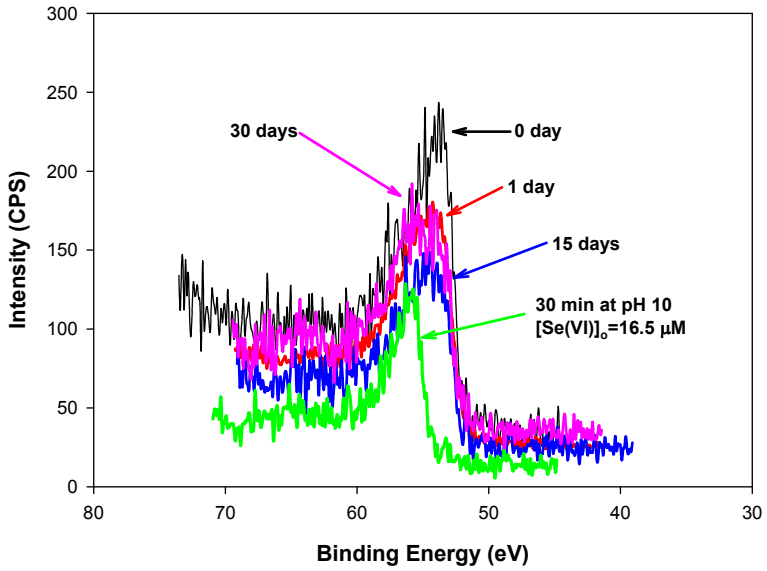

Figure 128. Comparison of Se 3d spectra for Se(VI) (16.5 µM) contacted mackinawite (1 g/L) at pH 10 for 30 minutes with the previous XPS data Se(VI) (3.1 mM) contacted with mackinawite (1 g/L) at pH 8 for 1, 15, 30 days.

CONCLUSIONS

Experimental Methods

Experimental procedures were developed and verified for the important constituents to be measured during this project. These include two oxidation states of arsenic (As(III) and As(V)), two oxidation states of selenium (Se(IV) and Se(VI)), mercury and iron. For each analysis, calibration curves were produced that were linear and showed little error, as indicated by high values of R^2. Replicate analyses demonstrated that the techniques had good to excellent precision and accuracy. Method detection limits were much lower than required to conduct the experiments. These results show that the analytical procedures will provide accurate analyses of target compounds during experiments to determine the ability of iron sulfide and pyrite to remove these compounds from ash and scrubber pond waters.

Characterization of Adsorbent-Reactants

Analysis of pyrite and iron sulfide by TEM showed that they have particle sizes of 100 – 1000 nm and < 100 nm, respectively. Results of XRD analysis confirmed that pyrite crystals were being produced by the synthesis method employed and that the form of iron sulfide being produced was mackinawite.

Surface characterization by XPS was conducted for pyrite (FeS_2) and mackinawite (FeS) without contacting the solids with any target contaminants. XPS target elements included Fe (2 $p_{3/2}$), S (2p) and O (1s). Fe $2p_{3/2}$ spectra of pyrite contained peaks associated with Fe(II)-S, Fe(III)-S and Fe(III)-O species. Existence of Fe(III) species indicated that some oxidation occurred, probably due to oxygen intrusion during sample handling. S 2p spectra showed one doublet that corresponded to S_2^{2-} species. No peaks associated with elemental sulfur were observed for the synthetic pyrites prepared in the laboratory. The O 1s spectra showed peaks associated with O_2^-, OH^- and molecular H_2O.

Fe $2p_{3/2}$ spectra for synthetic mackinawite had a long left tail which indicated presence of additional species beyond Fe(II)-S, such as Fe(II)-O, Fe(III)-S, and Fe(III)-O. The presence of Fe(II)-O could be the result of surface hydroxylation (Demoisson, et al., 2007). The presence of some Fe(III)-O species could originate from oxidation of Fe(II) by exposure to air during sample transfer prior to XPS analysis. The S 2 p spectra for mackinawite showed existence of polysulfides and elemental sulfur in addition to sulfide.

Arsenic Removal and Stability

Experiments on arsenic removal by pyrite showed that removal of As(V) from solution was faster than removal of As(III). This indicates that As(III) and As(V) are interacting differently with the pyrite surface. Mass transport limitations to removal kinetics should be similar for both As(III) and As(V), so any difference in removal kinetics must be attributed to differences in rates of reaction with the surface. The extent of removal of both As(III) and As(V) were more accurately described by the Langmuir model than the Freundlich model. Removal of As(III) was observed to increase as pH increased across the range investigated (pH 7 – pH 10). However, an optimum pH in the range between pH 8 and pH 9 was observed for removal of As(V). Sulfate had little effect on removal of As(III) or As(V) at the concentrations investigated (0, 1, 10 mM). There were small decreases in the amount of arsenic removed at the highest concentration of sulfate and the effect was more apparent with As(V) than with As(III). This

indicates that removal of arsenic by pyrite in ash pond waters should not be substantially affected by sulfate concentrations found there.

XPS analysis of pyrite after contact with As(III) showed evidence of oxidation of surface Fe, but little change to surface S or O. No change in the As 3d spectra, which indicates little reaction of As(III) on the pyrite surface.

Stability tests for mixtures of As(III) and pyrite showed low removal at low pH, increasing removal as pH was increased and moderate stability, i.e. moderate levels of release as pH was decreased, but not returning to levels of removal observed initially in the experiment.

XPS analysis of pyrite after contact with As(V) showed evidence of oxidation of surface Fe, but little change to surface O. There was some evidence that contact with As(V) led to more sulfate on the pyrite surface. There was a minor shift in a peak in the As 3d spectra that indicated possible reduction of As(V).

Stability tests for mixtures of As(V) and pyrite showed behavior that was similar to that for As(III), except low removals were observed initially at high pH, removals increased as pH decreased and moderate to high levels of stability were observed as pH was raised back to the initial values.

Removal of As(III) by FeS was fast with half life that is less than 10 minutes. This indicates that removal of As(III) on FeS is probably limited by external transport of the soluble compound to the surface of the solid. The effect of pH on removal of As(III) by FeS was moderate with highest removals occurring at intermediate pH (pH 8, pH 9). Classic isotherm models were not very effective in correlating data on removal of As(III) because of the irregularly shaped relationships between solid phase concentration and liquid phase concentration. The inability of isotherm models to describe systems in which surface reactions are probably occurring is not surprising. Sulfate inhibited removal of As(III) by FeS, but there was little difference between the effect of 1 mM and 10 mM sulfate, except at the highest concentrations of As(III).

XPS analysis of FeS after contact with As(III) for 30 days showed evidence for the reduction of arsenic and the oxidation of surface iron and sulfur species.

Stability tests that were conducted with mixtures of As(III) and FeS showed low removal of As(III) at high pH, increasing removal as pH was decreased, and nearly complete stability (no contaminant release) as pH was raised back to initial values. Surface analysis of mixtures of arsenic and FeS showed some evidence of change in redox state, which indicates that the high levels of stability are due to formation of strong bonds by redox reactions.

Removal of As(V) by FeS was fast, with a half-life that is less than 10 minutes. Removal of As(V) was faster than that of As(III), with nearly complete removal observed at the first sampling time (10 minutes). There was a strong effect of pH on removal of As(V) by FeS, with greater removals observed at lower pH. Isotherm models were not very effective in correlating data of solid-phase concentration as a function of liquid phase concentration, because the data did not show behavior that is typical of systems that have achieved adsorption equilibrium. Sulfate reduced removal of As(V) by FeS at higher concentrations of As(V), but showed a smaller effect at lower concentrations.

XPS analysis of FeS after contact with As(V) for 30 days showed evidence for the reduction of arsenic and the oxidation of surface iron and sulfur species.

Stability tests that were conducted with mixtures of As(V) and FeS showed similar behavior as that observed for mixtures of As(III) and FeS, but the levels of stability were moderate to high. Surface analysis of FeS after contact with As(V) showed some evidence of change in redox state, which indicates that the high levels of stability are due to formation of strong bonds by redox reactions.

Mercury Removal and Stability

Rates of removal of mercury were very rapid at lower ratios of mercury/pyrite. Concentrations of mercury in solution were below detection limits within 10 minutes. The mercury/pyrite ratio needed to be increased by a factor of 25 to obtain measurable concentrations over a wide time period. This behavior supports the hypothesis that external transport limitations to removal kinetics are minimal and that removal kinetics are controlled by surface reactions that become important at higher loadings of mercury on the pyrite surface. Pyrite was observed to removal much more mercury than arsenic. Maximum loadings of arsenic were in the range of 0.10 – 0.30 mmol/g, while loadings of mercury typically exceeded 6 mmol/g and in some cases exceeded 20 mmol/g. These loading mean that the mass of mercury removed exceeded the mass of pyrite. The pH of the solution did not appear to have a major effect on the extent of removal. However, there was a substantial amount of variability within the results of removal experiments at different pH. Exceptionally high removals of mercury could be the result of surface reactions that are initiated in some systems more rapidly than in others. The more rapid initiation of surface reactions could be caused by differences in surface characteristics of some pyrite particles. If experiments were conducted over longer time periods that would allow for initiation of surface reactions in all system, then these differences would tend to decrease. Sulfate was observed to have little effect on removal of mercury by pyrite over the concentration range that was investigated (0 – 10 mM). The rapid removal kinetics, the high loadings and the lack of inhibitory effects of sulfate support application of pyrite to removal of mercury from ash and scrubber pond waters.

XPS analysis of pyrite after contact with Hg(II) showed evidence of oxidation of surface Fe(II) species, but no evidence of changes in oxidation state of surface sulfur. However, there was little evidence that Hg(II) was being reduced by interaction with the pyrite surface.

Stability tests for Hg(II)/pyrite were conducted at two initial concentrations of Hg(II) to better evaluate stability. Nearly complete removal (>98%) was observed in all samples when the initial concentration was low. XPS analysis provided some evidence of mercury reduction and iron oxidation on the surface. When the initial concentration was high, low removal was observed at low pH, high removal as pH was raised to the range pH 4 – pH 6 and moderate removals at higher pH. Good stability was observed when pH was reduced. XPS analysis showed little evidence of mercury reduction, but good evidence of iron oxidation and formation of sulfur species that support formation of precipitates such as HgS or Hg_2S.

Removal of Hg(II) by FeS was observed to be rapid and extensive with amounts removed per mass FeS being in excess of 50 mmol/g. Fe(II) was not observed to be released to solution, so it must be retained in some manner in the solid phase. This could occur by formation of iron hydroxide solid phases, or formation of mixed iron-mercury solid phases. Anions would be required to be removed from solution to balance the charge of the mercury ions being removed and this could be accomplished by hydroxide, chloride or sulfate. A BET model best described the relationship between solid-phase and aqueous phase concentrations of Hg(II) in contact with

FeS at pH 10, which indicates that surface reactions probably occurred at the higher solid-phase concentrations. Such behavior was not observed at lower pH values during the reaction period (24 hours) examined. However, evidence of surface reactions at lower pH might be observed if experiments were conducted for longer time periods. Sulfate tended to increase the amounts of Hg(II) removed by FeS, but the effect was not large. This indicates that sulfate concentrations in ash pond and scrubber pond waters should not hinder removal of mercury.

XPS analysis of FeS after contact with Hg(II) for 30 days shows the presence of Hg(I) in addition to Hg(II). It also indicates the presence of more oxidized iron and sulfur species, which supports the conclusion that Hg is reduced by reaction with surface iron and sulfur.

Stability tests for Hg(II)/FeS were conducted at two initial Hg(II) concentrations. At low initial concentration, results showed good removals were observed for all pH and good stability. SEM images showed the presence of small particles surrounding FeS particles. XPS showed little change in the chemical nature of Hg, but showed some evidence of oxidation of Fe and S. At high initial concentration of Hg(II), high removals were observed under all conditions and high levels of stability were measured. SEM images showed formation of new particles and XPS analysis indicated little change in oxidation state of Hg, but oxidation of Fe and S.

Selenium Removal and Stability

Removal of Se(IV) by pyrite was slow, with half-lives of about 25 and 55 hours at pH 7 and pH 10, respectively. The slower removal kinetics indicate that surface reactions control the rates of removal rather than external mass transport kinetics. The effect of pH on removal of Se(IV) by pyrite was small. The extent of removal was a little greater at lower pH, possibly due to the faster removal kinetics. Sulfate inhibited removal of Se(IV) by pyrite at higher concentrations of Se(IV), but the effect was smaller, or non-existent, at lower concentrations.

XPS analysis of pyrite after contact with Se(IV) indicated that the presence of Fe(III)-O increased, which indicate oxidation of surface Fe(II) by Se(IV) or other compounds. Evidence was found for the presence of additional sulfur species, such as sulfide and sulfate. This indicates that the sulfur at the surface of pyrite (S_2^{2-}) can be both oxidized and reduced after contact with Se(IV). Binding energies of peaks in the Se 3d spectra were observed to increase with time after pyrite was contacted with Se(IV). This could be due to reactions of Se(IV) sorbed to the pyrite surface.

Results of stability tests for mixtures of Se(IV) and pyrite showed it to be a stable mixture. Nearly complete removal was observed as pH was lowered from an initial high value and no release of Se(IV) back to solution was seen after pH was subsequently raised. XPS indicated that the high level of stability could be due to reduction of Se(IV) to more stable forms.

Batch kinetic experiments showed rapid removal of Se(VI) by pyrite, especially at the lower initial concentrations of Se(VI). There was little effect of pH observed on removal of Se(VI) when the aqueous-phase concentrations were low. However, at higher aqueous-phase concentrations pH did affect the amounts removed, with greater removals observed in the order pH 7 > pH 8 ≈ pH 9 > pH 10. Sulfate had a negligible effect on removals at low aqueous-phase concentrations of Se(VI). However, unusual behavior was observed at higher concentrations, where the presence of sulfate reduced the amounts of Se(VI) removed. Furthermore, presence of sulfate resulted in lower removals at higher aqueous-phase concentrations of Se(VI) than at lower concentrations.

XPS analysis of pyrite after contact with Se(VI) indicated that the presence of Fe(III)-O increased, which indicate oxidation of surface Fe(II) by Se(VI) or other compounds. No substantial changes in the sulfur XPS spectra were observed after contact with Se(VI). No changes in Se 3d spectra were observed with time after contact of pyrite with Se(VI).

Stability tests with mixtures of Se(VI) and pyrite showed higher removals at extreme pH, but there was little stability observed.

Se(IV) was removed very rapidly and extensively by FeS, although not as extensively as was Hg(II). Evidence for surface reactions of Se(IV) on FeS was visible in removal patterns at pH 7 and pH 8, because they followed the pattern of a BET model. Sulfate had a negligible effect on removal of Se(IV) by FeS, so it should not hinder application of the process to ash or scrubber pond water.

XPS analysis of mackinawite after contact with Se(IV) showed evidence of continuous oxidation of surface Fe(II). S 2p spectra showed some evidence of oxidation of surface S(-II) resulting in formation of polysulfides, elemental sulfur, and possibly sulfate. Se 3d spectra showed evidence of reduction of Se(IV) by contact with the mackinawite surface. These observations support the conclusion that Se(IV) sorbs to the surface of mackinawite and oxidizes surface species of iron and sulfur.

Stability tests for mixtures of Se(IV) and FeS showed nearly complete removal at all but the high initial pH, so this mixture demonstrates high stability.

Removal of Se(VI) by FeS was less extensive than removal of Se(IV) or Hg(II). Some evidence of surface reactions was observed during kinetic tests conducted at the highest initial concentration examined (126 μM). Removals in this experiment increased at long contact times after being relatively constant for several hours. Additional evidence for surface reactions was observed in the removal patterns for experiments conducted at pH 7 and pH 8, which followed the BET model. Similar behavior might be observed at higher pH if longer reaction times were investigated. Sulfate (1, 10 mM) had little effect on removal of Se(VI) by FeS, but there was some indication that sulfate improved removal at intermediate concentrations.

XPS analysis of mackinawite after contact with Se(VI) also showed evidence of oxidation of surface Fe(II), but not to the extent observed with Se(IV). There was little evidence for formation of more oxidized forms of sulfur, so it appears that Se(VI) is a weaker oxidant for the surface of mackinawite, either because it sorbs less strongly or that it reacts less strongly after sorption. There was little evidence of reduction of Se(VI) after contact with mackinawite.

Stability tests for mixtures of Se(VI) and FeS showed moderate removal at low pH, a minimum removal near pH 6 and nearly complete removal at high pH. Very high stability was observed with negligible release as pH was decreased. SEM analysis indicated that thin rod-like solids were formed and XPS indicated that Se(VI) was chemically reduced.

Applicability to Treatment Systems

The focus of this research has been to evaluate the chemical interactions between target compounds (As(III), As(V), Hg(II), Se(IV), Se(VI)) and two adsorbent-reactants (FeS_2, FeS). Results of these experiments have generally shown that both solid phases can effectively remove the target compounds and form stable residuals that resist release of contaminants. In most cases, evidence was found that surface reactions occurred to change the chemical nature of the

target compounds to more stable forms. The effects of sulfate on removal were usually small or moderate, indicating that sulfate levels found in FGD wastewaters may not inhibit the process. Therefore, the process of applying pyrite or mackinawite to remove arsenic, mercury and selenium from power plant wastewaters appears to be feasible chemically. However, for development into a treatment process issues related to the methods of contacting the wastewater with the adsorbent-reactants must be solved.

The adsorbent-reactant solids are sub-micron in size, so methods must be developed to effectively contact them with the wastewater and then remove them from the wastewater. This may be done by application of ultrafiltration, but issues of fouling must be evaluated. Addition of coagulants might enhance removal, but this issue must be investigated. Another alternative would be to incorporate the sub-micron scale adsorbent-reactant particles into macro-scale particles. This might be accomplished by aggregating the sub-micron particles into larger aggregates, while maintaining sufficient porosity to allow for sufficiently fast removal kinetics. Another approach would be to produce the adsorbent-reactant particles within the existing framework of a porous solid phase such as silica.

REFERENCES

Behra, P.; Bonnissel-Gissinger, P.; Alnot, M.; Revel, R.; Ehrhardt, J. J. XPS and XAS Study of the Sorption of Hg(II) onto Pyrite. *Langmuir*. **2001**, 17, 3970-3979.

Bonnissel-Gissinger, P.; Alnot, M.; Ehrhardt, J-J.; Behra, P. Surface Oxidation of Pyrite as a Function of pH. *Environ. Sci. Technol*. **1998**, 32, 2839-2845.

Bostick, B.; Fendorf, S. Arsenite Sorption on Troilite (FeS) and Pyrite (FeS_2). *Geochimica et Cosmochimica Acta*, **2003**, 67, 909-921.

Bower, J.; Savage, K.S.; Weinman, B.; Barnett, M.O.; Hamilton, W.P; Harper, W.F. Immobilization of Mercury by Pyrite (FeS_2). *Environ. Pollution.* **2008**, 156, 504-514.

Demoission, F.; Mullet, M.; Humbert, B. Investigation of Pyrite Oxidation by Hexavalent Chromium: Solution Species and Surface Chemistry. *J. Colloid Interface Sci.* **2007**, 316, 531-540.

Dong, R.; Yu, L. Y. E., Investigation of surface changes of nanoparticles using TM-AFM phase imaging. *Environ. Sci. Technol*. **2003**, 37, (12), 2813-2819.

Dzombak, D.E.; Morel, F.M.M. Surface Complexation Modeling-Hydrous Ferric Oxide; Wiley: New York, **1990**.

Eaton, A.D., Clesceri, L.S., Greenberg, A.E., (1995) *Standard Methods for the Examination of Water and Wastewater 19th Edition*, American Public Health Association, Washington DC.

Ehrhardt, J. J.; Behra, P.; Bonnissel-Gissinger, P.; Alnot, M. XPS Study of the Sorption of Hg(II) onto Pyrite FeS_2. *Surface Interface Anal*. **2000**, 30, 269-272.

Farquhar, M.; Charnock, J.; Livens, F.; Vaughan, D. Mechanisms of Arsenic Uptake from Aqueous Solution by Interaction with Goethite, Lepidocrocite, Mackinawite, and Pyrite: An X-ray Absorption Spectroscopy Study. *Environ. Sci. Technol*. **2002**, 36, 1757-1762.

Gallegos, T.J.; Hyun, S.P.; Hayes, K.F. Spectroscopic Investigation of the Uptake of Arsenite from Solution by Synthetic Mackinawite. *Environ. Sci. Tech*. **2007**, 41, 7781-7786.

Gibbs, C. R. *Analytical Chemistry* **1976**, *48*, 1197-1201

Gibbs, C. R., "Characterization and Application of FerroZine Iron Reagent as a Ferrous Iron Indicator", *Analytical Chemistry* **1976**, 48:1197-1201.

Hyland, M.; Jean, G.; Bancroft, G. XPS and AES Studies of Hg(II) Sorption and Desorption Reactions on Sulfide Minerals. *Geochimica et Cosmochimica Acta*. **1990**, 54, 1957-1967.

Ihanus, J., Lambers, E., Holloway, P. H., Ritala, M., and Leskela, M., 2004. XPS and electroluminescence studies on SrS1-xSex and ZnS1-xSex thin films deposited by atomic layer deposition technique. *Journal of Crystal Growth* **260**, 440-446.

Jeong, H.Y.; Klaue, B.; Blum, J.D.; Hayes, K.F. Sorption of Mercuric Ion by Synthetic Nanocrystalline Mackinawite (FeS). *Environ. Sci. Technol*. **2007**, 41, 699-705.

Knipe, S.; Mycroft, J.; Pratt, A.; Nesbitt, H.; Bancroft, G. X-ray Photoelectron Spectroscopic Study of Water Adsorption on Iron Sulphide Minerals. *Geochimica et Cosmochimica Acta*, **1995**, 59, 1079-1090.

Masscheleyn, P.H., Delaune, R.D., Patrick, W.H., "A Hydride Generation Atomic Absorption

Technique for Arsenic Speciation", *Journal of Environmental Quality*, **1991**, 20:96-100.

Naveau, A.; Monteil-Rivera, F.; Guillon, E.; Dumonceau, J. Interaction of Aqueous Selenium(-II) and (IV) with Metallic Sulfide Surfaces. *Environ. Sci. Technol*. **2007**, 41, 5376-A

Nesbitt, H. W. and Muir, I. J.,. X-Ray photoelectron spectroscopic study of a pristine pyrite surface reacted with water-vapor and air. *Geochim. Cosmochim. Acta* **1994**, 58, 4667-4679.

Schaufuss, A.; Nesbitt, H.; Scaini, M.; Hoechst, H.; Bancroft, M.; Szargan, R. Reactivity of Surface sites on Fractured Arsenopyrite (FeAsS) toward Oxygen. *Am. Mineral*. **2000**, 85, 1754-1766.

Wang, K.; Lee, H.; Cooper, R.; Liang, H., Time-resolved, stress-induced, and anisotropic phase transformation of a piezoelectric polymer. *Applied Physics a-Materials Science & Processing* , **2009**, 95, (2), 435-441.

Wei, D. Osseo-Asare, K., (1996) "Particulate pyrite formation by the Fe^{3+}/HS^- reaction in aqueous solutions: effects of solution composition", *Colloids and Surfaces A: Physicochemical and Engineering Aspects*, 118: 51-61.